3D MR Spirometry

Nathalie Barrau

université PARIS-SACLAY

3D MR Spirometry

Spirométrie 3D par résonance magnétique

Thèse de doctorat de l'université Paris-Saclay

École doctorale n°575, electrical, optical, bio : physics and engineering (EOBE)
Spécialité de doctorat : Physique et imagerie médicale
Graduate School : Sciences de l'ingénierie et des systèmes. Référent : Faculté des sciences d'Orsay

Thèse préparée dans l'unité de recherche **Laboratoire d'Imagerie Biomédicale Multimodale Paris Saclay (Université Paris-Saclay, CEA, CNRS, Inserm)**, sous la direction de **Vincent LEBON**, Professeur des Universités-Praticien Hospitalier, le co-encadrement de **Xavier MAÎTRE**, Chargé de recherche, **Claire PELLOT-BARAKAT**, Chargée de recherche, et **Tanguy BOUCNEAU,** Ingénieur

Thèse soutenue à Paris-Saclay, le 27 juin 2024, par

Nathalie BARRAU

Composition du jury

Membres du jury avec voix délibérative

Luisa CIOBANU Directrice de recherche, Université Paris-Saclay	Présidente
Elise BANNIER Ingénieure de recherche - HDR, Université Rennes 1	Rapporteure & Examinatrice
Bruno MADORE Maître de conférence - Harvard Medical School	Rapporteur & Examinateur
Nadjia KACHENOURA Directrice de recherche, Sorbonne Université	Examinatrice

THESE DE DOCTORAT
NNT: 2024UPAST077

université PARIS-SACLAY

ÉCOLE DOCTORALE
Physique et ingénierie : Electrons, Photons, Sciences du vivant (EOBE)

Titre: Spirométrie 3D par résonance magnétique

Mots clés: Poumon; IRM; Spirométrie; Ventilation; Biomécanique; Exploration fonctionnelle respiratoire

Résumé:

La ventilation est une fonction complexe, avec des variabilités naturelles intra- et inter-individuelles imprévisibles, parfois inhomogènes dans le volume pulmonaire. La spirométrie standard est l'examen de référence pour évaluer la fonction ventilatoire à partir de courbes débit-volume mesurées à la bouche et en respiration forcée. Cette technique simple et fiable est limité par la nécessaire coopération du patient, ainsi que par la nature globale de sa mesure. Étant donné que la respiration est intrinsèquement un phénomène tridimensionnel et que les maladies pulmonaires sont généralement régionales, la ventilation devrait être sondée localement.

Malgré les difficultés inhérentes à l'application de l'IRM au poumon, de récent progrès ont permis de révéler le potentiel de l'IRM fonctionnelle pulmonaire à partir d'acquisitions standards facilement transposables en clinique. Depuis une quinzaine d'années des développements évaluent la ventilation à partir de la variation du signal IRM au cours de la respiration. Ces techniques reposent sur une hypothèse forte de linéarité du signal IRM avec la densité de tissus pulmonaire. Une nouvelle méthode évaluant la ventilation localement et dynamiquement à partir des déformations a été développée : la spirométrie 3D par IRM. A partir d'un cycle respiratoire moyen, le Jacobien des déformations et sa dérivée temporelle permettent d'inférer les courbes débit-volume locales. Cette thèse s'attache à valider la spirométrie 3D par IRM, à l'amener à la recherche clinique, et à approfondir la compréhension de la mécanique ventilatoire.

Le caractère multidimensionnel de la spirométrie 3D par IRM intègre la complexité de la fonction respiratoire mais la technique encore neuve doit être développée et éprouvée. Les évolutions méthodologiques entreprises durant cette thèse incluent une reconstruction optimisée de la dynamique pulmonaire, une segmentation précise des structures lobaires, la définition de biomarqueurs quantitatifs, ainsi qu'une normalisation des cartes fonctionnelles pour permettre des comparaison intra- et inter-sujets. Une étude prospective sur 25 volontaires (10 femmes, 45 ± 17 ans) respirant librement a été menée, avec des acquisitions répétées en position allongée. La fiabilité de la technique a été approchée selon deux critères : sa répétabilité et son exactitude. Les mesures de volumes courants locaux intégrés sur le volume pulmonaire correspondent à ce qui peut être mesuré par segmentation des volumes pulmonaires. Une excellente répétabilité globale a été trouvée, avec une variabilité résiduelle induite par celle intrinsèque à la respiration.

La sensibilité de la spirométrie 3D par IRM a été d'abord étudiée sur 25 volontaires sains en position allongée sur le dos puis sur le ventre. Les cartes fonctionnelles mettent en évidence un gradient de ventilation vers les régions les plus dépendantes à la gravité, démontrant la sensibilité de la technique à la physiologie. Des atlas fonctionnels ont été établis à partir des cartes individuelles normalisées, révélant les motifs nominaux de la ventilation pulmonaire reproductibles sur la cohorte de volontaire. Les distributions spatiales mettent en évidence l'inhomogénéité de la ventilation en respiration libre.

Enfin, la sensibilité de la spirométrie 3D aux pathologies obstructives et restrictives est évaluée à travers plusieurs études de cas de maladies neuromusculaires, COVID-19 longue durée, asthme et bronchopneumopathie chronique obstructive (BPCO). Ces recherches soulignent l'importance de caractériser les modes de respiration avec les contributions des muscles respiratoires. La réversibilité de l'asthme à l'administration d'un bronchodilatateur a été trouvé, avec une augmentation marquée des débits après bronchodilatateurs. Une étude longitudinale sur un cas d'asthme sévère a aussi mis en évidence l'efficacité de la biothérapie pour améliorer la fonction ventilatoire, réduisant le volume résiduel ainsi que l'obstruction.

université PARIS-SACLAY

ÉCOLE DOCTORALE
Physique et ingénierie : Electrons, Photons, Sciences du vivant (EOBE)

Title: 3D MR Spirometry

Keywords: Lung; MRI; Spirometry, Ventilation; Biomechanic; Pulmonary functional testing

Abstract:

Ventilation is a complex function, with unpredictable natural intra- and inter-individual variabilities, sometimes heterogeneous in lung volume. Standard spirometry is the reference exam to assess the ventilatory function from flow-volume loops measured at the mouth during forced expiration. This simple and reliable technique is limited by the necessary cooperation of the patient, as well as by the global nature of its measurement. Since breathing is inherently a three-dimensional phenomenon and lung diseases are generally regional, ventilation should be probed locally.

Despite the inherent difficulties in applying MRI to the lung, recent advancements have revealed the potential of functional pulmonary MRI from easily translatable standard acquisitions in clinical settings. Over the past fifteen years, developments have evaluated ventilation based on MRI signal variation during respiration. These techniques rely on a strong assumption of linearity of the MRI signal with lung tissue density. A new method evaluating ventilation locally and dynamically from deformations has been developed: 3D spirometry by MRI. From an average respiratory cycle, the deformation Jacobian and its temporal derivative allow inference of local flow-volume curves. This thesis aims to validate 3D spirometry by MRI, bring it into clinical research, and deepen the understanding of ventilatory mechanics.

The multidimensional nature of 3D spirometry by MRI integrates the complexity of respiratory function, but the new technique must still be developed and tested. Methodological developments undertaken during this thesis include optimized reconstruction of pulmonary dynamics, precise segmentation of lobar structures, definition of quantitative biomarkers, as well as normalization of functional maps to enable intra- and inter-subject comparisons. A prospective study on 25 volunteers (10 females, 45 ± 17 years old) breathing freely was conducted, with repeated acquisitions in the supine position. The reliability of the technique was approached by two criteria: its repeatability and accuracy. Measures of local tidal volumes integrated over the lung volume agreed to the measured lung volumes from segmentation. Excellent overall repeatability was found, with residual variability induced by that intrinsic to respiration.

The sensitivity of 3D MR spirometry was first studied in 25 healthy volunteers in lying supine and prone positions. Functional maps highlight a gradient of ventilation toward the more gravity-dependent regions, demonstrating the sensitivity of the technique to physiology. Functional atlases were established from normalized individual maps, revealing reproducible nominal patterns of pulmonary ventilation across the volunteer cohort. Spatial distributions highlight the heterogeneity of ventilation during free breathing.

Finally, the sensitivity of 3D MR spirometry to obstructive and restrictive pathologies is evaluated through several case studies of neuromuscular diseases, long COVID-19, asthma, and chronic obstructive pulmonary disease (COPD). These studies emphasize the importance of characterizing breathing patterns with contributions from respiratory muscles. Reversibility of asthma with bronchodilator administration was found, with a marked increase in flow rates after bronchodilators. A longitudinal study on a case of severe asthma also demonstrated the effectiveness of biotherapy in improving ventilatory function and reducing residual volume and obstruction.

Aknowledgments

Je remercie profondément toutes les personnes qui ont contribuées à ce travail doctoral. Vos conseils, expertises et soutiens ont rendu cette aventure possible.

Tout d'abord, je remercie le jury qui a évalué cette thèse. Spécifiquement, Luisa Ciobanu, Elise Bannier, Bruno Madore, et Nadjia Kachenoura qui ont rapporté et examiné cette thèse, ainsi que Hélène Salvator, PU-PH et pneumologue à l'Hôpital Foch, qui a été invitée au jury pour discuter des apports de la technique en pratique clinique. Les discussions avec l'ensemble du jury ont développées les perspectives de recherches autour de la spirométrie 3D par IRM.

Je souhaite également exprimer ma gratitude à l'équipe qui a encadré ce travail doctoral, Xavier Maître, Claire Pellot-Barakat, Tanguy Boucneau et Vincent Lebon, pour votre confiance et vos retours qui ont grandement enrichi la qualité de ce travail. Vos qualités humaines m'ont permis de réaliser ce travail avec liberté et écoute.

Un grand merci à l'équipe IRM, dont les discussions et nombreux retours constructifs m'ont fait progresser. La richesse des expertises et des qualités humaines dans l'équipe permettent une synergie collaborative inspirante et réconfortante, que j'ai beaucoup appréciée et que j'espère retrouver. Je remercie en particulier Angéline Nemeth, qui m'a beaucoup aidée lors de mes questionnements en physique de l'IRM et traitement des données, ainsi qu'Alexiane Pasquier, pour ses importantes relectures du manuscrit. Les réunions du mardi resteront de très bons souvenirs, entre le plaisir des réflexions scientifiques et les dégustations de gâteaux cuisinés par des personnes aux nombreux talents.

Je remercie le laboratoire et l'équipe DMI pour leur accueil chaleureux. Merci à Vincent Brulon pour le support technique apporté dans l'extraction des données, ainsi que Georges Willoquet pour le soutien indéfectible et très répété lors des petits (minis) soucis informatiques.

L'équipe des doctorant.es, post-doctorant.es, stagiaires, ainsi que les ancien.nes, ont également été d'un grand soutien pour ces années. Merci pour votre énergie, la bienveillance, l'entraide, les sorties, et votre humour de qualité. Je ne serai pas loin.

Enfin merci aux personnes qui ont mis des paillettes dans ma vie, en particulier mes ami.es des petites classes aux plus grandes, ainsi que les fanfares aux passions boxe et cuisine. Je remercie ma famille qui m'a soutenue à chaque étape de ce projet académique et professionnel, et notamment ma sœur pour sa très belle illustration de la spirométrie standard. Un merci spécial à Camille pour ces très belles années à tes côtés et tes conseils de docteure avisée.

Je souhaite une passionnante recherche aux suivant.es sur le projet V|LF-Spiro3D : Ithar Gharmaoui, Adrien Duwat, Yassine Nihou et Quentin Herszkowicz. Je suivrai avec intérêt votre travail et vos avancées.

Contents

Glossary

ADC . . . . . Analog to Digital Converter

ADI . . . . . Anisotropy Deformation Index

AZTEK . . . . Adaptive zero TE k-space trajectories

BW . . . . . BandWidth

COPD . . . . . Chronic Obstructive Pulmonary Disease

DLCO . . . . . Diffusion Capacity of the lung for carbon monoxide (CO)

FD . . . . . Fourier Decomposition

FEV1 . . . . . Forced Expiratory Volume at 1 s

FRC . . . . . Functional Residual Capacities

FSH . . . . . Facioscapulohumeral Muscular Dystrophy

FVC . . . . . Forced Vital Capacity

GE . . . . . General Electric

ICC . . . . . Intraclass correlation coefficient

IQR . . . . . InterQuartile Range

N4ITK . . . . Nonparametric nonuniform intensity normalization (N3) algorithm Insight Toolkit

PET . . . . . Positron Emission Tomography

RF . . . . . RadioFrequency

RV . . . . . Residual Volume

SAR . . . . . Specific Absorption Rate

SEF . . . . . Spontaneous Expiratory Flow

SPECT . . . . Single-Photon Emission Computed Tomography

SPEF . . . . . Spontaneous Peak Expiratory Flow

SNR . . . . . Signal to Noise Ratio

SRI . . . . . Slab to Rod Index

TE . . . . . Echo time

TR . . . . . Repetition time

TV . . . . . Tidal volume

UTE . . . . . Ultra short echo time

ZTE . . . . . Zero echo time

Introduction

Spirometry is the gold standard technique to assess the individual's ability to inhale and exhale efficiently. From flow-volume loops measured at the mouth during forced respiratory cycles, clinicians can characterize obstructive and restrictive syndromes. This technique is simple, reliable, and widely used in clinical routine for ventilation functional testing. However, it requires forced breathing, which is not always possible, and the measure at the mouth is only global, whereas diseases are generally localized. In the early stages of the disease, such measurements have been shown to lack sensitivity, as local impairments may not lead to global effects.

Magnetic resonance imaging (MRI) is a powerful tool for assessing local lung function. The development of hyperpolarized MRI in the late 90s has made it possible for the first time to assess ventilation at the voxel level throughout the lung volume. A hyperpolarized tracer gas is inhaled, and density is mapped at the end of inhalation using MRI. Despite wide research demonstrating the clinical interest of such regional measurements, an effective clinical translation in routine practice has been hindered by high costs, the complexity of the equipment, and protocol. Proton MRI, largely available in hospitals, was long neglected for lung application due to a low signal-to-noise ratio in the parenchymal tissues. From the work of Bauman *et al*, a gain of interest has been developed towards proton MRI for functional lung imaging, using the Fourier Decomposition of the MR signal over the dynamic acquisition. These approaches are based on the bold hypothesis of a linear relationship between the MR signal and ventilation.

Building on the foundation of functional lung imaging, the BioMaps laboratory has pioneered a novel approach to quantify the local ventilatory dynamics: 3D spirometry using MR imaging. This technique leverages dynamic lung MRI by combining an Ultrashort Echo Time (UTE) sequence integrated with an adaptive k-space trajectory. An average respiration is reconstructed from the ten-minute acquisition. Unlike standard spirometry, 3D MR spirometry is performed during free breathing and lying supine, making the examination accessible to patients who cannot be asked to cooperate like young children or patients with neurologic disorders. Moreover, this approach uses deformation fields to compute ventilation instead of

variations of the absolute magnitude of the MR signal, which makes it more robust to the intrinsic variability of the MR signal. The Jacobian of the strain tensor determines local ventilatory volumes, and local flow rates are derived by temporally differentiating these volumes. This approach provides a voxel-wise flow-volume loop, characterizing the local ventilation and its dynamic. A proof of concept was demonstrated with a single volunteer by comparing 3D spirometry maps for different types of breathing by Boucneau *et al.* The challenge now is to translate the technique into clinical research and explore its potential in lung pathophysiology.

Thesis outlines

Three-dimensional MR spirometry represents a real paradigm shift from standard spirometry, as measurements are conducted during free breathing in a lying position and are extracted over time in three dimensions rather than as global scalar values. The aim of this doctoral work was to develop and validate the technique to take it from the laboratory to clinical research and to deepen the understanding of spontaneous lung ventilation in healthy and obstructed lungs. This includes improving the robustness of the framework, assessing its reliability, testing its sensitivity in healthy volunteers and patient cohorts, and exploring the spatial distribution of ventilation patterns. The manuscript consists of the following five chapters.

Chapter 1 - The human lung pathophysiology

In this chapter, the human respiratory system is introduced, specifically the anatomy and function of the lung and their nominal variability. The pathology of the ventilatory system is then reviewed with a focus on the main obstructive respiratory diseases: asthma and chronic obstructive pulmonary disease (COPD). These two particular conditions are difficult to discriminate using conventional pulmonary functional tests and their potential subgroups are areas of research. This chapter describes standard exams to assess lung function, which is encompassed in what is called pulmonary function tests (PFTs). Their associated biomarkers of the global lung function are described with their pathophysiological insights. Finally, the role of imaging techniques for the ventilation function is highlighted.

Chapter 2 - MR ventilation imaging

In this chapter, the issues involved in performing lung imaging, and more specifically, lung functional imaging, are reviewed in detail. First, the principles of magnetic resonance imaging are revised with special attention to the challenges associated with lung tissue and respiration. The most common approaches used

to overcome these limitations and develop functional lung MRI are then presented. The assessment of local ventilation impairments is then evaluated through a review work of the literature over the last 5 years. Hyperpolarized gas MRI, oxygen-enhanced MRI, ^{19}Fluorine MRI, and non-enhanced proton MRI are thus compared with respect to their methodology, findings, and measurement specificities. Their different local ventilation biomarkers are presented, including gas distribution, dynamic markers, motion descriptors, and structural properties. The characterization of regional ventilation defects and their diagnostic insights are examined through clinical studies in asthmatic and COPD patients.

Chapter 3 - Methodological developments in 3D MR spirometry for clinical investigations

Throughout this doctoral work, several sources of instability affecting 3D MR spirometry have been identified and addressed, particularly during both the acquisition and post-processing steps. This includes navigating through the issues that arise when imaging lung dynamics during free breathing from hardware calibrations. Computational and methodological hurdles in processing the resulting data were addressed, with a focus on dynamic reconstruction, segmentation of the lung structures, and refinement of airflow computations to ensure reliable quantification of spirometric parameters. Clinical investigations were performed on healthy volunteers to evaluate the consistency of the technique with other modalities (CT and Fourier Decomposition MRI), its repeatability (global and local), and its global accuracy.

Chapter 4 - Nominal respiratory features of the lung function

This chapter evaluates the sensitivity of 3D MR spirometry in healthy volunteers and the nominal distribution of the extracted biomarkers. A prospective clinical study was performed in 25 healthy volunteers to evaluate the sensitivity of the technique to gravity lung dependence. Intra- and inter-subject variability was

handled with morphological normalization, and feature scaling was then described. Ultimately, reproducible functional patterns of the healthy lung were highlighted by constructing an atlas of the ventilatory function. Finally, lobar quantification of the dynamic ventilation was performed for the first time in free breathing.

Chapter 5 - Preliminary findings in obstructive and restrictive diseases using 3D MR spirometry

In this chapter, the sensitivity of 3D MR spirometry to restrictive and obstructive pulmonary conditions is assessed in individual cases and small patient cohorts. Long COVID-19, asthmatic, COPD, and neuromuscular conditions were explored. The specific reversibility of the asthmatic lung with a bronchodilator was evaluated against COPD and healthy groups. The effect of biotherapy was evaluated in an asthmatic patient and the potential of 3D MR spirometry to track improvements and changes in lung function that standard methods missed. These findings highlight the value of advanced imaging techniques in improving the diagnosis and patient care in respiratory medicine.

1

The human lung pathophysiology

The human respiratory system is vital for maintaining the balance between the need of the body for dioxygen and its need to eliminate carbon dioxide waste by enabling exchanges between the inside of the body and the outside environment. This chapter reviews lung anatomy, function, main respiratory disorders, and associated clinical exams. Understanding the pathophysiology of the human lung is essential for devising effective diagnostic and therapeutic strategies. Although this chapter will present the essential concepts for this thesis, a more in-depth description of lung pathophysiology can be found in Peracchia *et al.*[1]

1.1 Respiratory system physiology

In human cells, dioxygen is consumed during energy production from nutrients, and carbon dioxide is produced in a process called "cellular respiration", a part of the cell metabolism critical for maintaining its acid-base balance. The physiology of the respiratory system refers to the study of the mechanisms that ensure seamless gas exchange from the environment into the bloodstream and ultimately for cell metabolism. This part describes the lung anatomy with fundamental vocabulary, nominal functions of the respiratory system, and their intrinsic variability.

1.1.1 Anatomy of the respiratory system

The respiratory system comprises upper and lower tracks (see Figure 1.1). The upper respiratory tract includes the nasal and buccal passages, pharynx, and larynx, which filter, temper, and humidify incoming air. The lower respiratory tract comprises, on average, 23 divisions from the trachea to bronchi, then bronchioles and acini, until the smallest pulmonary unit, the alveoli, where the gas is ultimately conveyed. The surrounding tissue is referred to as lung parenchyma. There are around 480 million alveoli in humans, each having an average volume of $4.2 \times 10^(-3)$ µL.[2]

[1] Camillo Peracchia and Nasr Anaizi. *Lung function in health and disease. Basic concepts of respiratory physiology and pathophysiology.* Mar. 2014.

[2] Matthias Ochs et al. *American Journal of Respiratory and Critical Care Medicine*, 2004.

The surface area of these alveoli is estimated to be around 130 square meters,[3] providing an extensive area for gas exchange, as seen in the microscopic pictures of lung tissue (Figure 1.1). Airways diameter and thickness shrink over the divisions. Starting from the 15^{th} division, the airway wall begins to be decorated with alveoli, leading to the first interfaces of the respiratory tracts for gas exchanges. After three generations, the airway wall is completely decorated with alveoli, and gas diffuses through the thin air-blood tissue barrier estimated at 2.2 µm.[4] The lobule is the ultimate lung unit composed of alveolar ducts, alveolar sacs, and alveoli (see Figure 1.1). Lung alveolar walls are covered by a surfactant fluid, which decreases the surface tension of the alveoli, preventing the alveoli from collapsing at the end of expiration and making inflation easier. Tiny passageways (10-15 m in diameter) connect neighboring alveoli and enable gas and surfactant exchange within an alveolar sac to favor gas pressure equalization and to prevent lung collapse.[5]

[3] E. R. Weibel. *Swiss Medical Weekly*, 2009.
[4] P. Gehr et al. *Respiration Physiology*, 1978.
[5] Kohn Hans. *Muench Med Wochnschr*, 1893.

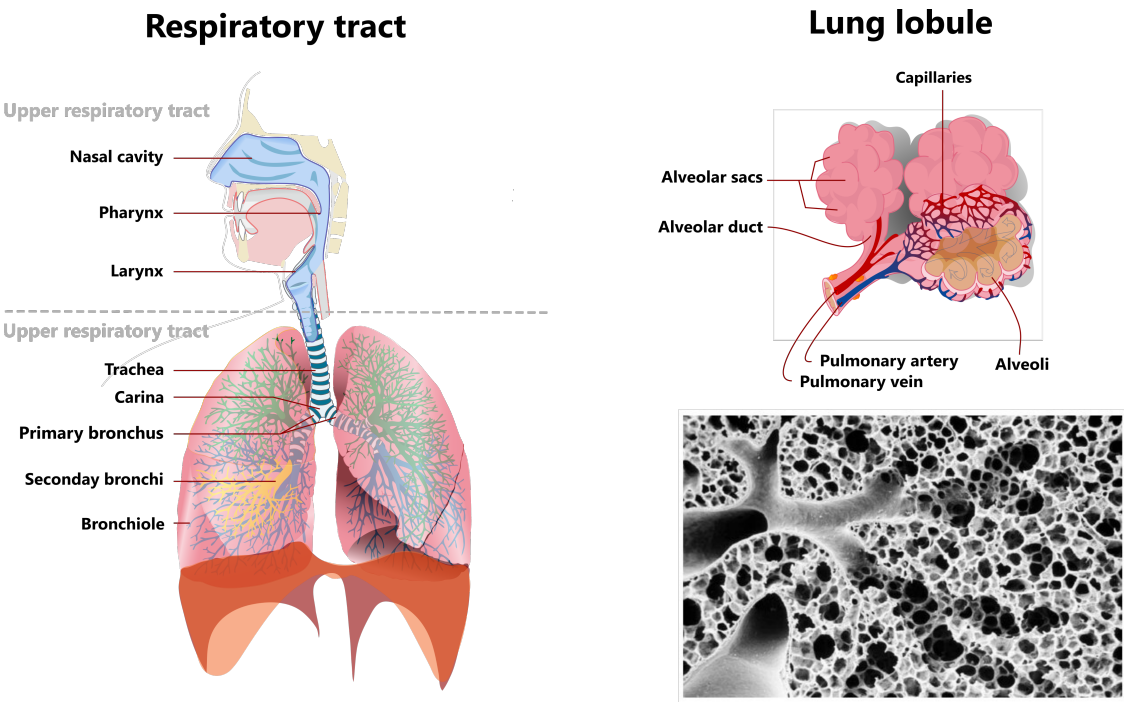

Figure 1.1: On the left, the upper and lower respiratory tracts. The trachea branches into 23 sequential generations of airways, with the first 15^{th} being conductive only; those between 15 and 18 are partly conductive and partly diffusive as some alveolar sacs appear on the wall; some gas transfers through the air-blood tissue barrier. Those beyond 19 are progressively more gas-exchanging with more and more alveoli. On the right, the final element: the pulmonary lobules of the human lung schematized (top) and viewed (bottom) from a scanning electron micrograph, from Maury *et al.* [6], where its sponge-like tissue structure is well visible.

The diaphragm and intercostal muscles are mobilized for the respiratory efforts, mechanically creating a pressure gradient throughout the lung tissue, enabling fresh air to flow in the respiratory tract. As it contracts, the diaphragm moves downward and flattens, creating a force opening the lung toward the inferior region. The intercostal muscles cover the anterior thorax and contribute to expanding the chest toward the anterior region. In free breathing, the muscles are used only for inspiration, while expiration comes through a spontaneous return to the balance of internal and external pressures.

The lung is the organ containing the lower respiratory tract and parenchymal tissues. The different divisions of airways presented above define other pulmonary units (see 1.2): right and left lungs are supplied in air by bronchi, lobes by secondary bronchi, and segments by tertiary bronchi. A human lung typically consists of five

lobes: three in the right lung (upper, middle, and lower) and two in the left lung (upper and lower). They are separated by pleural tissue, which creates a fissure visible with high-resolution imaging and enables the separation of the lungs from the chest wall. These lobes can be subdivided into ten segments for each right and left lung, each being supplied by its own segmental bronchus and artery. This lung division into lobes and segments, as based on the arborization of the bronchi, presents equivalent physiological functions for equivalent units.

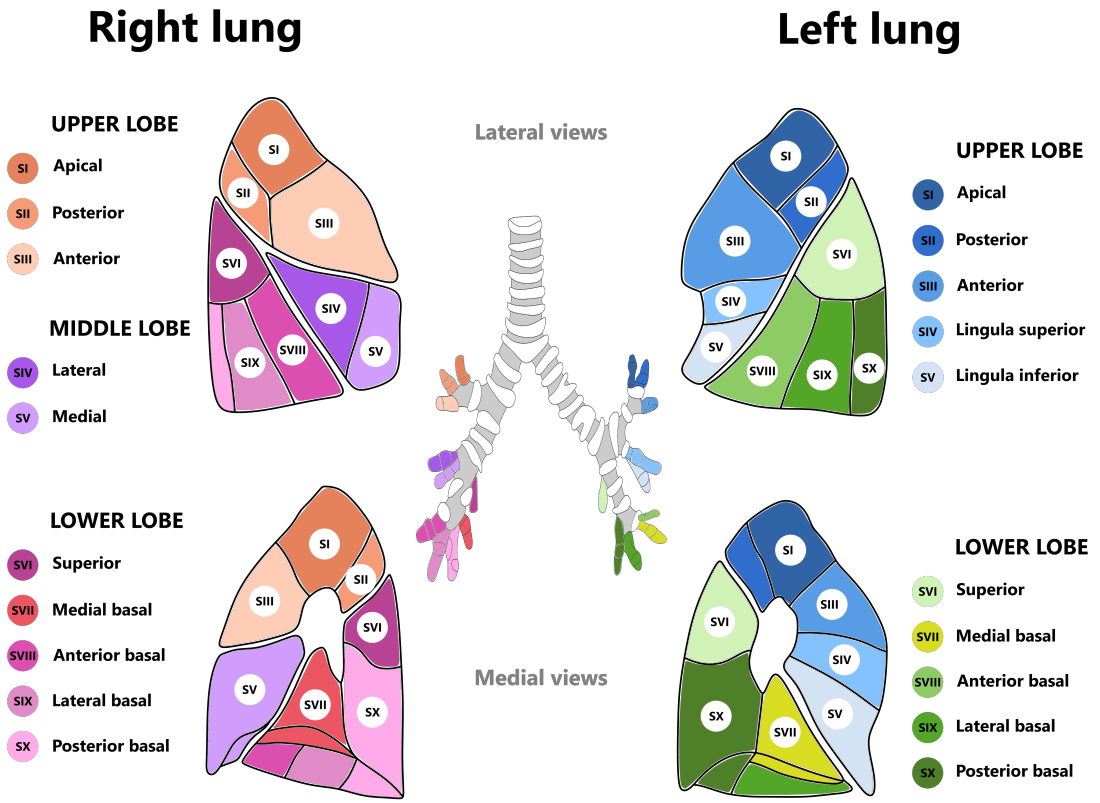

Figure 1.2: Bronchopulmonary segments and lobes for both lungs in lateral view (upper) and medial view (bottom), defined from secondary and tertiary bronchi (also called segmental bronchi) represented in the center. Each segment is a portion of the lung supplied by its bronchus and artery, thus functionally and anatomically independent. A segmental symmetry exists between the right and left lungs, even though the left lung is smaller and has only two lobes, while the right lung has three lobes.

1.1.2 Pulmonary functions

The pulmonary system supports three main functions presented in Figure 1.3: the mechanical circulation of air between the outside and inside of the lungs, gas exchanges between the pulmonary alveoli and the blood capillaries, and the transport of gases by the bloodstream between the lungs and the other organs.

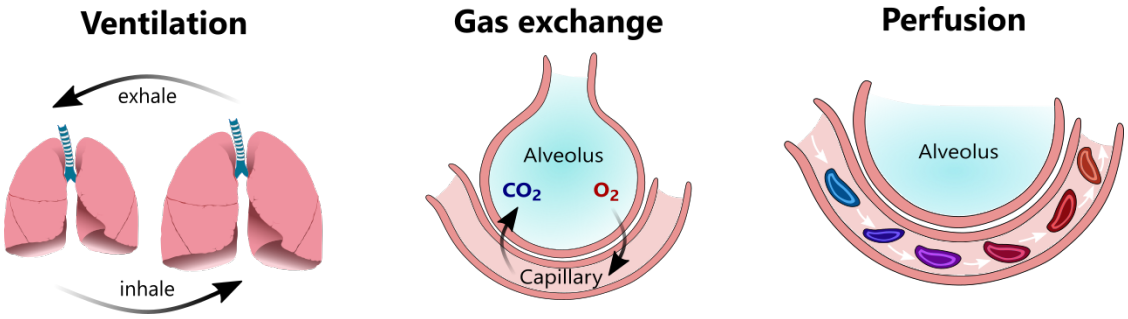

Figure 1.3: The three main pulmonary functions are: 1) the ventilation consists of inspiration of fresh air with a high concentration of O_2 followed by expiration of some of the lung gas to expel air saturated in CO_2 after biological exchanges, 2) gas exchanges consist of the diffusion of O_2 and CO_2 through the septal membrane to equilibrate partial pressure between alveoli and capillaries, and 3) the perfusion consists of the circulation of the blood throughout the vascular system enabling the transport of the gas bound to blood components.

A. Ventilation

Pulmonary ventilation, or shortly the ventilation, is defined by the circulation of air between the inside of the respiratory tracts and the outside environment. It involves two distinct processes: inspiration and expiration. During inspiration, the respiratory muscles contract to expand the lung, causing a decrease in intrapulmonary pressure. As a result, air rushes into the lungs along the pressure gradient. Expiration is usually a passive process primarily driven by the relaxation of inspiratory muscles, with the thoracic cavity returning to its resting position, creating an increased intrapulmonary pressure that expels air from the lungs. The expiration process can become active when muscles are forced to expel some gas, for

several diseases, or when we conscientiously control it.[7] At rest, after a normal and passive exhalation, 2.5 L of air remains in the lungs, called the functional residual capacity. During free breathing, we usually inhale an additional 500 mL of fresh air. By metonymic abuse of language, the term "ventilation" is sometimes used to designate this tidal volume of air ventilated through a respiratory cycle.

B. Gas exchange processes

In the alveolar region, gas exchange equalizes the partial pressures of dioxygen and carbon dioxide between the alveolus and the surrounding blood capillaries. Dioxygen diffuses from the alveolar gas into the blood of the pulmonary capillaries through a thin and porous septal membrane (in the order of a micrometer). Inside the bloodstream, the dioxygen can then bind to hemoglobin for transport through the body. Simultaneously, carbon dioxide diffuses from the bloodstream into the alveoli and can eventually be exhaled through ventilation. In practice, 0.25 s of close interaction between the gas inside the alveoli and the blood inside the capillaries is needed to reach this diffusive equilibrium during free breathing. To ensure an efficient exchange, the blood perfusion should match the ventilation.[8] The spatial match of this feature can be evaluated through ventilation-perfusion (V/Q) imaging techniques.[9]

C. Perfusion

Perfusion is the process of blood circulation throughout the bloodstream, enabling gas transport between the lungs and organs. Perfusion is driven by the pumping action of the heart. Gas is then bonded to blood components through chemical reactions: dioxygen is primarily transported in the blood through hemoglobin, which makes blood look brighter red. Carbon dioxide is transported in three forms:

[7] Deniz Inal-Ince and Aslihan Cakmak. "Chapter 19 - Kinesiology of respiration". In: *Comparative Kinesiology of the Human Body*. Ed. by Salih Angin and Ibrahim Engin Şimşek. Academic Press, Jan. 2020. DOI: 10.1016/B978-0-12-812162-7.00019-9.

[8] John B. West. *American Review of Respiratory Disease*, 1977.

[9] John Palmer et al. *Journal of Nuclear Medicine*, 2001.

dissolved in plasma, bound to hemoglobin, and as bicarbonate ions (which assists in buffering pH changes).

Besides these pulmonary functions, the respiratory system has a regulatory function to optimize dioxygen and carbon dioxide levels in each situation. These mechanisms rely on precise control of breathing rate depth and perfusion in response to factors like dioxygen and carbon dioxide concentrations in the blood and pH levels. This regulation allows our body to adapt to needs while physical effort needs, altitude, or certain pulmonary dysfunctions occur.

1.1.3 Nominal variability of the respiratory functions

Lung functions exhibit intrinsic variability even in healthy individuals. This poses a significant challenge when determining whether deviations from a nominal range represent a true impairment or are within the bounds of healthy variability. This last case can be called nominal variability, although this name may seem paradoxical: reference values are intended not to deviate much between healthy individuals. In the case of ventilation, it has been estimated that intra-individual variations account for 50 % of inter-individual variations,[10] demonstrating the need to consider this nominal variability. These variations can occur locally and globally, with homogeneous or inhomogeneous incidence throughout the volume, leading to challenging interpretations of lung function exams.

It is known that factors such as age, height, genetics, or environmental variables can affect global lung function.[11]. The respiratory system adapts to the individuals' morphologies and associated metabolism: taller people have greater muscle activity, requiring an increase in pulmonary function activities. When dioxygen becomes scarce with the altitude, the ventilation increases to optimize the dioxygen supply in the blood.[12]. Diurnal variations of the pulmonary function are also reported.[13] However, some particularities and singularities are specific to each person, defined as "respiratory personality" [14] and seem quite reproducible over time. The way of breathing seems unique for every individual and characterizes her or him, as can be seen in Figure 1.4.

[10] X. Baur et al. *Respiration*, 2009.
[11] Graham L. Hall et al. *The European Respiratory Journal*, 2021.
[12] Robert B. Schoene. *Journal of Experimental Biology*, 2001.
[13] Boris I. Medarov et al. *International Journal of Clinical and Experimental Medicine*, 2008.
[14] S. A. Shea and A. Guz. *Respiration Physiology*, 1992.

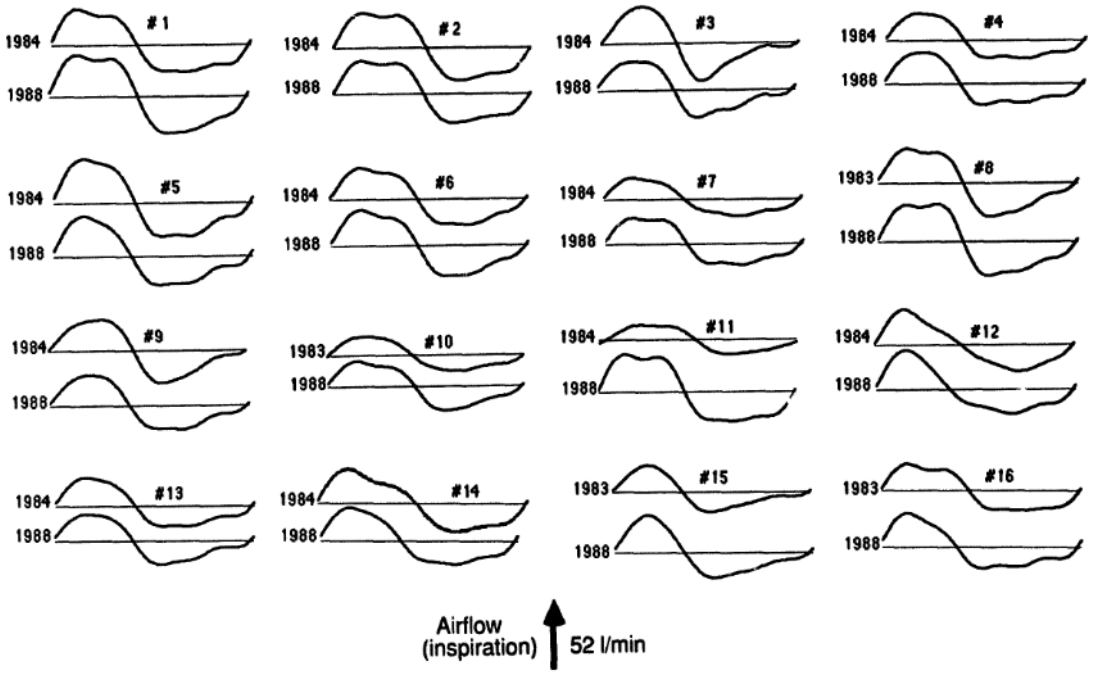

Figure 1.4: This Figure is reproduced from the work of Benchetrit *et al.*,[15] and highlights respiratory personalities from an analysis of airflows of participants from two studies separated by 4-5 years. A harmonic analysis was performed to extract mean shapes of digitalized airflow signals, which were then normalized over time.

These variations are sometimes not homogeneous throughout the lung, adding a layer of complexity to lung pathophysiology. One prominent factor affecting local lung function in everyday life is gravity.[16] The spatial distribution of ventilation in the lungs is influenced by gravity, resulting in regional variations. In the upright position, for instance, the basal region of the lung is more ventilated than its apical region due to the gravity field. Aging can exacerbate these local variations: reduced elasticity of lung tissue and related chest wall compliance also impair regional lung function. These local disparities in ventilation pose a challenge to assessing lung health. It emphasizes the need for a comprehensive understanding and interpretation of global and regional lung function measurements in clinical practice.[17]

[16] J. Milic-Emili et al. *Journal of Applied Physiology*, 1966.
[17] Michael A. Roman et al. *European Respiratory Journal*, 2016.

1.2 Ventilatory system pathology

This thesis aims to evaluate the ventilatory function in healthy human adults and adult patients with chronically obstructed lungs. This part addresses the disorders of the ventilatory function, focusing on the functional and structural modifications resulting from the two most common obstructive diseases: asthma and chronic obstructive pulmonary disease.

1.2.1 Respiratory diseases impairing the ventilatory function

Soriano *et al.* [18] found that nearly 545 million people worldwide suffered from a chronic respiratory disease in 2017, mostly affecting the ventilatory function. Although health is improving individually, the population is aging and growing, leading to a global increase of 40 % in these patients to care compared with 1990. Recently, the virus SARS-CoV-2 has significantly increased the number of patients with chronic respiratory dysfunction,[19] placing respiratory diseases at the heart of public health issues.

The section will focus on the main pathologies primarily affecting the ventilatory function, i.e., the ability to inhale and exhale efficiently: the restrictive and obstructive respiratory diseases. Some of the most prevalent diseases are presented for each category. As obstructive and restrictive syndromes might occur concomitantly, mixed patterns will also be discussed.

A. Restrictive Respiratory Diseases

Restrictive respiratory diseases involve reduced lung compliance and limited thoracic cage expansion, leading to decreased lung volumes. A mnemonic called "PAINT" categorizes the causes of restrictive lung disease into pleural, alveolar,

[18] Joan B. Soriano et al. *The Lancet Respiratory Medicine*, 2020.
[19] A. V. Raveendran et al. *Diabetes & Metabolic Syndrome: Clinical Research & Reviews*, 2021.

interstitial, neuromuscular, and thoracic cage abnormalities. However, the discrimination of intrinsic and extrinsic lung diseases is preferred.[20] Intrinsic lung diseases refer to diseases affecting the lung parenchyma. These conditions cause inflammation or scarring of the lung tissue (interstitial lung disease) or the occupation of alveolar space (pneumonitis). Extrinsic lung diseases refer to extrapulmonary diseases. It is caused by dysfunction of some components of the respiratory pump, such as the chest wall, pleura, and respiratory muscles. Some examples of intrinsic lung diseases are idiopathic pulmonary fibrosis, sarcoidosis, acute interstitial pneumonia, systemic sclerosis, or hypersensitivity pneumonitis. Some examples of extrinsic lung diseases are kyphoscoliosis, pleural conditions, ascites, or neuromuscular disorders.

The prevalence of restrictive diseases is difficult to estimate precisely because the groups involve multiple pathological conditions, and important differences are reported between geographical clusters. A survey conducted between 2007 and 2013 in the United States estimated that 6.5 % of participants from a nationwide probability sample had restrictive impairment.[21] Idiopathic pulmonary fibrosis and sarcoidosis are briefly presented as the two most prevalent interstitial lung diseases in Europe and North America.[22]

– **Idiopathic Pulmonary Fibrosis (IPF):** IPF is a progressive and often fatal interstitial lung disease characterized by excessive collagen deposition and lung tissue scarring (fibrosis). This leads to stiffening of the lungs, resulting in decreased lung volumes. Common symptoms of IPF include persistent, dry cough, shortness of breath during physical activity and even at rest, fatigue, and chest discomfort. As the disease progresses, individuals may experience reduced exercise tolerance and breathing difficulties, leading to respiratory failure. The exact cause of IPF is unknown, and it usually affects older adults. Timely diagnosis and management, which may include medication and lung

[20] Pedro J. Martinez-Pitre et al. "Restrictive Lung Disease". In: *StatPearls*. Treasure Island (FL): StatPearls Publishing, 2023.
[21] Earl S. Ford et al. *Chest*, 2013.
[22] Bhavika Kaul et al. *Frontiers in Medicine*, 2021.

transplant evaluation in severe cases, are essential to slow the progression of the disease and improve the quality of life.

– **Sarcoidosis:** Sarcoidosis is a multisystemic inflammatory disease that begins more frequently between 20 and 40 years of age and represents the most frequent interstitial lung disease.[20] This rare inflammatory disease affects multiple organs, most commonly the lungs, in 90 % of cases. Its exact cause is unclear, but it involves the formation of tiny clusters of inflammatory cells called granulomas in various organs. In pulmonary sarcoidosis, granulomas impair lung expansion and gas exchange. Sarcoidosis can manifest with many symptoms, including a persistent cough, shortness of breath, fatigue, fever, swollen lymph nodes, skin rashes, joint pain, and eye discomfort or vision problems. The severity and organ involvement vary from person to person, making diagnosis and treatment challenging. Treatment may involve medications to reduce inflammation and alleviate symptoms, but the condition may sometimes resolve independently.

B. Obstructive Respiratory Diseases

An increased resistance to airflow characterizes obstructive respiratory diseases due to narrowed or obstructed airways. Obstructive syndromes represent 80 % of the pulmonary syndromes. The Forum of International Respiratory Societies considers asthma and chronic obstructive pulmonary disease (COPD) as the two main obstructive respiratory diseases and two of the 5 five most important lung diseases worldwide from a prevalence standpoint.[23] Although these two pathologies are largely predominant in obstructive lungs, other diseases induce obstructive syndromes: it is, for example, the case of cystic fibrosis, bronchiectasis, bronchiolitis obliterans, etc.

– **COPD** Chronic Obstructive Pulmonary Disease (COPD): ranks as the third most prevalent cause of mortality, with about 3.2 million patients dying each

[23] Stephanie M. Levine and Darcy D. Marciniuk. *Chest*, 2022.

year worldwide.[23] It constitutes 81.7 % of all deaths attributed to chronic respiratory conditions. In 2017, its global prevalence was estimated at 3.92 %.[18] This progressive and irreversible lung disease is characterized by chronic inflammation and airflow obstruction in the lungs. Common symptoms include persistent cough, increased production of mucus, shortness of breath (especially during physical activity), wheezing, and chest tightness. COPD is primarily caused by long-term exposure to irritants such as smoking, air pollution, and occupational dust or chemicals. It is a debilitating condition that can significantly impact a person's quality of life and, if left untreated, can lead to severe complications like respiratory infections and respiratory failure. Early diagnosis and management, including lifestyle changes, medications, and pulmonary rehabilitation, can help alleviate symptoms and slow disease progression.

– **Asthma:** In 2017, asthma global prevalence is estimated at 3.57 %.[18] It is the most common chronic disease of childhood, with an increased prevalence for the past three decades.[23] Among 301 acute or chronic diseases and injuries, asthma was the 11th leading cause of disability in terms of years of life lost in good health in 2015.[24] This chronic inflammatory disorder causes reversible airflow obstruction due to bronchial hyperresponsiveness and airway inflammation. Triggers such as allergens or irritants can lead to bronchoconstriction and increased mucus production. Avoidable asthma deaths (about 1000 per day) occur due to inappropriate management and control of the disease, with geographical variabilities. This is often due to excessive reliance on reliever medications and insufficient use of preventive medications.[25]

Patients can present concomitant features of asthma and COPD, particularly elderly patients, defining the Asthma-COPD Overlap Syndrome (ACOS) recently

[23] Stephanie M. Levine and Darcy D. Marciniuk. *Chest*, 2022.
[18] Joan B. Soriano et al. *The Lancet Respiratory Medicine*, 2020.
[18] Joan B. Soriano et al. *The Lancet Respiratory Medicine*, 2020.
[23] Stephanie M. Levine and Darcy D. Marciniuk. *Chest*, 2022.
[24] Theo Vos et al. *The Lancet*, 2016.
[25] GBD 2019 Diseases and Injuries Collaborators. *Lancet (London, England)*, 2020.

introduced in medical care. The shared symptoms of asthma and COPD, as well as this mixed ACOS condition, are a real challenge in clinical practice for high specificity of diagnostics.

C. Mixed patterns

Some patients exhibit the features of both obstructive and restrictive syndromes. This condition is, however, rare: a retrospective study in 2010 evaluated 43,212 pulmonary function tests and found 130 patients with combined obstructive and restrictive syndromes.[26] Mixed patterns are primarily caused by the combination of pulmonary parenchymal and non-pulmonary disorders (48 % of the cases) and secondly by pulmonary parenchymal disorder (38 % of the cases). The most prevalent diseases associated with combined obstructive and restrictive patterners are COPD, sarcoidosis, and non-parenchymal lung diseases such as congestive heart failure.

1.2.2 Structural and functional alterations in asthma and COPD

The prevalence of obstructive diseases, particularly asthma and COPD, and their difficult diagnosis justifies the importance of focusing on these two pathologies. These chronic respiratory conditions are characterized by shared structural changes in the airways and tissues, altering lung function. However, they differ in their underlying causes and some clinical features. Understanding these structural and functional particularities is crucial for a sensitive and specific diagnosis and management of these respiratory conditions.

In COPD, the lung tissues gradually deteriorate due to prolonged irritant exposure. This leads to the destruction of alveoli, resulting in emphysema (see Figure 1.5) with reduced elasticity and reduction of the surface area for dioxygen and carbon dioxide exchange. Chronic airway inflammation (bronchitis) and increased

[26] Enrique Diaz-Guzman et al. *Respiratory Care*, 2010.

mucus production contribute to airway narrowing and obstruction, leading to irreversible airflow limitation. Fibrosis or scarring of lung tissue can appear over time due to prolonged inflammation and diminishing compliance, increasing the amount of effort required to inhale and exhale. This dysfunction of lung ventilation is mainly assessed in clinical routine with spirometry measurements: airflow is measured at the mouth during forced expiratory maneuvers. Morphological anomalies can be detected at an early stage of the disease using imaging techniques through X-ray findings, such as signs of inflammation and thickening in airway walls, lung hyperinflation with bullae, fibrosis, or scarring in the lung tissues.

Asthma is characterized by reversible bronchoconstriction, mainly when triggered by allergens or irritants inducing smooth muscle spasms (see Figure 1.5). Over time, chronic inflammation (driven by an increased number of immune cells such as eosinophils) can lead to structural changes in the airways, such as thickening of the airway walls, increased mucus, and increased smooth muscle mass. They contribute altogether to further airflow obstruction. These features can be observed variably (as a function of the current environment) using morphological imaging techniques such as CT, particularly to characterize airway inflammation, hyperinflation, and air trapping. However, the function of bronchoconstriction and its reversibility need to be assessed for a specific exam to rule out COPD.

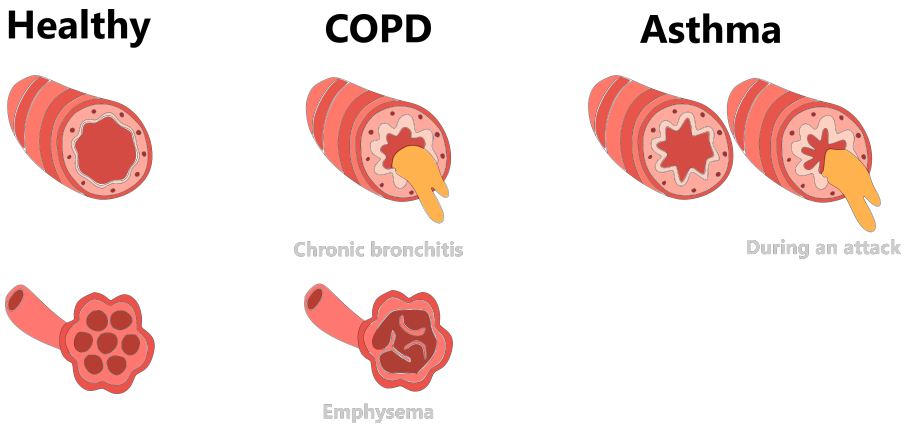

Figure 1.5: Airways and alveoli structural changes under obstructive disorders. COPD is characterized by chronic bronchitis (airway inflammation and excess mucus) and emphysema (destruction of alveolar membranes). Asthma is characterized by a hyperresponsiveness of airways, leading to chronic moderate bronchitis and episodes of asthma attacks when triggered.

Asthma and COPD are chronic respiratory diseases with close but distinct structural and functional changes in the airways and lungs. Asthma is characterized by reversible bronchoconstriction, airway inflammation, and hyperresponsiveness, while COPD involves irreversible airflow limitation, chronic bronchitis, and emphysematous changes. However, the two diseases have overlapping symptoms, and the differentiation can be difficult. Moreover, some patients present mixed symptoms of asthma and COPD, particularly in elderly patients, increasing the difficulty of obtaining specific diagnoses.

1.3 Standard characterization of pulmonary diseases

Several lung functions can be affected, leading to discomfort or increased danger for patients. Based on empirical knowledge, a standardized examination routine has been built to assess whether the lung functions correctly and what underlying illness could be present. Most of these exams require the cooperation of the patient.

1.3.1 Pulmonary functional tests (PFT)

Patients follow a clinical routine called pulmonary function tests (PFTs) to diagnose and monitor respiratory diseases. The main tests assess ventilatory capacity, blood gas transfer, and blood dioxygen levels.

A. Spirometry

The best-known and most widely used test is spirometry. The spirometer measures the flow of air inspired and expired at the mouth as a function of time during forced inspiration-expiration cycles. Standard spirometry can reach recruitable volumes, i.e., the different lung volumes we can access through muscular action. As flow Q is the first derivative of volume ($Q = \frac{dV}{dt}$), it is possible to plot flow-volume conjointly, in what finally is the phase portrait of the volume. Key parameters obtained from spirometry include:

- Forced Vital Capacity (FVC) and Forced Expiratory Volume in 1 second (FEV1), which are evaluated under the Tiffeneau coefficient
- Forced Expiratory Flows (FEF) at different fractions of the forced vital capacity (often 25 %, 50 % and 75 % of FVC).
- Peak Expiratory Flow (PEF)

These measurements are compared to reference equations of the Global Lung Initiative (GLI) [27,28] based on the sex, age, weight, height, and ethnicity of the patients and are regularly updated. It provides information about airflow limitation and potential obstruction or restriction in the airways, as illustrated in Figure 1.6.

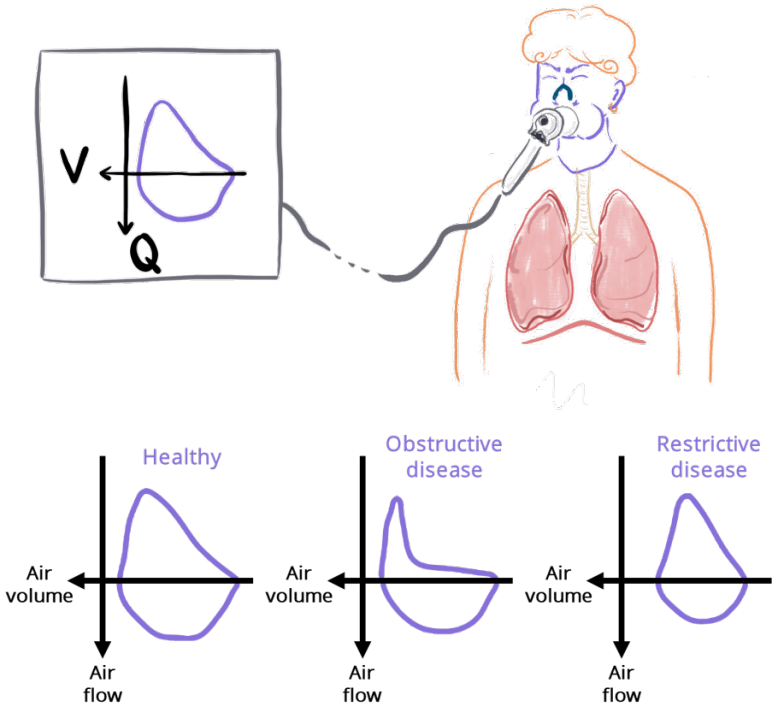

Figure 1.6: Principles of standard spirometry. Typical differences in flow-volume loop shapes depend on the pathology.

B. Plethysmography

Plethysmography measurements provide insight into non-recruitable lung volume, such as the total lung capacity (TLC), residual volume (RV), and functional residual capacity (FRC). It enables the characterization of lung conditions like restrictive lung diseases and hyperinflation. Helium dilution is another technique to assess these non-recruitable volumes. However, body plethysmography is usually recommended as it is more robust to complex cases of strong airway obstructions.[29]

[27] Philip H. Quanjer et al. *The European Respiratory Journal*, 2012.
[28] Cole Bowerman et al. *American Journal of Respiratory and Critical Care Medicine*, 2023.
[29] Claudio Tantucci et al. *Respiration*, 2016.

The person sits in a sealed chamber and breathes in and out against a closed valve. Changes in pressure within the chamber reflect lung volume changes, providing insights into lung capacity and function through the Boyle law. The Figure 1.7 defines the main volumes assessed through plethysmography exams.

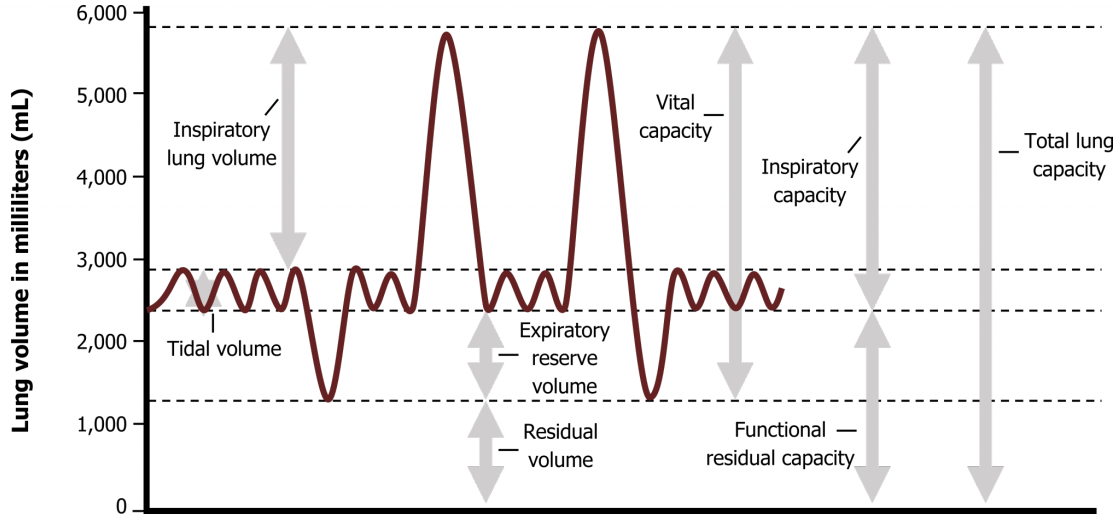

Figure 1.7: Lung volumes designations during tidal and forced expiratory cycles. Extrema in the curve represents maximal and minimal reachable respiratory states. Figure extracted from Kindred Grey .[30]

C. Diffusion Capacity (DLCO)

Diffusion capacity measures the ability of the lungs to transfer gases from the alveoli to the bloodstream. Patients inhale a small amount of carbon monoxide mixed with a trace amount of another gas like helium. They hold their breath briefly, allowing the carbon monoxide to be absorbed into the bloodstream through the alveolar-capillary membrane, while the inert gas does not cross the alveolar wall. The concentration of carbon monoxide in the exhaled breath is measured after the breath-hold and compared with the initial concentration, factoring in the lung volume and the time of breath-hold. This diffusion capacity of the lung for carbon monoxide (CO) is called D_{LCO} and is generally measured in mL/min/kPa. A lower D_{LCO} value indicates impaired gas exchange capacity, suggesting potential issues with the alveolar-capillary interface, such as inflammation, fibrosis, or reduced surface area for diffusion.

The outcome provides insights into a diffusing capacity for dioxygen (D_{LO_2}), which would be the preferred measurement as O_2 is the molecule involved in cellular metabolism. D_{LO_2} is defined as the rate at which the lungs absorb dioxygen, divided by the partial pressure of dioxygen between the alveoli and blood. Measuring D_{LO_2} is a complex task as it necessitates an invasive procedure to obtain the partial pressure of dioxygen in the pulmonary artery. In contrast, the partial pressure of carbon monoxide in the blood is typically disregarded due to its strong affinity with red blood cells, making it readily absorbed by them. This is why D_{LCO} is employed instead of D_{LO_2} to estimate pulmonary diffusing capacity, as explained by West *et al.*[31]

D. Multiple breath washout (MBW)

MBW is a technique that measures the concentration of an insoluble gas (commonly nitrogen) over multiple washin/washout breathing patterns. Along with the expired volume per breath during a washout, it enables the assessment of the specific ventilation heterogeneity of the gas transport through respiratory tracts. This technique was introduced in the 1950s and is still available in clinical routine.[32] The metric returned is a global measurement of specific ventilation heterogeneity.

E. Arterial blood gas composition

The arterial blood gas (ABG) composition of blood drawn from an artery allows us to measure key parameters that include pH, partial pressure of dioxygen, partial pressure of carbon dioxide, bicarbonate, base excess, and dioxygen saturation. ABG analysis provides crucial information about a person's respiratory and metabolic status.

All these exams are quite simple and reliable. However, their resulting measurements require the cooperation of the patients, which is not always possible.

[31] John-B. West. *La physiologie respiratoire*. 6e édition. Maloine, Nov. 2003.
[32] Paul D. Robinson et al. *Respiration*, 2009.

Furthermore, these exams only provide global measurement. Because many lung diseases affect specific lung regions (such as pulmonary embolism, pneumothorax, or lung cancer, for example), and because healthy regions can compensate for local defects globally, it is necessary to develop techniques allowing regional diagnoses of pulmonary function.

1.3.2 The role of imaging techniques in respiratory studies

Imaging techniques provide complementary information compared with traditional pulmonary function tests by providing visual, structural, and sometimes functional information about the respiratory system. They provide unique insights about the location and extent of lung impairments while allowing a better understanding of lung pathophysiology in its spatial complexity.

In clinical practice, lung images from conventional radiography are the most common routine exam to reveal structural abnormalities such as lung opacities in pneumonia, lung masses, cavity shape distortion in emphysema, or pneumothorax. This exam is fast, widely available, and relatively cheap compared to other imaging strategies. Some examples of conventional radiography can be observed on the Figure 1.8 extracted from Wang *et al.* work.[33] These 2D projections reflect the attenuation of X-rays by biological tissues, giving information on the structure of organs but also the physical properties of tissues (absorption coefficient in the range of electromagnetic radiation between 10^{16} Hz and 10^{20} Hz).

However, diagnoses are not always possible on these 2D projection images, despite efforts in machine learning strategies to support radiologists' analysis. Computed Tomography (CT) allows the acquisition of higher-resolution images of X-ray contrast through the three-dimensional reconstruction of multiple X-ray projections, allowing for more detailed assessments of lung anatomy and diseases. Its

[33] Xiaosong Wang et al. "ChestX-ray8: Hospital-scale Chest X-ray Database and Benchmarks on Weakly-Supervised Classification and Localization of Common Thorax Diseases". In: *2017 IEEE Conference on Computer Vision and Pattern Recognition (CVPR)*.. July 2017. DOI: 10.1109/CVPR.2017.369.

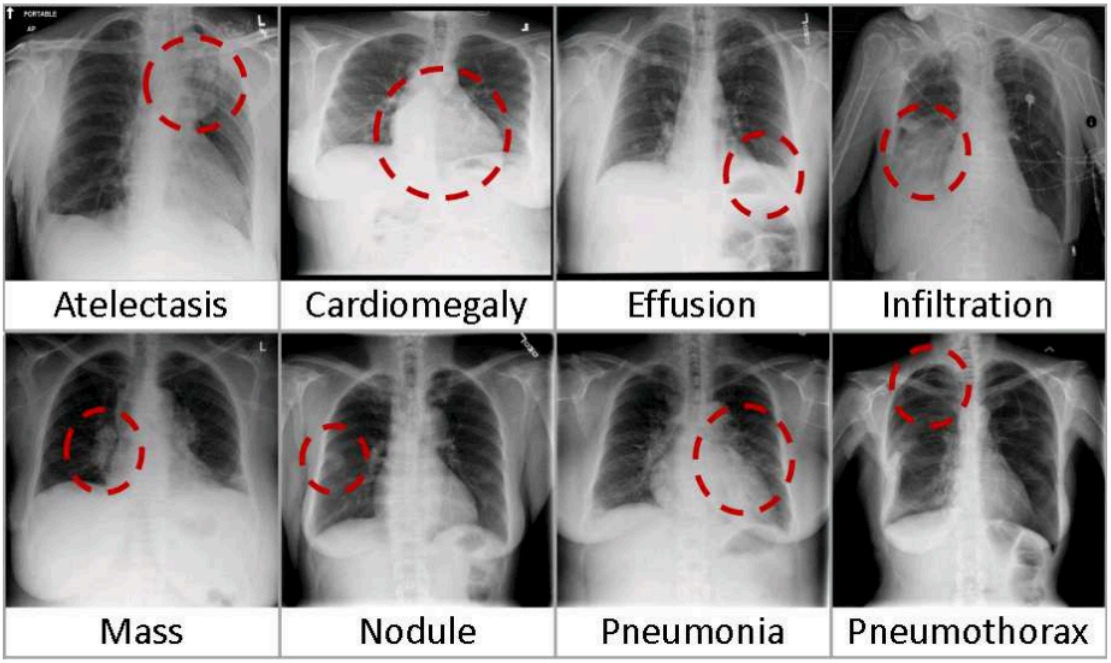

Figure 1.8: Several chest radiography automatically labeled with associated diseases extracted from Wang *et al.* work.[33] For example, air trapping (atelectasis) results in a high residual lung volume and a flattened diaphragm.

ionizing nature limits its wide clinical application for high volumes, dynamic acquisition, and longitudinal studies. Recent technical progress has made the same image quality possible to use an average 75 % effective radiation dose using photon-counting detectors.[34,35] Deep learning reconstructions are also strong assets for low-dose CT imaging.[36] These examinations are usually only morphological and do not provide information regarding lung function.

To access pulmonary function, specifically pulmonary ventilation, one strategy consists of making two CT acquisitions: one at the end of inspiration and one at the end of expiration. Analyzing the two images enables quantifying the ventilation and its possible defects. However, the patient must cooperate to carry out the breath-hold acquisitions, and ionization does allow neither longitudinal monitoring nor temporally resolved acquisition.

[34]Thomas Flohr et al. *Physica Medica*, 2020.
[35]Matthias Michael Woeltjen et al. *Diagnostics*, 2022.
[36]E. Immonen et al. *Radiography*, 2022.

Using an exogenous radioactive tracer to radiate gamma rays directly or indirectly, the ventilation can be estimated conjointly with the perfusion. These exams are usually used to diagnose pulmonary embolism. They rely on scintigraphy or Single Photon Emission Computed Tomography (SPECT) and are commonly referred to as V/Q scintigraphy or V/Q SPECT. The "V/Q" stands for the ventilation-to-perfusion ratio inferred, which should match to ensure the optimal gas exchange. The ventilation maps result from administering an aerosol of radionuclides distributed throughout the respiratory tracts. In contrast, the perfusion maps result from an intravenous injection of a radionuclide, which remains in the vascular system.[37]

Magnetic Resonance Imaging (MRI) has been little used in clinical routine due to its low availability, high cost, and the technical difficulties in the pulmonary application that have hitherto been significant. Similar to CT acquisitions, the two respiratory phases at the end of inspiration and expiration can be analyzed in clinical routine. However, its innocuousness allows dynamic and longitudinal exams while maintaining high-resolution imaging, considering it an alternative to CT imaging.[38] More recent developments in fundamental research reveal the strong potential of the technique for both morphological and functional examinations, including strategies with a small transfer gap for clinic usage.

[37] Paul J. Roach et al. *Journal of Nuclear Medicine*, 2013.
[38] Michael Puderbach and Hans-Ulrich Kauczor. *Pediatric Radiology*, 2008.

2

MR ventilation imaging

Imaging techniques pave the way for improved diagnostic capabilities with regional sensitivity and a deeper understanding of lung pathophysiology. Conventional radiography and CT scans are the most common methods available in clinics. However, there is growing interest in using pulmonary MRI to image lung function. Its innocuity means that dynamic and longitudinal lung function studies can be carried out, and technical advances support its potential to characterize the local lung function fully. This chapter introduces first why MRI is, at first sight, not expected to be a relevant exam for lung function testing. The second part focuses on recent developments that have made pulmonary functional MRI feasible and a promising technique. Finally, state-of-the-art proton MRI approaches to assess the ventilatory function are presented.

2.1 MRI of the lungs: an odd idea

MR imaging of the lung has long been a queer application. This section presents the fundamental physical principles of MRI that challenge its use for lung imaging. To delve deeper into the physics of MRI and its sequences, it is advisable to refer to Bloch's seminal article,[39] as well as referenced books like Brown *et al.*,[40] and Bernstein *et al.* [41] The difficulties linked to lung imaging by MRI are also explored in greater detail in the review paper by Kauczor *et al.* [42]

Quantum physics is widely used to describe the underlying physics of nuclear magnetic resonance. However, MRI usually deals with very large ensembles of spins (on the order of 10^{19} hydrogen nuclei contained in a typical ($1.5 \times 1.5 \times 1.5$) mm^3 lung voxel) such that Bloch's classical theory is suitable to describe the involved phenomena.[43]

[39] F. Bloch. *Science (New York, N.Y.)*, 1953.

[40] Robert W. Brown et al. *Magnetic Resonance Imaging: Physical Principles and Sequence Design*. 2e édition. Wiley-Blackwell, May 2014.

[41] Matt A. Bernstein et al. *Handbook of MRI Pulse Sequences*. 1st edition. Amsterdam ; Boston: Academic Press, Sept. 2004.

[42] Hans-Ulrich Kauczor and Mark Oliver Wielpütz. *MRI of the Lung*. Softcover reprint of the original 2nd ed. 2018 édition. Springer Nature Switzerland AG, Dec. 2019.

[43] Lars G. Hanson. *Concepts in Magnetic Resonance Part A*,. 2008.

2.1.1 The origin of the signal in nuclear magnetic resonance

In a sample of matter, each nucleon particle of an atom nucleus is associated with a spin, an intrinsic quantum property. For non-zero spins s under a magnetic field $\vec{B_0}$, the spin ensemble presents a total magnetic moment that provides the MR signal. The magnetization $\vec{M_0}$ is defined as the density of the total magnetic moment and is preferred to describe nuclear magnetic resonance (NMR) physics. At the sample thermal equilibrium, $\vec{M_0}$ is given by the Boltzmann law [40]:

$$M_0 \simeq \rho_0 \frac{s(s+1)\gamma^2\hbar^2}{3kT} B_0 \qquad (\hbar\omega_0 << kT) \tag{2.1}$$

where k is Boltzmann's constant, T is the absolute temperature of the sample, ρ_0 the spin density, $\hbar$ is the Planck's constant divided by 2π, and γ is the gyromagnetic ratio of the nuclei.

The net magnetization $\vec{M_0}$ is aligned and proportional to $\vec{B_0}$. Following the Larmor work, the experienced magnetic field produces a torque on $\vec{M_0}$, resulting in its clockwise precession at the Larmor angular frequency $\omega_{\mathrm{L}} = \gamma B_0$. Local frequencies can shift depending on the effective magnetic field $\vec{B_0}$ experienced by nucleon particles relative to their environment. It is characterized by susceptibility effects at the atomic or molecular level, that is, their ability to get magnetized as they experience a magnetic field.[44,45] For hydrogen MRI, it was shown that the averaged resonance frequency increased by 230 Hz at 1.5 T (3.6 ppm) in the lung tissues compared to mediastinal muscle, which can induce artifacts at the interfaces.[46,47]

The hydrogen nuclei, ^{1}H, commonly called "protons" (only one proton in its nucleus), have a spin of 1/2, leading to a non-zero dipolar magnetic moment. This nucleus is particularly interesting and primarily used in MRI because of its natural

[44] M. N. Hood et al. *Radiographics: A Review Publication of the Radiological Society of North America, Inc*, 1999.
[45] Devesh Raj et al. *Physics in Medicine & Biology*, 2000.
[46] C J Bergin et al. *Radiology*, 1991.
[47] Hiroto Hatabu et al. *Radiology*, 2020.

abundance in human biological tissues composed mainly of water molecules (around 10^{27}) H_2O.[48] Moreover, the Larmor frequency of the hydrogen nuclei can be reached with ordinary hardware (gyromagnetic ratio of 42.58 MHz·T^{-1}). The stimulation of the nuclear magnetic resonance at the resonant Larmor frequency enables the measurement of the total magnetic moment of the sample in a transverse plane. However, the lungs, filled with gas, contain little hydrogen nuclei compared to other tissues: the average hydrogen density is 0.1 in healthy lung tissue.[42]

This low density is the first limitation of proton lung MRI, as the magnetization, thus the MRI signal, is proportional to it, see (2.1). Some other nuclei with 1/2 spins, such as ^{129}Xe, ^{3}He or ^{19}F, are also used. The dipolar magnetic moments from 1/2 spins are preferred as they are easier to handle than larger dipolar moments, where coupling Zeeman effects occur. However, they require specific hardware tuned to associated resonant frequencies, and these nuclei are not naturally present in lung tissues. If inhaled in a gaseous form, it nevertheless becomes possible to image them (as it will be detailed in section 2.2.1). For this section, we will focus on ^{1}H MRI physics, but the physical underpinnings are similar for the other nuclei.

2.1.2 Relaxation in parenchymal tissues

As previously mentioned, the MR signal is obtained by measuring temporal variations of the total magnetic moment in a plane perpendicular to $\vec{B_0}$. A transversal radiofrequency excitation pulse $\vec{B_1}$ oscillating at Larmor frequency (63.87 MHz at 1.5 T and 127.74 MHz at 3 T) stimulates the nuclear magnetic resonance. The magnetization is flipped away from its equilibrium along the $\vec{B_0}$ direction. In the rotating frame, the net magnetization $\vec{M_0}$ processes around $\vec{B_1}$ at $\omega_1 = \gamma B_1$. The RF application pulse duration is defined as $T_\alpha = \frac{\alpha}{\gamma B_1}$, for a complete flip of the magnetization $\alpha = \pi/2$, t and commonly in the millisecond range. After the RF pulse, the magnetization vector returns to the equilibrium state $\vec{M_0}$ following Bloch *et al.* empirical equation,[39] which includes the relaxation phenomenon. Under an

[48] R. Pethig and D. B. Kell. *Physics in Medicine & Biology*, 1987.
[39] F. Bloch. *Science (New York, N.Y.)*, 1953.

external static magnetic field $\vec{B_0}$, the magnetization in the rotating frame of a sample can be described by :

$$\frac{d\vec{M}}{dt} = \underbrace{\gamma\vec{M} \times \vec{B_0}}_{\text{precession}} \overbrace{+ \frac{1}{T_1}(\vec{M_0} - \vec{M_{\parallel}})}^{\text{spin-lattice interaction}} \underbrace{- \frac{1}{T_2^*}\vec{M_{\perp}}}_{\text{spin-spin interaction}} \tag{2.2}$$

with $\vec{M_{\parallel}}$ and $\vec{M_{\perp}}$, the parallel and perpendicular components of the magnetization relative to the magnetic field direction $\vec{B_0}$. In the equation (2.2), two relaxation components are defined:

- T_1 relaxation (longitudinal relaxation): After the RF pulse is being tipped away from $\vec{B_0}$, the magnetization returns to equilibrium. This process is governed by T_1 relaxation, with T_1 the temporal constant of the exponential signal decay characterizing the longitudinal component of the magnetization $\vec{M_{\parallel}}$. T_1 describes the rate at which energy is transferred from the spins to the lattice, releasing energy as heat to the surrounding molecular matrix. T_1 depends on the molecular structure and environment, which sets the frequency of the molecular collisions ν_C. If ν_C is closed to $2\pi\omega_0$, the energy transfer fastens, and T_1 is shortened. Gadolinium-based contrast agents are sometimes used in MRI to shorten T_1 and thus the resulting MR signal can be increased for T_1 weighted sequences.
- T_2^* relaxation (transverse relaxation): The spins of the excited nuclei also lose phase coherence due to their interactions with the spins of the neighboring nuclei. This loss of coherence is characterized by T_2^* relaxation, with T_2^* the temporal constant of the exponential decay characterizing the transversal component of the magnetization $M_{\perp}$. The first factor of dephasing occurs at a microscopic scale where magnetic moments randomly influence each other (T_2). A second factor happens at a macroscopic scale, where slight inhomogeneities cause a loss in transverse magnetization as the moments dephase (T_2'). T_2^* (also called "apparent T_2") is related to its two components

by: $\frac{1}{T_2^*} = \frac{1}{T_2} + \frac{1}{T_2'}$. T_2^* or T_2 usually sets the signal decay and a limit for sampling it.

Particularly, in the lung parenchyma, which is composed of an important air-tissue interface (130-140 m^2), differences in local magnetic susceptibilities χ ($\Delta\chi =$ 8 ppm at parenchyma-air interfaces at 1.5 T) lead to local magnetic field inhomogeneities. T_2^* is thus extremely low: in the order of 2.1 ms at 1.5 T and 0.7 ms at 3 T,[49] while, for example, common T_2^* for muscles are in the order of tens of milliseconds.[50].

The temporal evolution of transverse magnetization, which is a free induction decay (FID), can be probed using a simple radiofrequency coil and directly assessed along its derivative through Faraday's law. For an FID signal after a pulse flipping the magnetization, we would measure a demodulated signal $S(t) \propto \rho \exp(-t/T_2^*)$. The extremely short T_2^* of the lung parenchyma induces rapid signal loss.

2.1.3 Imaging a moving object

The FID signal does not contain any information regarding the spatial origin of the signal as we measure the total magnetic moment of the sample. Lauterbur [51] and Mansfield [52] set the ground for the fundamental principles of modern MR imaging by employing time-varying magnetic gradients, noted $G_x(t)$, $G_x(t)$, $G_x(t)$, corresponding to the MRI system Cartesian axes. These homogenous gradients lead to a linearly-varying magnetic field with the corresponding spatial dimension. It causes the precession frequency of protons to vary spatially in the field of view (FOV) as $\omega(x) = \gamma(B_0 + G_x x)$. These gradients are used to encode spatial information in the phase or frequency of the MR signal. For a gradient G_x applied conjointly with the data acquisition, the signal $S(t)$ measured with the receive coil is [40]:

[49] Jiangsheng Yu et al. *Magnetic Resonance in Medicine*, 2011.
[50] Charlotte Zaeske et al. *PLOS ONE*,. 2022.
[51] P. C. Lauterbur. *Pure and Applied Chemistry*, 1974.
[52] P. Mansfield. *Contemporary Physics*, 1976.

$$S_{\mathrm{FID}}(t) \propto \iiint_{\mathrm{FOV}} \sin(\alpha) \exp(-\frac{t}{T_2^*}) M_0(x,y,z) \exp\Big(-i(k_{\mathrm{x}}(t)x + k_{\mathrm{y}}(t)y + k_{\mathrm{z}}(t)z)\Big) dxdydz \tag{2.3}$$

with:

$$k(t) = \frac{\gamma}{2\pi} \int_0^t G(\tau) d\tau \tag{2.4}$$

where k_{x}, k_{y}, and k_{z} are the spatial frequencies encoded by the gradient along the three directions. We can recognize the 3D Fourier transform of the initial magnetization. In MRI, we navigate through magnetic gradients directly into the Fourier volume, called the k-space.

We can retrieve the image by the inverse Fourier transform of the acquired k-space. To obtain a whole 2D or 3D image, a full k-space, either 2D or 3D, must be acquired. Usual acquisition times in MRI range between a few seconds to several minutes. In lung MRI, breathing imposes a movement to the imaged sample during the acquisition with an average respiratory rate of 12 to 20 cycles per minute.[53] The reconstructed image combines information corresponding to different views of respiratory states. This leads to blurring and aliasing.

The contrasts obtained between tissues on MR images depend on RF pulse and magnetic gradient schemes. Diverse contrasts and measures can be driven by two main parameters:

- the echo time (TE): refers to the time between the RF pulse and the data acquisition, which is usually when the total magnetic moment is refocused and maximal in the transverse plane;
- the repetition time (TR): refers to the time between two repeated excitation RF pulses and thus two different acquired lines in the k-space volume.

[53] J. Brady Scott and Ramandeep Kaur. *Respiratory Care*, 2020.

2.2 Recent developments in lung MRI

All the aforementioned limitations present strong caveats for lung MRI. They have been alleviated thanks to innovative methods and technical advances in both hardware and computer processing. Voskrebenzev *et al*.[54] recently discussed these issues and the current directions of the research in a review.

This section presents the most common strategies to cope with low signals in lung tissues and respiratory motion and an overview of the main techniques assessing lung function. The last section 2.3 will deepen MR functional lung imaging with a review.

2.2.1 Tackling low signal in parenchymal tissues

A. Changing the nucleus for magnetic resonance

As the density of hydrogen nuclei is inherently low in lung tissue, other nuclei have been used for lung MRI and, particularly, hyperpolarised ^{3}Helium and ^{129}Xenon.[55] They can be prepolarized up to 92 %, leading to a net magnetization greater than the value at thermal equilibrium by five to six orders of magnitude before being inhaled and imaged. A fast acquisition is performed, usually at breath-hold, and a clear image of the airways, where the gas goes, can be obtained (see Figure 2.1).

However, to carry MRI for these nuclei, in addition to the sparse supply of ^{3}Helium and the cost of the gases, it is necessary to have an MRI equipped with the suitable RF channels tuned to emit and receive RF signal at the Larmor frequency of these nuclei (^{129}Xe at 35.33 MHz and ^{3}He at 97.29 MHz at 3 T).

This use of hyperpolarized gases will be further detailed in section A..

[54] Andreas Voskrebenzev and Jens Vogel-Claussen. *Journal of Magnetic Resonance Imaging*, 2021.
[55] David M. L. Lilburn et al. *Journal of Magnetic Resonance*, 2013.

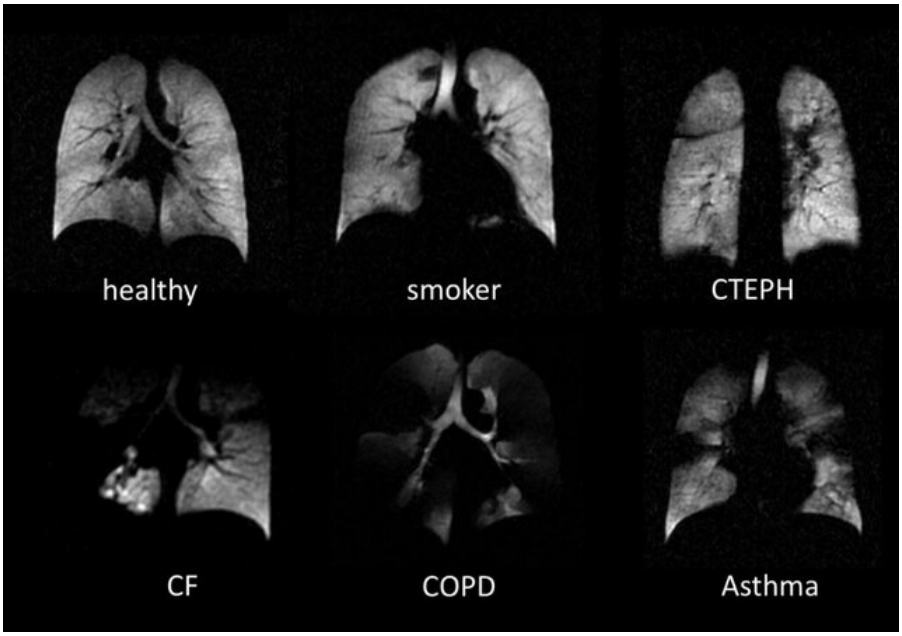

Figure 2.1: ^{3}Helium lung MRI in a healthy volunteer and different subjects with smoking habits, chronic thromboembolic pulmonary hypertension (CTEPH), cystic fibrosis (CF), chronic obstructive pulmonary disease (COPD), and asthma.[56] Poorly ventilated areas, i.e. regions the gas does not reach, appear hypointense.

B. Original sequences

Other developments focus on sequences that mitigate the T_2^* effects of magnetic susceptibility inhomogeneities, which are significant in parenchymal tissues and vary with lung inflation. Gradient echo acquisitions are generally used for shorter total acquisition times. In any case, measuring the signal before its complete decay along T_2^* is necessary. For this, ultra-short echo time (UTE) [57] sequences and a zero echo time (ZTE) [58] variant have been developed. They make it possible to obtain contrasts without any T_2^* weighting and close to the proton density, namely the tissue density, and thus close to the contrasts obtained by CT (Figure 2.2).

Balanced steady-state free precession (bSSFP) sequences also allow a short echo time for image encoding.[60] Moreover, the ^{1}H magnetization is refocused instead of spoiled after each encoding step, permitting higher flip angles than spoiled

[57] Kevin M. Johnson et al. *Magnetic Resonance in Medicine*, 2013.
[58] Markus Weiger et al. *Magnetic Resonance in Medicine*, 2011.
[60] Govind B. Chavhan et al. *RadioGraphics*, 2008.

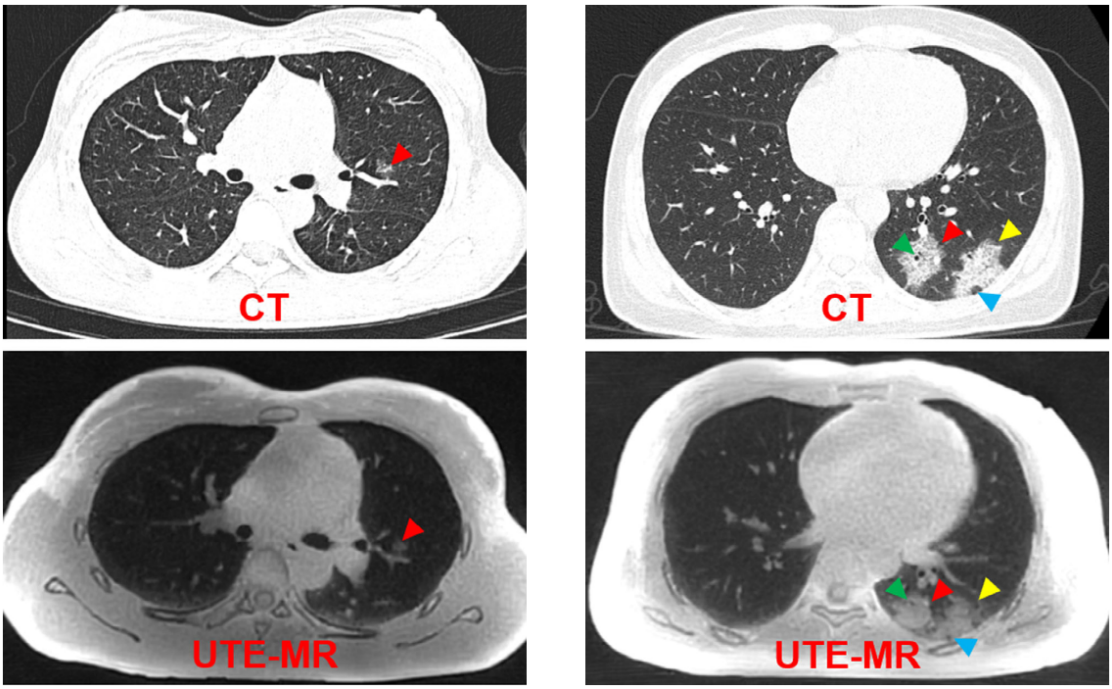

Figure 2.2: CT (top) and 3 T UTE MRI (bottom) axial slices in the lung of two COVID-19 patients (left and right). These figures are extracted from Jang *et al.*[59] The same radiological findings are found for both modalities: ground-glass opacities (red arrows), ground-glass opacities consolidation (yellow arrow), air bronchogram (green arrow), and pseudocavity (blue arrow). CT and UTE MRI present similar contrasts in the lung parenchyma, which can associated to the soft tissue proton density. The UTE MRI image has a lower resolution but it is not ionizing.

gradient-recalled (SPGR) sequences. This, in turn, results in an enhanced signal-to-noise ratio in parenchymal tissues and blood (up to 4 times in comparison to standard UTE acquisitions at 1.5 T [61]) although it comes at the cost of an increased specific absorption rate (SAR), which can lead to radiofrequency-induced patient heating. Thanks to the inherent combination of T_2 and T_1 relaxation time contrast, bSSFP images yield a "bright blood" signal, providing a clear visualization of pulmonary vessels (Figure 2.3).

[61] Grzegorz Bauman and Oliver Bieri. *Magnetic Resonance in Medicine*, 2020.

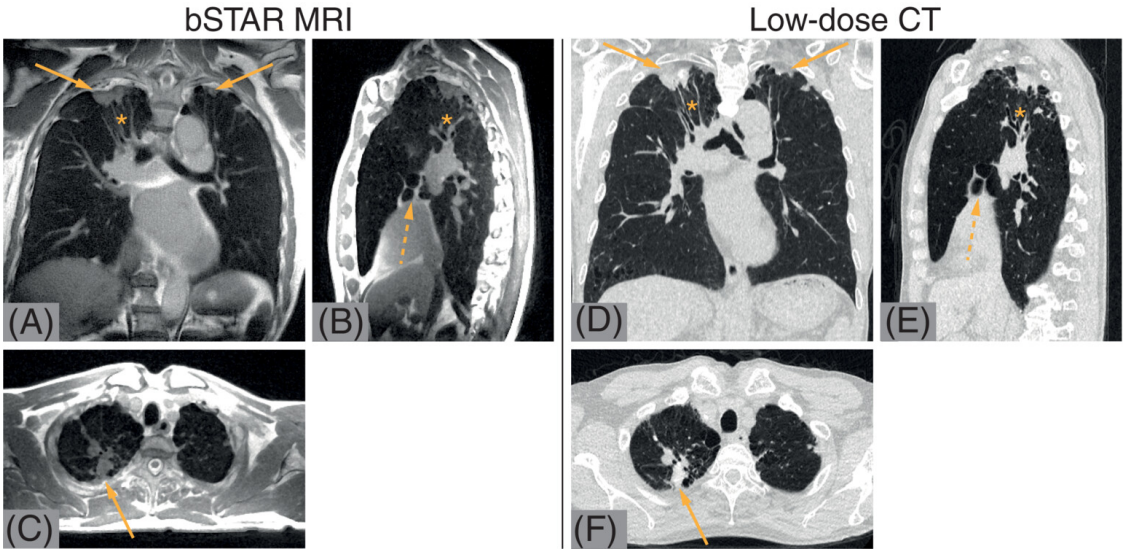

Figure 2.3: bSTAR MRI (left) and CT (right) 3D images in the lung of a 74-year-old patient with granulomatous lung disease.[62] The bSTAR sequence is derived from balanced steady-state free precession (bSSFP) sequences with the addition of a second echo. Contrasts differ, but the excellent signal-to-noise ratio (SNR) obtained with the bSTAR sequence enables distal vessels to be imaged with a submillimetric resolution (0.9 mm isotropic resolution in a 12:50 min acquisition).

C. Toward lower field ?

When we seek to increase the SNR of MR images, it is usual to image at higher fields as the SNR is expected to increase linearly with the field B_0 for magnetic fields higher than 0.4 T.[40] This could encourage imaging the lung at higher fields.[63] However, the local magnetic gradients induced by the differences in magnetic susceptibilities between the gas and the parenchymal tissue also increase with the magnetic field. The benefit of imaging the lung at lower fields has been experimentally demonstrated by comparing 1.5 T with 3 T,[64] and, more recently, 1.5 T with 0.55 T.[65] The T_2^* is 2.11 ± 0.27 ms at 1.5 T, 0.74 ± 0.1 ms at 3.0 T, and approximately 10 ± 2 ms at 0.55 T,[49] demonstrating a non-linear effect of the field on the decay in T_2^*. No model predicts the SNR in the lung parenchyma according to the magnetic field. Acquisitions at lower fields have been carried out at 0.2 T [66] and 0.35 T.[67] However, hardware differences between such systems and conventional ones at 1.5 T are too wide to enable magnetic field comparison based on image quality. Ultra-low-field (< 0.1 T) proton MRI has not yet been published, to my knowledge. How low we should go to maximize the signal-to-noise ratio in the lung is still an open question.

[63] Mathieu Lederlin and Yannick Crémillieux. *Journal of magnetic resonance imaging: JMRI*,. 2014.
[64] Guillaume Chassagnon et al. *Radiology*, 2019.
[65] Adrienne E. Campbell-Washburn. *American Journal of Respiratory and Critical Care Medicine*, 2020.
[49] Jiangsheng Yu et al. *Magnetic Resonance in Medicine*, 2011.
[66] Maren Zapke et al. *Respiratory Research*, 2006.
[67] Rabea Klaar et al. *Radiation Oncology*, 2023.

2.2.2 Handling the respiratory motion

Although often perceived as a "problem" for lung imaging, the respiratory motion carries valuable pathophysiological information. Different strategies are adopted depending on the acquisition objectives: motion-free (we avoid the motion), motion-compensated (we remove the motion), or motion-resolved (we reconstruct the dynamic, each respiratory state being "motion-free"). Large organs require long MRI acquisition times for a resolution of the order of millimeters. In clinical practice, fast acquisitions are typically performed in apnea to avoid respiratory artifacts, so 3D spatial coverage, SNR, and spatial resolution must be traded off. It is also possible to use ultra-fast 2D sequences and thus acquire time series for a lung slice.[68] Despite losing real-time resolution, only three-dimensional acquisitions can capture completely the breathing motion. Three-dimensional approaches developed in research are based on considering the motion prospectively (at the acquisition) or retrospectively (during image reconstruction). These methods all rely on using a respiratory signal surrogate and use the pseudo-cyclicity of the respiratory motion.

A. Estimation of the respiratory motion

The most common method available in the clinic to monitor respiratory movement is the use of a pneumatic belt placed at the upper abdomen or the chest of the patient. The device expands and contracts as the patient's girth changes with breathing. A distant sensor is linked through an air hose and measures inner air pressure variations. However, the signal carries partial information about respiration as it only assesses the anteroposterior and left-right motion while the breathing is mainly along the superior-inferior direction. Another strategy is to capture motion information through a supplementary step in the acquisition sequence: they

[68] Grzegorz Bauman et al. *Magnetic Resonance in Medicine*, 2016.

are called "navigators" and can be 0D, 1D, 2D, or 3D.[69] –[73] These navigations increase acquisition time, but this is compensated by the time saved in setting up the belt. Finally, an approach proposed by Pipe *et al.* in 1999 demonstrates the extraction of a respiratory signal surrogate from the k-space center.[74,75] This is called self-navigation. The contrast information, corresponding to the low spatial frequencies in the center of the Fourier volume, evolves during respiration even though the phenomena involved and their weighting in the signal are not completely understood. Some physical explanations could rely onto the motion in and out of mediastinal contents (hypersignal) and gas inside respiratory tracts (hyposignal), the variation of coil sensitivities while lung parenchymal signal evolves with proton density, or the variation of the B_0 homogeneity. However, it has been shown empirically that the DC signal at the center of the k-space correlates well with those of the respiratory belt, demonstrating the reliability of their measurement.[76]

B. Prospective gating

Prospective gating is a technique for which MR data is acquired only when the probed system reaches a selected motion state. For example, in the lung, the end of expiration for respiratory motion (Figure 2.4 left) can be selectively acquired where the subject can naturally stay a few seconds without further motion. This triggered acquisition can be performed for several motion gates.[77] A real-time navigator triggers the acquisition at the required respiratory state. This strategy enables data acquisition to be planned with an apparent motion-free k-space. As the acquisition is triggered, it leads to longer acquisition times.

[69] R. L. Ehman and J. P. Felmlee. *Radiology*, 1989.
[70] Stefan Weick et al. *Journal of Magnetic Resonance Imaging*, 2013.
[71] Thomas A. Spraggins. *Magnetic Resonance Imaging*, 1990.
[72] Y Wang et al. *Radiology*, 1996.
[73] Edward Brian Welch et al. *Magnetic Resonance in Medicine*, 2002.
[74] James G. Pipe. 1999.
[75] Wenwen Jiang et al. *Magnetic Resonance in Medicine*, 2018.
[76] Christoph Kolbitsch et al. *Physics in Medicine & Biology*, 2018.
[77] Guang Li et al. *International journal of radiation oncology, biology, physics*, 2017.

C. Retrospective gating

Retrospective gating is a technique where MR data is acquired continuously, and gating or binning is performed retrospectively during the reconstruction process according to a reference respiratory signal Figure 2.4 right). Images are then reconstructed for each gated dataset to form the respiratory dynamic. When the gating is performed on the self-navigator signal, it is called "self-gating". A first demonstration was made by Pipe *et al.* [74] This technique is now widely used for lung dynamic imaging. From this dynamic, strategies have been developed to obtain increased quality images (high SNR and more anatomical details) based on iterative motion-compensation reconstructions.[78] The deformation field is inferred from image registration and incorporated into the 3D+t reconstruction. It provides valuable morphological information but is computationally very expensive.

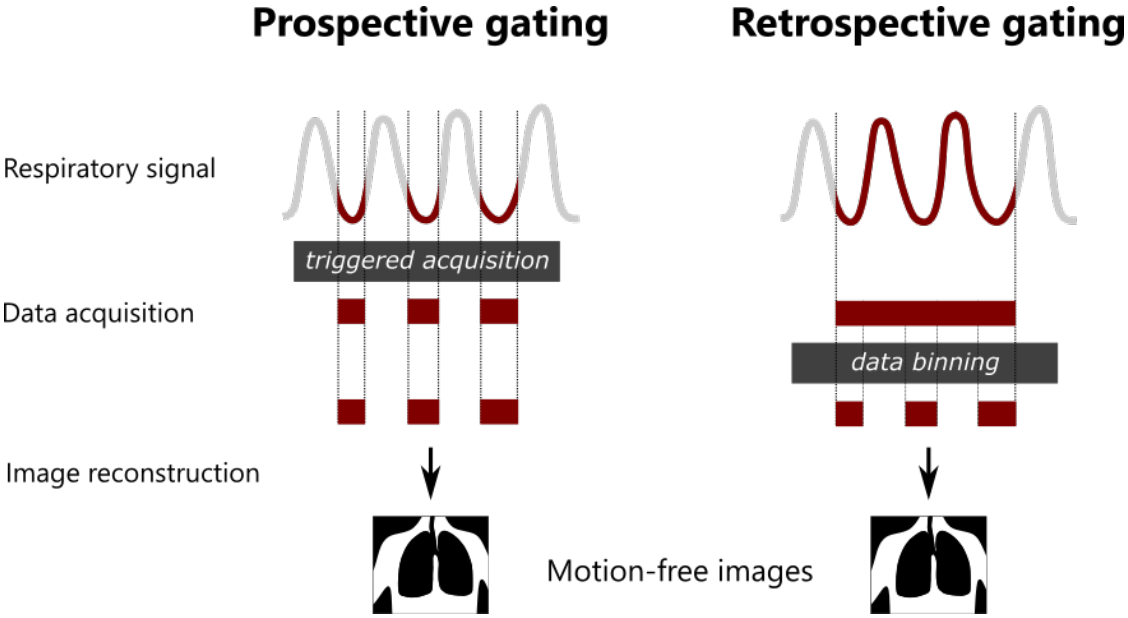

Figure 2.4: Motion-free acquisition strategies for lung MRI based on prospective or retrospective gating of one respiratory state. The prospective gating (left) relies on the triggered acquisition: the signal is acquired only when the lung is at a chosen respiratory state (usually end-of-expiration). The retrospective gating is based on data processing to extract only the data at certain respiratory states.

[74] James G. Pipe. 1999.
[78] Xucheng Zhu et al. *Magnetic Resonance in Medicine*, 2020.

These two techniques can be considered motion-free, with a negligible intra-bin motion, and can be derived into more complex motion-resolved approaches where several respiratory phases are prospectively acquired or retrospectively reconstructed. Some works demonstrate the feasibility of correcting motion in dynamic images by inferring lung deformations induced by respiration.[79,80] A motion-compensated image is reconstructed at one fixed respiratory state. For any of these techniques, the use of sequences less sensitive to motion and with self-navigation is preferred: radial sequences, for example, introduce an inconsistency in aliasing artifacts and lead to improved image quality at the reconstruction (mainly when using compressed sensing).

2.2.3 MR functional lung imaging

This section introduces the main techniques used to assess lung function. More in-depth and comprehensive presentations of these techniques can be found in Kauczor *et al.* [42] and Ohno *et al.* [81] Although, for clarity, the different lung functions are separated in this section, they are all intertwined. Furthermore, this part aims only to provide a summary overview of pulmonary function imaging. Section 2.3 will deepen techniques used for ventilation imaging upon a state-of-the-art review over the last 5 years.

A. Ventilation

In lung MRI, exogenous contrast agents or tracers can be administered through inhalable aerosols to cope with the low MR signal in the lung parenchyma. Dioxygen-enhancement MRI (OE-MRI), initially reported by Edelman *et al.*,[82] is based on the shortening of the T_1 relaxation time after the inhalation of 100 % O_2 (hyperoxic) instead of 21 % O_2 (normoxic). Therefore, the MR signal of ventilated lung

[79] Fei Tan et al. *Magnetic Resonance in Medicine*, 2023.
[80] Can Wu et al. *Physics in Medicine & Biology*, 2023.
[81] Yoshiharu Ohno et al. *Pulmonary Functional Imaging: Basics and Clinical Applications*. 1st ed. 2021 édition. Springer Nature Switzerland AG, Dec. 2020.
[82] R. R. Edelman et al. *Nature Medicine*, 1996.

tissues increases, improving the visualization of ventilated lung tissue. The data obtained can be presented as dioxygen signal-enhancement maps, or image intensities can be analyzed pixel-by-pixel to generate a lung T_1 map. The functional information obtained through OE-MRI combines ventilation, gas exchange, and perfusion weighting. By assuming that signal enhancement maps primarily capture changes in local dioxygen concentration, it becomes possible to quantify the local proportion of gas exchanged in a single breathing cycle based on the dynamics of dioxygen wash-in and wash-out and depict regional ventilation defects. However, separating sources of signal variation is not easy. This strategy based on proton MRI is readily accessible in clinical use with the additional administration of O_2. However, the required acquisition time is long (around 20 minutes).

A more widespread strategy, still considered as the gold standard for MRI of the respiratory function, is using hyperpolarized gases as tracers (primarily ^{3}Helium or ^{129}Xenon), as seen in section A.. The tracer gas is hyperpolarized outside the magnet, usually using optical pumping to reach out-of-equilibrium polarizations 5 to 6 orders of magnitude higher than thermal polarizations.[83] The hyperpolarized gas is then administered before being imaged. Ventilation maps, where the hyperpolarized gas goes, can be obtained either dynamically during inhalation (wash in) and exhalation (wash out) or statically during breath-hold. All these techniques based on inhaled tracer gas can be used statically (breath-hold) or dynamically with adapted rapid sequences. While ^{3}Helium remains in the airways, ^{129}Xenon can get dissolved in the blood and the tissue, so perfusion maps can also be obtained with chemically-shifted signal originating from the dissolved tracer. While ^{3}Helium MRI leads to SNRs twice higher at 1.5T than ^{129}Xenon MRI,[84] the latter offers a more economical alternative and no gas shortage so it is more widely used. However, the need for specialized signal acquisition hardware, gas polarization equipment, and expertise poses significant barriers to routine clinical use. To

[83] Edwin J.R. van Beek et al. *Journal of Magnetic Resonance Imaging*, 2004.
[84] Bilal A. Tahir et al. *International Journal of Radiation Oncology*Biology*Physics*, 2018.

overcome this limitation, the use of gases that contain fluorine atoms (^{19}Fluorine) is also investigated,[85,86] but their use is still not widespread due to the weaker signal.

Ventilation can also be assessed by post-processing a proton MRI series. The most popular relies on Fourier Decomposition principles, first described by Bauman *et al.* [87] This allows a simple clinical assessment of ventilatory function, making this strategy particularly attractive for clinical practice. These non-contrast-enhanced MR ventilation strategies will be detailed in the next section of this chapter 2.2.4, as they are at the heart of this thesis. Ventilation is sometimes assessed indirectly by evaluating the perfusion function: a perfusion defect can be indirectly identified by hypoxic vasoconstriction.[88]

B. Gas exchange

As explained above, OE-MRI maps provide mixed information on ventilation, gas exchange, and perfusion. The use of hyperpolarized ^{129}Xe is more commonly used in the literature to assess solely gas exchange. Thanks to the solubility and chemical shift of ^{129}Xe in the lung, it is possible to assess gas exchange specifically.[89] When inhaled, most of the gas remains in the airspace. At the same time, a small fraction enters pulmonary tissues and dissolves (Ostwald solubility of 0.27 in red blood cells (RBCs) and 0.10 in barrier/blood-plasma).[89] Two distinct resonances correspond to ^{129}Xe in interstitial tissue and plasma (collectively called the barrier) and in the RBCs. Xenon MRI can thus be an almost ideal probe for diffusive gas exchange.

[85] Marcus J. Couch et al. *Radiology*, 2013.
[86] Ahmed F. Halaweish et al. *Chest*, 2013.
[87] Grzegorz Bauman et al. *Magnetic Resonance in Medicine*, 2009.
[88] J. Biederer et al. *Seminars in Respiratory and Critical Care Medicine*, 2014.
[89] S. Sivaram Kaushik et al. *Magnetic resonance in medicine*, 2016.
[89] S. Sivaram Kaushik et al. *Magnetic resonance in medicine*, 2016.

C. Perfusion

To image pulmonary vascularization, we can distinguish two main approaches in lung MRI.[90,91] The first approach involves MR angiography (MRA) to evaluate the structure of the pulmonary arterial and venous system with higher spatial resolution. The second approach employs perfusion MRI with lower spatial resolution but higher temporal resolution, facilitating the assessment of tissue perfusion at the capillary level. Most MRA approaches rely on gadolinium contrast-enhanced perfusion proton MRI, relying on baseline acquisition followed by one or several contrast-enhanced acquisitions. The injected gadolinium in the bloodstream induces T_1 shortening in the vascular tree, enhancing the MR signal in T_1 weighted sequences. The signal enhancement is directly related to gadolinium concentration in the blood vessel. Contrast-enhanced MRA refers to a static but high-resolution image. At the same time, it is possible to use dynamic contrast-enhanced (DCE) MR images to access perfusion with lower spatial resolution but high temporal resolution similarly.[92] Although vascularisation assessments are often performed in clinical routines with contrast agents, recent developments promote techniques without contrast agents.

ECG-gated Fast Spin Echo (FSE) sequences use the T_2-weighted signal differences between fast and slow flows to generate such images without exogenous contrast. During systole, when the arterial flow is rapid, the MR signal intensity decreases, while the signal in diastole at low flow remain at high intensity. Subtracting the systolic image from the diastolic image results in a contrast that highlights the arterial system only.[93] The in-flow effect of the blood circulation can be exploited to produce time-of-flight MRA images.[94] Finally, the previously presented Fourier decomposition for ventilation imaging also allows perfusion-weighted imaging in a stack of 2D acquisitions, as it indirectly uses in-flow effects along

[90] Susan R. Hopkins et al. *Journal of Applied Physiology (Bethesda, Md.: 1985)*, 2012.
[91] Christopher S. Johns et al. *European Journal of Radiology*, 2017.
[92] Yaron Gordon et al. *Cardiovascular Diagnosis and Therapy*, 2014.
[93] Satoru Morita et al. *Radiographics: A Review Publication of the Radiological Society of North America, Inc*, 2011.
[94] Andrew J. Wheaton and Mitsue Miyazaki. *Journal of Magnetic Resonance Imaging*, 2012.

the cardiac frequency. The latter can lead to quantitative measurements of the perfusion, as demonstrated by Kjorstad *et al.*,[95] ultimately leading to the local evaluation of V/Q matching.[96]

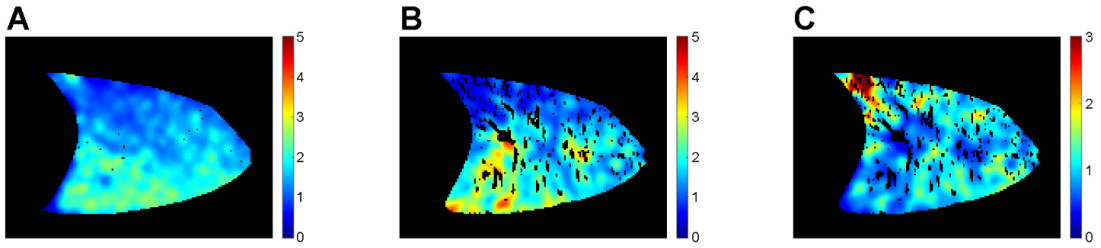

Figure 2.5: Figure extracted from Sà *et al.* work [97] using oxygen-enhanced MRI. Maps of the alveolar ventilation V_a (A), perfusion Q (B), and V_a/Q ratio (C) in a sagittal slice of the right lung in a healthy volunteer lying in the supine position. V_a and Q are expressed in ml/min/ml of lung. Ventilation-perfusion matching mainly occurs in the posterior dependent regions.

D. Biomechanics

Intrinsically linked to ventilation is the study of respiratory muscle mechanics and lung parenchyma deformation.[98] These methods are often limited to comparing two 3D MR images acquired respectively at the end of inspiration and at the end of expiration. Several diaphragm landmarks lead to muscle excursion between the two lung states at different locations.[99] Global lung volumes can be assessed through segmentation.[100] These approaches, widely available in clinical practice, have low spatial and temporal resolutions. Acquisitions based on spin tagging [101,102] or MR elastography [103,104] enable the encoding of motion in the magnetization's phase or magnitude and give insights into deformation velocity. However, the motion encoding gradient requires large echo times (around 10 ms), much longer than T_2^* in the lung. Refocused field echo sequences can be used to minimize the

[95] Åsmund Kjørstad et al. *Magnetic Resonance in Medicine*, 2013.
[96] Åsmund Kjørstad et al. *Zeitschrift Fur Medizinische Physik*, 2015.
[98] Ryan Amelon et al. *Journal of Biomechanics*, 2011.
[99] Khurram Saleem Khan et al. *Medical Sciences (Basel, Switzerland)*, 2019.
[100] Ayako Shimada et al. *Academic Radiology*, 2022.
[101] Jing Cai et al. *International journal of radiation oncology, biology, physics*, 2009.
[102] Q. Chen et al. *Magnetic Resonance in Medicine*, 2001.
[103] Yogesh K. Mariappan et al. *Journal of Magnetic Resonance Imaging*, 2011.
[104] Faisal Fakhouri et al. *NMR in biomedicine*, 2019.

T_2^* effects. Their acquisition time is, however, too long for clinical application. Finally, approaches using dynamic breathing series from ^{1}H MRI to estimate the deformation seem promising, as readily applicable in clinical routine.[105]

[105] Tanguy Boucneau et al. *Scientific Reports*, 2020.

2.2.4 Non-contrast enhanced MR ventilation imaging

The methods previously presented provide rich access to specific pathophysiological information. However, most of these methods are complex and expensive to integrate into clinical practice. Free-breathing proton MRI strategies without contrast agents or tracer gases have recently been improved to allow regional estimation of ventilation and respiratory dynamics while being easily translatable to clinical practice.[106] These methods are based on dynamic acquisitions of the lung volume along a given number of respiratory phases. They follow two main methodological strategies: intensity-based and deformation-based estimation of the gas intake and output. The principles of both methods are summarized for two respiratory phases in Figure 2.6.

[106] Chuan T. Foo et al. *Frontiers in Medicine*, 2023.

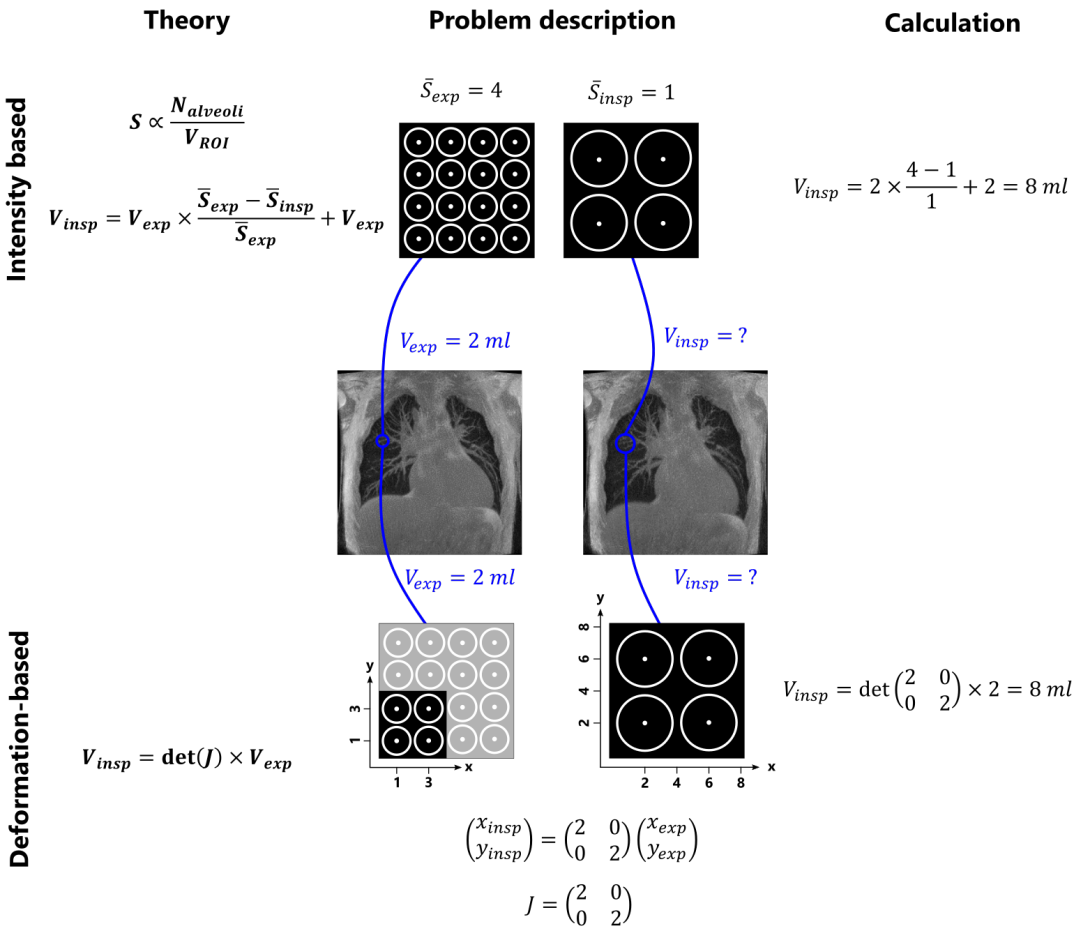

Figure 2.6: Intensity-based and deformation-based ventilation quantification using lung MRI. Circles represent alveoli. In the intensity-based approach (top), the MR signal is assumed to decrease with the density, which yields directly to an estimation of the associated gas fraction in the voxel. The schematic is inspired by Kjorstad *et al.* [107] In the deformation-based approach (bottom), the determinant of the Jacobian matrix (J) of the deformation provides the volume variations of a voxel between the two respiratory phases.

A. Intensity-based

In 2006, Zapke *et al.* set grounds for an innovative technique to infer local ventilation through MR acquisition without contrast agent and in free-breathing.[66] Fast MR pulse sequences enable to acquire a series of 2D images, which are retrospectively registered non-rigidly on a reference respiratory phase. The MR signal intensity is assumed to be directly proportional to the density, decreasing from end-of-expiration to end-of-inspiration, where proton density decreases as the gas enters the alveoli. The MR signal intensity is thus used to estimate the associated gas fraction in the voxel and subsequently infer the amount of ventilated gas as explained in Figure 2.6.

Bauman *et al.* [87] developed this idea with a method referred to as Fourier Decomposition (FD) pulmonary MRI. It conjointly infers ventilation and perfusion components from one dynamic MR acquisition. The technique relies on the dependencies of the MR signal on both hydrogen proton density changes and the in-flow effects of the circulating blood. The MR signal is filtered for each voxel using a temporal Hann window. The power spectrum of the Fourier transforms highlights the main dependencies on respiratory and cardiac frequencies. Ventilation and perfusion components are separated automatically, and the area under each peak provides surrogate measures for ventilation and perfusion mapping at respiratory and cardiac frequencies, respectively. This work set grounds for a new research scope, where researchers focused on post-processing developments to obtain quantitative measurements of the inhaled gas, improvements of the robustness of the technique, and opening up to 3D ventilation acquisitions. For this, we can, in particular, mention SENCEFUL,[108,109] PREFUL,[110,111] matrix pencil decomposition (MP),[112] NuFD [113] techniques. NuFD and MP were developed to improve

[66] Maren Zapke et al. *Respiratory Research*, 2006.
[87] Grzegorz Bauman et al. *Magnetic Resonance in Medicine*, 2009.
[108] André Fischer et al. *NMR in Biomedicine*, 2014.
[109] L. Mendes Pereira et al. *Magnetic Resonance in Medicine*, 2019.
[110] Andreas Voskrebenzev et al. *Magnetic Resonance in Medicine*, 2018.
[111] Filip Klimeš et al. *Magnetic Resonance in Medicine*, 2021.
[112] Grzegorz Bauman and Oliver Bieri. *Magnetic Resonance in Medicine*, 2017.
[113] David Bondesson et al. *Magnetic Resonance in Medicine*, 2019.

spectral estimation robustness of respiratory and cardiac amplitudes. PREFUL and SENCEFUL propose dynamic reconstructions of an average respiratory cycle, allowing the study of more quantitative dynamic parameters. They introduced 3D ventilation mapping as an extension of the Bauman*et al.* work.[109,111]

B. Deformation-based

Plathow *et al.* [114] first introduced in 2009 the idea to extract deformation using a registration approach on 3D dynamic lung images covering the respiratory cycle. No quantification of lung volumes was then established. Kjorstad *et al.* introduced in 2014 the use of the determinant of the Jacobian matrix applied to the deformation field to infer local lung volumes along the respiratory cycle [107] in 2D dynamic series. Kolb *et al.* [115] use a mesh model of the lung to estimate local deformation and flow-volume variations from a retrospectively gated acquisition. A more complete and recent approach combines these approaches and the latest developments in MRI sequences, referred to as 3D MR spirometry.[105] The method combines a 3D UTE acquisition, a retrospective 3D+t reconstruction of the respiratory dynamics, and elastic registration to estimate deformations. Relative volumes, and their temporal derivative, relative flow rates, are estimated from the Jacobian determinant of deformations as illustrated in Figure 2.6. It assumes the incompressibility of parenchymal tissues to associate local volumic variations to local ventilation only.

C. Approach comparison

Fourier decomposition (FD) techniques are very interesting for clinicians due to their versatility and implementation simplicity: obtaining ventilation, perfusion, and V/Q maps in one acquisition is possible. However, this double measurement is only possible with 2D acquisition stacks to preserve the in-flow effect of the

[109] L. Mendes Pereira et al. *Magnetic Resonance in Medicine*, 2019.
[111] Filip Klimeš et al. *Magnetic Resonance in Medicine*, 2021.
[114] Christian Plathow et al. *Korean Journal of Radiology*, 2009.
[107] Åsmund Kjørstad et al. *Magnetic Resonance Materials in Physics, Biology and Medicine*, 2014.
[115] Christoph Kolb et al. *Journal of Computer Assisted Tomography*, 2016.
[105] Tanguy Boucneau et al. *Scientific Reports*, 2020.

perfusion. Ventilation mapping from FD usually has a better spatial resolution than deformation-based techniques: smoothing approaches commonly used in the former are usually sharper (around 5 voxels isotropic) than the registration kernel size used in the latter (around 20 voxels isotropic). However, FD techniques rely on the strong assumption of the linear evolution of the signal with proton density, while it is known that several factors concomitantly affect the MR signal during respiration:

- Proton density: the primary effect of parenchymal signal variation during respiration.
- Gas composition: dioxygen concentration changes along the respiratory cycle (gas rich in O_2 while inhaling and poor while exhaling), and its presence shortens T_1, the resulting MR signal evolves.
- Microstructural changes: the inflation of alveoli induces a decreased density of the interface between gas and parenchymal tissue, leading to reduced magnetic susceptibility effects and, thus, an increase of T_2^*.
- Coil sensitivities: as the lung deforms during the respiratory motion, each coil element is not sensitive to the same parenchymal tissue element, leading to respiratory-varying loading of the coil.
- B_0 shift: when a consequent amount of air is inhaled, a global shift of the macroscopic resonant frequency from that of water toward that of air can occur (3.6 ppm at 1.5 T [46]) inhomogeneously across the lung, leading to a shift towards higher frequencies at inspiration and thus increased magnetization.
- Blood flow dependence of the respiratory state [116]: the perfusion changes during the respiration with slight variations of the transpulmonary pressure at tidal breathing which can affect the MR signal.[117 –119]

Quantitative intensity-based methods make the bold hypothesis of a linear evolution of the MRI signal with the proton density, which might not be true at 1.5 T

[46] C J Bergin et al. *Radiology*, 1991.
[116] K. Toska and M. Eriksen. *The Journal of Physiology*, 1993.
[117] Jie J. Cao et al. *Journal of magnetic resonance imaging: JMRI,*. 2011.
[118] Christian Fink et al. *Investigative Radiology*, 2005.
[119] Gerhard A. Brecher and Charles A. Hubay. *Circulation Research*, 1955.

or 3 T. Measurements based on the Jacobian of deformation are not subjected to the caveats mentioned above. Two comparisons of the Jacobian-based and the intensity-based approaches have also been carried out to my knowledge, finding a better reliability of the Jacobian-based method.[107,120]

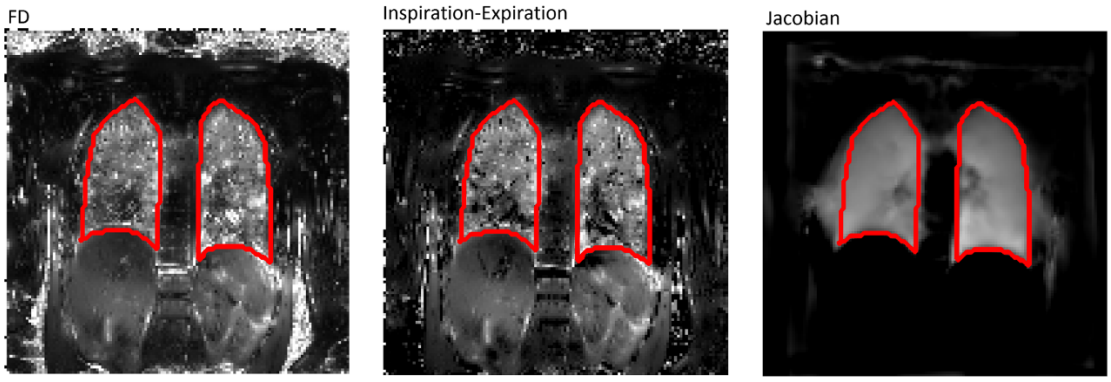

Figure 2.7: Mappings of the lung ventilatory function using dynamic MRI, extracted from Kjorstad *et al.*[107] Three fractional ventilation surrogates are inferred from 2D+t acquisitions in free-breathing: temporal Fourier decomposition to evaluate MR signal variations (left), intensity differences (middle) and the Jacobian of the deformation (right) between end-of-inspiration and end-of-expiration respiratory states. Intensity-based and deformation-based approaches result in different ventilation patterns, which could arise from the difference in smoothing, MR signal bias, or errors in the registration process.

Unlike ventilation imaging using gas tracers, non-contrast-enhanced MR ventilation techniques do not assess the concentration of gases moving through the lung volume but rather assess the volume of gas for different respiratory phases.

[107] Åsmund Kjørstad et al. *Magnetic Resonance Materials in Physics, Biology and Medicine*, 2014.

[120] Fei Tan. *Structural and Functional Ultra-short Echo Time (UTE) Proton Lung MRI: Techniques and Clinical Applications*. PhD thesis. UCSF, 2023.

2.3 Local impairments characterization of the ventilation: a state-of-the-art review

Weighted or quantitative ventilation mapping approaches flourish in lung MRI, each research group having its own methods, biomarkers, and pathophysiological data analysis framework. However, the literature is scarce when it comes to questioning the physiological information carried by each functional map. This section reviews the literature over the last 5 years to discuss the ventilatory biomarkers among functional lung MRI methods, their underlying pathophysiological insights, the definition of ventilation defect maps, and their clinical interest in asthma and COPD.

2.3.1 Methodological trends in MR ventilation imaging

A PubMed search was performed in July 2023 for articles on MR imaging techniques assessing local ventilation, using the following search terms in the title or the abstract for better filtering: [(MR OR MRI) AND (ventilation OR respiratory mechanics OR respiratory dynamic) AND (local OR regional OR voxel-wise)]. We limited the search to the last 5 years (2018-2023) and to journal papers, yielding 133 works evaluated for this synthesis. Forty-six of these works were not articles or about ventilation MRI, resulting in 85 articles finally being included (see Figure 2.8).

We notice that hyperpolarised gas MRI and non-contrast-enhanced MRI are the two most common approaches used in recent years. More specifically, ^{129}Xenon MRI is more common than ^{3}Helium MRI, with respectively 40 and 17 articles. In the non-contrast-enhanced proton MRI, we can mostly distinguish the Fourier Decomposition technique (and affiliated), which is the most prevalent among studies.

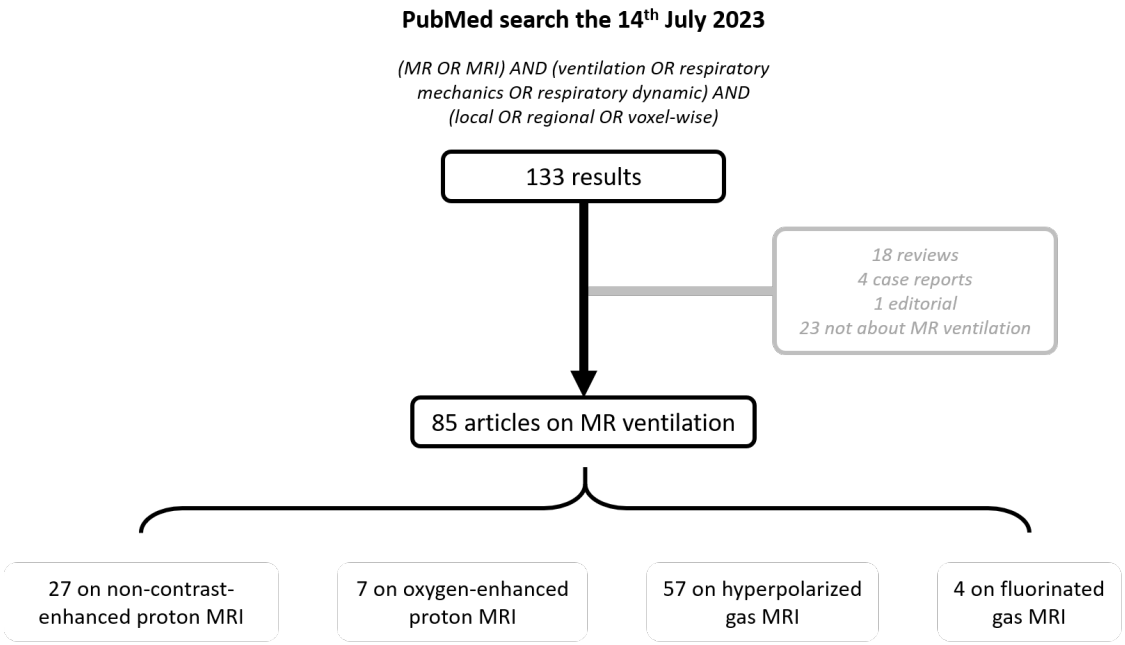

Figure 2.8: Flow diagram of the systemic review performed about MR ventilation techniques. PubMed search on July 14th, 2023. The search was limited to the last 5 years (2018-2023).

A comparison of ventilation maps from four techniques based on a tracer gas is given in Figure 2.10.[121]

A. Hyperpolarized gas MRI

^{3}Helium and ^{129}Xenon lung function MRI rely on similar methodologies and are thus presented jointly. The two techniques have been historically the first approaches to assess lung ventilation from MR imaging.[122,123] and are today still very popular. ^{3}Helium MRI is used in 18 % of selected studies. Two advantages are put forward: the very good SNR (higher gyromagnetic ratio and greater achievable polarization compared to ^{129}Xenon [124]) and the fact that helium almost does not cross the alveolar-capillary barrier compared to ^{129}Xenon, leading to more precise evaluation of ventilation only, more specifically, the distribution of the tracer gas in the lung. Because of rising costs and scarcity of ^{3}Helium, the MR lung

[121] Lukas Ebner et al. *European Journal of Radiology*, 2017.
[122] M. S. Albert et al. *Nature*, 1994.
[123] Peter Bachert et al. *Magnetic Resonance in Medicine*, 1996.
[124] Ummul Afia Shammi et al. *Academic Radiology*, 2022.

imaging community is now switching to ^{129}Xenon, with 43 % of articles using this technique. ^{129}Xenon is less diffusive than ^{3}Helium ($D_{\text{Xenon}} = 0.12$ cm^2/s vs $D_{\text{Helium}} = 0.88$ cm^2/s in the air), which could be perceived as a drawback: some regions partially obstructed will not be reached by the gas, and no further analysis can be performed. However, lower diffusivity also makes a better sensitivity to ^{129}Xenon MRI.[124]

Moreover, the advantageous solubility of ^{129}Xenon has recently been exploited using Dixon methods to separate between components with different resonance frequencies.[125] while ^{3}Helium is almost not soluble in surrounding tissues (Ostwald coefficients in water and blood are respectively: ~ 0.010 and ~ 0.009), the large polarisable electron clouds of ^{129}Xenon allow it to dissolve largely in parenchymal tissues, plasma, and red blood cell (Ostwald coefficients are respectively: ~ 0.1, ~ 0.09, and ~ 0.2 [126]) Each frequency associated with the gas dissolved in different environments allows for the specific differentiation of ventilation, septal transfer of gas, and its transport into red blood cells.

For both tracers, fast gradient echo pulse sequences, like SPGR or SSFP, are preferred to manage signal decay (T_2^* and diffusion-induced caused by imaging gradients).[127]) Most acquisitions are performed at breath-hold. A few of them used 2D rapid dynamic acquisitions to enable the study of dynamic hyperpolarized gas transport in the respiratory tract during breathing cycles and quantitatively infer the local ventilated gas volume. Some works used diffusion acquisition to assess lung microstructure.[128 –130] Different volumes were imaged: FRC + 1 L, FRC + adjusted volumes to subjects' height, and TLC. The images acquired after inhalation of hyperpolarized ^{3}Helium provide ventilation-weighted maps and, more specifically, reflect the gas transport in certain pulmonary regions. This transport

[124] Ummul Afia Shammi et al. *Academic Radiology*, 2022.
[125] Ziyi Wang et al. *The European respiratory journal*, 2019.
[126] Helen Marshall et al. *Progress in Nuclear Magnetic Resonance Spectroscopy*, 2021.
[127] Ramanpreet Sembhi et al. *Diagnostics (Basel, Switzerland)*, 2023.
[128] Agilo Luitger Kern et al. *Magnetic Resonance in Medicine*, 2019.
[129] Naz P. Taskiran et al. *Tomography (Ann Arbor, Mich.)*, 2022.
[130] Ziyi Wang et al. *Journal of Applied Physiology*, 2021.

can be convective (in the large proximal airways) or diffusive (in the peripheral regions).[131]. Physiological information can differ greatly depending on the inhaled gas volume evaluated.[132] The effect of airway opening between FRC + 1 L and TLC demonstrates a decreased heterogeneity with more ventilated areas. 1 L bags are the most common inhaled volume used for hyperpolarized gas MRI protocol, which can, however, correspond closely to TLC for smaller patients.

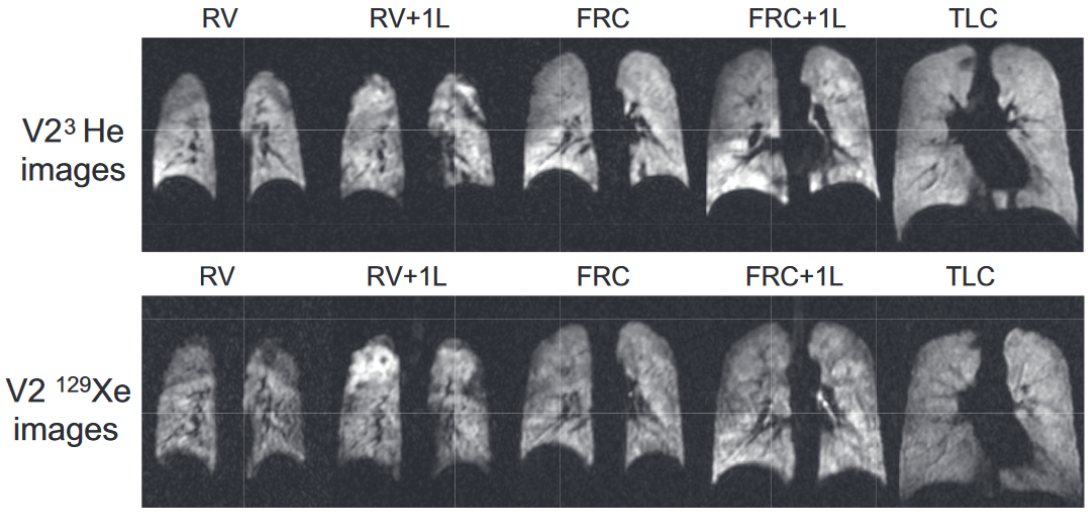

Figure 2.9: Ventilation maps of volunteer 2 (V2) using both ^{3}Helium (top) and ^{129}Xenon (bottom) at different lung volumes: RV (residual volume), RV + 1L (residual volume plus 1 liter of gas mixture), FRC (functional residual capacity), FRC + 1L (functional residual capacity plus 1 liter of gas mixture), and TLC (total lung capacity). The reduced heterogeneity of the gas distribution at TLC is depicted. The Figure is extracted from Hughes *et al.*[132]

B. ^{19}Fluorine MRI

Fluorinated gases can be used with thermal polarization. They are nontoxic and chemically inert. However, dedicated hardware is required to assess the MR signal, which resonates at lower frequencies ($\gamma = 40.08$ MHz/T), and the SNR is lower than previously presented hyperpolarized gases due to the low polarized ^{19}Fluorine signal. The low solubilities in water and blood enable a specific ventilation assessment.

[131] Helen Marshall et al. *Journal of Allergy and Clinical Immunology*, 2021.
[132] Paul J. C. Hughes et al. *Journal of Applied Physiology*, 2019.

The imaging protocol is similar to previous techniques based on tracer gas acquisition for ventilation assessment. Accelerated ^{19}Fluorine dynamic MR imaging has been evaluated and compared to hyperpolarized dynamic imaging.[127] Ventilation-weighted MRI for the different tracer gas lungs is presented in Figure 2.10. The repeatability of ^{19}Fluorine MRI has been demonstrated for quantitative gas volume ventilation from wash-out decay of the MR signal.[133] Optimization of acquisition parameters and benefits of compressed sensing reconstruction have been evaluated.[134]

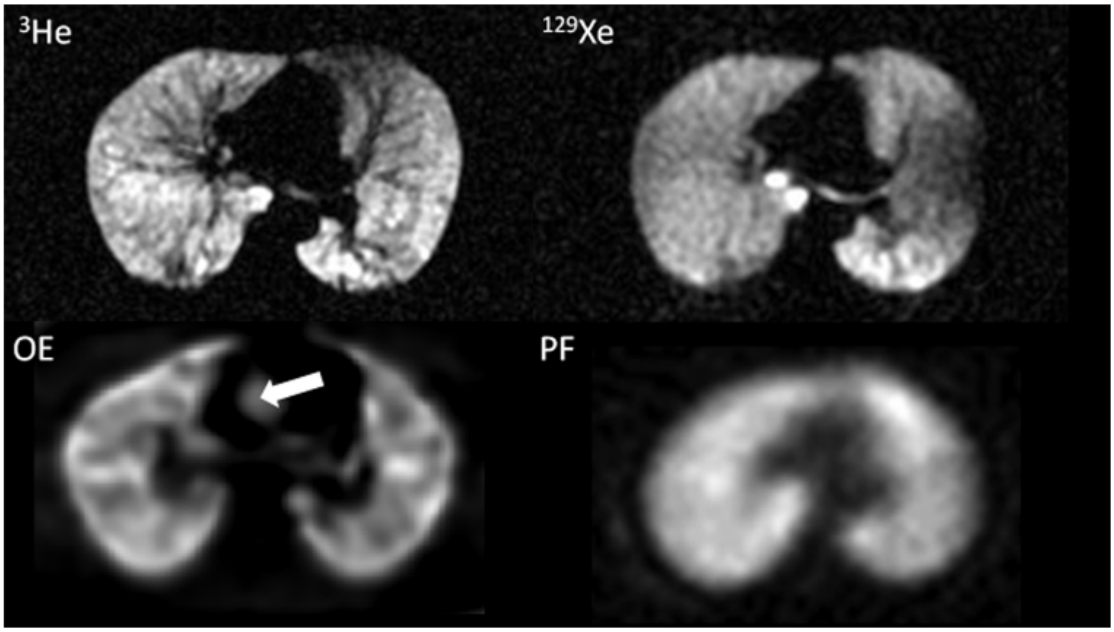

Figure 2.10: Tracer gas MR ventilation maps using ^{3}Helium (top left), ^{129}Xenon (top right), oxygen enhanced (bottom left), and perfluorinated gas (bottom right). The Figure is extracted from Ebner *et al.* [121] In oxygen-enhanced MRI, the signal enhancement extends beyond the lungs into the ascending aorta (indicated by the arrow). Each technique displays a representative slice extracted from a 3D or 2D stack covering the entire lung volume. ^{3}Helium MRI has the highest SNR, while ^{129}Xenon demonstrates a similarly high SNR. Oxygen-enhanced MRI seems less homogeneous as its signal depends on perfusion and gas exchanges. ^{19}F MRI demonstrates a good SNR with a simpler acquisition protocol than hyperpolarized gas MRI.

[127] Ramanpreet Sembhi et al. *Diagnostics (Basel, Switzerland)*, 2023.
[133] Marcel Gutberlet et al. *Academic Radiology*, 2019.
[134] Mary A. Neal et al. *Magnetic Resonance in Medicine*, 2019.

C. Oxygen-enhanced MRI

As oxygen-enhanced MRI (OE-MRI) uses the sensitivity of the MR signal to the paramagnetism of dioxygen molecules, resulting in T_1 shortening, T_1-weighted fast imaging is thus preferred to assess local dioxygen concentration. OE-MRI is readily available as acquisitions are performed using standard MR scanners and hardware. Moreover, the contrast agent, pure oxygen, is broadly available. However, the signal is conjointly dependent on ventilation, perfusion, and gas transfer, with hardly distinguishable components. The combined lung function affects the MR signal and induces differences with ^{3}Helium MRI, measuring ventilation only, as shown in Figure 2.11. This technique is used in 7 % of recent articles. It has been evaluated at 0.55 T where T_1 relaxivity of oxygen is enhanced compared to the one at standard 1.5 T, and thus the sensitivity of oxygen-enhanced lung MRI is improved.[135] Some protocols are based on the relation between dynamic signal changes from fast variations of inhaled oxygen concentrations and the quantitative measure of the specific ventilation.[136]

D. Non-enhanced proton MRI

Ventilation imaging using proton MRI without contrast agents or tracer gases is gaining interest due to the recent progress of lung imaging using proton MRI combined with the simplicity of its clinical transfer. We count 28 % of included research articles using these techniques. However, some do not provide ventilation maps but use imaging to evaluate aspects of respiratory mechanics, often global or at specific landmarks. For example, some protocols evaluate the movement of the diaphragm from dynamic MRI images.[99] This type of study allows a specific assessment of diaphragmatic function and is used for neuromuscular diseases. Lung segmentation can also be performed on several respiratory phases to assess global ventilation.[139]

[135] Ipshita Bhattacharya et al. *NMR in biomedicine*, 2021.
[136] Eric T. Geier et al. *Journal of Visualized Experiments: JoVE*,. 2019.
[99] Khurram Saleem Khan et al. *Medical Sciences (Basel, Switzerland)*, 2019.
[139] Yubing Tong et al. *Radiology*, 2019.

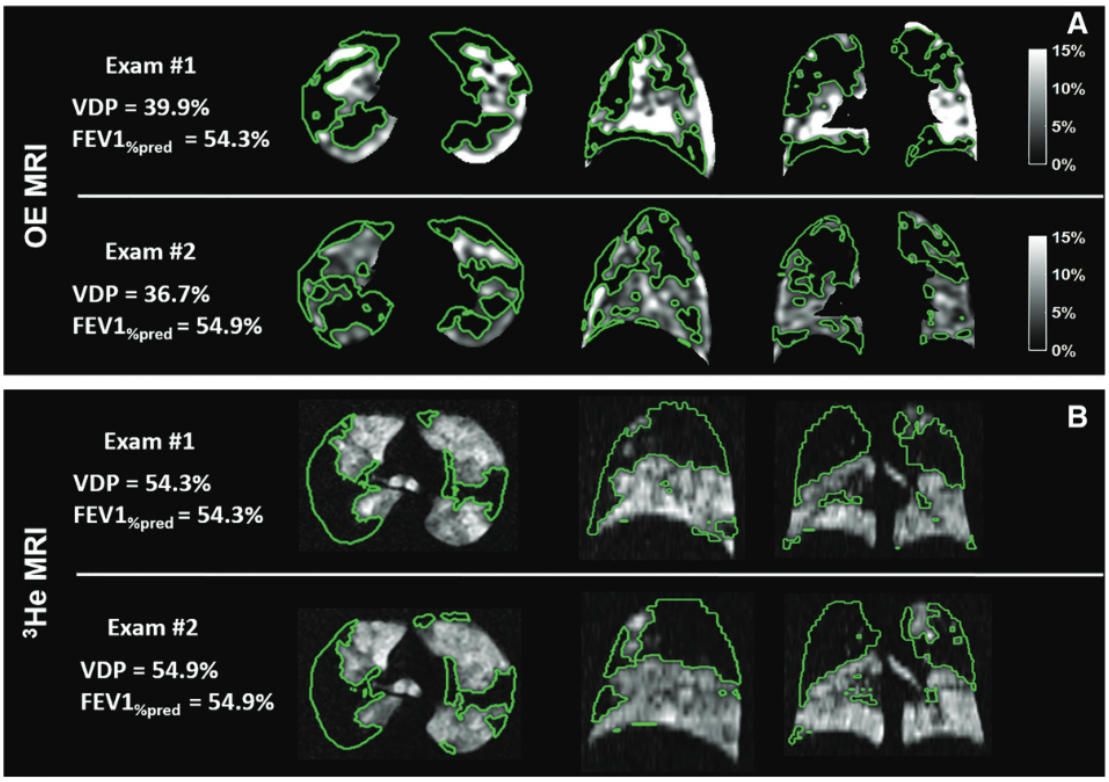

Figure 2.11: The repeatability of ventilation defect percentage (VDP) was assessed using oxygen-enhanced MRI and hyperpolarized ^{3}Helium MRI in a 37-year-old woman with cystic fibrosis. The examinations, conducted a week apart, showed a similar VDP despite slight variations in spatial locations of large focal defects outlined in green. Defects regions are consistent between techniques but not their surfaces. The average Dice coefficient [137] for regional defects between examinations was 0.48 for oxygen-enhanced MRI and 0.72 for ^{3}Helium MRI, indicating better repeatability with 3He MRI. The Figure is extracted from Zha *et al.* [138]

Multivolume lung MRI

Multivolume MRI defines the technique of multiple MR acquisition at different lung volumes (i.e. respiratory states) to explore the ventilatory function. Intensity changes between expiratory and inspiratory breath-hold images acquired are used as a surrogate of the ventilation. Only four publications report this method despite its clinical availability. Proton-density change maps are the most common and set grounds for defining ventilation defects.[140] Other physical or physiological effects on the MR signal are not considered nor discussed in the papers. Some works use the

[140] Francesca Pennati et al. *European Respiratory Journal*, 2019.

multivolume technique to focus on structural markers and lung morphologies.[139]

Fourier Decomposition and derivated methods

The study of ventilation is carried out using dynamic acquisitions. Local ventilation analysis is then performed based on variations in the MRI signal during respiration, often using methods derived from "Fourier decomposition".[87] These techniques are increasingly used and represent 77 % of non-enhanced proton MRI techniques evaluating ventilation and 21 % of all MR ventilation techniques used these last 5 years. In particular, Phase-Resolved Functional Lung (PREFUL)-MRI ventilation uses a Fourier decomposition on retrospectively rephased thoracic images once registered on a reference respiratory phase. It uses a sine model to estimate each image's cardiac and respiratory phases, allowing it to reconstruct retrospectively dynamic images of the cardiac and respiratory cycles and then assess ventilation and perfusion map.[110] This method has received significant clinical attention with studies of its reliability in cohorts of patients: chronic lung allograft dysfunction,[141 –143] COPD,[144,145] cystic fibrosis [146,147] or bronchopulmonary dysplasia.[148] This technique makes it possible to generate ventilation and perfusion maps only using multislice 2D acquisitions (to preserve the inflow effect to evaluate perfusion). A 3D strategy has been developed to assess ventilation only.[111] A study showed that using a bSSFP type sequence makes it possible to improve the robustness of the Fourier decomposition approach to field inhomogeneities.[149]

[139] Yubing Tong et al. *Radiology*, 2019.
[87] Grzegorz Bauman et al. *Magnetic Resonance in Medicine*, 2009.
[110] Andreas Voskrebenzev et al. *Magnetic Resonance in Medicine*, 2018.
[141] A. Voskrebenzev et al. *American Journal of Transplantation: Official Journal of the American Society of Transplantation and the American Society of Transplant Surgeons*, 2018.
[142] Tawfik Moher Alsady et al. *Journal of magnetic resonance imaging: JMRI*,. 2019.
[143] Jens Vogel-Claussen et al. *Radiology*, 2023.
[144] Gesa H. Pöhler et al. *Journal of magnetic resonance imaging: JMRI*,. 2021.
[145] Andreas Voskrebenzev et al. *Radiology. Cardiothoracic Imaging*, 2022.
[146] Till F. Kaireit et al. *Journal of magnetic resonance imaging: JMRI*,. 2021.
[147] Samal Munidasa et al. *Magnetic Resonance in Medicine*, 2023.
[148] J. P. Dyke et al. *Pediatric Radiology*, 2023.
[111] Filip Klimeš et al. *Magnetic Resonance in Medicine*, 2021.
[149] Efe Ilicak et al. *Magnetic Resonance in Medicine*, 2022.

Deformation field methods

A paper based on non-enhanced proton MRI does not use the signal intensity variations but the deformation field extracted from image registration of the respiration dynamic.[105] The surrogate of the ventilation is computed from the Jacobian of the deformation, similar to common CT ventilation mapping approaches. From the Green-Lagrange tensor, motion descriptors are also extracted to characterize the deformation. Moreover, the paper evaluates the full dynamic upon 32 respiratory phases at inspiration and expiration.[150] This technique has no equivalent in the published studies carried out during the last 5 years. The principle does not rely on the assumption of linear evolution of MR signal with proton density. However, only a single proof of concept has been given so far. Only a few other papers reported the use of the Jacobian approach.[107,115,151] It would require an evaluation of the reliability of the technique and its clinical relevance for pulmonary disease diagnosis. It is the purpose of this doctoral work.

The strengths, weaknesses, or issues of each MR ventilation modality are summarized in Table 2.1. The Table focuses on the feasibility and simplicity of clinical translation (difficulty of techniques and costs), ventilation biomarkers, and the progress of research scope, particularly the demonstration of clinical sensitivity to main pulmonary diseases with ventilatory dysfunction.

[105] Tanguy Boucneau et al. *Scientific Reports*, 2020.
[150] Edward Castillo et al. *Medical Physics*, 2019.
[107] Åsmund Kjørstad et al. *Magnetic Resonance Materials in Physics, Biology and Medicine*, 2014.
[115] Christoph Kolb et al. *Journal of Computer Assisted Tomography*, 2016.
[151] Fei Tan et al. *bioRxiv*, 2023.

	^{3}He	^{129}Xe	^{19}F	Oxygen-enhanced	Multi-volumes	FD	Green-Lagrange
Protocol							
Cost	+++	+++	++	++	+	+	+
Specific hardware	yes	yes	yes	yes	no	no	no
Trained staff	+++	+++	+++	++	+	+	+
Scanning time	+	+	++	+++	+	+	+
Processing time	+	+	+	+	+	+++	+++
Image resolution							
Spatial	+++	+++	+	++	++	++	+
Temporal	NA	NA	NA	+	NA	+++	+++
Ventilatory biomarkers							
Gas distribution	yes	yes	yes	yes+	yes+	yes	yes
Dynamic	no	no	no	explored	no	yes	yes
Motion	no	no	no	no	no	no	yes
Clinical interest							
Lung functions	V	V, Q, GE	V	mixed V, Q, GE	mixed V, Q, GE	V, Q	V
Clinical validation	+++	+++	+	++	+	++	+

Table 2.1: Summary of the key differences between techniques assessing the lung ventilatory function using MRI.

2.3.2 Biomarkers of the local ventilation

Different biomarkers are extracted from the methods presented, offering diverse pathophysiological information. This part presents these ventilation measurements, sometimes local, sometimes global, according to the clinical information they can provide. These biomarkers are divided into gas distribution, dynamic, and motion descriptors. Structural biomarkers, coupled with functional analysis, are provided as an indirect surrogate of the ventilatory function.

A. Gas distribution

Most ventilation studies evaluate gas distribution at a given time and associated lung volume. Indeed, ventilation can be seen as the ability to distribute gases optimally through the bronchial tree down to the terminal alveoli. Most non-proton MRI studies evaluate the MR signal magnitude at a given lung volume,

usually at functional lung capacity plus the volume of administered gas mixture.[152] The alveolar oxygen partial pressure (PaO2) is assessed from the evaluation of the decay of the hyperpolarized ^{3}Helium signal over breath-hold.[129] For proton MRI, it is necessary to evaluate the local MR signal magnitude between two respiratory phases acquired in breath-hold, usually at the end of inspiration and end of expiration.[140,153] Absolute or differential MR signal magnitude maps thus provide information on the gas spatial distribution, that is, the relative amount of gas at any lung location at a given respiratory state. Even though they are labeled "ventilation maps", they are more specifically surrogates of inhaled gas volume maps. The most common ones are:

- Specific ventilation (SV): fraction of the reference lung volume that is replaced by fresh gas that is: $SV = \frac{V_f}{V_{ref}}$
- Fractional ventilation (FV): fraction of total lung volume of fresh gas on end-of-inspiration, that is: $FV = \frac{V_{ref}}{V_{ref}+V_f}$ with V_f the volume of fresh gas and V_{ref} the volume of reference.

The percentage of ventilated volume (%VV) or, its opposite equivalent, the ventilation defects percent (VDP) are global metrics of the lung function commonly evaluated.[131] For non-proton MRI, the total lung volume (TLV) is measured on a reference image where lung morphology can be assessed. %VV and VDP are generally computed relatively to the TLV, but some studies divide the lung into proximal and peripherical regions,[131]or lobes and segments.[154] These "ventilated" and "non-ventilated" regions are defined either by thresholding or by segmenting ventilation maps (using different approaches and bin numbers, usually 4 or 6 bins [155,156]).

[152]Bilal A. Tahir et al. *Physics in Medicine and Biology*, 2019.
[129]Naz P. Taskiran et al. *Tomography (Ann Arbor, Mich.)*, 2022.
[140]Francesca Pennati et al. *European Respiratory Journal*, 2019.
[153]Julius Frederik Heidenreich et al. *Radiology*, 2023.
[131]Helen Marshall et al. *Journal of Allergy and Clinical Immunology*, 2021.
[131]Helen Marshall et al. *Journal of Allergy and Clinical Immunology*, 2021.
[154]Kamran Poorbahrami et al. *Journal of Applied Physiology*, 2019.
[155]David G. Mummy et al. *Radiology*, 2021.
[156]Mu He et al. *Academic Radiology*, 2019.

The inhomogeneities gas distribution maps are also evaluated. Inhomogeneity maps are computed using a kernel over the ventilated map to ultimately estimate regional coefficients of variations. Some global statistics can then be extracted over the entire lung from these maps to provide global biomarkers of the gas distribution: interquartile range (IQR), median or mean ventilation.[132,157]

B. Dynamic

Imaging the complete respiratory dynamic combined with three-dimensional space requires long acquisition times and is not feasible for every lung MRI modality. A strong methodological barrier appears for protocols using gas mixture inhalations because of the low availability of gas, imaging cost, MR magnetization decays, and potential health impact for higher gas dose inhalation.[158] Subjects are thus mostly asked to hold their breath at a certain lung volume defined by that gas mixture bag capacity. Advanced acquisition and reconstruction techniques are explored to accelerate acquisition greatly (33 frames in less than 7 s in Xiao *et al.* [159]). Some studies compute dynamic markers of the ventilation: wash-in and wash-out methods to compute wash-in and wash-out times constants,[127,160,161] or delayed ventilation which is measured from delays of ventilation peaks between each lung region and the trachea.[162]

Most dynamic biomarkers are computed from proton MRI non-contrasted imaging while the subject freely breathes. Particularly, retrospective gating provides a dynamic view of an integrated respiratory cycle during the acquisition time, i.e. dynamic respiration images over the acquisition time. The most used functional maps are minute ventilation (inhaled volume per minute) [163], time to peak ventilation

[132]Paul J. C. Hughes et al. *Journal of Applied Physiology*, 2019.
[157]Laurie J. Smith et al. *European Respiratory Journal*, 2018.
[158]S. Sivaram Kaushik et al. *Magnetic Resonance in Medicine*, 2011.
[159]Y. Xiao et al. *IEEE Transactions on Medical Imaging*, 2020.
[127]Ramanpreet Sembhi et al. *Diagnostics (Basel, Switzerland)*, 2023.
[160]Anne-Christianne Kentgens et al. *Respiratory Medicine and Research*, 2023.
[161]Joseph G. Mammarappallil et al. *Military Medicine*, 2020.
[162]Mitchell Chen et al. *European Radiology*, 2020.
[163]F. Klimeš et al. *NMR in Biomedicine*, 2019.

(percentage of respiratory time needed to reach local maxima of ventilation) [164], and flow-volume loops.[105,142]

C. Motion descriptors

Lung displacement and deformation measurements, particularly of the diaphragm and the chest wall, can be obtained from multivolume acquisitions obtained at different respiratory states. This can involve landmarks placed in areas of interest [99] or volume variations analysis through global segmentations.[139] Voxel-wisel deformations can also be inferred from image registration,[105] ultimately leading to the extraction of strain components (along the superior-inferior, right-left, anteroposterior axes or eigenvectors), anisotropy deformation index (ADI), or slab-to-rod index (SRI). By using models, it could then be possible to trace the local mechanical properties of tissues themselves.

D. Structural properties for indirect assessments of the ventilation

Using imaging to assess lung function reveals underlying structures. As the disease progresses, both function and structure change concurrently at the macroscopic and microscopic levels. These structural changes thus provide supplementary information, indirectly informing about ventilatory function.

Lung morphology

MR imaging enables direct assessment of lung morphology. Abnormal morphologies can be associated with pathologies: it could be, for example, a flattened diaphragm (gas retention for emphysema or diaphragm dysfunction), obstructed

[164] Filip Klimeš et al. *Journal of magnetic resonance imaging: JMRI*,. 2021.
[105] Tanguy Boucneau et al. *Scientific Reports*, 2020.
[142] Tawfik Moher Alsady et al. *Journal of magnetic resonance imaging: JMRI*,. 2019.
[99] Khurram Saleem Khan et al. *Medical Sciences (Basel, Switzerland)*, 2019.
[139] Yubing Tong et al. *Radiology*, 2019.
[105] Tanguy Boucneau et al. *Scientific Reports*, 2020.

main airways, or abnormalities in respiratory tracts, all of them leading to restriction or obstruction in the ventilatory function. Despite such analyses being carried out using lung MRI, conventional radiology, and CT scans are generally favored in clinical practice due to their higher availability and higher spatial resolution, few studies quantify these aspects using proton MRI in the corpus of selected articles. In Tong *et al.*,[165], a symmetry index between right and left lung volumes is proposed. The same team used thoracic and lumbar Cobb angles (degree of spinal curvature [166]) to evaluate their influence on tidal volumes for thoracic insufficiency syndrome.[139] An explanation for this lack of such biomarkers in the corpus may be that the keyword search query did not specifically target techniques assessing lung morphology.

Alveolar microstructures

Biomarkers are extracted from hyperpolarized MR imaging to describe the alveolar structure and functions. The alveolar microstructure size (alveolar volume or acinar duct radius) is the most common parameter evaluated in the literature. From the apparent diffusion coefficient, the distance of gas molecules restricted by the alveolar wall can be assessed from voxel-by-voxel decaying exponential fit of the 5 b-value data.[167] Similarly, accessible alveolar volume can be computed from ^{129}Xe mapping of ventilation, interstitial barrier uptake, and red blood cell transfer.[130] Septal wall thickness is retrieved from dissolved gas recovery curves.[168] Local diffusing capacity for carbon monoxide (DL_{CO}) relies strongly on the local structure and can be assessed, under a model, from ^{129}Xe mapping of ventilation, interstitial barrier uptake, and red blood cell transfer.[130]

[165] Yubing Tong et al. *Chest*, 2021.
[166] Hana Kim et al. *RadioGraphics*, 2010.
[139] Yubing Tong et al. *Radiology*, 2019.
[167] Laura L. Walkup et al. *Annals of the American Thoracic Society*, 2019.
[130] Ziyi Wang et al. *Journal of Applied Physiology*, 2021.
[168] Haidong Li et al. *Science Advances*, 2021.
[130] Ziyi Wang et al. *Journal of Applied Physiology*, 2021.

Biomarkers providing absolute values are scarce, whether they are morphological or dynamic. Furthermore, most biomarkers assess heterogeneity of gas distribution at a single respiratory volume, whereas it is known that heterogeneity is very dependent on the volume studied.[131] An evaluation of the temporal dynamics would be beneficial as spirometry demonstrates the importance of flow rates, even during free breathing,[169] and peak ventilation phases have shown their sensitivity on PREFUL clinical investigations.[164]

[131] Helen Marshall et al. *Journal of Allergy and Clinical Immunology*, 2021.
[169] K. H. Carlsen and K. C. Lødrup Carlsen. *The European respiratory journal*, 1994.
[164] Filip Klimeš et al. *Journal of magnetic resonance imaging: JMRI*,. 2021.

2.3.3 Define local ventilation impairments

It is generally difficult to report measurement results of local functional ventilation mapping because of the inherent dimensionality (3D or 4D), the density of information, and the intra- and inter-subject expected morphological and dynamical variations when dealing with human lungs. Furthermore, radiologists often expect a simple and global metric.

Diagnostic tools developed by the pulmonology and radiology communities aim to define "impairments" and "defects". These notions are philosophically challenging and prone to bias: can we differentiate between normal and abnormal, healthy and unhealthy? This part reports methods defining such impairments based on functional lung MRI and some of their methodological limits, as well as diagnostic performance.

A. Recent developments in ventilation defect mapping

A ventilation defect map is a binary segmentation of the lung volume to highlight regions defined as abnormally low-ventilated. From a quantitative map of pulmonary ventilation, a threshold is defined to discriminate between healthy and defective regions. Methods can vary from one ventilation imaging modality to another and from one research team to another, and there is no absolute threshold for all lung pathologies. The choice of statistics for assessing ventilation function and the thresholding strategy for discriminating between healthy and defective regions are crucial.

Most studies use the mapping of the gas ventilated through the experiment as the surrogate for assessing the ventilation function. A few studies in proton MRI, based on the PREFUL technique, assess a correlation between a reference flow-volume loop with local pseudo-flow-volume loops throughout the lung.[145,147,170]

[145] Andreas Voskrebenzev et al. *Radiology. Cardiothoracic Imaging*, 2022.
[147] Samal Munidasa et al. *Magnetic Resonance in Medicine*, 2023.
[170] Tawfik Moher Alsady et al. *Magnetic Resonance in Medicine*, 2024.

This map assesses the gas distribution and the dynamic of the ventilation conjointly, which reported a good sensitivity to chronic lung allograft dysfunction [142] and COPD.[144]

Most approaches to discriminate healthy regions from defective regions on ventilation maps are inspired by the literature on hyperpolarized MRI, as it pioneered the field of functional lung MRI. The two main approaches to analyze histograms of the ventilation biomarker over the lung volume are either single thresholding (from previous analysis [143,171]), or non-binary binning [135] usually into 4 or 6 bins. Most reported studies use mean anchored linear binning for the latter, but linear binning based on a reference population and Atropos (n-class open-source segmentation framework [172]) are common.[173] The Figure 2.12 extracted from the work of He *et al.* summarizes binning methods.[156]

It would be necessary to benchmark the diagnostic performance of the ventilation defect mapping strategy (biomarker choice and defect binning approach) for each method and each pathology. Moreover, impairments are almost exclusively devoted to studying low-ventilated regions (commonly called "defects") in the literature. Only in one work, highly ventilated regions are evaluated, which is sensitive to local lung function impairment for COVID-19 patients.[174]

[142] Tawfik Moher Alsady et al. *Journal of magnetic resonance imaging: JMRI*,. 2019.
[144] Gesa H. Pöhler et al. *Journal of magnetic resonance imaging: JMRI*,. 2021.
[143] Jens Vogel-Claussen et al. *Radiology*, 2023.
[171] Laura L. Walkup et al. *The European respiratory journal*, 2019.
[135] Ipshita Bhattacharya et al. *NMR in biomedicine*, 2021.
[172] Brian B. Avants et al. *Neuroinformatics*, 2011.
[173] Peter J. Niedbalski and Zackary I. Cleveland. *NMR in biomedicine*, 2021.
[156] Mu He et al. *Academic Radiology*, 2019.
[174] Cheng Wang et al. *European Radiology*, 2022.

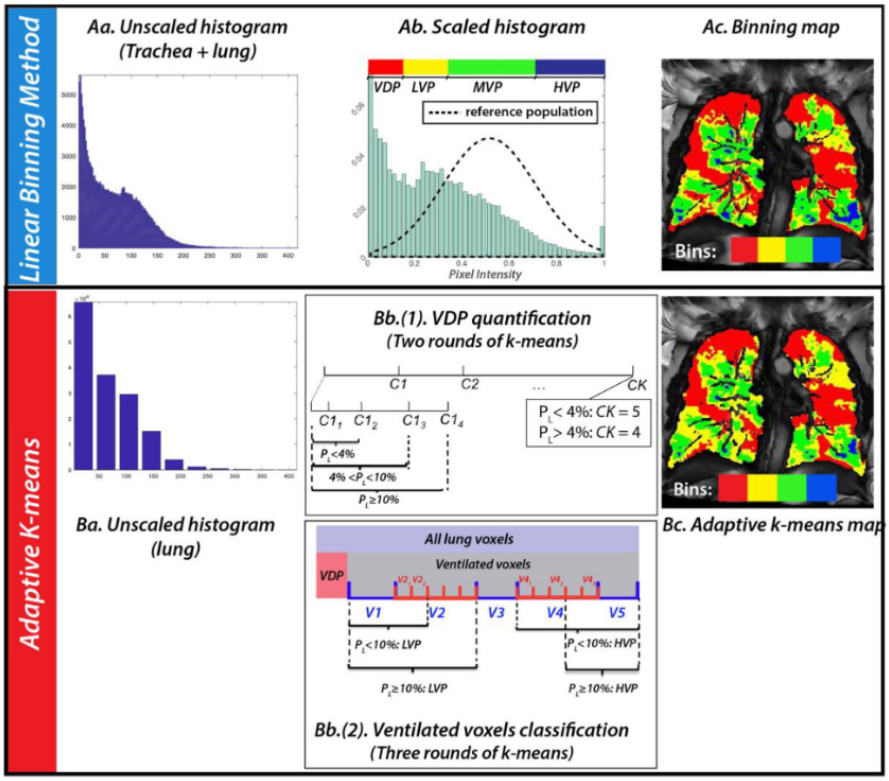

Figure 2.12: The pipeline of two hyperpolarized ^{129}Xe MRI ventilation binning (with red areas corresponding to defect mapping) presented extracted from the work of He *et al.*[156]: the linear binning, and adaptive K-means algorithm. In the linear binning approach, the intensities are scaled to a range of 0-1 based on the top percentile within the thoracic cavity mask, and pixels are assigned to intensity clusters using thresholds derived from a healthy reference population's standard deviation. The adaptive K-means algorithm involves reducing the histogram to 10 clusters and determining whether the lowest intensity cluster contains less than 4 %, between 4-10 %, or at least 10 % of all lung voxels. Defect clusters are identified based on this percentage after two rounds of K-means, and subsequently, low, medium, and high-ventilation clusters are classified from the remaining ventilated voxels based on intensity after two more rounds of K-means, leading to the generation of an adaptive K-means map.

B. Characterization of impairments in asthma and COPD

In the selected corpus of this review, six papers evaluate the ventilatory function in asthmatic patients, all using hyperpolarized gas MRI. It has been shown that the severity of asthma is well correlated with standard lung function tests for adult and pediatric cohorts and can predict increased health care needs.[175] Segmental ventilation defects of ^{3}Helium MRI are highly associated with CT mucus obstruction scoring of the corresponding segmental bronchi.[176] Ventilation defects maps are reproducible for global and slice-by-slice ventilation defects in asthmatic patients,[177] and modeling of asthmatic lung structure and function was achieved, predicting the pathological flow and airway mechanics.[178] Especially the peripheral lung has a greater response to bronchodilator than the proximal lung.[131] These spatial evaluations of bronchodilator effects can nonetheless be nuanced as aerosol depositions may vary between asthmatic patients and depend on inhalation at fast or slow rates.[154]

Six papers evaluate the lung ventilatory function of chronically obstructed patients using various methodologies: hyperpolarized gas MRI, oxygen-enhanced MRI, or proton MRI. It has been found that hyperpolarized gas MRI and oxygen-enhanced MRI correlate with CT findings and are sensitive to the alterations in emphysematous patients.[129,179,180] PREFUL reliability for COPD patients has been demonstrated with repeatability assessment.[144] Still, the combination of modalities helps to discriminate between affected functions (ventilation, perfusion, gas exchange), which can vary greatly between patients. However, PREFUL demon-

[175] Nancy Y. Lin et al. *Journal of Allergy and Clinical Immunology*, 2021.
[176] David G. Mummy et al. *Radiology*, 2022.
[177] Sarah Svenningsen et al. *Academic Radiology*, 2021.
[178] Jessica M. Oakes et al. *IEEE Transactions on Biomedical Engineering*, 2019.
[131] Helen Marshall et al. *Journal of Allergy and Clinical Immunology*, 2021.
[154] Kamran Poorbahrami et al. *Journal of Applied Physiology*, 2019.
[129] Naz P. Taskiran et al. *Tomography (Ann Arbor, Mich.)*, 2022.
[179] Kun Qing et al. *Academic radiology*, 2019.
[180] Yoshinori Fuseya et al. *PLoS ONE*,. 2018.
[144] Gesa H. Pöhler et al. *Journal of magnetic resonance imaging: JMRI*,. 2021.

strates its inner sensitivity to indacaterol/glycopyrronium COPD treatment, demonstrating its efficiency, which was validated against standard spirometry.[145,181]

The main biomarkers extracted and used in ventilation assessment in MR imaging techniques are summarized in Figure 2.13. Clinical trials on asthmatic and COPD patients mainly use gas volume distribution in the lung to assess the state of ventilatory function, leading to VDP (or its equivalent %VV) statistics.[177,178] For asthma, some include the measurement of the dynamic of the ventilation with flow-volume loops, as standard spirometry demonstrates the inner sensitivity of flows for obstructive diseases.[111] In the case of COPD, some biomarkers aim to characterize emphysema as perfusion (and V/Q matching) or oxygen uptake. The spatial distribution can improve the sensitivity of the technique for early disease with spatialized defects, and many works include lobular, segmental, or proximal-distal segmentations to characterize obstructions.[131,178]

The collected studies do not evaluate the diagnostic performance of the lung function imaging techniques they use in terms of sensitivity and specificity. This is explained by the fact that the current gold standard used in the clinic relies on global measurements and that it is less efficient than these techniques. Furthermore, comparisons should be cautious as examination protocols differ: local to global measurement, lying or standing position, free or forced breathing, static or dynamic, and physical origin of the signal. 3D MR spirometry is compared to other functional lung imaging approaches in the next chapter, despite these limitations.

[145] Andreas Voskrebenzev et al. *Radiology. Cardiothoracic Imaging*, 2022.
[181] Dave Singh et al. *Respiratory Research*, 2022.
[177] Sarah Svenningsen et al. *Academic Radiology*, 2021.
[178] Jessica M. Oakes et al. *IEEE Transactions on Biomedical Engineering*, 2019.
[111] Filip Klimeš et al. *Magnetic Resonance in Medicine*, 2021.
[131] Helen Marshall et al. *Journal of Allergy and Clinical Immunology*, 2021.
[178] Jessica M. Oakes et al. *IEEE Transactions on Biomedical Engineering*, 2019.

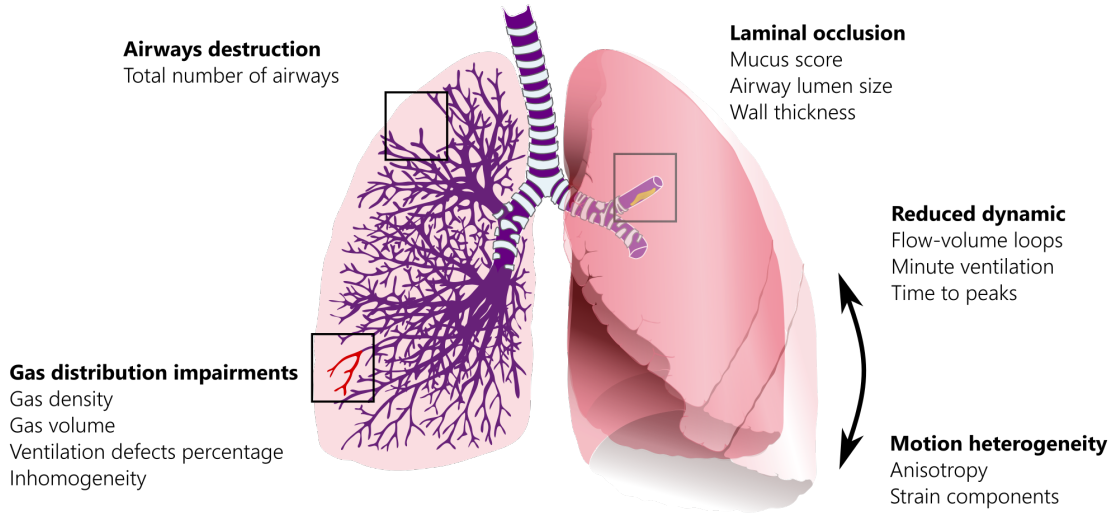

Figure 2.13: Biomarkers assessing the ventilatory function in obstructive conditions using magnetic resonance imaging techniques. They provide complementary physiological information from gas distribution, dynamic, structure, or motion descriptors. They are able to evaluate airway destruction, laminal occlusion, local gas distribution impairments, and reduced dynamic motion heterogeneity. Local structural biomarkers are computed only from hyperpolarized gas MRI, while dynamic and motion descriptors are provided by hydrogen MRI dynamic lung imaging. Ventilatory biomarkers can be combined, when available, with gas exchange and perfusion analysis to improve the sensitivity of pulmonary impairments.

3

Methodological developments in 3D MR spirometry for clinical investigations

The aim of this PhD is to further develop the work started by Boucneau *et al.* [105] and to move it from a feasibility study to clinical research. The proof of concept includes a number of innovative strategies for local function estimation and, more specifically, local flow and volume measurements. The approach implies a double paradigm shift from standard to 3D MR spirometry. It is performed in free breathing and lying position, while standard spirometry is performed standing or sitting along forced inspiratory and expiratory cycles. Moreover, information is no longer scalar, measured at the mouth, but three-dimensional, measured everywhere throughout the lung at the voxel level. The multidimensionality of 3D MR spirometry provides important information about lung mechanics, but the technique needs to be properly challenged before aiming at investigational trials in patients. This chapter introduces the original framework, its limitations, the methodological developments undertaken during this doctoral work, and the evaluation of the reliability of the parametric maps obtained in healthy volunteers breathing freely in supine and prone positions.

3.1 Questioning the proof of concept

The 3D MR spirometry proof of concept, published in 2020, presents the key principles of the new modality framework. However, the reproducibility and robustness of its outcomes have not been assessed yet. The technique is challenged in this chapter to highlight its limitations and raise questions about its outcomes. This section presents the difficulties, limitations, and questions when reproducing 3D MR spirometry.

3.1.1 Original framework

This subsection presents the original framework from obtaining a dynamic image of a respiratory cycle to extracting 3D MR spirometric parameters from

[105] Tanguy Boucneau et al. *Scientific Reports*, 2020.

the dynamic. The original framework is detailed in Tanguy Boucneau's PhD dissertation.[182] The main steps, summarized in Figure 3.1 are detailed in the following part to allow a better understanding of the methodological developments already done and yet to be done.

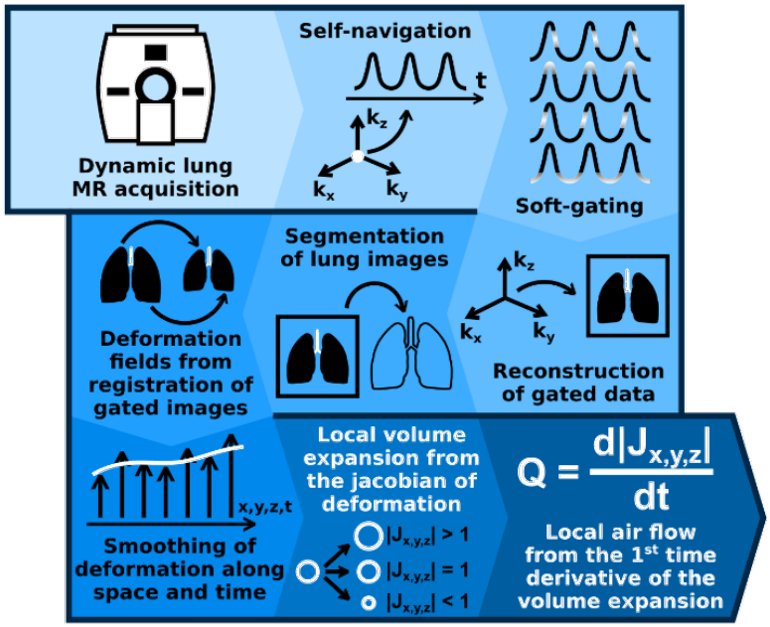

Figure 3.1: Original framework to obtain local flow-volume loops using 3D magnetic resonance spirometry:[182] 3D lung MRI dynamic acquisition, retrospective gating, lung segmentation, computation of deformation fields and smoothing, calculation of local flow-volume loops.

A. Imaging lung dynamics in free-breathing

MR acquisition

In the 3D MR spirometry original framework, a ten-minute dynamic lung MRI is performed at 3 T (on a GE Signa PET/MR scanner) in free breathing using a UTE sequence to tackle fast signal decay in lung tissues and is combined with an adaptative Koosh ball adaptative zero TE k-space trajectory AZTEK.[183] AZTEK is suited for imaging moving objects as it allows a uniformly fast covering of the k-space com-

[182] Tanguy Boucneau. *Magnetic resonance imaging of respiratory mechanics*. PhD thesis. Université Paris Saclay (COmUE), July 2019.
[183] Tanguy Boucneau et al. *Magnetic Resonance in Medicine*, 2021.

bined with parameters to tune the sampling scheme. The UTE pulse sequence diagram and the AZTEK trajectory with its parameters are illustrated in Figures 3.2.

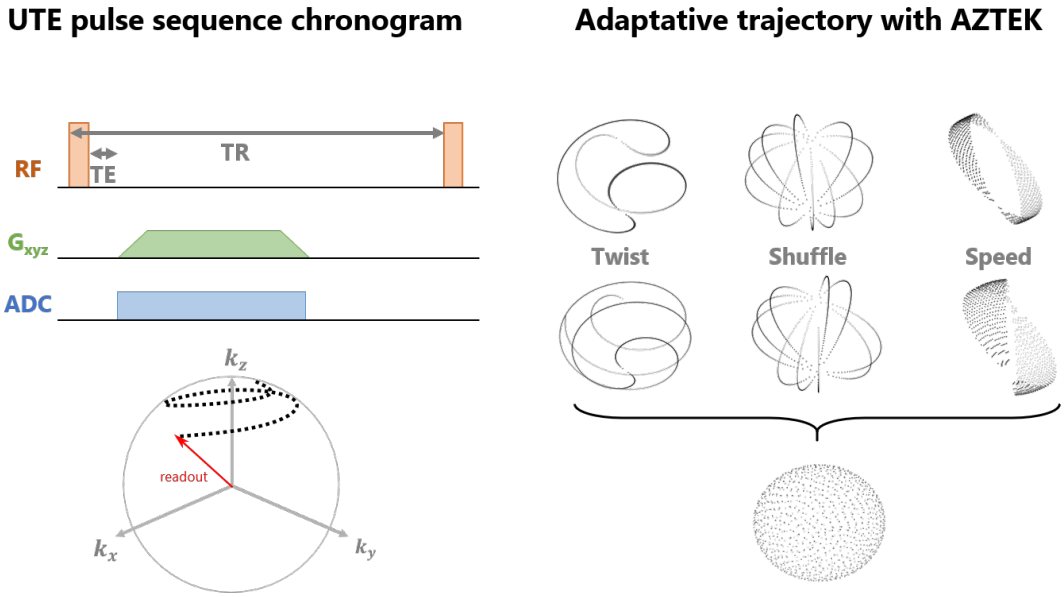

Figure 3.2: Acquisition strategy for 3D MR spirometry. Chronogram of the 3D UTE sequence (left) with radial sampling starting from the k-space center at the readout. The parameters are provided in Table 3.1. The successive spokes follow an adaptive trajectory (AZTEK) to secure a uniform coverage of the k-space during respiration (right). Combining the three parameters "speed", "twist", and "shuffle", defined in Boucneau *et al.*,[183] can optimize the covering of the first 1000 spokes out of the 40,000 that are usually used for a full lung volume reconstruction. Only the last point of each radial spoke is plotted for the visualization.

The main acquisition parameters are summarized in Table 3.1. The RF excitation is performed with a square RF pulse without any slice or slab selection gradient. However, phase cycling, according to a quadratic law, spoils the remaining transverse magnetization (commonly called "RF spoiling"). Starting at the k-space center, 192 points are sampled along the spoke during the readout, with a ramp-up sampling for the first 42 points and constant sampling for the following. To minimize the acquisition time and maximize MR signal intensity, a minimal echo time of 12 µs is reached with a short TR of 2 ms. The bandwidth is ± 100 kHz, high enough to limit transverse relaxation effects during readout and to allow short acquisition time (1 ms) with respect to T_2^*. The targetted isotropic spatial resolution of 1.5 mm is a good compromise between the signal-to-noise ratio (SNR)

TR	2 ms
TE	12 µs
Flip angle	3 °
Bandwidth	± 100 kHz
Extended Dynamic Range	yes
AZTEK speed	31
AZTEK twist	4
AZTEK shuffle	2

Table 3.1: MRI main acquisition parameters used for 3D MR spirometry

and the spatial resolution required for anatomical landmarks. No gradient spoiling was needed as the AZTEK trajectory samples spokes close in the k-space: the readout gradient for one spoke spoils the transverse magnetization from previous spokes. The flip angle, 3 °, was optimized to achieve the Ernst steady conditions law.[40] Spine and thoracic coils sum up to a 30-channel coil array for receiving the MR signal from the thoracic region.

Image reconstruction of the dynamic

As mentioned in the previous Chapter see C., a self-navigator can be extracted from the center of the k-space, where the contrast variations induced by the patient's breathing are the highest (see 2.2.4). This surrogate respiratory motion signal is then used to gate the data into 32 respiratory phases. The gating is performed onto the signal amplitude and phase after splitting inspiration and expiration phases into 16 bins each. This allows an integrated respiratory cycle to be represented over the ten minutes of acquisition. The acquired and gated spokes are shared across the respiratory phases using a view-sharing strategy [184] to improve the dynamic SNR while limiting respiratory motion blurring. Each spoke data is weighted according to its distance (phase and amplitude) to the gate center to reduce motion artifacts and help the reconstruction achieve faster convergence. Berkeley Advanced Reconstruction Toolbox (BART) is used to reconstruct the 3D MR spirometry non-cartesian data using advanced strategies:

[40] Robert W. Brown et al. *Magnetic Resonance Imaging: Physical Principles and Sequence Design*. 2e édition. Wiley-Blackwell, May 2014.

[184] Jeffrey Tsao and Sebastian Kozerke. *Journal of Magnetic Resonance Imaging*, 2012.

parallel imaging and compressed sensing. This open-source software offers a wide array of tools for MRI reconstruction, including numerous advanced reconstruction algorithms.[185] Figure 3.3 depicts images of the final reconstructed dynamic for 3 respiratory phases over the 32 effectively reconstructed over the cycle.

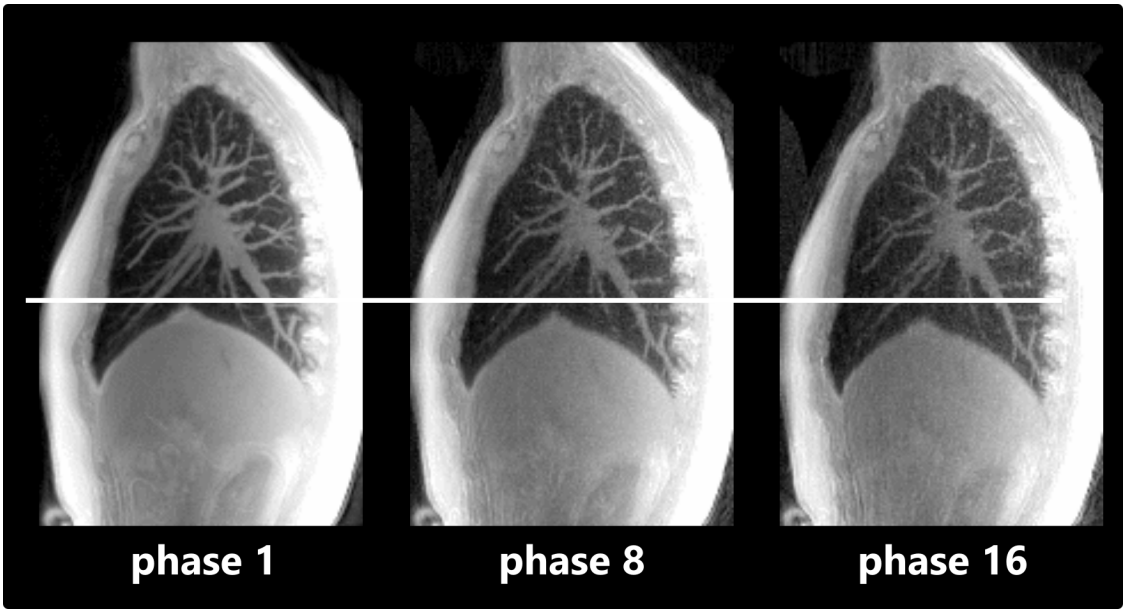

Figure 3.3: Lung dynamics in 3D MR spirometry (sagittal views with a maximal intensity projection over 3 cm) in a healthy volunteer freely breathing in a lying supine position (male, 27 years old) at different respiratory phases. The final dynamic is reconstructed retrospectively upon 32 respiration phases (16 at inspiration and 16 at expiration) using compressed sensing and parallel imaging priors. In free breathing, the respiratory dynamics are relatively weak, with a few centimeters displacement, mainly along the superior-inferior direction, as underlined by the white horizontal line.

B. Computation of flow-volume loops and biomechanical parameters

The images of a respiratory cycle carry motion and mechanical information, specifically the deformations of respiration. The strain tensor is inferred by elastic registration on images of each respiratory phase (moving images) into the end-expiratory phase (fixed image) using the Elastix toolbox.[186] The moving images are iteratively transformed to align spatially with the fixed image until a cost function

[185] Martin Uecker. "Berkeley Advanced Reconstruction Toolbox". In. Toronto, 2015.
[186] S. Klein et al. *IEEE Transactions on Medical Imaging*, 2010.

is minimized for an optimal transformation on a grid. Several resolutions can be used to obtain a more efficient and accurate alignment: initially focusing on larger-scale features and progressively refining the alignment at finer scales helps to handle large deformations between images while avoiding convergence to local minima. The reference image is taken at the end of expiration when the motion is minimal, and the achieved image quality is maximal: most of the available details of the vascular system, bronchial tree, and lung contour are obtained, which is essential to guide the registration. The main registration parameters are listed in Table 3.2. A pre-processing step is applied to mask regions that could interfere with the lung respiratory motion. Indeed, a sliding motion occurs at the interface between the parenchymal tissues and the rib cage. This can induce underestimation or overestimation of the lung tissue deformations if inferred using a continuous assumption and thus transform during the registration process. For that purpose, thoracic cage landmarks are saturated to avoid estimating sliding motion at the interface.

Fixed Image	End-of-expiration
Transform	B-Spline tansform
Metric	Normalized mutual information
Number of resolution	4
Final grid spacing	16 voxels (24 mm) isotropic
Number of spatial samples	10,000

Table 3.2: Main parameters used for an elastic registration using Elastix.[186]

As the resulting deformation is estimated independently on each respiratory phase, the temporal dimension can be very noisy, especially in regions with small deformations.[182] As respiratory physiology expects a smooth deformation over the respiratory cycle, the deformation field is temporally smoothed using an algorithm based on the discrete cosine transform developed at CREATIS.[187] The periodicity of breathing is ensured by smoothing on a looped deformation.

Volumetric maps are then derived from the Jacobian determinant, also called the Jacobian. The Jacobian matrix determines the deformation gradient tensor $\vec{F}$.

[187] Damien Garcia. *Computational Statistics & Data Analysis*, 2010.

Its determinant ultimately quantifies volume changes. Using $\vec{u}$ the displacement field extracted from the registration, the Jacobian can be computed with:

$$\vec{F} = \begin{pmatrix} 1 + \partial u_x/\partial x & \partial u_x/\partial y & \partial u_x/\partial z \\ \partial u_y/\partial x & 1 + \partial u_y/\partial y & \partial u_y/\partial z \\ \partial u_z/\partial x & \partial u_z/\partial y & 1 + \partial u_z/\partial z \end{pmatrix} \tag{3.1}$$

$$J = \det(\vec{F}) \tag{3.2}$$

Finally, absolute local volumes, δV, are retrieved for each temporal phase (see Figure 3.4, top) of the breathing from (3.2) and the element of volume, the voxel size, δV_0 from the fixed image used as reference during the registration:

$$\delta V = J \times \delta V_0 \tag{3.3}$$

Local flow rates, δQ, are derived by temporal derivation of local volumes (see Figure 3.4, bottom):

$$\delta Q = \delta \dot{V} \tag{3.4}$$

Times stamps are inferred for each respiratory phase as a weighted sum of gated data own time stamps in their corresponding respiratory cycle, establishing the first respiratory phase at $t = 0$ (Figure 3.4, bottom row).

Finally, 3D MR spirometry computes a flow-volume loop in each voxel of the lung, with a full characterization of the local ventilation, as presented in Figure 3.5.

Moreover, by computing the Green-Lagrange strain tensor, the biomechanical behavior of respiratory-induced deformations can be further assessed:

$$\epsilon^G = \frac{1}{2}({}^T\vec{F}\vec{F} - Id) \tag{3.5}$$

Particularly, the anisotropic deformation index (ADI) and slab-to-rod index (SRI) can be computed from the eigenbasis ϵ_i^G, $i \in [1, 2, 3]$ of the Green-Lagrange tensor. SRI assesses the ratio between the dimensions of slab-like structures and

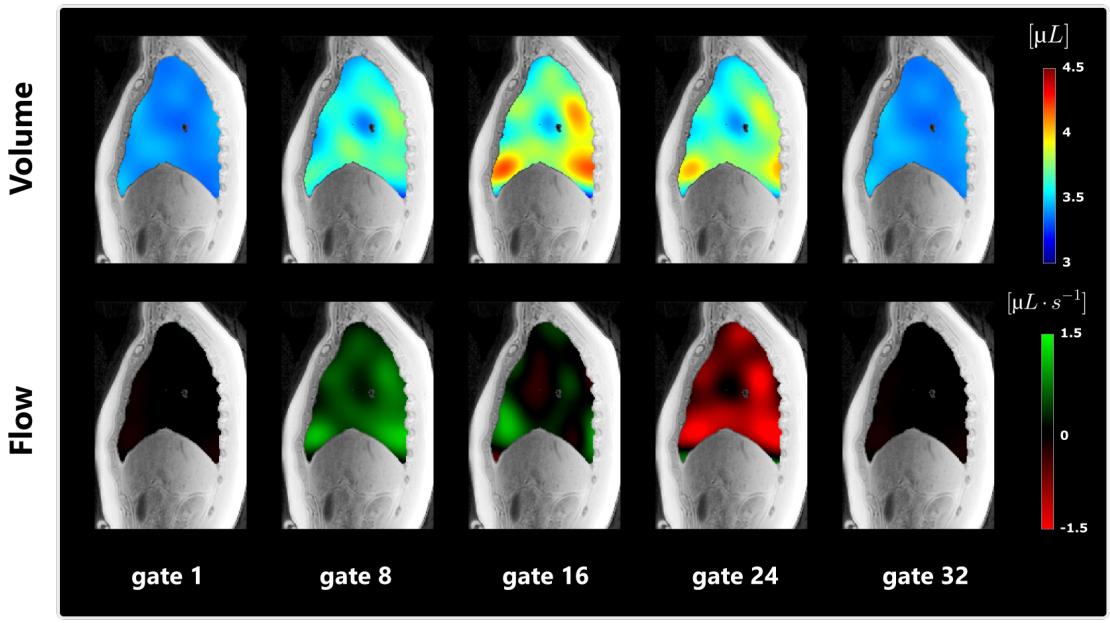

Figure 3.4: Gas volume maps (top row) and gas flow maps (bottom row) in a healthy volunteer for 5 different respiratory phases distributed along the 32 reconstructed gates (sagittal view of the right lung). As inspiration and expiration have been equally sampled, the first 16 gates correspond to the inhalation, while the remaining 16 gates correspond to the exhalation.

rod-like structures. ADI quantifies the extent of directional variation in deformation. The two biomarkers are represented in Figure 3.6. With $\lambda_i = \sqrt{1 + 2\epsilon_i^G}$ and $i \in [1, 2, 3]$:

$$\mathrm{ADI} = \sqrt{\left(\frac{\lambda_1 - \lambda_2}{\lambda_2}\right)^2 + \left(\frac{\lambda_2 - \lambda_3}{\lambda_3}\right)^2} \tag{3.6}$$

$$\mathrm{SRI} = \frac{\pi}{2} \tan^{-1}\left(\frac{\lambda_3(\lambda_1 - \lambda_2)}{\lambda_2(\lambda_2 - \lambda_3)}\right) \tag{3.7}$$

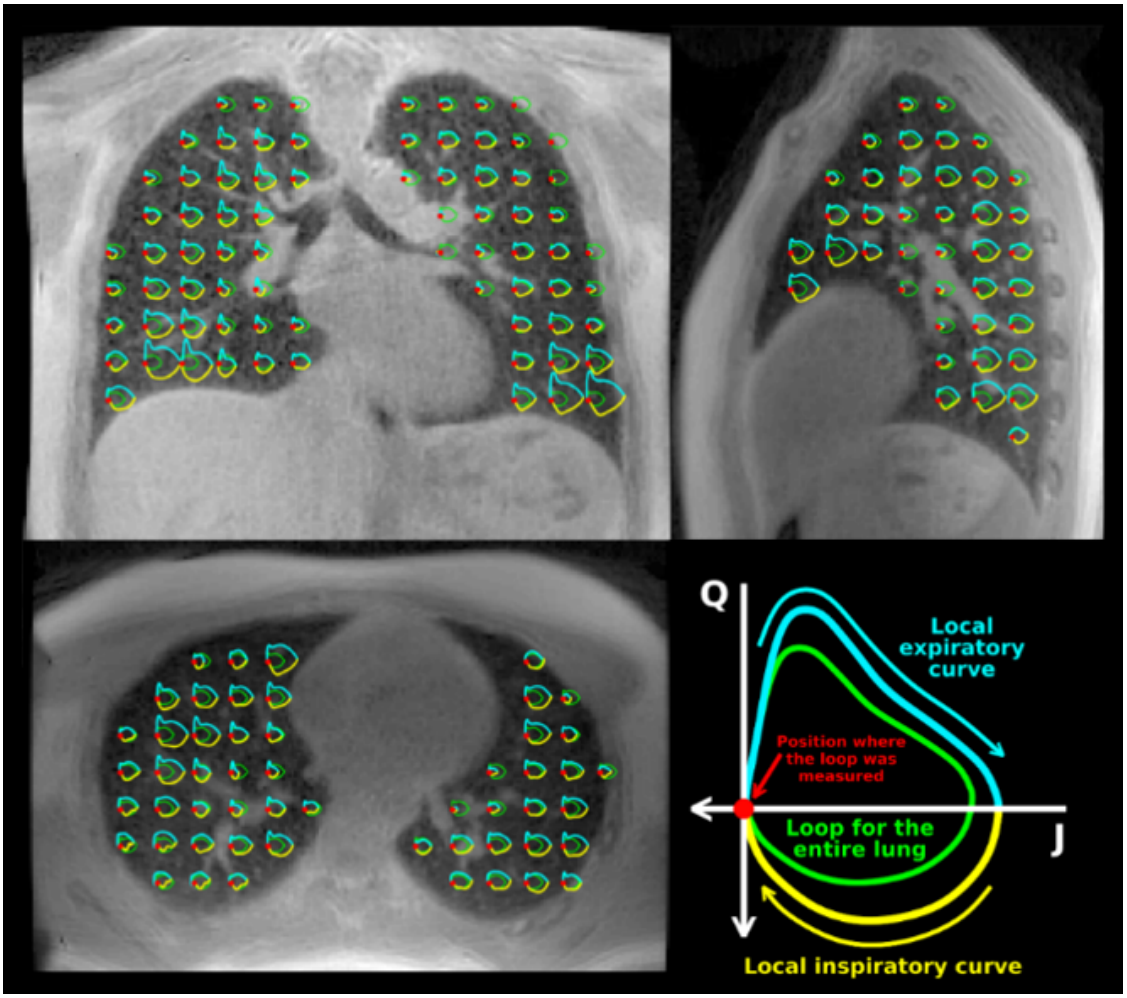

Figure 3.5: Axial, sagittal, and coronal views of local flow-volume loops for a healthy volunteer, extracted from Boucneau *et al.*[105] Only one loop over 20 loops is superimposed. The mean flow-volume loop over the lung volume is depicted in green for reference. The color and axis conventions for both local and global loops are presented in the bottom right corner.

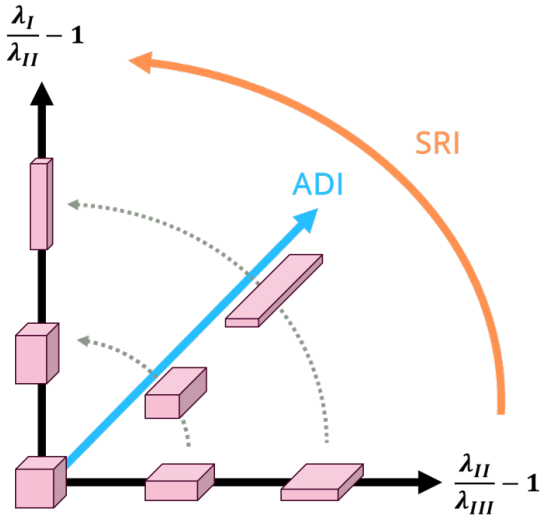

Figure 3.6: Mechanical biomarkers to assess anisotropy and shape of the deformation are illustrated: the slab-to-rod index (SRI) assesses the ratio between the dimensions of slab-like structures and rod-like structures, and anisotropic deformation index (ADI) quantifies the extent of directional variation in deformation. Through their directional information, they provide insights into local constraints.

3.1.2 Reproducing 3D MR spirometry

Since the original pipeline was implemented and optimized to process data from a single volunteer with 3 types of breathing (spontaneous, diaphragmatic, and thoracic), the robustness of the approach was challenged by its application and repetition to new datasets acquired in different volunteers with various morphologies. A dataset of 25 healthy volunteers (described in Chapter 4) is used in this chapter to develop the methodology. In this section, the difficulties encountered in performing 3D MR spirometry are discussed, especially image artifacts, post-processing instabilities, and computational complexity.

A. Artefacted images

Dynamic lung images were acquired using the original sequence as Boucneau *et al.* and reconstructed using the same algorithms. Artifacts that had not previously been encountered were observed in the resulting lung volumes. The two main causes were identified as:

- Temporal delays on the effective k-space trajectory due to a delayed effective start of the gradients.
- Poor digitization of the MR signal, particularly caused by an RF overflow in the receive chain.

These issues followed a PET-MR scanner software update, which led to artifacted data from the original sequence, which was optimized in the previous software configuration.

Gradient delays

Using a temporally shifted trajectory for the image reconstruction, which differs thus slightly from the true trajectory associated with acquired raw data, leads to what is commonly known as "gradient delay artifacts",[188] highlighted by the

[188] Ethan K. Brodsky et al. *Magnetic Resonance in Medicine*, 2009.

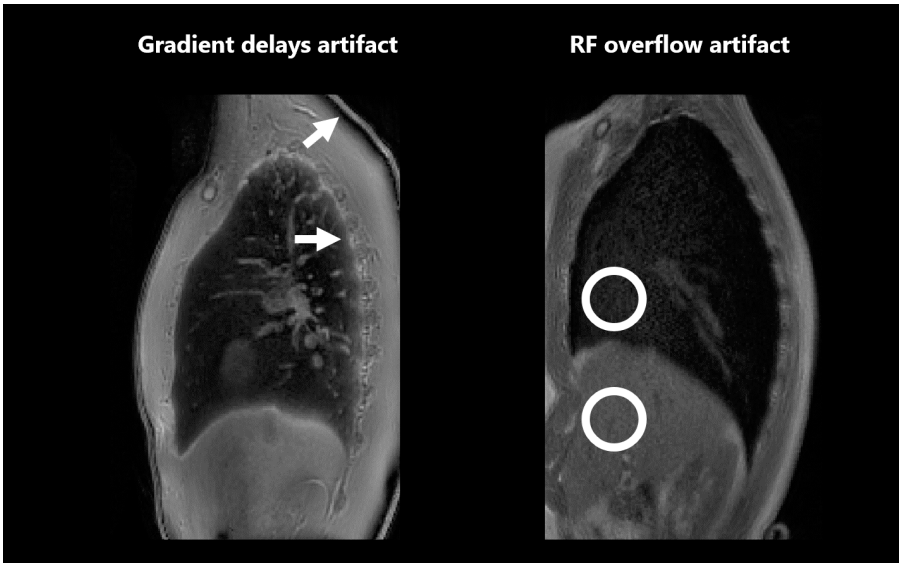

Figure 3.7: Illustration of gradient delays (left) and RF overflow artifacts (right). Arrows are employed to delineate regions affected by gradient delays because the effective trajectory deviates slightly from the theoretical trajectory. Consequently, contrasts at tissue interfaces undergo spatial shifts, with artifacts more pronounced towards the periphery of the field of view, resulting in black or white bands. Additionally, circular markers denote artifacts stemming from RF overflow, thereby modulating the overall image contrast. This results in accentuated signals in low-intensity areas and diminished signals in regions of high intensity.

arrows on the left image in Figure 3.7. In radial imaging, these artifacts are more pronounced in the most remote regions of the field of view, where the gradient amplitudes are the highest and, therefore, where the misestimation of the trajectory position is the greatest. An artifact can be noticed, similar to chemical shift artifacts: a combination of a slight effective frequency shift compared to theory and a spatial shift in intensity information. A black band appears under the skin (which should not), and a hypersignal band appears at the air-tissue interface on the lung tissue side with the back of the rib cage (see Figure 3.7, left).

RF overflow

Calibration is a critical and complex step in properly tuning the MRI settings for the acquisition. A prescan step is usually used to set receive gains automatically. However, the prescan of the 3D UTE sequence stopped working after the software update. Despite the intervention of a GE expert in sequence programming, we

could not find how to debug the sequence code. The problem is that if the reception gains are not correctly calibrated for digitization, the signal is not well encoded, leading to a noisy (signal underflow) or artifacted (signal overflow) reconstructed image (as shown in Figure 3.7, right). In our experimental setup based on 3D radial acquisition, the measured total magnetic moment comes from the entire sample, which is the entire magnetized body. So, the received signal was often too high for the reception chain, particularly for the analog-to-digital converter (ADC). The latter encodes a false value for input signal intensities higher than the ADC upper bound, and the reconstructed signal led to artifacts commonly called "clipping artifact" or "RF overflow".[189] The contrast is thus artifacted globally, with reduced signal in hypersignal tissues combined with increased signal in hyposignal tissues (see Figure 3.7, right).

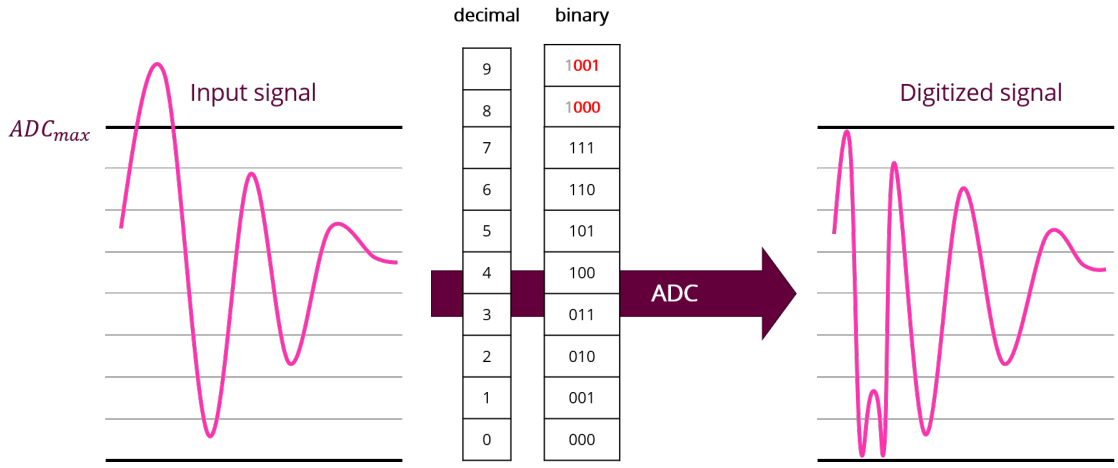

Figure 3.8: Digitization of overflow signal in the analog-to-digital converter (ADC). The analog signal exceeds the ADC limit value (left), inducing false digitization of binary values and, thus, digital signal reconstruction (right).

Manual calibration can be carried out to set the acquisition gains adequately, but it is not straightforward, with a delicate compromise between maximizing the gains and maximizing the dynamics while avoiding overflow. Certain data, despite manual calibration, were thus in overflow. With radial center-out acquisitions, overflows occur for the first points, corresponding to the center of the k-space,

[189] John Jackson et al. *Magnetic Resonance in Medicine*, 1989.

affecting the contrast. A loss of signal in the tissues and an increased signal in the air can be observed, as in Figure 3.7 (right).

B. Unrobust processing

Three-dimensional MR spirometry data from the seminal article was reproduced successfully. However, some of the lack of robustness of the post-processing framework was highlighted in the newly acquired data. When applying the same processing as the original experiment on new data sets, we could mainly notice strong motion blurring, bad segmentation of lung structures, and abnormal flows. The section 3.2 addresses these defects by implementing robust improvements.

Dynamic image reconstruction

Some reconstructions displayed motion blurring, particularly noticeable at high respiratory dynamics, such as the end of inspiration. The diaphragm appears blurred (as seen in Figure 3.9 for gate 17) as the rephasing of k-space data throughout the respiratory cycle was not optimal. The parameterization of the gating code was thus not robust over newly acquired data, leading to poor dynamic reconstruction.

Segmentation of the lung volume

The proposed automatic segmentation was highly dependent on the tuning of several parameters (including image filtering, thresholds, number of iterations, etc.), which defeats the purpose of automatic segmentation. The empirical search for an optimal set of parameters is often too complex, with poor segmentation results as presented in Figure 3.10.

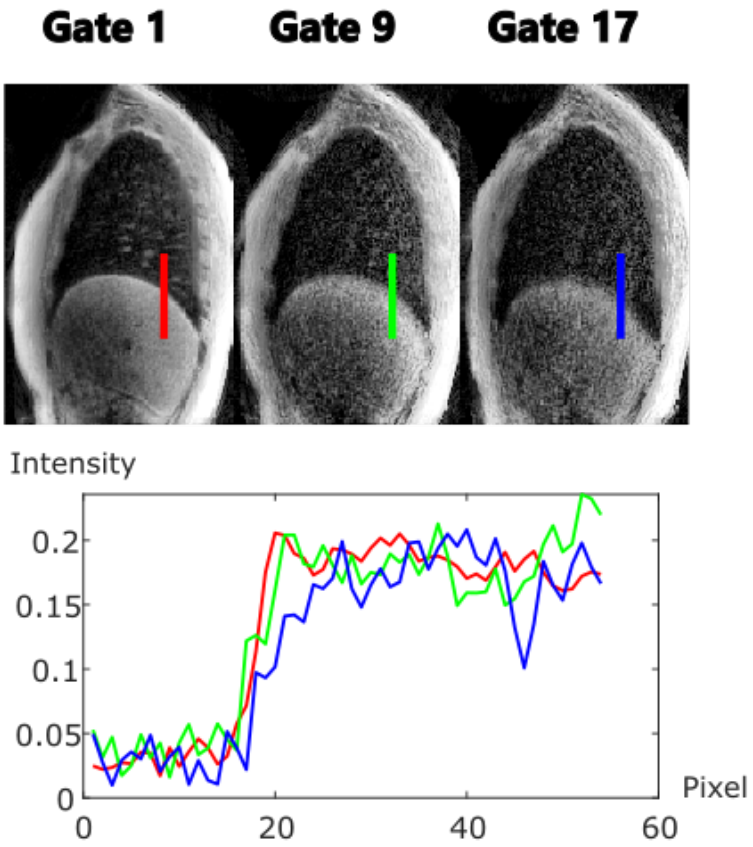

Figure 3.9: Sagittal views of different respiratory gates (top) correspond to the end of expiration (gate 1), mid-inspiration (gate 9), and end of inspiration (gate 17). Motion blurring can be noticed at the diaphragm, mainly for the end of inspiration, where the respiratory dynamic is at its highest. The signal intensities are plotted along a line (bottom) for each respiratory state. The blue line, corresponding to the end-of-inspiration, depicts a smooth signal increased over 10 pixels (= 1.5 cm) from the lung parenchyma to the diaphragm tissues induced by motion blurring.

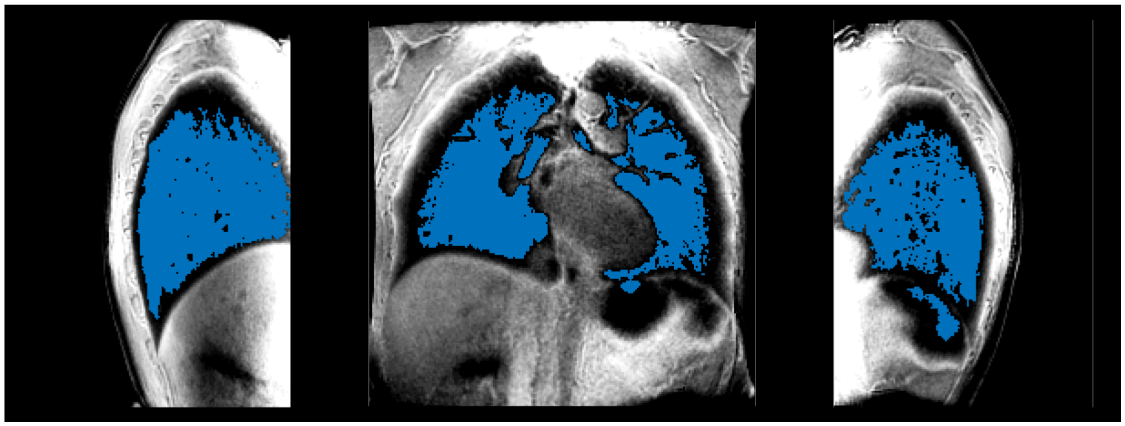

Figure 3.10: Sagittal and coronal views for an image at the end of expiration. The segmentation was optimized but the resulting lung mask is bad. Large lung regions remain unsegmented, while the stomach is partially caught in the mask.

Flow computation

After local spirometric loop computation, some estimated flows presented a strong peak at some respiratory phase. Figure 3.11 illustrates the artifact with the corresponding temporal differential used to compute flows from the temporal derivation of volumes.

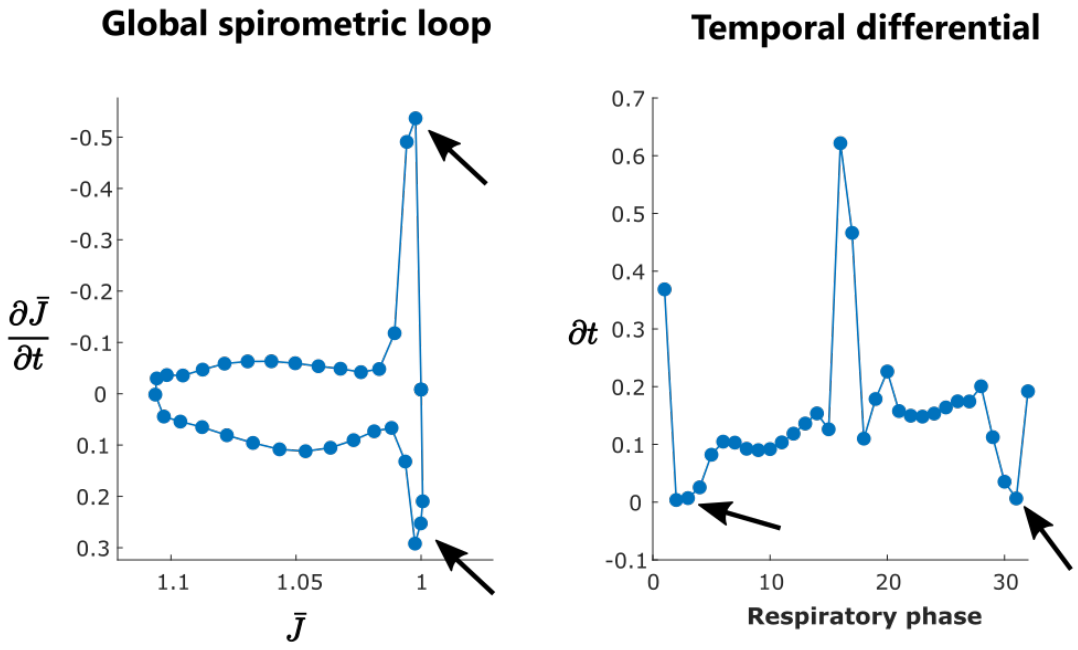

Figure 3.11: On the left, the global spirometric loop (average over the lung volume of local spirometric loops) is plotted, with artefacted flows at the beginning of the inspiration and at the end of expiration (arrows). On the right, the corresponding differential time between respiratory phases used to derive flows from volumes, with differential very close to zero (arrows). When differential times are very small, it is associated with very high flows.

This peak at the end of inspiration is also observable in the original article, as can be seen in Figure 3.5. In forced spirometry, such extrema are expected, but in spontaneous spirometry, it is known that flow rates exhibit smoother temporal variations. As we do not have an equi-temporal sampling of the respiration, this effect can be understood from the calculation of flows:

$$Q_n = \frac{1}{t_{n+1} - t_{n-1}} \left(\frac{t_{n+1} - t_n}{t_n - t_{n-1}} (J_n - J_{n-1}) + \frac{t_n - t_{n-1}}{t_{n+1} - t_n} (J_{n+1} - J_n) \right) \tag{3.8}$$

with J_n the Jacobian as defined in (3.2) , t_n the corresponding time in the respiratory cycle, and n each respiratory phase.

Over the quick evolution around the end of inspiration, temporal steps are smaller, just like Jacobian variations. Very small temporal variations can be reached compared to consecutive ones. Noting $t_{n+1} - t_n = \varepsilon$ with $\varepsilon \ll 1$ s, it can be shown that:

$$Q_n \approx \frac{J_{n+1} - J_n}{\varepsilon} \tag{3.9}$$

The measured flow is here dominated by the measurement noise in $J_{n+1} - J_n$, and the temporal differentiation amplifies the artifact. This calculation step determining the flow rates is particularly critical since 3D MR spirometry relies on temporal derivation.

C. Computational resources

The 3D MR spirometry reconstruction process is time-consuming, requiring intensive use of human and computational resources. As explained in the previous part, the tuning of parameters and test-retest experiments were very time-consuming. Moreover, the reconstruction framework involved heavy datasets (15 Gb of raw data for a common acquisition) and complex computation tasks. It requires approximately 64 Gb of RAM and 6 hours of computing for 32 dynamics of an average lung MR acquisition. The computer uses an Intel(R) Xeon(R) Gold 5218R processor model at 2.10 GHz (max turbo frequency at 4 GHz, 80 processing units) combined with 128 Gb of RAM. Computation times are summarized in Table 3.3.

Time for :	**Reconstruction**	**Segmentation**	**Registration**
Per dynamic	5 min	10 mn	3 min
For 32 dynamics	160 min	10 mn	90 min

Table 3.3: Computation times of main processing steps for 3D MR reconstructions, as shown in Figure 3.1.

3.2 Developing the 3D MR spirometry modality

The first part of this doctoral work was to overcome the challenges introduced in the previous paragraphs by developing an efficient, repeatable, reproducible, and stable processing pipeline for 3D MR spirometry. This section presents the methodological developments performed regarding image quality, reconstruction, and production of the associated code. The following developments were performed and challenged over a dataset of 25 healthy volunteers presented in Chapter 4, in Table 4.1.

3.2.1 Artifact mitigation

Once identified, artifact mitigation during the processing associated with an optimized prospective acquisition methodology was to be investigated. This part presents the implementations designed to avoid or correct the main artifacts. MRI acquisitions were carried out with the parameters given in Table 3.1, except for the TE, which could be minimized at 14 µs after an MRI system software upgrade.

A. Gradient delays

Gradient delays must be optimized directly on the MRI system when installing the sequence. Several acquisitions with several gradient delays in the sequence can help identify the best parameters. Only a few microseconds of delay in the command chain can induce the associated artifacts. By evaluating the SNR from Gudbjartsson *et al.* definition,[190] and visually assessing the hyposignal/hypersignal bands at the edges, it is possible to define the best set of delays along the three gradients of the system (Figure 3.12). Delays were found isotropic on our system, and the following delay corrections are applied to each axis independently.

[190] Hákon Gudbjartsson and Samuel Patz. *Magnetic resonance in medicine*, 1995.

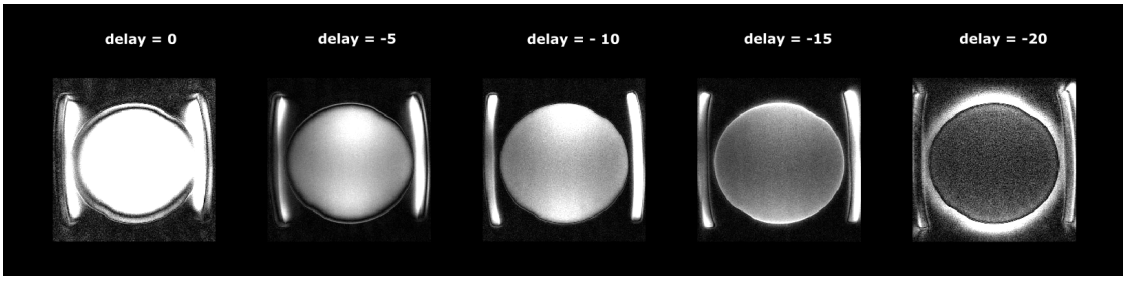

Figure 3.12: Calibration of gradient delays in the MRI system. From left to right, signal-to-noise ratios are respectively: 3.9, 6.1, 12, 3.9, 0.7. The calibration with delay = - 10 is optimal. If the delay correction is too low, hyposignal bands appear at interfaces. If delay correction is too high, hypersignals appear outside the sample.

Intrinsic gradient delays of the system are not supposed to vary significantly over time. However, when updating the system software, important variations can appear from hardware calibrations or new software parameters. Nevertheless, if the data acquisition is delayed with respect to the programmed sampling trajectory, a retrospective correction can be performed with a good overall image quality. This correction relies on the correction of the trajectory used to reconstruct images: the experimental trajectory exported by the system, used to control gradients, does not represent the effective trajectory. Such corrections were required in some of our datasets after a system update. The estimation of the effective trajectory, k_{eff}, in the k-space, is defined with the estimated delay Δt_{err} that needs to be empirically estimated for each MR system. The equation (2.4) is then modified in:

$$k_{\text{eff}}(t) = \frac{\gamma}{2\pi} \int_0^t G(\tau - \Delta t_{\text{err}}) d\tau \tag{3.10}$$

In the 3D-UTE AZTEK sequence, seen Figure 3.2, gradients are being defined by a ramp from $t = 0$ to $t = t_{\text{ramp}}$, then are constant over time, resulting in:

$$G(\tau) = \begin{cases} \frac{G_{\max}}{t_{\text{ramp}}} \cdot \tau & \text{for } \tau \leq t_{\text{ramp}} \\ G_{\max} & \text{for } \tau > t_{\text{ramp}} \end{cases} \tag{3.11}$$

Finally, our effective trajectory corresponds to:

$$k_{\text{eff}}(t) = \begin{cases} \frac{\gamma G_{\max}}{4\pi t_{\text{ramp}}}(t^2 - 2t\Delta t_{\text{err}}) & \text{for } t \leq t_{\text{ramp}} \\ \frac{\gamma G_{\max}}{4\pi t_{\text{ramp}}}(t_{\text{ramp}}^2 - 2t_{\text{ramp}}\Delta t_{\text{err}} + 2t_{\text{ramp}}(t - t_{\text{ramp}})) & \text{for } t > t_{\text{ramp}} \end{cases} \tag{3.12}$$

Four reconstructions were performed with Δt_{err} ranging from - 5 µs to -15 µs on the same dataset. The highest signal-to-noise ratio (SNR), calculated from Gudbjartsson et al. definition,[190] combined with the visualization of hyposignal/hypersignal bands at the edge, reveals the effective delay Δt_{err} (Figure 3.13). The correction $\Delta t_{\text{err}} = -12$ µs gave the best image quality with the highest SNR of 11 and no hypersignal/hyposignal bands at interfaces.

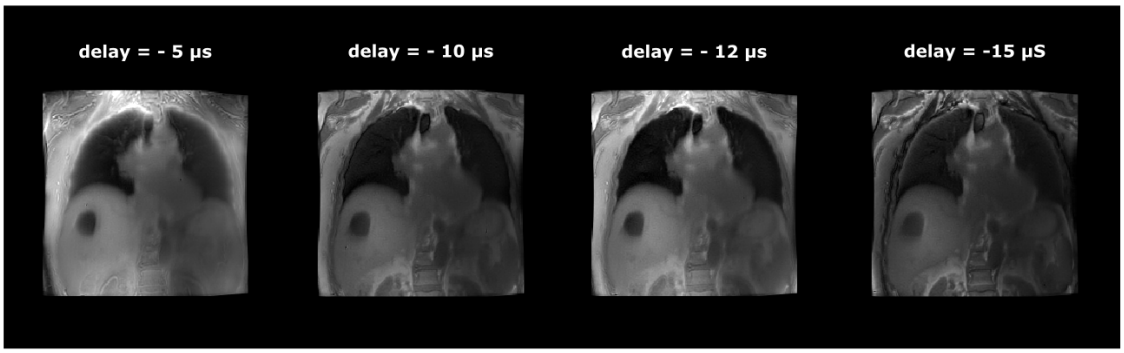

Figure 3.13: Reconstructed lung images using different values of Δt_{err} in the trajectory equation. From left to right, signal-to-noise ratios are respectively: 9.8, 7.2, 11, 2.6. The correction of $\Delta t_{\text{err}} = -12$ µs is thus the best correction, with less abnormal hypersignal in the posterior lung and abnormal hyposignal band at the skin interface.

An interesting asset would be to estimate this delay from raw data automatically. A method from diametrical radial data has been proposed by seeking the maximum signal along spokes.[191] However, this approach could not be applied to our radial data due to another artifact in the receiver chain: ADC filtering.

B. ADC filtering

As the acquisition chain opens for the first time, the center of the Fourier volume is acquired at maximal signal amplitude when the signal decays in T_1 and

[190] Hákon Gudbjartsson and Samuel Patz. *Magnetic resonance in medicine*, 1995.
[191] Sebastian Rosenzweig et al. *Magnetic Resonance in Medicine*, 2019.

T_2^* have not started yet. This is equivalent to a switch from 0 to a few volts in less than a microsecond for the acquisition chain which cannot be digitized perfectly by our system. Indeed, the maximal signal amplitude is reached only after a few points, suggesting signal filtering.

We performed an experiment with Luc Darasse, Sina Marhabaie, Angéline Nemeth, and Xavier Maître to characterize the filtering. For this, a single loop coil emitting at 30 kHz above the Larmor frequency was placed inside the MR scanner to emulate a perfect sample signal. The digitalized signal recovered by the receive chain was then recorded (without any RF pulse or gradients). Figure 3.14 presents (top) the real and imaginary parts of the recorded signal oscillating at 30 kHz (after demodulation at the Larmor frequency) and (bottom) the magnitude of the corresponding signal. On the magnitude signal, oscillations caused by the truncation of frequencies (Gibbs phenomenon) can be noticed. Moreover, the signal is filtered over the first 3 points with a first digitized value close to zero until reaching the mean magnitude of the signal, that is, over the first 15 µs of acquisition (sampling bandwidth at ±100 kHz. This filtering can also be noticed on the first points of the imaginary and real parts (Figure 3.14, top).

Following this experiment, a slight gradient delay was added to sample the center of the k-space for the first 3 points of each spoke. This improves the overall contrast of the image, and the post-processing correction tackles the artifacts presented previously.

C. Clipping

As the calibration of the gains was not always optimal, some data presented clipping artifacts.[189] The first approach is an unwrapping strategy to retrospectively correct clipped digitized k-space data by inferring true values from their temporal neighboring values. However, an important limitation was discriminating between corrupted signals and correct data points.

[189] John Jackson et al. *Magnetic Resonance in Medicine*, 1989.

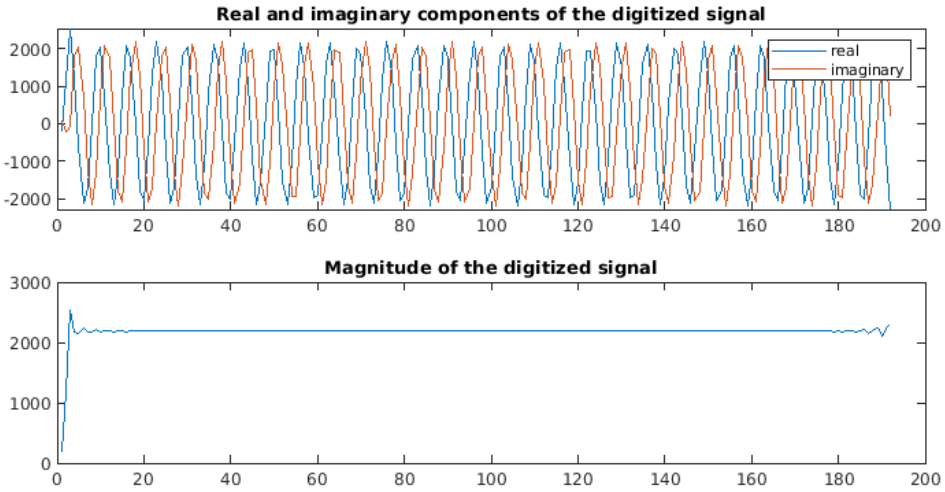

Figure 3.14: Emulated sinusoidal signal at ±100 kHz digitized by the receive chain. Gibbs phenomenon from truncation sampling and low pass filtering effect on the first 3 points (corresponding to the first 15 µs) can be observed, highlighting ADC effects on the first points for ultra-short time echo acquisitions. The last points also present some ringing from Gibbs phenomenon.

A receive thoracic coil with 30 elements was used in our acquisition setup. The signal of each element is digitized along the acquisition. As the analog and digital gains were globally calibrated for all the elements on the first coil element only, some might contain clipped signals while others do not. Therefore, the first strategy adopted was to detect and filter coil elements that contain too many data points close to the 2^{32} upper limit of digitization. I filtered out coil signals with more than 6 % spokes with a maximal value higher than 2^{29} to empirically compromise between SNR and the absence of clipping artifact as shown in Figure 3.15. This strategy is not ideal, as data is lost, and it is not ensured that all clipped signal is removed. The second strategy was to maximize the gains at the acquisition (during the manual prescan step) while checking on every coil element, and no clipping occurred. It was only applied later in the acquisition protocol.

Figure 3.15: Sagittal views of an image acquired with RF overflow. The resulting clipping artifact can be seen in the left image, with hypersignal in the parenchymal tissues, while some vessels suffer from signal loss. The clipping filter effect can be seen on the right image, enabling the recovery of distal vessels and the contrast of the image (right arrow).

D. Magnitude inhomogeneities

Because the coil channels have different sensitivities when receiving the MR signal, intensity biases are present in the final image. This poses problems for traditional image processing steps, particularly for large field-of-view over which the coil sensitivities can vary a lot. In 3D MR spirometry, the registration step includes image saturation to tackle sliding motion (as detailed in B.), which can be biased by magnitude inhomogeneities. Moreover, the segmentation step is also sensitive to contrast and intensities and might be less performant on images with strong inhomogeneities. As MRI lacks absolute intensities, variability appears across acquisitions, volunteers, and systems. Inhomogeneity correction improves the overall robustness of the image processing framework.

N4ITK (successor to N3) is a robust and popular algorithm for correcting intensity inhomogeneities, particularly in lung MRIs.[192] The technique relies on the assumption that the histogram of the biased image is a blurred version of the histogram of the true image. The inverse problem is solved on the log-transformed image, from which the added bias is estimated using a Wiener deconvolution.[193] The process is relatively long for a volume (around 10 min); an average N4ITK correction has been implemented for all dynamics from the average image over the dynamics (Figure 3.16).

Finally, despite the very fast MR acquisition, the overall image quality enables reaching peripheral vessels, as presented in Figure 3.17.

All images reconstructed and displayed in this manuscript have undergone the specified image processing steps from this point forward.

[192] Nicholas J. Tustison et al. *IEEE transactions on medical imaging*, 2010.
[193] J. G. Sled et al. *IEEE transactions on medical imaging*, 1998.

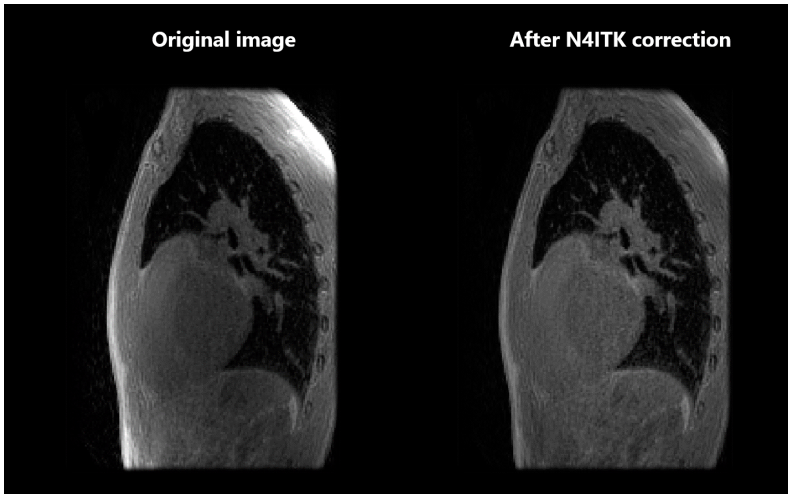

Figure 3.16: Intensity inhomogeneities correction using N4ITK in a sagittal view of a healthy volunteer. Higher intensities are observed at the body's periphery, close to the receive coil, whereas lower intensities are detected in the body's center.

Figure 3.17: Final images were obtained using a 12 µs gradient delay retrospective correction and an N4 correction of magnitude inhomogeneities.[192] Maximal intensity projection over 3 cm slices for coronal (center) and sagittal views (left and right).

3.2.2 3D MR spirometry reconstruction framework

The reconstruction framework has been optimized for better robustness and automation, reliable quantification of biomarkers, and preliminary efforts to speed up the processing time. Beyond all the corrections introduced above, this subsection presents the improvements that were carried out in the 3D MR spirometry process: a new soft-gating approach, image pre-processing, segmentation strategies, and temporal regularization.

A. Soft-gating in the spirometry domain

To improve the dynamic reconstruction, specifically improve its robustness to the variability of breathing patterns, a new retrospective gating algorithm was computed. The most common self-gating method is based on the amplitude of the respiratory signal extracted from the center of the Fourier volume. However, such a method does not allow the recovery of the ventilation hysteresis phenomenon. I took advantage of the richer information that is available in the phase portrait of the respiratory signal, a space analogous to the flow-volume space of spirometry, to perform a spatial gating. The respiratory signal is plotted against its temporal derivative, representing the phase portrait, with each respiratory cycle corresponding to a single loop. Then, each respiratory cycle is detected and interpolated into 100 sampling points using a third-order B-spline. The Euclidean barycenter of all samples is computed to retrieve a reference respiratory cycle. From this reference respiratory cycle, 32 respiratory phases, equidistant in the phase portrait, are defined (left, Figure 3.18). A KD-tree algorithm [194] finds the N closest points of each gate center to define a respiratory gate and its associated acquired spokes (right, Figure 3.18). The image reconstruction of the N spokes finally yields a 3D lung image for each of these respiratory states. We usually need 45,000 spokes to reconstruct each respiratory phase so that gates overlap.

[194] Jon Louis Bentley. *Communications of the ACM,*. 1975.

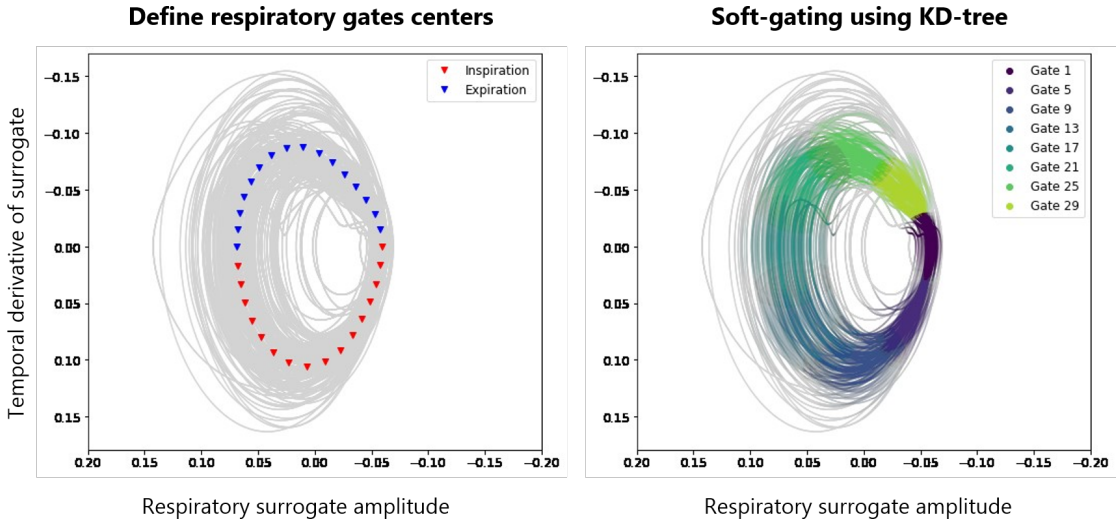

Figure 3.18: Soft-gating in the phase portrait of the respiratory surrogate, which is extracted from the k-space center using a principal component analysis (self-navigation). The left figure displays the phase portrait of the respiratory surrogates (gray) with the reference respiratory cycle defined by the 32 equidistant triangles (red for inspiration and blue for expiration). The retrospective gating of acquired k-space data is then performed using a KD-tree algorithm [194], which finds the N nearest neighbors for each gate center (right figure).

For each spoke and each respiratory gate, weight is defined according to the distance in the phase portrait of the gate center to the spoke associated navigator position. This weight is used as a density compensation function at the reconstruction for faster convergence and motion blurring reduction. A Gaussian is chosen as suggested in the literature [195],[182] In a given gate, for s a tuning parameter for the soft-gating strength, the weight w_{spoke} of each spoke i is defined as:

$$w_{\text{spoke}}(i) = \exp\left(-\frac{1}{s} \times \frac{d_{\text{spoke-center}}}{d_{\max} - d_{\min}}\right) \tag{3.13}$$

with:

$$\sum_i w_{\text{spoke}(i)} = 1 \tag{3.14}$$

and $d_{\text{spoke-center}}$ the distance of the spoke navigator point with the gate center, $d_{\max}$ the maximal distance between a selected spoke for the gate and the gate center, and

[195] Christoph Forman et al. *Magnetic Resonance in Medicine*, 2015.

d_{min} the minimal distance between a selected spoke for the gate and the gate center.

Although all respiratory gates are defined and reconstructed with the same amount of spokes, the weighting induces increased SNR variation at the reconstruction. Lower SNR for high dynamics is found; however, it is combined with less respiratory motion. The soft-gating reduces respiratory motion by limiting the diversity of available k-space information for the inverse problem resolution, which reduces the SNR. A compromise between SNR and motion artifact should be found, which is data dependent. This soft-gating approach intrinsically handles this balance, with the distance from the gate center being used as a weight for image reconstruction. If not sufficient, the parameter s allows fine-tuning the soft-gating strength. A value of $s = 0.5$ was found robust on the dataset of 25 healthy volunteers presented in Chapter 4. The respiratory blurring is illustrated in Figure 3.19 for four representative participants of the cohort.

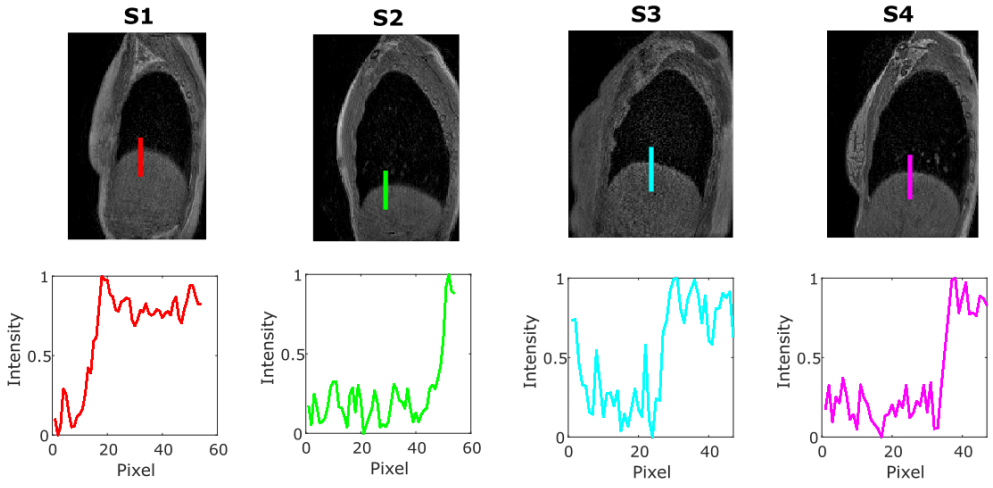

Figure 3.19: Sagittal views (top) corresponding to the end of the inspiration of four healthy volunteers lying in the supine position. The end of expiration is commonly the respiratory state the most affected by respiratory motion blurring. Here, the motion blurring is almost not perceptible in the MR images. The signal intensities are plotted for each volunteer along a line (bottom). The blurring seems to occur for 5 to 10 pixels (corresponding to 0.8 to 1.5 cm)

B. Segmentation of lung structures

As the previous automatic segmentation turned out not to be robust on the newly acquired dataset, different approaches have been explored to extract the lung volume and its main structures. This part presents a newly developed adaptive active contour approach, a registration-based strategy, followed by the work carried out in collaboration with the ARTEMIS team (Catalin Fetita, Antoine Didier, and Rezkellah Noureddine Khiati) to infer the main pulmonary structures. Ultimately, a deep learning model has been trained to automatically and efficiently segment lung lobes in upcoming protocols. The following developments were performed and challenged over a dataset of 25 healthy volunteers (presented in Chapter 4, in Table 4.1).

Automatic lung volume segmentation

Two automatic methods have been developed to extract the lung volume automatically. The techniques are compared here on a single volunteer at the volume corresponding to his end of expiration, using manual segmentation as ground truth. Manual segmentation was performed using the "volumeSegmenter" Matlab tool in 4 hours onto the reference image. The techniques were compared by computing the Dice Score between the manually segmented image ($\mathbf{X}$) and the segmented images ($\mathbf{Y}$) obtained using the newly developed technique:

$$\text{Dice} = \frac{2 \times |X \cap Y|}{|X| + |Y|} \tag{3.15}$$

The Dice score can vary between 0 and 1, 1 corresponding to a perfect agreement between the two segmentations.

An adaptive active-contour strategy was thus specifically developed for the dataset of this doctoral work. From a rough segmentation of the lung volume using K-means, a Chan-Vese active contour strategy is then applied to better discriminate

the interface between lung tissues and the thoracic cage.[196] The active contour is applied on batches of slices with increasing iterations in the more dependent lung region. The contrast between the parenchyma and the thoracic cage diminishes as the lung deforms under gravity, with a higher proton density in the posterior lung while lying supine. The computation time was around 1 min. Despite the gradient of iterations, the technique does not perfectly reach the interface between the dependent parenchyma and the thoracic cage (Figure 3.20).

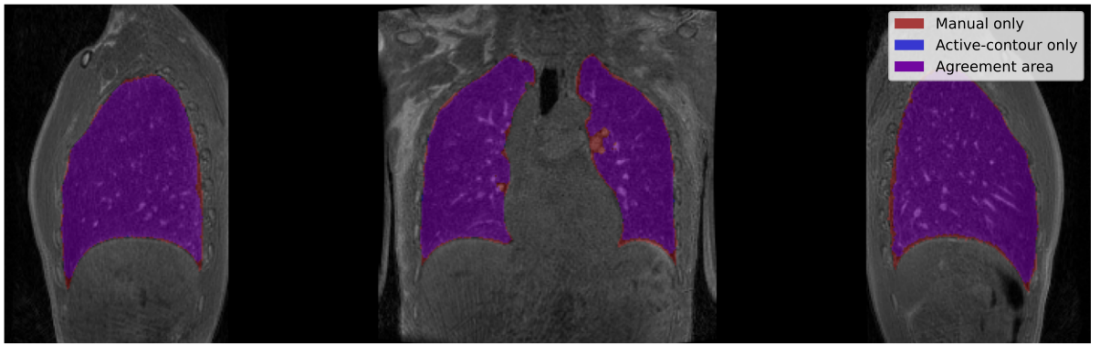

Figure 3.20: Manual and automated active-contour lung segmentation for the reference image in a healthy volunteer in the supine position. A manual mask (red) can be considered as the reference mask, while a registration-based (blue) is assessed. Colors are additive. The large purple area demonstrates the agreement between the two labelisations. However, in both sagittal views, it can be seen that the active contour is less efficient in the posterior region. Despite an increased number of iterations in the most gravity-dependent regions (the posterior regions), the contrasts between parenchymal tissues and the thoracic cage are too low.

Another approach was the use of image registration between unlabeled images and a reference labeled image using Elastix.[186] The elastic registration process finds the best transform between the labeled image and the unlabeled image based on the solid anatomical landmarks of the lung. The application of the transform on the reference mask infers the lung volume of the unlabeled image. The computation time was around 2 min per image. Once a reference image is segmented, registration-based segmentation is thus a relatively quick process and quite robust. However, it can have difficulty reproducing sharp shapes, as shown in Fig-

[196] T.F. Chan and L.A. Vese. *IEEE Transactions on Image Processing*, 2001.
[186] S. Klein et al. *IEEE Transactions on Medical Imaging*, 2010.

ure 3.21. Moreover, lung shapes that are too different from the reference dataset can also be poorly segmented.

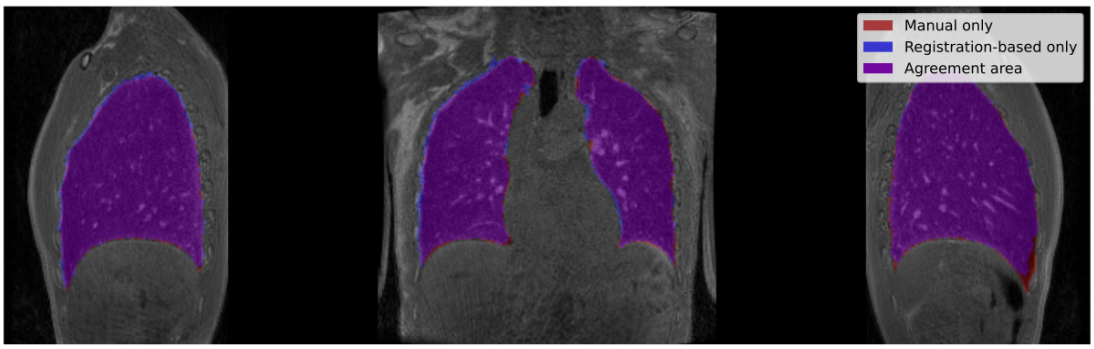

Figure 3.21: Comparison of different segmentation approaches using additive color: the manual mask (red) can be considered as the reference, while registration-based (blue) is assessed. The purple area demonstrates the large agreement between the two segmentations. However, in the right sagittal view, it can be seen that the registration transform fails to reach the basal singularity fully. The segmentation was performed on the end-of-expiration image of healthy volunteers freely breathing in the supine position.

Dice scores	Adaptative active-contour	Registration-based
Manual	0.951	0.952

Table 3.4: Table of Dice scores computed between reference manual segmentations and two iterative approaches:[137] adaptative active-contour segmentation and registration-based segmentation. The comparison is performed on a sole dataset that was manually segmented for reference. The accuracies of both techniques are high and very similar.

Both techniques are fairly accurate, with a similar Dice score of 0.95 with the manual reference (Table 3.4). The lung volume can now be segmented, and a segmentation of the main lung structures was sought.

Structural segmentations: from vessels and airways to lung lobes

A combined framework of airways and vessel segmentation was developed during this doctoral work from the adaptative active contour approach framework. Main airways, particularly the trachea, are removed using a Frangi vesselness filter combined with a prior of main bronchi location.[197] Main vessels were extracted us-

[197] Alejandro F. Frangi et al. "Multiscale vessel enhancement filtering". In: *Medical Image Computing and Computer-Assisted Intervention — MICCAI'98*. Ed. by William M. Wells et al. Lecture Notes in Computer Science. Berlin, Heidelberg: Springer, 1998. DOI: 10.1007/BFb0056195.

ing an Otsu thresholding and active contour.[198] The global computation of global lungs, airways, and vessels was around 4 min per image. However, the segmentation was not robust, and parameters needed to be tuned for several datasets.

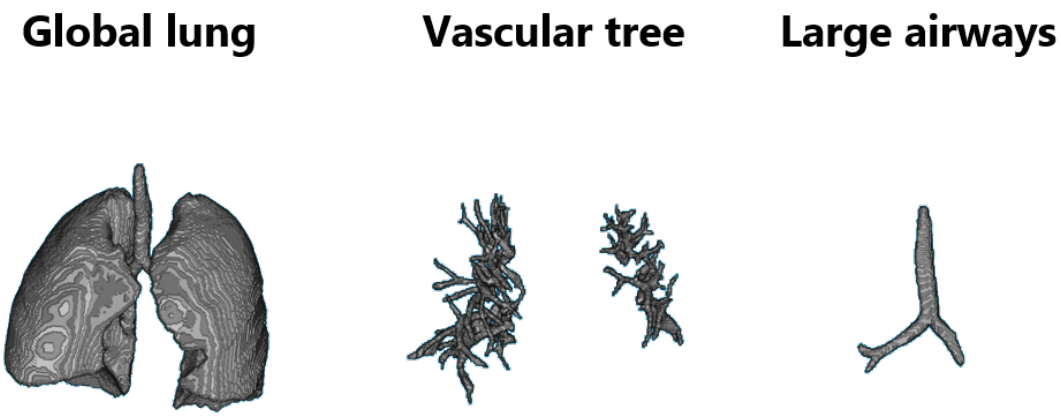

Figure 3.22: Segmentation of main lung structures: the global lung (left) is extracted using an adaptative active contour algorithm, the vascular tree is computed from an Otsu thresholding fine-tuned with an active contour strategy (middle), and large airways inferred from a Frangi vessel with an apriori of their location (right).

In collaboration with the ARTEMIS group, a more robust lung structure segmentation approach was adapted from their previous work on CT lung images [199] to MRI. Lung lobes are inferred from partitioning vessel clusters, intrinsically present with fissures, as shown in Figure 3.23. Indeed, vessels are better contrasted in MRI, and intrinsic clusters appear between lung lobes, separated by a non-vascularized membrane (center, Figure 3.23). The expertise of the ARTEMIS group allowed us to obtain labels of parenchyma and lobes from the acquired MR UTE images after manual adjustments by the operator. Particularly, beyond a few generations, the segmentation of the airways is not feasible because of the poorer contrast and spatial resolution of MRI compared to CT.

As this algorithm is still semi-automatic for MR images, the ARTEMIS team is currently working on a new and automatic vessel clustering.[200] In the meantime,

[198] Nobuyuki Otsu. *IEEE Transactions on Systems, Man, and Cybernetics*, 1979.

[199] Catalin I. Fetita et al. *IEEE transactions on medical imaging*, 2004.

[200] Khiati Rezkellah Noureddine. "Vessel-based lung lobe partitioning in ultra-short time echo proton MRI for regional ventilation assessment | SPIE Medical Imaging". In. San Diego, 2024.

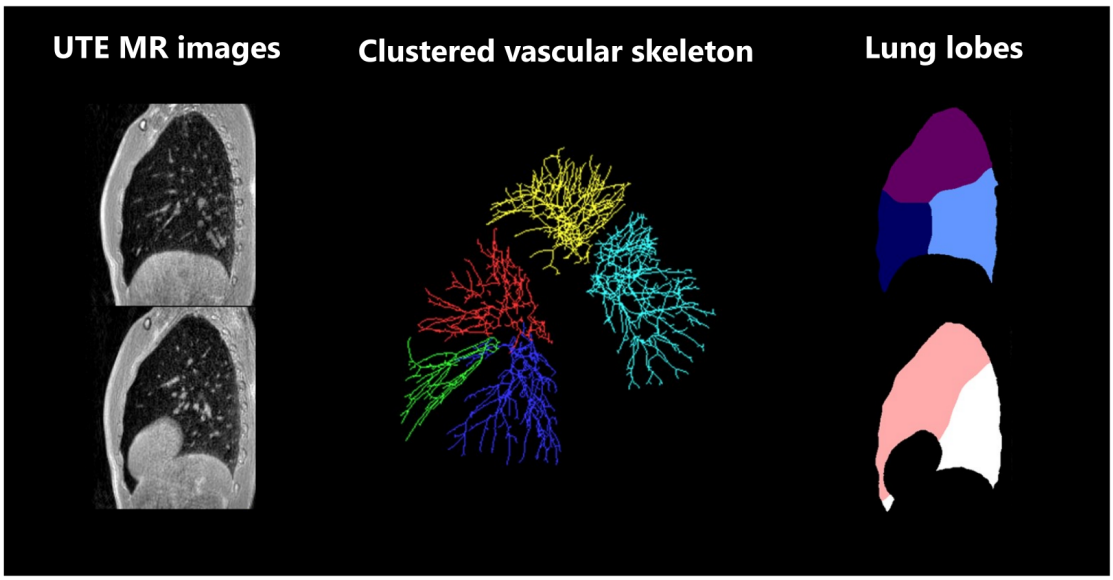

Figure 3.23: Segmentation of lung and its lobes from UTE MR images acquired at the end of expiration on healthy volunteers, based on the ARTEMIS group. A partitioning is carried out based on the intrinsic existence of clusters of vessels in the structural anatomy of the lung, as shown in the center of the Figure. The right (top) and left (bottom) lungs are separated into three and two lobes, respectively. The figure displays the segmentation results for sagittal views of the right and left lungs.

image registration from a reference image with labeled lobes was used in this work to infer pulmonary lobes on the acquired datasets.

Accelerating the process with a robust Deep Learning model

To accelerate the process and improve its robustness, a multiclass automatic segmentation method based on the nnUNet framework has been developed [201]: 5 encoding steps and 4 decoding steps, each including 2 convolutions (see Figure 3.24).

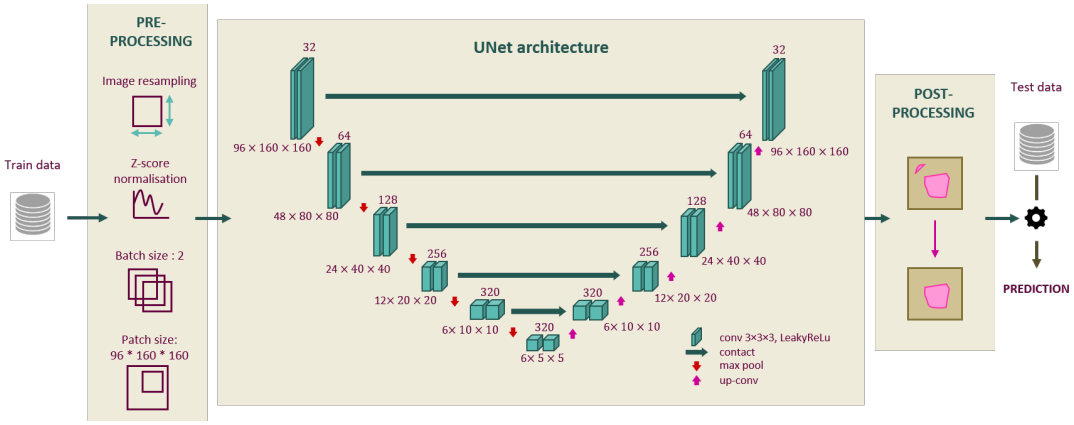

Figure 3.24: nnUNet framework [201]: the pre-processing, the UNet network architecture, and the post-processing is adapted to the characteristics of the data and GPU constraints. The provided architecture parametrization was used for lung lobe segmentation on UTE MR images of healthy volunteers. The method was presented at the IABM 2024 congress.[202]

The database was built from images acquired from 25 healthy volunteers lying in supine and prone positions and for the 8 respiratory phases. The labels of lung lobes were obtained by registration on a reference volume (see Appendix), labeled using the structural segment of the ARTEMIS group, and manually corrected by Catalin Fetita and Antoine Didier. Finally, the dataset contained 640 training and 168 test volumes. Average Dice scores between 0.86 (right middle lobe) and 0.95 (right lower lobe) are obtained (Figure 3.25), demonstrating the efficiency of the model. Moreover, it can be seen that the nnUNet segmentation can overperform the original labels: on the left inferior lobe in the Figure 3.25, the most basal region of the lung is better segmented than the original labeled image. The average segmentation time of the framework is 4.8 s for each lung volume (corresponding to 2-3 minutes for the 32 respiratory phases). Ongoing works explore the reliability of the model from different data labeling approaches.[200] A prospective

[201] Fabian Isensee et al. *Nature Methods*, 2021.

study at the Erasmus Medical Center plans to perform CT and UTE-AZTEK MR acquisitions on the same patients, allowing the approach to be validated on lung lobes segmentation from CT scans.

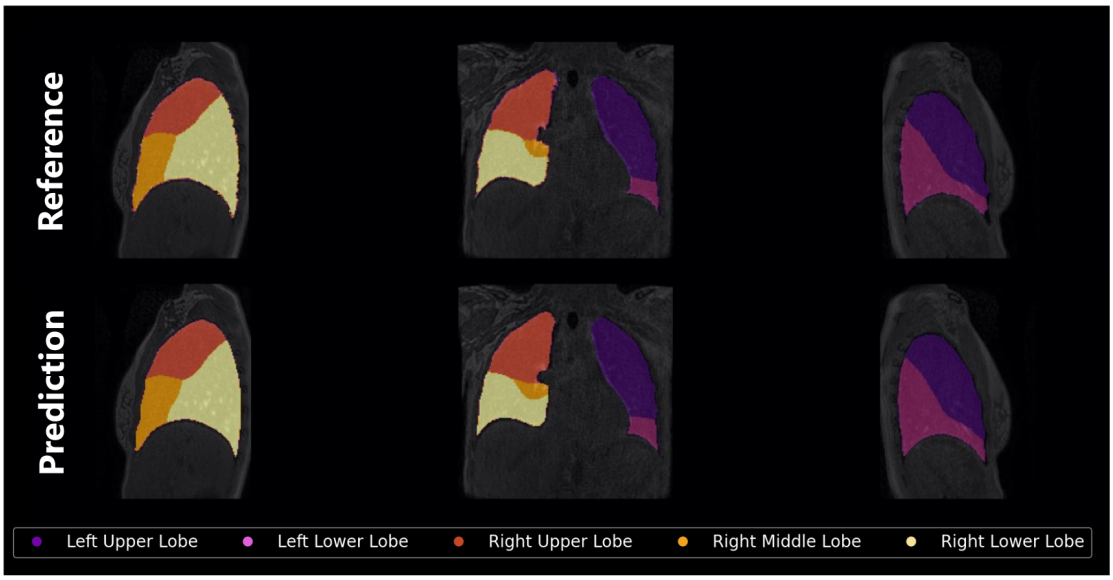

Figure 3.25: Lung lobe predicted by the nnUNet framework for a healthy volunteer lying supine. The model was trained on 640 images labeled using the registration-based approach on a reference dataset. Average Dice scores between 0.86 (right middle lobe) and 0.95 (right lower lobe) were obtained. The lower left lung is better segmented using the nnUNet framework than the original labeled image, demonstrating the efficiency of UNet architecture in learning segmentation tasks.[202]

C. Registration with a temporal regularization

Deformation fields inferred from the pairwise registration are noisy in the temporal dimension, where small displacements occur between successive respiratory phases. In the original pipeline, a smoothing strategy tackles the noise.[105,203] However, the accuracy of the smoothed deformation is not considered nor verified. In the original pairwise registration (see section B.), choosing the reference image can induce a significant measurement bias.[163] A groupwise registration with an adapted temporal resolution enables a consistent and robust deformation estimation, which

[105]Tanguy Boucneau et al. *Scientific Reports*, 2020.
[203] Damien Garcia. *smoothn (https://www.mathworks.com/matlabcentral/fileexchange/25634-smoothn), MATLAB Central File Exchange. Retrieved December 6, 2023.* Dec. 2023.
[163]F. Klimeš et al. *NMR in Biomedicine*, 2019.

is no longer an issue when performing a groupwise approach. Besides, the cyclicity of the respiratory cycle can be used in the registration to enforce the continuity of the flow-volume loop between the end of expiration and the beginning of inspiration. The Elastix toolbox was used to compute a groupwise registration on all respiratory phases altogether,[186] using a cyclic constraint on the deformation, based on the work of Metz *et al.* [204] The smoothed pairwise and the groupwise approaches have been compared using equivalent registration parameters, reported in Table 3.5. A Pearson correlation coefficient assesses their linear relationship

Type of registration	Pairwise	Groupwise
Transform	B-Spline transform	B-Spline transform
B-Spline order	3	3
Metric	Normalized mutual information	Variance over last dimension
Number of resolution	2	2
Final grid spacing	20 voxels isotropic 32 respiratory phases	22 voxels isotropic 6 respiratory phases
Number of spatial samples	12000	12000
Use cyclic transform	NA	True

Table 3.5: Main parameters for dynamic lung MRI registration for pairwise and groupwise approaches. The final spatial resolution is slightly larger for groupwise registration as the virtual fixed image corresponds to a larger lung volume (averaged volume along the 32 respiratory states), while the end-of-expiration state was used for pairwise registration.

TV maps are computed from Jacobian maps obtained by these two approaches (Figure 3.26). Maps of smoothed pairwise and groupwise approaches are moderately correlated (Pearson correlation coefficient of $\rho = 0.63$), demonstrating a certain consistency between the two approaches. The groupwise approach should be used as the smoothness of the deformation along the temporal dimension is regularized and not forced afterwards. Moreover, the virtual state used as a fixed image for the groupwise registration might improve reproducibility. However, future work should be carried out to develop and validate the approach. The 3D MR spirometry maps

[186] S. Klein et al. *IEEE Transactions on Medical Imaging*, 2010.
[204] C. T. Metz et al. *Medical Image Analysis*, 2011.

presented in this manuscript were computed using a smoothed pairwise approach, whose reliability is assessed later in this chapter 3.3.1.

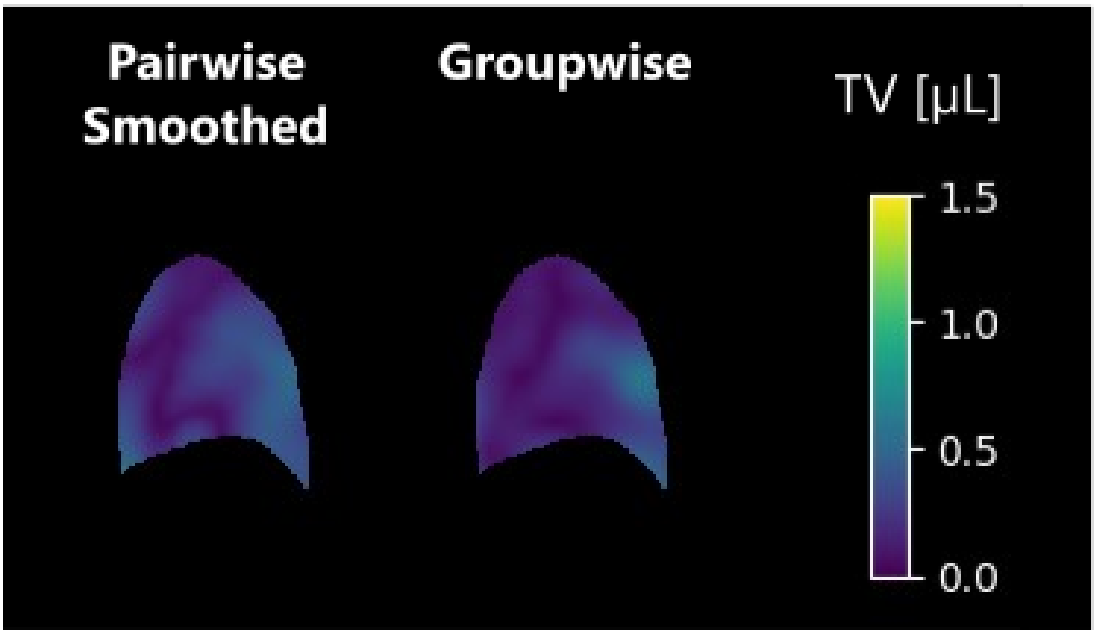

Figure 3.26: Maps of tidal volumes were obtained through smoothed pairwise and groupwise registrations.

3.2.3 Computation of quantitative biomarkers of the ventilation

Three-dimensional MR spirometry supplies voxel-wise flow-volume loops throughout the lung volume. Similarly to standard spirometry, many biomarkers can be extracted, embodying their own different physiological information. Furthermore, since the method relies on the Green-Lagrange tensor estimation, biomarkers of the respiratory mechanics are accessible, specifically the deformation patterns.

A. Spirometry-based biomarkers

From the flow-volume loops, measurements were implemented during this doctoral work, inspired by the standard spirometry literature and physiological knowledge (see Figure 3.27). It is the first time absolute quantifications were implemented, as only ratios were previously used.[105,110,115]

Volume-based biomarkers:

- Tidal volume (TV)
- Volume at 1 s of spontaneous expiration (SEV1)
- Volume at spontaneous peak expiratory flow (V_{SPEF})

Flow-based biomarkers:

- Spontaneous peak expiratory flow (SPEF)
- Spontaneous expiratory flow at 25 % of remaining volume (SEF25)
- Spontaneous expiratory flow at 50 % of remaining volume (SEF50)
- Spontaneous expiratory flow at 75 % of remaining volume (SEF75)

Time-based biomarkers:

[105] Tanguy Boucneau et al. *Scientific Reports*, 2020.
[110] Andreas Voskrebenzev et al. *Magnetic Resonance in Medicine*, 2018.
[115] Christoph Kolb et al. *Journal of Computer Assisted Tomography*, 2016.

- Time at peak expiratory flow (t_{SPEF})
- Time to inspire (T_{insp})
- Time to expire (T_{exp})

The maps of tidal volumes (TV) assess the spatial distribution of the gas inhaled over spontaneous respiration, highlighting inhomogeneities and regions with hypo or hyper-ventilation. To access dynamic information, SEV1 for the volume and SEF25, SEF50, and SEF75 for the flows evaluate the distribution of gas at certain respiratory states of the expiration. These biomarkers can better infer the local efficiency of the expiration, that is, the ability to expel gas in a short amount of time. As these biomarkers rely on finite temporal indices, some spatial discontinuities appear on the maps at high respiratory dynamics and for low-ventilated regions. These artifacts are nonphysiological and should be corrected; however, the main patterns are still accessible. Time-based biomarkers were computed but not explored during this doctoral work.

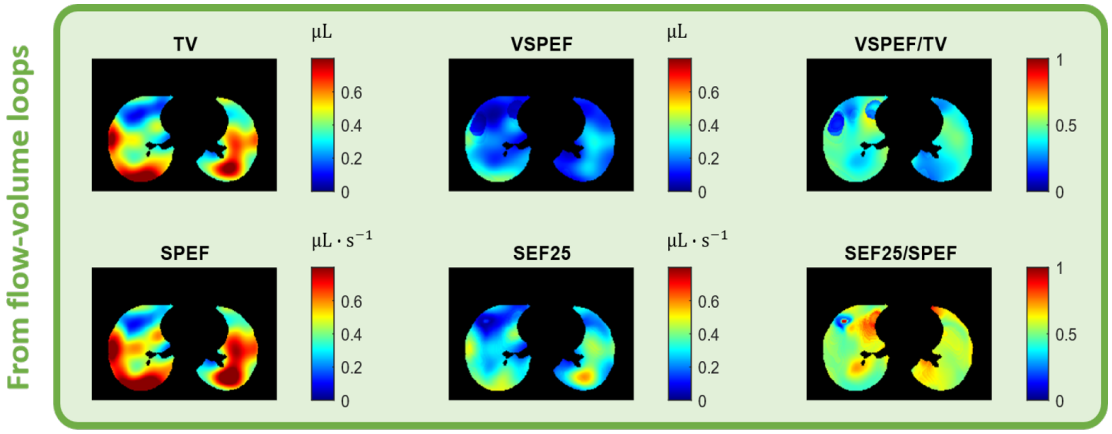

Figure 3.27: Axial middle slice of 3D spirometry biomarker maps for a healthy volunteer in the supine position. From spirometry-based measurements, some ratios were computed, all of them evaluating the ability to efficiently exhale in an inter-volunteer normalization frame.

B. Mechanical-based biomarkers

From the Green-Lagrange tensor, 3D+t tensors are accessible and describe the mechanical behavior of the deformation, as described earlier in the seminal article [105] and earlier in this section B.. They provide directional or adirectional information about motion for each respiratory phase. During this doctoral work, the biomarkers were evaluated at their maximal value along the respiration, leading to volumic maps.

Directional information:

- Strain components tensor along the superior-inferior direction (ϵ_{SI})
- Strain components tensor along the right-left direction (ϵ_{RL})
- Strain components tensor along the anterior-posterior direction (ϵ_{AP})

Adirectional information:

Anisotropic deformation index (ADI)

Slab-to-rod index (SRI)

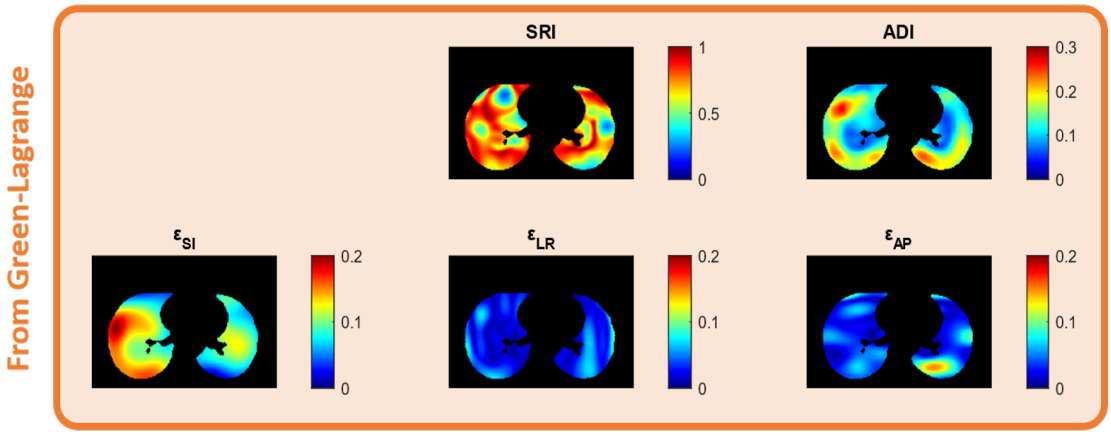

Figure 3.28: Axial middle slice of mechanical biomarker maps for a healthy volunteer in the supine position.

The directional biomarkers can be used to better understand the motion behavior, relying on the tissue properties, the effect of pressure, and the surrounding

[105] Tanguy Boucneau et al. *Scientific Reports*, 2020.

muscles. Particularly, the anisotropy highlights anatomical constraints such as the rib cage. Diaphragmatic or thoracic muscle contributions could also be discriminated since their motion is mostly along different planes. Finally, the motion can be used to model the parenchymal compliance using biomechanical models.[205] A collaboration with Martin Genet has been discussed to transfer such a model to UTE-MRI dynamic images.

3.2.4 Python reconstruction and processing package

To enable the effective implementation of the technique in clinical research and particularly in partner centers, I developed the framework to make its code as accessible as possible. My main objectives for code production were:

- Use an open-source programming language
- Produce documentation
- Create a readily available package

Three-dimensional MR spirometry framework codes were originally developed in `Matlab`, a language still widely used in research due to its algorithm performances and relative ease of use. However, in recent years, open-source codes have become widespread, making research more easily reproducible and reproduced. `Python` is the most popular language, and many researchers today know how to use it. Open-source rendering of the codes is under consideration, but they are not currently available.

[205] Cécile Patte. *Personalized pulmonary mechanics : modeling, estimation and application to pulmonary fibrosis.* PhD thesis. Institut Polytechnique de Paris, Dec. 2020.

3.3 Challenging the reliability in healthy volunteers

To assess the clinical benefit of the technique, it is essential to first ensure its reliability: that is to say, its ability to provide values in a repeatable, accurate, and precise manner. The reliability of 3D MR spirometry has thus been challenged on two levels: the repeatability of the measurements in healthy volunteers for two consecutive scans and the consistency of its outcomes with functional lung CT imaging and Fourier Decomposition MRI.

A clinical study was conducted on 25 healthy volunteers lying in supine and prone positions. The acquisitions were repeated for each position. As an external reference, a respiratory belt monitored the abdominal motion through the acquisitions.

3.3.1 3D MR spirometry repeatability

A. Intrinsic variability in free-breathing

The ventilation was intuited extremely repeatable as integrated over the 10 min of the MRI acquisition. Indeed, over a long time, it can be supposed that a homeostasis of the respiratory function is reached. However, over the 25 healthy volunteers, we recorded with the respiratory belt an intrinsic variability of spontaneous breathing with median variations between successive acquisitions of 4.4 % on the mean signal amplitude and 9.7 % on the mean signal frequency, as presented in the Bland-Altman analysis on the Figure 3.29. A small bias is measured with a conjoint respiratory frequency increase while amplitude decreases between successive acquisitions; however, it is not statistically significant ($p = 0.18$ with a paired Wilcoxon test [206]).

[206] Frank Wilcoxon. *Biometrics Bulletin*, 1945.

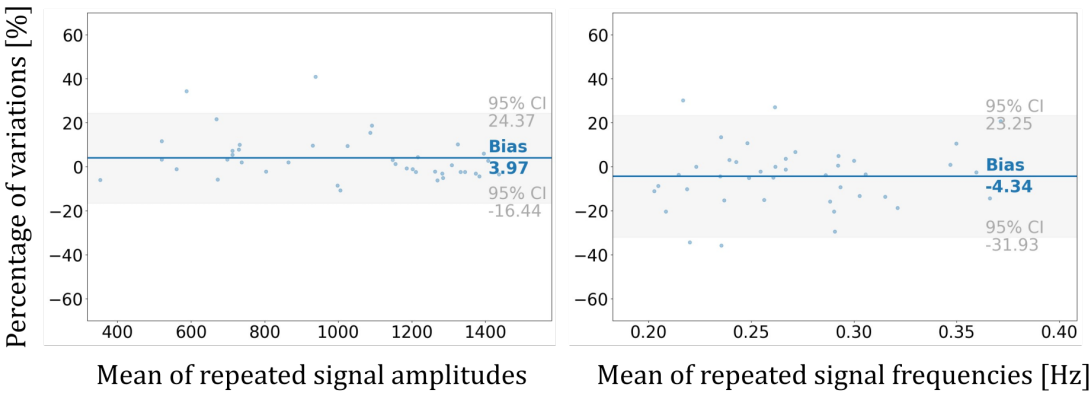

Figure 3.29: Bland-Altman plot on the recorded respiratory belt signal amplitude and frequency between two successive acquisitions. The intrinsic variability of spontaneous breathing is measured through 100 datasets conducted on 25 healthy volunteers lying in the supine and prone positions.

As presented in Chapter 1, this variability is known to the scientific community and reported in previous free-breathing studies.[10,207,208] This variability is a nominal phenomenon of ventilation that bounds the evaluation of 3D MR spirometry repeatability.

B. Global repeatability

As presented in the previous section, 3D MR spirometry assesses absolute volumes and flows of respiration from the determinant of the Jacobian matrix of the strain tensor and its temporal derivative. The resulting 3D+t parametric maps allow to assess multiple biomarkers. Here, we focus on two biomarkers: the tidal volume (TV) and the spontaneous peak expiratory flow (SPEF). By integrating the two biomarkers over the lung volume, measurements equivalent to those obtained with a standard spirometer are retrieved. For two successive acquisitions, median variations of 7.7 % for global TV and 8.1 % for global SPEF (see Figure 3.30) are found. These variations are of the same order of magnitude as those measured with the respiratory belt, indicating that the technique is reliable despite the intrinsic breathing variability. A slight positive bias is measured, indicating higher tidal

[10] X. Baur et al. *Respiration*, 2009.
[207] Andreas Voskrebenzev et al. *Magnetic Resonance in Medicine*, 2016.
[208] James F. Morris et al. *American Review of Respiratory Disease*, 1971.

volumes and flows during the first acquisition, which is consistent with the amplitude of the respiratory belt signal. This bias is significant for both parameters ($p < 0.01$ with a paired Wilcoxon test).

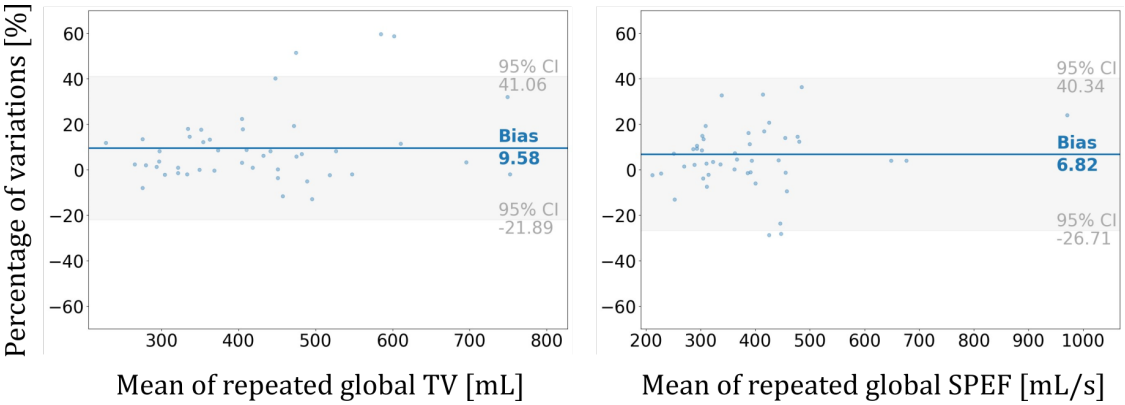

Figure 3.30: Bland-Altman plots of global tidal volumes (left) and peak expiratory flows (right) in supine and prone positions. The global repeatability of 3D MR spirometry is measured through 100 datasets conducted on 25 healthy volunteers lying in the supine and prone positions.

A common approach is to normalize the parameters from one acquisition to another to cope with this inherent physiological variability. This allows better reproducibility of local measurements.[207]

C. Local repeatability

The second acquisition is spatially normalized using an elastic registration to the first to evaluate local repeatability. A Bland-Altman analysis is then performed voxel-wise for all the acquisitions for local tidal volumes (TV) and peak expiratory flows (SPEF). Median local variations are 15.50 % for TV and 20.89 % for SPEF. These relative variability measurements, expressed as a percentage here, should be taken cautiously since parameter values close to 0 tend to amplify the variability despite median metrics remaining relatively robust to this bias. As illustrated by the Bland-Altman plots in Figure 3.31, local TV and SPEF are repeated respectively with 95 % confidence intervals of [-0.33 µL, 0.43 µL] and [-0.45 µL/s, 0.51 µL/s].

[207] Andreas Voskrebenzev et al. *Magnetic Resonance in Medicine*, 2016.

Local repeatability thus seems quite low relatively to the mean and median values of TV (mean: 0.62 µL; median: 0.56 µL) and SPEF (mean: 0.56 µL/s; median: 0.49 µL/s) measurements. Normalization strategies should be explored to improve local repeatability, and some approaches are presented in Chapter 4.2.1. However, variability in ventilation spatial distribution also seems intrinsic to spontaneous breathing. The repetition of 6 successive acquisitions (over an hour) was experimented with no findings on the apparition of a form of longitudinal homeostasis, nor a trend, with better repeatability.

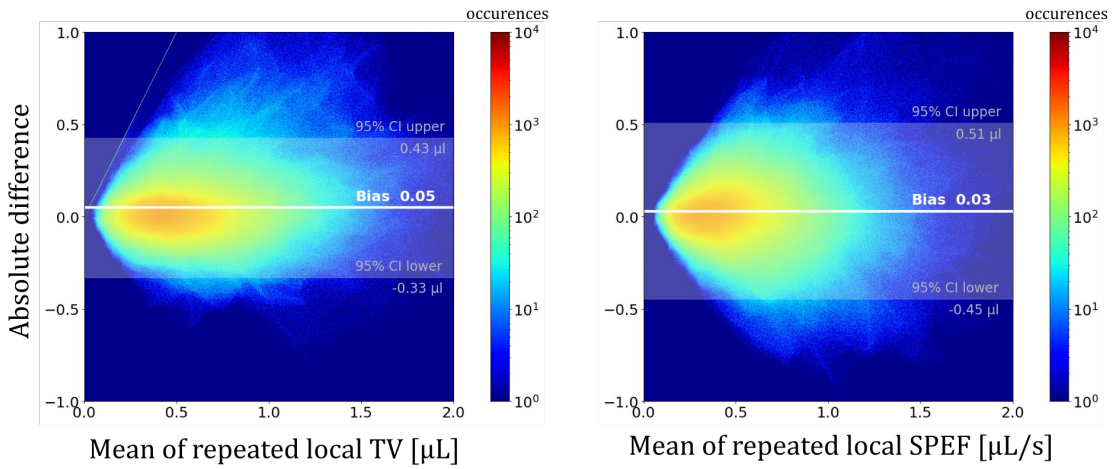

Figure 3.31: Bland-Altman plot of local tidal volumes (TV) and peak expiratory flows (SPEF) in supine and prone positions after spatial normalization of the repeated acquisition. This is performed using an elastic registration of the repeated image to the first one. SPEF is less repeatable than TV, with a large 95 % confidence interval (light gray) compared to the mean values. A positive bias is found for both parameters, suggesting higher ventilation at the second acquisition.

3.3.2 Accuracy evaluation

Another approach to evaluate the reliability of a method is to compare its results with those obtained with a technique considered as a gold standard by the community. An important difficulty in our study was finding comparable techniques with measurements of the same nature (local and absolute) carried out under comparable conditions (position, breathing rhythm). For this, different approaches were

explored: the segmentation of lung volumes for each respiratory phase, ventilation mapping based on the magnitude of the MR signal, and the Jacobian-based approach using CT acquisitions at two respiratory states.

A. Segmentation

One way to assess the accuracy of 3D MR spirometry post-processing is to compare the integral of all the local volumes estimated by 3D MR spirometry with the global volume estimated by segmenting the lung volume for each respiratory phase on the acquired MR images. The global volumes obtained should correspond to integrating all the local volumes measured by 3D MR spirometry. In Figure 3.32, a Bland-Altman analysis demonstrates the global accuracy of TV by comparing 3D MR spirometry to nnUNet segmented volumes. An intraclass correlation coefficient (ICC) (single fixed raters type [209]) of 0.98 is found, demonstrating the excellent agreement between the two measurements. A bias of 6.95 % is found with a Bland-Altman analysis (Figure 3.32) for TV_{seg} indicates a probable slight underestimation of volumes by 3D spirometry.

Although this comparison only allows a global evaluation of the accuracy of 3D MR spirometry, the strong agreement is a favorable indicator of the reliability of the technique.

B. Intensity-based approaches

To evaluate the accuracy of local quantification through 3D MR spirometry, a comparison with local parameters obtained using different ventilation mapping approaches is performed on a single volunteer freely breathing. Two techniques are used here compared to 3D MR spirometry on the same images, and both of them are based on the variation in magnitude of the MR signal during respiration. The first approach is based on the absolute differentiation of magnitudes between two respiratory phases, specifically the end-of-inspiration and the end-of-expiration.

[209] Raphael Vallat. *Journal of Open Source Software*, 2018.

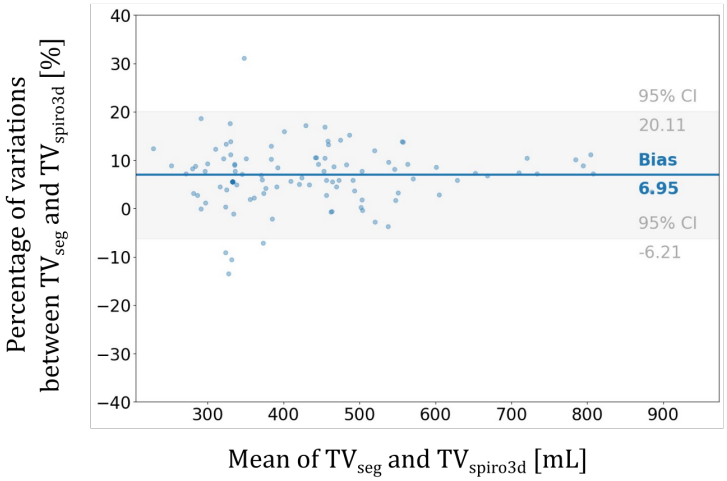

Figure 3.32: Bland-Altman plot showing the agreement between global tidal volumes obtained from the nnUNet segmentation (TV_{seg}) and the integration of local TVs measured by 3D MR spirometry over the lung ($TV_{spiro3D}$). A bias of 6.95% for TV_{seg} indicates a probable slight underestimation of volumes by 3D spirometry. The analysis was performed on a cohort of 25 healthy volunteers with repeated acquisitions in the supine and prone position, leading to 101 datasets finally evaluated.

The second approach is based on a Fourier decomposition along the temporal direction for a full dynamic image, using 32 respiratory phases. Both approaches are based on the assumption of the linear evolution of the MR magnitude signal with hydrogen proton density in parenchymal tissues, as detailed in Chapter 2.2.4.

Images were smoothed along the temporal direction with a Gaussian kernel (σ of 0.3). For the Fourier Decomposition, images were temporally interpolated into 128 respiratory phases to obtain the equitemporal dynamic of respiration. A Butterworth low pass filter was applied at 0.5 Hz. The ventilation map was computed by integrating the main ventilation peak in the frequency domain after the Fourier transform of the temporal signal. Intensity-based and Fourier Decomposition are correlated at 0.35 voxel-wise (Pearson). Tan *et al.* [120] reported a weaker correlation of global FD values with the segmentation of lung volumes.

Higher ventilation is observed in the posterior region for the three approaches but not in the same areas. Differences between Jacobian-based and Intensity-based

[120] Fei Tan. *Structural and Functional Ultra-short Echo Time (UTE) Proton Lung MRI: Techniques and Clinical Applications*. PhD thesis. UCSF, 2023.

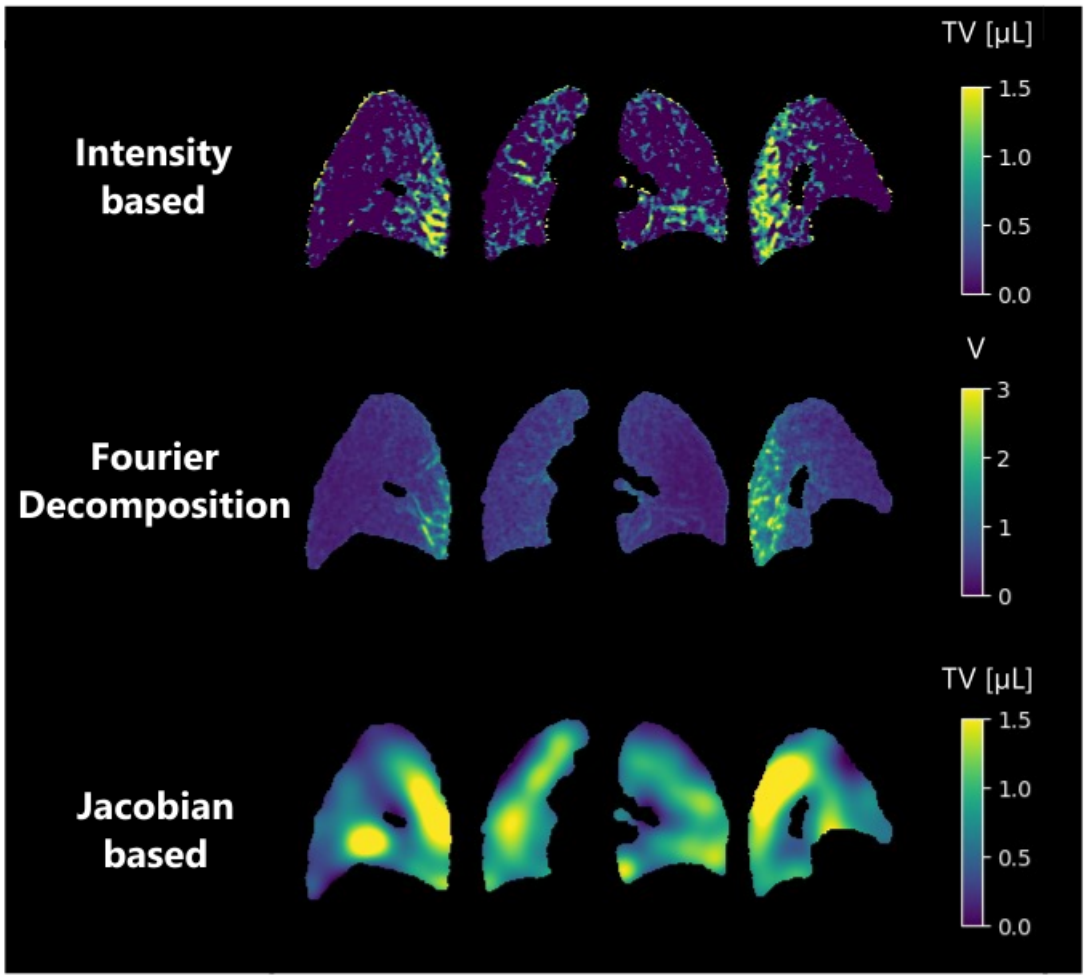

Figure 3.33: Ventilation mapping from three different approaches: the intensity differentiation of MR signal magnitude (top) between end-of-expiration and end-of-inspiration, the Fourier Decomposition along the respiration to extract the ventilatory components of MR signal magnitude variation (middle) and the Jacobian technique which measures the ventilation from local strain (bottom).

approaches have been reported by Kjorstad *et al.* [95] and Tan *et al.* but they did not propose any explanation for these differences. A local quantitative comparison with a hyperpolarized MRI approach at the same inhalation volumes could allow a better comparison and, thus, a better understanding of their corresponding reliability.

[95] Åsmund Kjørstad et al. *Magnetic Resonance in Medicine*, 2013.

C. Comparison with CT

CT acquisitions were performed at two respiratory phases (end-inspiratory and end-expiratory) at the Bicêtre hospital by Dr Olivier Mérignac. Then, a 3D MR spirometry exam was performed at the BioMaps laboratory. The study was performed on a healthy volunteer lying in the supine position. The volunteer was asked to hold the respiration close to the usual end of inspiration volumes at free breathing. This two-phase respiratory CT measurement method is commonly used in clinical practice to challenge ventilation (see Chapter 1.3.2). The end-inspiratory image was elastically registered to the end-expiratory image, enabling a local ventilation map to be inferred. Using the same post-processing steps, with the same registration, this measurement was compared to the two corresponding phases of dynamic lung MRI acquired with UTE sequence on a 10-minute long acquisition. The results obtained on the same subject are presented in Figure 3.34.

On the CT acquisition, both volumes were segmented using a k-means algorithm. The ventilated volume was estimated at 1.17 L from the difference of segmented volumes. The integrated Jacobian was estimated at 1.25 L. On the MRI acquisition, the tidal volume was 0.89 L from the segmented volume, while 0.91 L was found with the integrated Jacobian method. Higher ventilation is found in the posterior lung region for both images. However, the CT ventilation map seems more homogeneous. This might be caused by the difference in ventilated volumes, which was not controlled. The volunteer inhaled more volume in CT, even if his breath under MRI was deeper than the common free breathing (usually around 500 mL).

For a proper local comparison of 3D MR spirometry with another functional lung imaging technique, experiments should be conducted with controlled volumes of ventilated air and preferably at maximum inspiration, as the larger the volume of air inhaled, the more homogeneous and reproducible the gas distribution is in the lung volume.[132] However, to allow an unconstrained exam at free breathing,

[132] Paul J. C. Hughes et al. *Journal of Applied Physiology*, 2019.

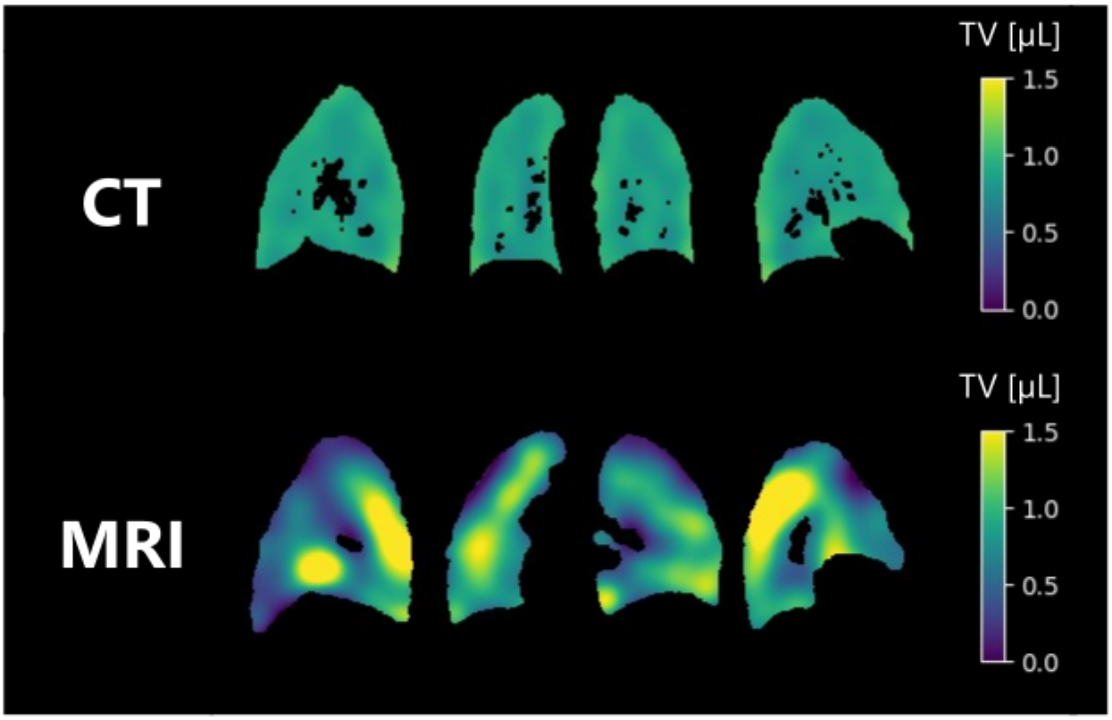

Figure 3.34: Local tidal volumes (TV) computed for a healthy volunteer lying in the supine position between end-of-expiration and end-of-inspiration for CT acquisitions (top) and MRI acquisition (bottom). The lung structure was segmented, and the main vessels (black holes) were removed. The global tidal volume was 1.17 L on CT and 0.89 L on MR acquisitions using k-means-based segmentations for both respiratory phases. Functional lung MRI reveals highly inhomogeneous patterns compared to CT, as some lung regions are not solicited. It might be explained by the difference in respiration for the two acquisitions that were not controlled: breath-hold for CT and free-breathing for MRI.

standardization, and atlas approaches could circumvent this issue by comparing local ventilation patterns to references.

4

Nominal respiratory features of the lung function

In the previous chapter, the reliability of the 3D MR spirometry workflow was demonstrated with repeatable and globally accurate measurements. As this technique carries unique insights into respiratory physiology, its potential and inputs for clinical practice are investigated. This chapter presents an exploratory study to assess the technique's sensitivity in healthy volunteers. This led to reliable atlases of the ventilatory function with nominal patterns of spontaneous respiration.

4.1 Challenging sensitivity to gravity lung dependence

Gravity effects on the ventilatory function is a known physical phenomenon, largely described for different postures in the literature.[163,210,211] Challenging the sensitivity of 3D spirometry to gravity allows to evaluate its clinical potential to physiological variations. This section describes a prospective study on gravity lung dependence, leading to standard mappings of gravity effects in healthy volunteers for lying supine and prone positions.

4.1.1 A prospective sensitivity study in healthy volunteers

Since the work of Milic-Emili and his team in 1966,[16] it is known that gravity affects the distribution of local ventilation, inducing increased volume variations in the most gravity-dependent regions. The parenchyma, subject to its own gravitational force, undergoes deformation characterized by the well-documented "Slinky® effect" [212] (Figure 4.1). It increases alveolar density and reduces transalveolar pressure in the dependent region, facilitating a more efficient flow and diffusion of gases.

[163] F. Klimeš et al. *NMR in Biomedicine*, 2019.
[210] K. Kaneko et al. *Journal of Applied Physiology*, 1966.
[211] Abhilash S. Kizhakke Puliyakote et al. *Experimental Physiology*, 2022.
[16] J. Milic-Emili et al. *Journal of Applied Physiology*, 1966.
[212] Susan R. Hopkins et al. *Journal of Applied Physiology (Bethesda, Md.: 1985)*, 2007.

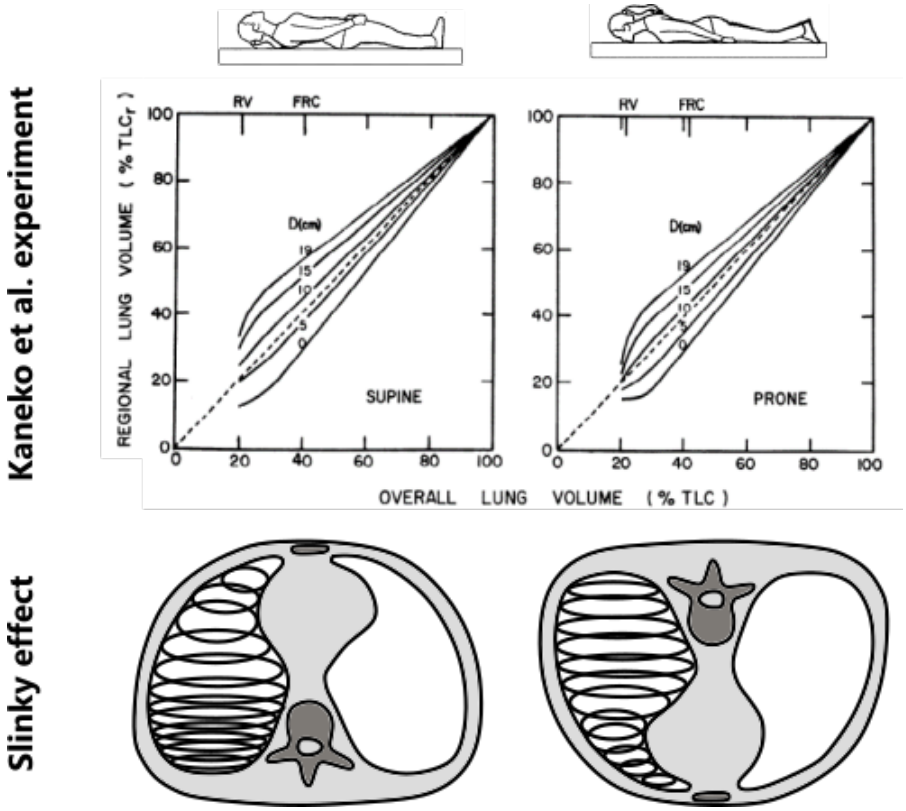

Figure 4.1: Gravity effects on lung volumes and ventilation: the upper plot presents the result of Kaneko *et al.* works, which shows the relationship between regional and total lung volumes. Using ^{133}Xenon, they measured the spatial variation along the anteroposterior axis of pulmonary ventilation in eight normal subjects across supine, prone, and lateral positions. They found a gradient of ventilation toward the more gravitity-dependent regions, which is more pronounced in the supine than prone position. The lower plot schematizes the Slinky® effect, inducing an increased alveolar density in the more dependent region, with a higher effect in the supine position where the shape of the lung increases the effect.

Gravity lung dependence was found to be a relevant physiological phenomenon to challenge 3D MR sensitivity in healthy volunteers. Indeed, gravity is highly stable, the change of position is a simple experimental parameter, and each volunteer is one's own reference. The literature describes the effect widely and offers thus valuable references for the gravity effects on regional ventilation. Particularly, Kaneko *et al.* evaluated its effect in the supine and prone positions,[210] where the gravity effect induced an increased volume variation in the more dependent regions (see Figure 4.1), which represents a positive ventilation gradient in the direction of gravity. In the supine position, the gravity dependence is stronger than in the

[210] K. Kaneko et al. *Journal of Applied Physiology*, 1966.

prone position, which is represented by a steeper slope in Figure 4.1. This can be explained by the chest wall shape.[213]

A prospective study was conducted between February 2021 and April 2022 at BioMaps on a cohort of twenty-five healthy and asymptomatic volunteers. Pr Vincent Lebon is the principal investigator of this study. We acquired data with Adrien Duwat, Killian Sambourg, Antoine Beurnier, Claire Pellot-Barakat, Angéline Nemeth, and Xavier Maître. The objective of the study was to evaluate the sensitivity of 3D MR spirometry to gravity lung dependence. Volunteers were instructed to breathe spontaneously while undergoing dynamic lung MRI acquisitions in the supine and prone positions. The local ethics committee approved the research protocol. Each volunteer underwent a comprehensive information session on the study protocol, followed by enrolment by the investigators, and provided informed consent.

The protocol was performed on a 3 T GE Signa PET/MR (GE Healthcare) with an Ultra-Short Echo Time (UTE) sequence with an adaptive Koosh ball AZTEK trajectory (speed = 31, twist = 4, shuffle = 2), described previously in section A.. A 30-channel thoracic coil array was used for signal reception. The main acquisition parameters were a TE (echo time) of 14 µs, a TR (repetition time) of 2 ms, a flip angle of 3 °, a bandwidth of +/-100 kHz, and a voxel size of 1.5 mm isotropic, as in Table 3.1. The field of view was adjusted to accommodate individual morphologies, resulting in variable acquisition times ranging from 8 to 12 minutes for a complete dynamic dataset.

Thirty asymptomatic and healthy volunteers were enlisted to participate in the study. Unfortunately, one participant could not undergo the MR exam due to claustrophobia, three datasets were acquired with incorrect parameters, and one

[213] Merryn H. Tawhai et al. *Journal of Applied Physiology (Bethesda, Md.: 1985)*, 2009.

Description of the population	Healthy volunteers (n=25)
Age (y)	
Mean ± standard deviation	44 ± 17
Median ± inter-quartile range	43 ± 29
Range	20 – 75
Sex	
Female	10
Male	15
Weight (kg)	
Mean ± standard deviation	70 ± 11
Median ± inter-quartile range	72 ± 13
Range	54 – 102
Height (cm)	
Mean ± standard deviation	171 ± 9
Median ± inter-quartile range	171 ± 16
Range	156 – 185

Table 4.1: Main physiological characteristics of the population included in the study: 25 asymptomatic healthy volunteers recruited between 2021 and 2022.

was lost during the export process. Consequently, the final cohort included twenty-five volunteers, consisting of 10 females and 15 males. As detailed in Table 4.1, the main physiological characteristics of the population exhibited a diverse distribution, encompassing ages from 18 to 75 years and body mass indexes ranging between 20 kg/m^2 and 31 kg/m^2.

4.1.2 3D MR spirometry sensitivity to gravity lung dependence

As presented in Chapter B., local ventilatory volumes were inferred from the determinant of the Jacobian matrix of the strain tensor and temporally derived to compute local flows. Absolute measurements of local flow-volume loops were thus produced as 3D+t parametric maps, defined in Chapter A.. Relying on the literature of free-breathing standard spirometry, we focused on three biomarkers evaluated here for every voxel throughout the lung: [169,214]

- the tidal volume (TV),
- the spontaneous peak expiratory flow (SPEF),
- the spontaneous expiratory flow at 25% of the tidal volume (SEF25).

We thus obtain an overall comparison of the effect of posture, and therefore of gravity, on ventilation. Moreover, the maximum anisotropy deformation index (ADI) was computed for every voxel to probe the non-isotropic nature of the pulmonary mechanics.[98]

By integrating the biomarkers over the lung volume, as if measured at the mouth, we can retrieve quantitative spirometric global parameters using MRI rather than a standard spirometer for the first time. The results are gathered in Table 4.2, demonstrating the global effect of posture and gravity on volumes, flows and anisotropy of the deformation. For free breathing, our measurements appear consistent with the literature. Particularly, a comparison of global tidal volumes (TV) reveals higher values in the prone position (436 ± 137 mL) compared to the supine position (380 ± 106 mL), as reported in Moreno *et al.* work.[215] The physiological community poorly understands the reason for higher ventilation parameters (TV, SPEF, SEF25) in the prone position. The higher anisotropy in

[169]K. H. Carlsen and K. C. Lødrup Carlsen. *The European respiratory journal*, 1994.
[214]K. C. Lødrup Carlsen et al. *The European Respiratory Journal*, 1994.
[98]Ryan Amelon et al. *Journal of Biomechanics*, 2011.
[215]Francisco Moreno and Harold A. Lyons. *Journal of Applied Physiology*, 1961.

Global lung function	Supine	Prone
TV (mL)		
Mean ± standard deviation	380 ± 106	436 ± 137
Median ± inter-quartile range	356 ± 130	423 ± 190
Range	251 – 727	209 – 816
SPEF (mL/s)		
Mean ± standard deviation	378 ± 124	386 ± 152
Median ± inter-quartile range	358 ± 128	373 ± 138
Range	219 – 925	204 – 1050
SEF25 (mL/s)		
Mean ± standard deviation	242 ± 55	256 ± 73
Median ± inter-quartile range	238 ± 65	247 ± 72
Range	155 – 378	170 – 486
ADI (x 10^4)		
Mean ± standard deviation	10.1 ± 3.7	11.1 ± 3.7
Median ± inter-quartile range	9.6 ± 3.0	10.7 ± 4.3
Range	5.0 – 23.1	4.1 – 19.5

Table 4.2: Parameters extracted from 3D MR spirometry integrated over the lung volume for twenty-five healthy volunteers (mean age, 45 years ± 17 [standard deviation]; 15 males) freely breathing in supine and prone positions: tidal volumes (TV), peak expiratory flows (SPEF), flows at the remaining 25% of expiratory volumes (SEF25), and anisotropic deformation index (ADI).

the prone position has not been previously reported and could be explained by the constraints of the rib cage promoting the superior-inferior axis for ventilation.

On a local scale, the effect of gravity is observed by a ventilation gradient, with greater flow rates and volumes in the direction of gravity. This is observed in Figure 4.2 (top), on a typical volunteer, where flow-volume loops seem bigger in the dependent lung. If we integrate the flow-volume loops on the anterior and posterior halves of the lung (Figure 4.2, bottom), the difference becomes explicit with higher values in the posterior region in the supine position and in the anterior region in the prone position.

Over the 25 volunteers, the gravity lung dependence is statistically significant

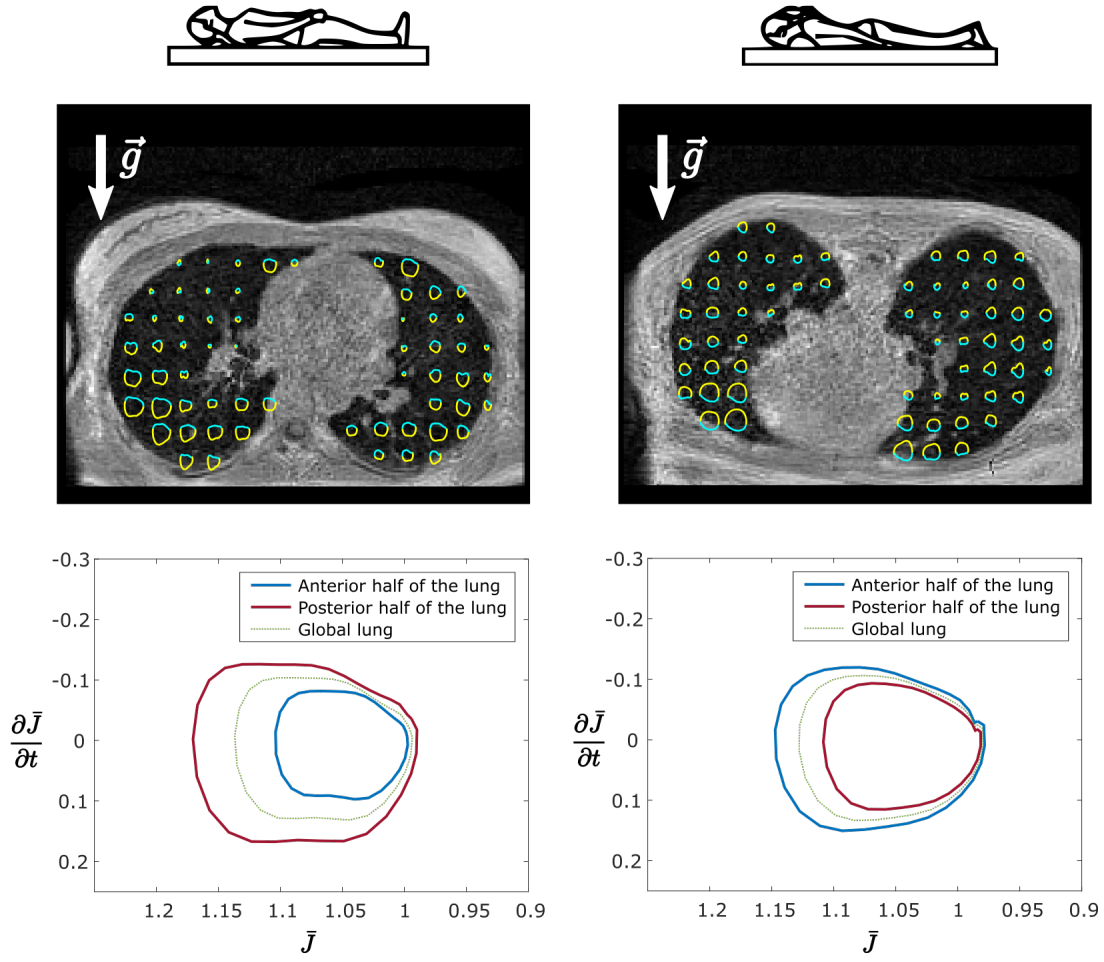

Figure 4.2: 3D MR spirometry in one healthy volunteer lying in the supine and prone positions. The top row shows axial maps of local clockwise flow-volume loops for one voxel out of 20 with inspiration (yellow) and expiration (cyan) phases. The area of flow-volume loops increases toward the more dependent region. The bottom row shows the average of spirometric loops (here, the temporal derivative of the Jacobian as a function of the Jacobian) on anterior and posterior volumes. The global spirometric loops over the lung are similar in supine or prone positions. However, when integrated over the anterior and posterior half regions, the spirometric loops largely differ between dependent and non-dependent regions, supporting the sensitivity to gravity of 3D MR spirometry.

when comparing the anterior and posterior halves of the lung for TV, SPEF, and SEF25 ($p < .001$, as determined by a paired Wilcoxon test). A significant difference is observed for ADI, with the posterior region consistently exhibiting higher values regardless of the supine or prone positions: ADI does not seem sensitive to gravity. However, anisotropy seems clearly affected by chest wall constraints.

TV, SPEF, and SEF25 appear more homogeneous in the prone position, with a lower coefficient of variations, that is, the ratio of standard deviation to the mean over the lobe volume (see mean and standard deviations reported in Table 4.2). Smaller volume and flow differences between the anterior and posterior regions (as shown in Figure 4.2 for one volunteer) are displayed. In the supine position, TV is 26.7 % higher in the posterior region than in the anterior region. In the prone position, it is 11.3 % higher in the anterior region than in the posterior region. Examining the impact on individual lungs, the right lung demonstrates a greater dependence on gravity effects in the supine position (36 % vs. 18 %). In comparison, the left lung exhibits greater dependence in the prone position (14 % vs. 9 %). This might be explained by the shape of the lung tissues for the prone positions and the nature of the right lung, which has intrinsically higher volumes than the left lung.

Finally, we evaluated variations of the spatial distribution between two successive acquisitions. After feature scaling, so the tidal volumes are globally equal between successive acquisitions, we found that TVs are significantly reduced in the most gravity-dependent region in the second repeated acquisition. Within a 15 mm thick peripheral layer, median variations of 4.4 % in supine and 3.9 % in prone were found ($p < .001$ using a paired Wilcoxon test). This might be caused by airways closing due to the weight of parenchymal tissues.

To compare this effect with the literature, the mean and standard deviations of local TVs per lung volume unit, are computed along the anteroposterior axis and

averaged for every 1.5 cm and every volunteer. Slopes of the tidal volumes per lung volume unit were computed for each position. This measurement is subject to bias because of the diversity of lung shapes across volunteers and the non-gaussian distribution of TV across slices. The usual computation of a linear slope does not respond to the non-linear curve we have obtained (Figure 4.3). However, these quantitative evaluations are commonly published results to asses gravity lung dependence in imaging techniques,[163,216,217] and are here provided for comparison.

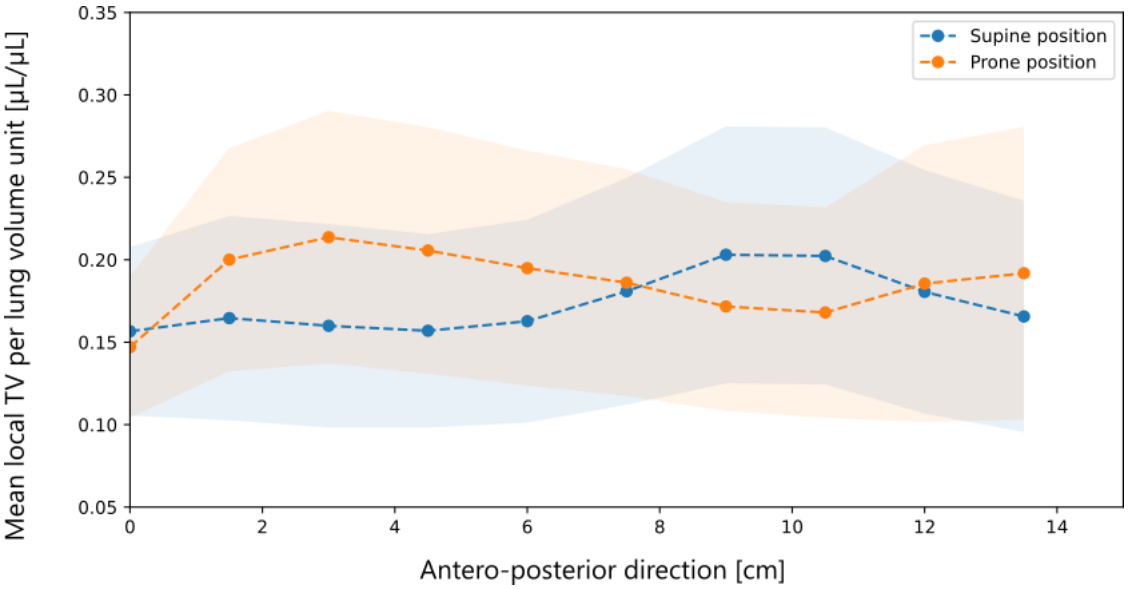

Figure 4.3: Averaged gravitational profiles of tidal volumes (TV) per unit lung volume for the 25 healthy volunteers in the supine and prone positions (98 datasets, 53 in supine and 45 in prone positions). Values in the graphs are means (dots) ± standard deviations (shadowed regions)

Slopes of tidal volumes per lung volume unit along the anteroposterior axis are 7.6×10^{-3} µL/cm/µL in the supine and -5.0×10^{-3} µL/cm/µL in the prone position. This highlights the inhomogeneity of lung ventilation, particularly in the supine position. These results are consistent with reported ventilation gradients, however, slightly lower.[216,218] Henderson *et al.*[217] reported gradients of 15×10^{-3} µL/cm/µL in the supine and 0.2×10^{-3} µL/cm/µL in the prone position.

[163] F. Klimeš et al. *NMR in Biomedicine*, 2019.
[216] Johan Petersson et al. *Respiratory Physiology & Neurobiology*, 2009.
[217] A. Cortney Henderson et al. *Journal of Applied Physiology (Bethesda, Md.: 1985)*, 2013.
[216] Johan Petersson et al. *Respiratory Physiology & Neurobiology*, 2009.
[218] Guido Musch et al. *Journal of Applied Physiology (Bethesda, Md.: 1985)*, 2002.
[217] A. Cortney Henderson et al. *Journal of Applied Physiology (Bethesda, Md.: 1985)*, 2013.

4.1.3 Pulmonary function intrinsic inhomogeneity

From the known effects of gravity (and those demonstrated above with 3D MR spirometry), there appears to be a spatial inhomogeneity intrinsic to ventilation in spontaneous breathing. Gravity, temporality, and individual body shapes are all known factors in these spatial variations.[13,16,219] Certain regions contribute to the most ventilation mechanics in free breathing. These inhomogeneities are visible on our functional maps for all our biomarkers in Figure 4.4. It is known that homogenization occurs when the lung is used to its maximum capacity in forced breathing: all regions are then involved much more evenly.[220] However, this type of breathing is not possible for everyone, reflects only the lung function in an extreme state, and is not capturable with 3D+t lung MRI as the usual acquisition time is too long.

[13]Boris I. Medarov et al. *International Journal of Clinical and Experimental Medicine*, 2008.
[16]J. Milic-Emili et al. *Journal of Applied Physiology*, 1966.
[219]Annalisa J. Swan et al. *Journal of Theoretical Biology*, 2012.
[220]Hooman Hamedani et al. *The Journal of physiology*, 2021.

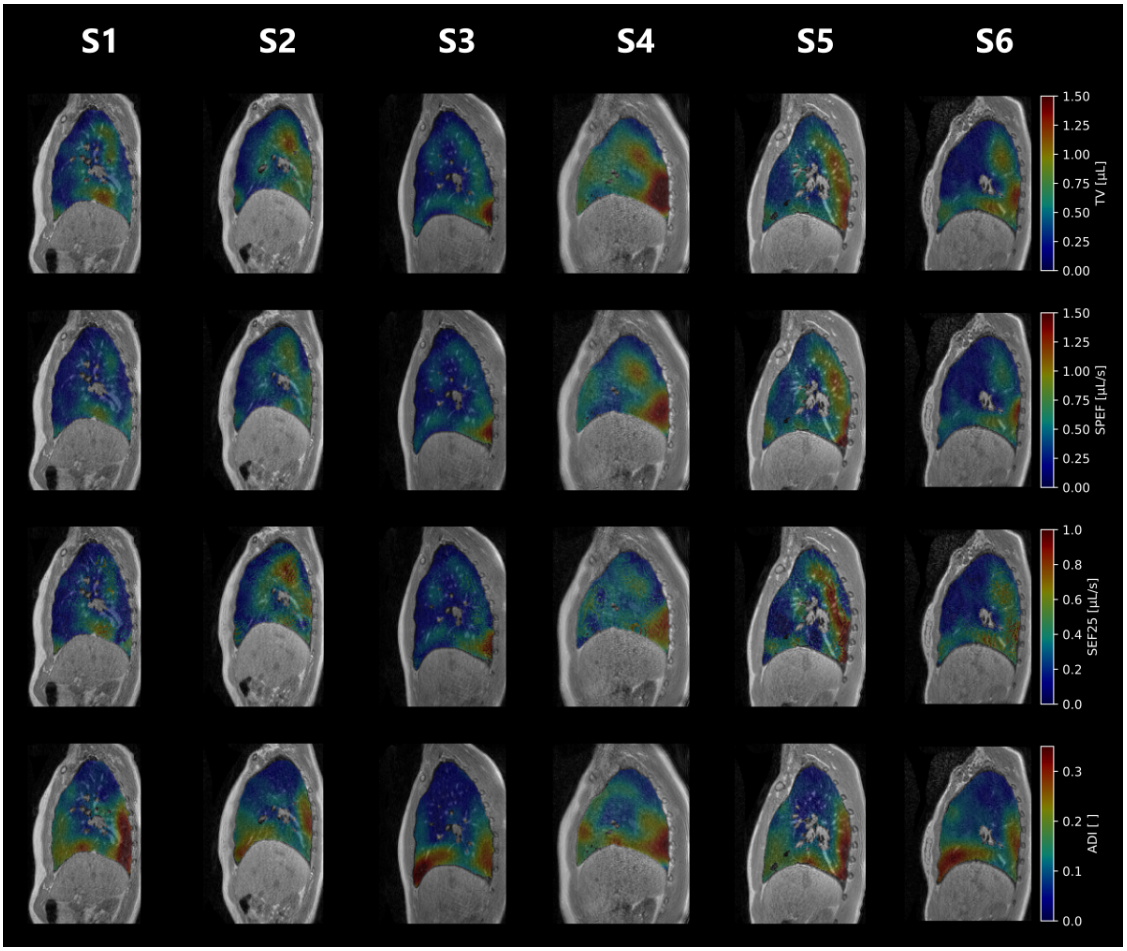

Figure 4.4: Functional 3D MR spirometry maps in 6 healthy volunteers breathing freely in the supine position for TV, SPEF, and SEF25. The anisotropic deformation index (ADI) is also provided for mechanical analysis of the deformation. Each column corresponds to a different healthy volunteer.

Ventilation inhomogeneity in free breathing is highlighted by 3D MR spirometry. However, in ongoing studies of free-breathing functional lung imaging, as presented in Chapter 2.3, the nominal spatial distribution of ventilation is not considered for ventilation defects mapping despite being subjected to gravity effects.[145] This could induce a bias, with commonly low-ventilated areas being depicted as defects, or a lack of sensitivity, with commonly highly-ventilated regions being depicted as healthy for lower ventilation patterns. For example, in the Kaireit *et al.* study, the ventilation defect maps of PREFUL-MRI have difficulties being sensitive to defected basal regions for the COPD patient (nominally highly venti-

[145] Andreas Voskrebenzev et al. *Radiology. Cardiothoracic Imaging*, 2022.

lated). At the same time, false positives are easily found in more apical regions (nominally low-ventilated).[146]

[146]Till F. Kaireit et al. *Journal of magnetic resonance imaging: JMRI*,. 2021.

4.2 3D MR spirometry atlases of the lung function

Gravity lung dependence demonstrates the need to consider nominal inhomogeneities in order to assess local ventilation. Besides, the subject's position could be imposed to reveal high-sensitivity ventilation impairments in the known nominally solicited segments. To explore the spatial distribution of ventilation, we applied normalization strategies to partly tackle the intrinsic variability of free breathing, the diversity of volunteers' morphologies, and their corresponding pulmonary capacities. Atlases of lung nominal ventilation could then be constructed.

4.2.1 Normalizations

Understanding nominal patterns for detecting functional anomalies transcends imaging modalities or applications. Brain functional MRI occupies a major place in the MR research community, offering avenues of innovative methods we could transpose to pulmonary functional MRI.[221] The main challenge for both brain and lung functional MRI is obtaining a common reference frame to map the function. For that purpose, a morphological normalization was implemented (to match similar anatomical regions) together with a feature normalization (to match the histogram scale), establishing common grounds for parametric maps comparisons.

A. Morphologies

The morphological normalization was performed using elastic registration (with affine and B-spline transforms) to match the volunteers' lungs to the lungs of a chosen reference dataset. The reference with the most anatomical details, with distal airways and vessels, was chosen (see Appendix). This registration approach on a

[221] Gary H. Glover. *Neurosurgery Clinics*, 2011.

reference image is common in most functional MRI analyses [222, 223, 224]. Figure 4.5 illustrates the registration efficiency on spatially normalized maps of tidal volumes for six out of 25 healthy volunteers.

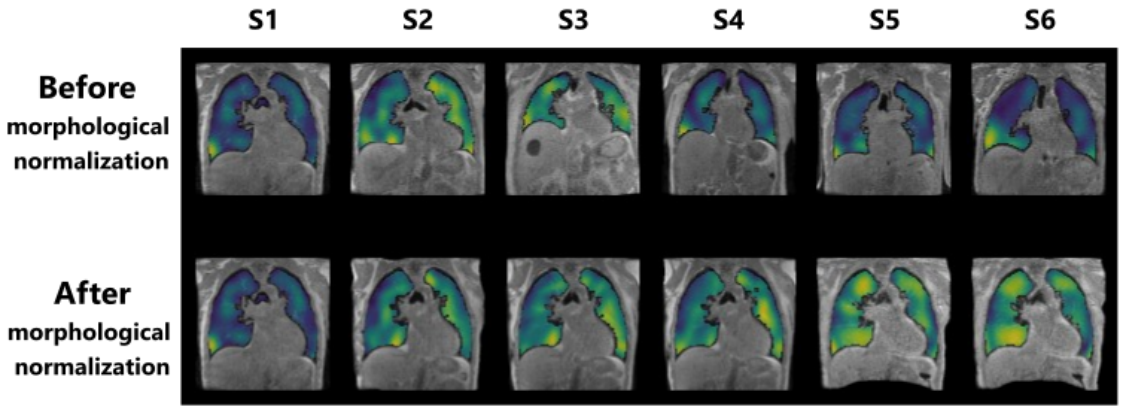

Figure 4.5: TV maps overlayed on the corresponding MR magnitude images of 6 healthy volunteers: before any normalization approach (top), and after morphological normalization with an elastic registration on the reference dataset (bottom).

A common drawback of registration is the strong assumption of identical landmarks and morphologies across volunteers or patients, which introduces a bias as there is a great variety of anatomies. Moreover, registration involves image interpolations, which might induce information loss. The pulmonary structures (lobes and segments) should be segmented to compare similar anatomical regions. This approach would be physiologically fairer while losing voxel-wise quantification. Only healthy volunteers are studied in this chapter, making the assumption of differences due to morphology stronger than those due to functional alterations.

B. Global ventilation

As demonstrated in the previous Chapter 3, intrinsic and multifactorial variability in free-breathing is an inherent limit to the repeatability and reproducibility of 3D spirometry measurements. Normalization of global values partly tackles this

[222] K. J. Friston and W. Penny. *NeuroImage*, 2003.
[223] Karl. J. Friston et al. *Human Brain Mapping*, 1995.
[224] K. J. Friston. *SPM - Statistical Parametric Mapping.*

issue, as already found in Voskrebenzev *et al.* [207] Apart from this individual variability, there are differences between individuals' pulmonary capacities, which are mainly determined by differences in height, age, and sex.[28] After spatial normalization, each parametric histogram was globally normalized to the reference dataset with feature scaling to tackle the global ventilation variability. More specifically, each parameter p_i was locally rescaled for every voxel i upon the parameter total value (i.e. summed over the lung volume) and the total value of the reference dataset: $p_i = p_i \times \frac{\sum p_i}{\sum p_{\text{ref}}}$. Figure 4.6 shows the effect of scaling on TV histograms corresponding to the maps of the 6 healthy volunteers in Figure 4.5.

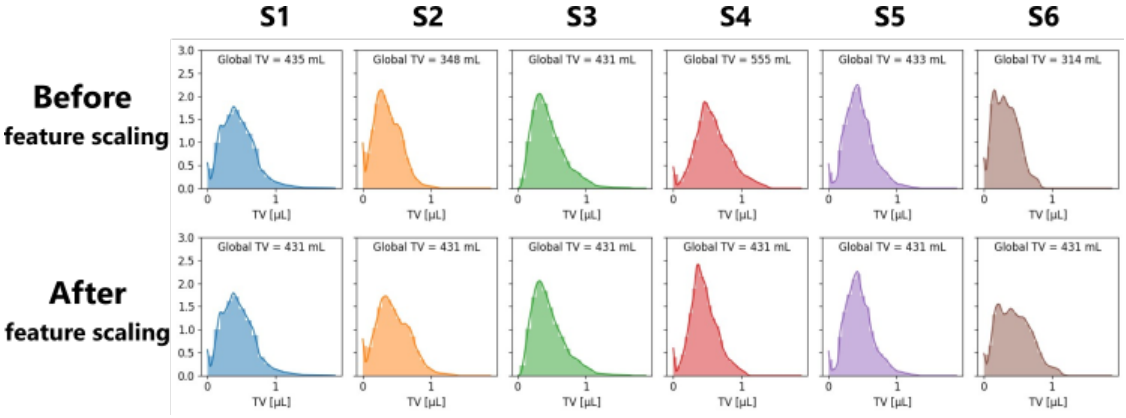

Figure 4.6: Histograms of tidal volumes for 5 healthy volunteers (out of 25) after morphological normalization: before histogram rescaling (top), after rescaling on global values (bottom) such that the resulting total TV, as it would be measured at the volunteer's mouth, equals the reference volunteer's value (431 mL).

After spatial and feature normalizations, the number of measurements for each equals the number of voxels of the reference volunteer, and the resulting global parameters, integrated over the lung, amount to the reference volunteer's values such that individual respiratory patterns can be compared.

The Bland-Altman analysis of local TV presented in Figure 4.6 demonstrates the efficiency of the normalization to improve the local reproducibility with median variations of local TV decreasing from 17.6 % to 15.3 %. The 95 % confidence interval varies from [-0.25 µL, 0.33 µL] (median: 0.37 µL) before normalization,

[207] Andreas Voskrebenzev et al. *Magnetic Resonance in Medicine*, 2016.
[28] Cole Bowerman et al. *American Journal of Respiratory and Critical Care Medicine*, 2023.

to [-0.26 µL, 0.26 µL] (median: 0.44 µL) after normalization. Notice the median values are higher after rescaling despite narrowing the interquartile range.

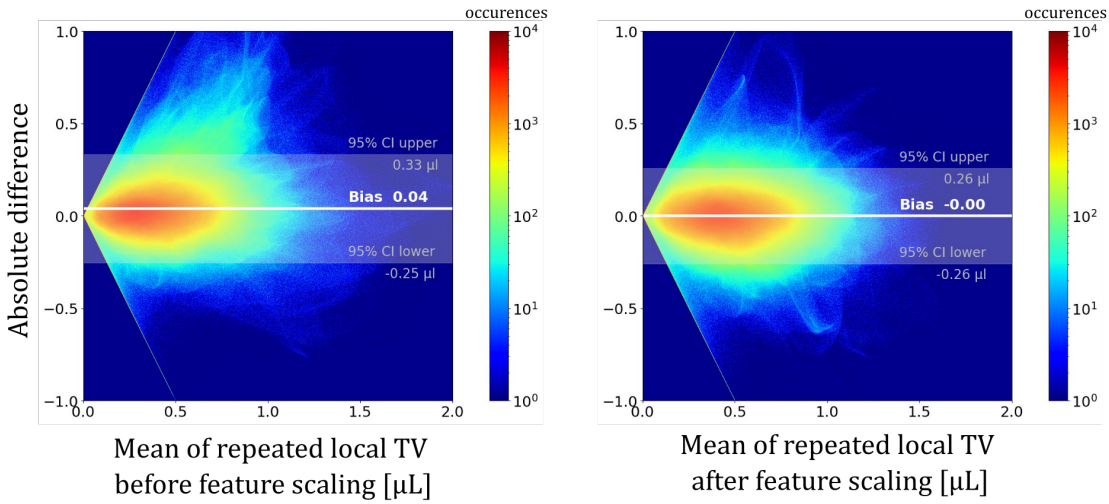

Figure 4.7: Bland-Altman graphs for local tidal volumes over the 25 healthy volunteers after spatial normalization and before and after feature scaling. After rescaling, the local repeatability is enhanced with a 95% confidence interval of [-0.26 µL, 0.26 µL].

The normalization of histograms thus allows better repeatability and reproducibility of the technique while guaranteeing the preservation of the distribution of ventilatory patterns as observed in Figure 4.5. However, this approach downplays the interest in 3D MR spirometry absolute quantitation.

4.2.2 Atlases definition

Once normalized, a nominal reference of lung function mapping are built, i.e. a set of atlases for 3D MRI spirometry parameters. To do this, different parameter-distance measurements are evaluated, of which the barycenter represents a nominal ventilation parameter representation. They can thus provide a reference for comparison, enabling clinicians to assess individual patient deviations from the defined norm. The Euclidean and Sinkhorn distances were explored for this purpose, providing different comparative representations.

A. Euclidean barycenters

Using the Euclidean mean of 3D MR spirometric maps allows for creating a reference for healthy patterns while being a familiar and straightforward metric. The barycenter is computed as the mean in each lung voxel across all the volunteers and their corresponding acquisitions. As maps have been formerly normalized, no bias is expected. The use of the Euclidean barycenter can be justified only if the distributions in each voxel along the volunteers follow a Gaussian law. This is verified by a quantile-quantile analysis shown in Figure 4.8, where theoretical quantiles of a Gaussian distribution are plotted against experimental quantiles.

The Euclidean barycenter is computed in every voxel of functional maps along the 25 volunteers as shown in Figure 4.9. As this barycenter represents the average ventilation across the cohort, it exhibits smoother spatial patterns than individual maps.

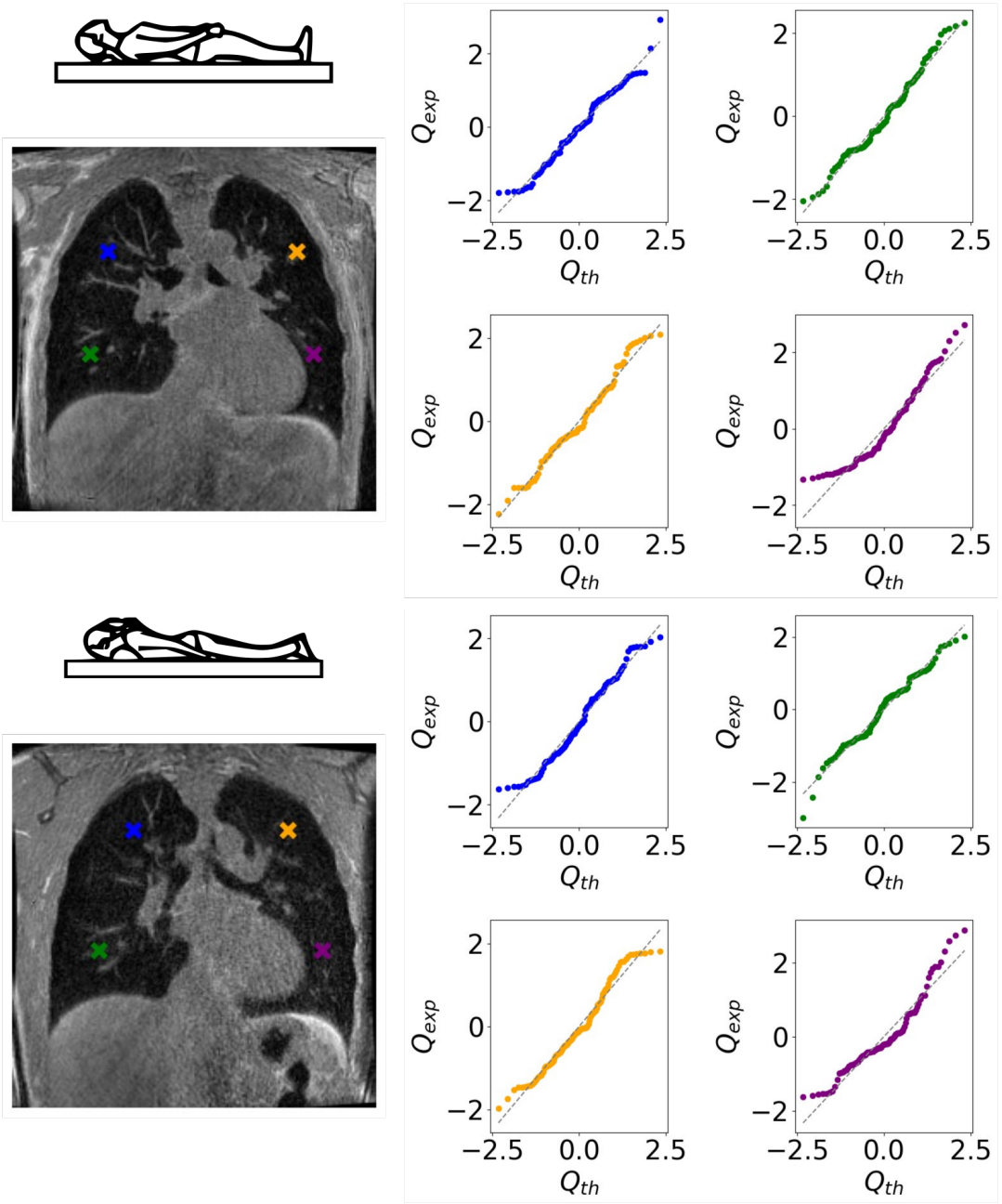

Figure 4.8: QQ-plots (quantile-quantile plots) of normalized tidal volume maps in four voxels of interest to evaluate the Gaussian distribution along the 25 healthy volunteers. The experimental quantiles are plotted against theoretical quantiles, which should be linear for a Gaussian distribution. Data seem to follow a normal distribution law.

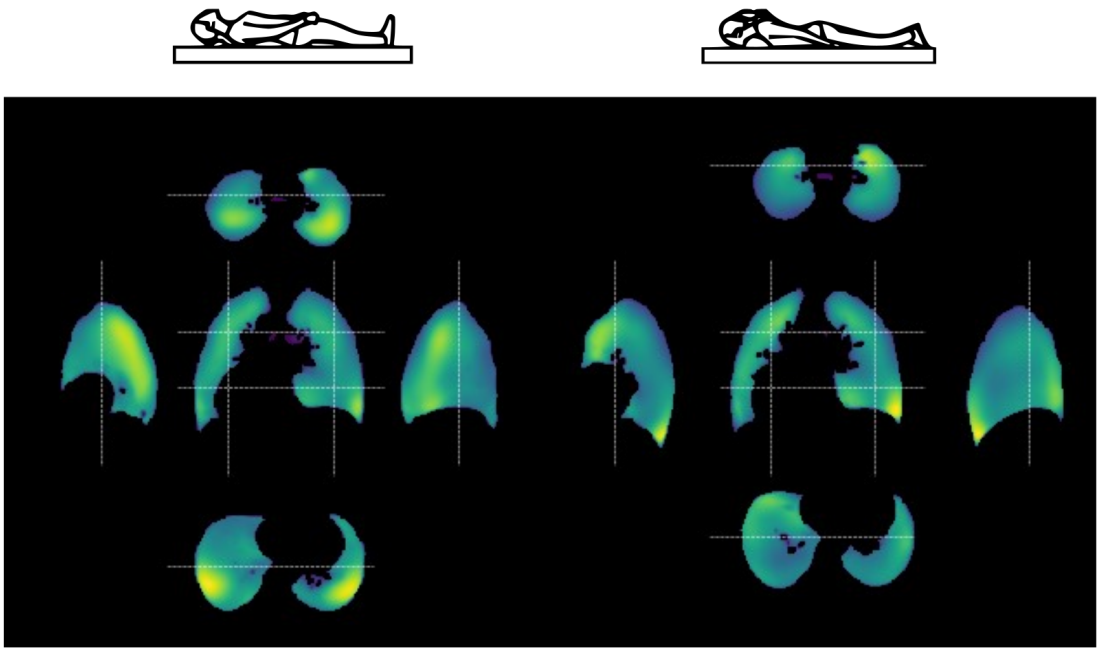

Figure 4.9: Exploded view of Euclidean barycenters of tidal volumes for supine and prone positions. The atlas has been built over 101 datasets acquired on 25 healthy volunteers with repeated acquisitions (54 datasets in the supine and 47 in the prone positions). White dash lines indicate the positions of the central coronal view, side right and left sagittal views, and apical and basal axial views.

B. Sinkhorn barycenters

Another statistical approach for computing representative atlases of lung ventilation parameters entails not representing the average of ventilation maps but a probabilistic representation of a ventilation map for a mean healthy volunteer. The rationale behind using the Sinkhorn barycenter in functional lung MRI is its ability to give this significant average under the Wasserstein distance metric [225] with a regularization term. The Wasserstein distance metric is a distance function defined between probability distributions. The use of a regularization term enhances convergence speed and improves robustness to noise. The Sinkhorn metric considers the spatial consistency of ventilation distributions.[226] Consequently, it produces precise and sharp patterns on templates. While the Sinkhorn barycenters lead to less smooth atlases, they preserve a more resolved spatial distribution of the functional patterns, potentially enabling access to lung segments.

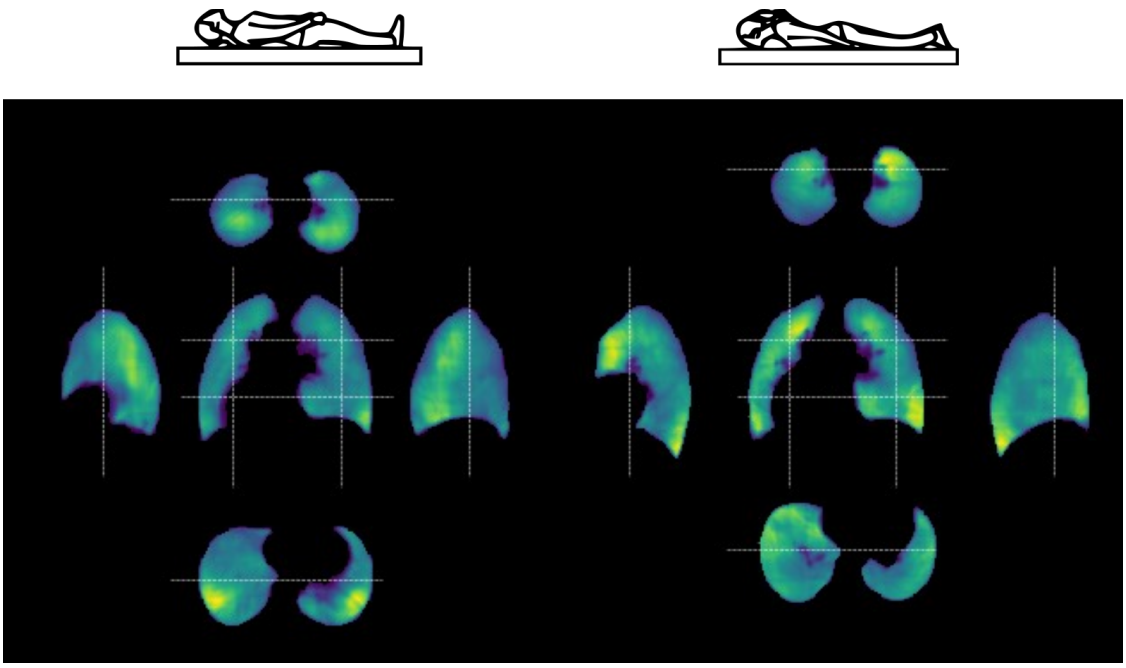

Figure 4.10: Sinkhorn atlases of tidal volume maps for supine and prone positions. White dash lines indicate the positions of the central coronal view, side right and left sagittal views, and apical and basal axial views.

[225] L. V. Kantorovich. *Management Science*, 1960.

[226] Ying Huang et al. *Medical image computing and computer-assisted intervention : MICCAI ... International Conference on Medical Image Computing and Computer-Assisted Intervention*, 2020.

The atlases require a large computational cost with a complexity in $n\log(n)$ and a large VRAM. For example, we produced the maps of Figure 4.10 in 20 minutes of calculation on GPU for images resolved by half (compared to a few milliseconds for the Euclidean barycenter). The total size of MRI images exceeds the limits of the machine (yet 24 Gb of VRAM). Although the Sinkhorn atlas preserves better ventilation patterns with sharper ventilation patterns than the Euclidean atlas. However, the memory limit combined with the computation time was a strong limit at the time. Future work should be carried out to explore the features of Sinkhorn barycenters, which could be of interest for the analysis of spatial distributions of ventilation. The following work is, however, based on the Euclidean atlases, as they have full resolution and would be better understood for analyses.

4.2.3 Relationships between parametric atlases

The atlases can be established for the different biomarkers of 3D MR spirometry. Four biomarkers were evaluated out of the twenty biomarkers that were computed and available in Appendix . The extent of the relationship between the computed biomarkers is evaluated to extract physiological information while avoiding redundancy. First, the Pearson correlation coefficients are computed between the main parametric atlases TV, SPEF, SEF25, and ADI (Figure 4.11). They assess the linear relationship between X and Y, two vectors of the same length, from the equation:

$$\rho = \frac{\sum (x_i - \bar{X})(y_i - \bar{Y})}{\sqrt{\sum (x_i - \bar{X})^2 \sum (y_i - \bar{Y})^2}} \tag{4.1}$$

Where x_i and y_i are the individual data points from each vector, $\bar{X}$ and $\bar{Y}$ are the means of each variable.

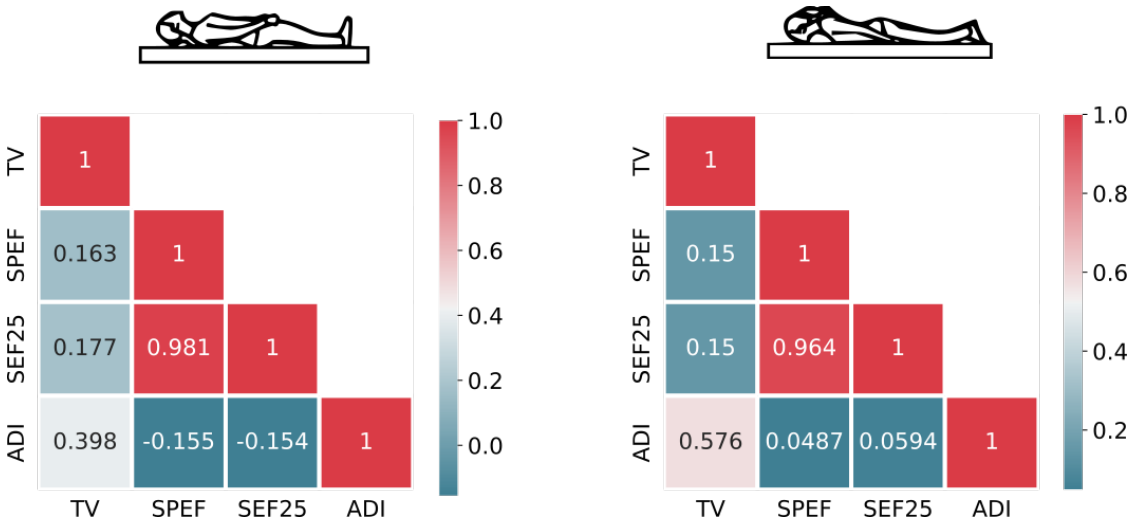

Figure 4.11: Heatmaps of Pearson correlation coefficients between four 3D MR spirometry biomarkers evaluated in this study in the supine (left) and prone (right) positions: TV, SPEF, SEF25, ADI.

Flows (SPEF and SEF25) and volumes (TV) are weakly correlated to each other in both supine and prone positions (0.17 and 0.15), whereas their correlation with ADI is drops down to near zero in the prone position. Maps of deformation

anisotropy display distinct patterns from other biomarkers and exhibit the weakest correlation with SPEF and SEF25 while being moderately correlated to TV for both positions. Flows might depict original information compared to the TV and ADI. SPEF and SEF25 are highly correlated for both positions (0.98 and 0.96), which might be a nominal behavior in a healthy cohort. Anisotropy increases with higher inhaled volumes as it might induce greater constraints to pulmonary structures.

The correlations do not imply a causal relationship between the biomarkers. Mutual information is thus computed to assess further the dependencies between the parameters (Figure 4.12). Mutual information is a quantity that measures a relationship between two random variables, specifically the amount of shared information. In other words, it quantifies how much knowing one variable reduces uncertainty about the other. Mathematically, for two discrete random variables X and Y, the mutual information (MI) is calculated as:

$$MI(X;Y) = \sum_{y \in Y} \sum_{x \in X} p(x,y) \log \left(\frac{p(x,y)}{p(x)p(y)} \right)$$

Where:

- $p(x,y)$ is the joint probability distribution function of X and Y.
- $p(x)$ and $p(y)$ are the marginal probability distribution functions of $\mathbf{X}$ and $\mathbf{Y}$, respectively.

Mutual information is widely used for tasks such as feature selection, dimensionality reduction, and measuring dependencies between variables.

The ADI seems to share much information with TV and lower with flow-based biomarkers. SPEF and SEF25 could lead to more diverse and physiological information from the dynamic of respiration. The prone position depicts higher entropy for each parametric map, which might be understood as maps with higher pattern complexity than in the prone position.

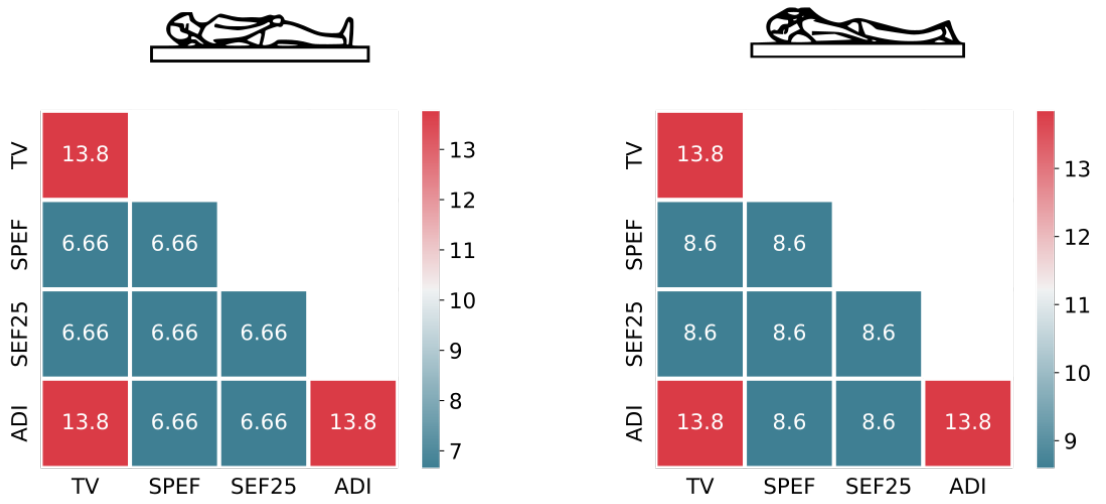

Figure 4.12: Heatmaps of mutual information of four 3D MR spirometry biomarkers evaluated in this study in the supine and prone positions: TV, SPEF, SEF25, and ADI.

These measurements performed on healthy volunteers give a first insight into nominal functional ventilation patterns locally and globally. However, this calculation should be performed on a cohort of patients for each disease, as it is unknown where physiological information could lie. Feature selection would then make it possible to model and grade disease severity.

4.3 Nominal patterns from 3D MR spirometry atlases

As shown in the previous section, atlases of healthy lung maps present nominal inhomogeneity throughout the lung with clear ventilation patterns. From the atlases, nominal patterns of ventilatory function can thus be assessed. This section first evaluates the reproducibility of the spatial patterns among the cohort of healthy volunteers, then shows histograms and spatial distributions of each parametric map.

4.3.1 Inter-subject reproducibility of ventilatory patterns

The atlas functional maps exhibit inhomogeneity across the lung volume, displaying coefficients of variations of 30 % for TV, 27 % for SPEF, 28 % for SEF25, and 34 % for ADI in the supine position (see top row of Figure 4.13). The mean normalized maps for 25 healthy volunteers reveal consistent ventilation patterns, whether lying supine or prone, during free breathing (see Appendix). for better visualization of patterns). The reproducibility of these patterns is evaluated through the corresponding maps of local standard deviation (see Figure 4.13, bottom). The Table 4.3 reports reproducibility statistics computed over these maps: mean and standard deviation for each map, and median of local CVs. The reproducibility is demonstrated through moderate local coefficients of variation across volunteers and acquisitions (median voxel-wise CVs in supine and prone positions: 38 % for TV, 35 % for SPEF, 42 % for SEF25, 34 % for ADI).

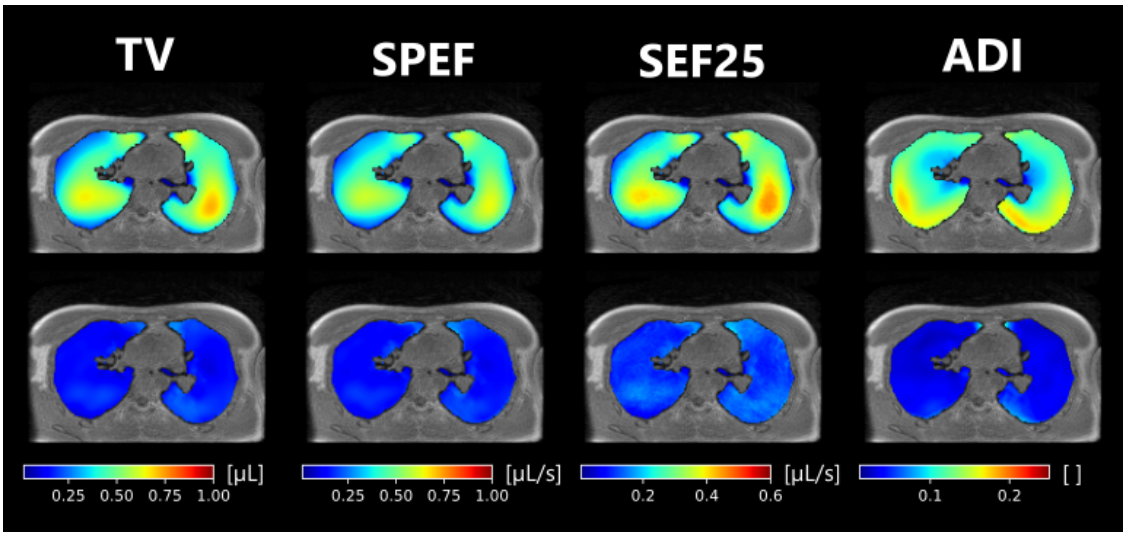

Figure 4.13: Axial views of voxel-wise means (top) and voxel-wise standard deviations (bottom) computed along the normalized maps from 25 healthy volunteers freely breathing in the supine position. The functional maps correspond to the four biomarkers of the study: TV, SPEF, SEF25, and ADI. The standard deviation low values demonstrate the reproducibility of the ventilation patterns over the 25 healthy volunteers revealed by the inhomogeneous mean maps.

	Supine position	Prone position
TV		
Local means (mean ± std)	0.45 ± 0.15	0.46 ± 0.14
Local standard deviation (mean ± std)	0.18 ± 0.06	0.17 ± 0.07
Median local CVs	0.39	0.35
SPEF		
Local means (mean ± std)	0.40 ± 0.15	0.38 ± 0.13
Local standard deviation (mean ± std)	0.18 ± 0.06	0.16 ± 0.06
Median local CVs	0.41	0.38
SEF25		
Local means (mean ± std)	0.27 ± 0.10	0.27 ± 0.09
Local standard deviation (mean ± std)	0.14 ± 0.04	0.13 ± 0.05
Median local CVs	0.49	0.44
ADI		
Local means (mean ± std)	0.13 ± 0.05	0.15 ± 0.05
Local standard deviation (mean ± std)	0.05 ± 0.02	0.05 ± 0.02
Median local CVs	0.34	0.31

Table 4.3: Table of reproducibility measurements of 3D MR spirometry biomarkers: TV, SPEF, SEF25, and ADI. For each biomarker the local means and standard deviations are assessed through mean and standard deviation. The median of the local coefficient of variations is also computed. Measurements in the prone position are more reproducible than in the supine position.

4.3.2 Spatial distribution of biomarkers

The patterns of the nominal ventilatory function can be observed in exploded views of the lung volume, such as in Figure 4.14 for TV in supine and prone positions and in Figure 4.15 for ADI. Similar views are given in the Appendix for the four biomarkers (TV, SPEF, SEF25, and ADI) and both supine and prone positions.

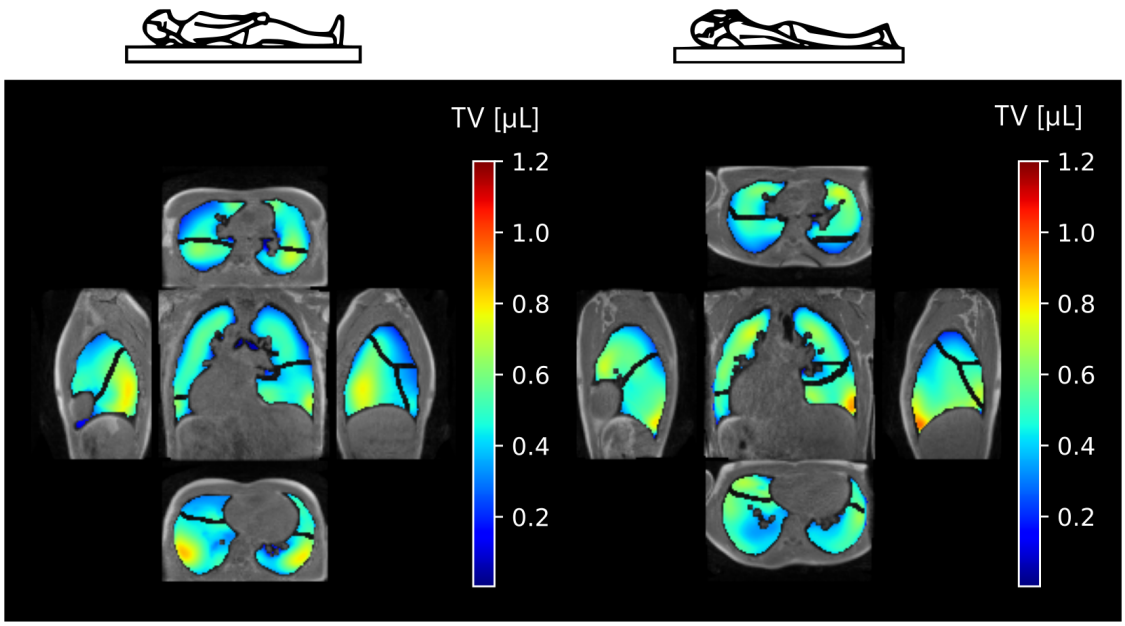

Figure 4.14: Exploded views of the tidal volumes atlas for supine and prone positions. The atlases were established using the Euclidean barycenter over acquisitions of 25 healthy volunteers freely breathing. Lung lobes are delineated with dark lines inside the parenchymal tissues. Higher ventilation is found in the more gravity-dependent region and inferior region. TV appears more homogeneous in the prone position than in the supine position.

Higher ventilation is found in the more dependent lung, that is, the posterior region in the supine position and the anterior and apical regions when in the prone position (see Figure 4.14). Higher ventilation is also found near the diaphragm and more predominantly at the junction with the rib cage. The left lung depicts more homogeneous ventilation for both positions, which might be explained by the lung shape constrained by the mediastinum and the presence of two lobes

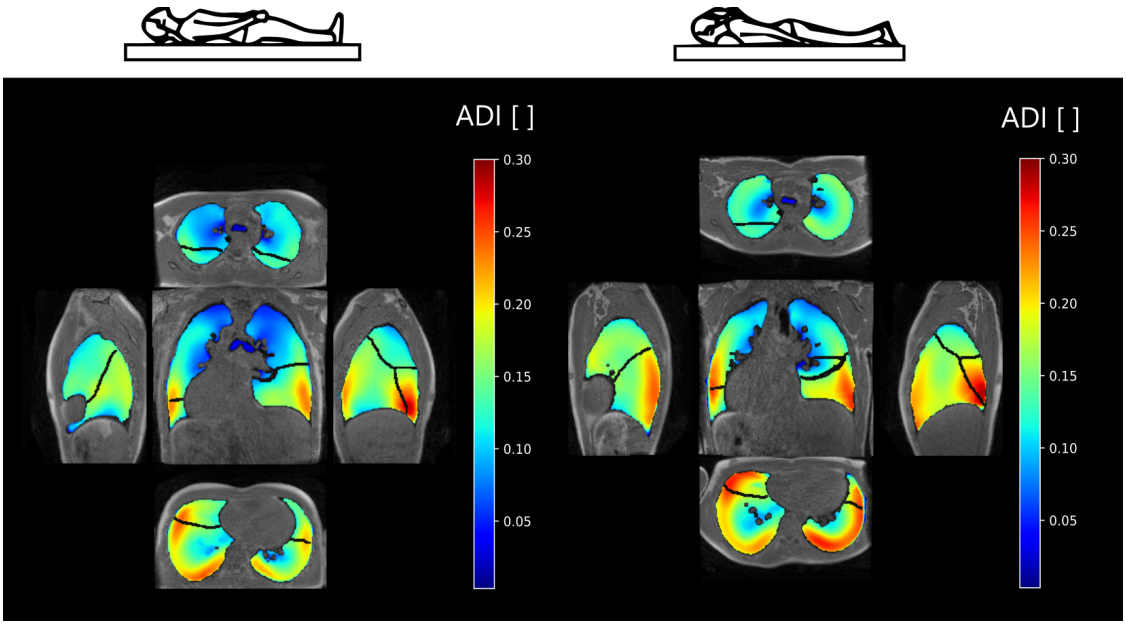

Figure 4.15: Exploded views of the ADI atlas for supine and prone positions. The atlases were established using the Euclidean barycenter over acquisitions of 25 healthy volunteers freely breathing. Lung lobes are delineated with dark lines inside the parenchymal tissues. Higher anisotropy is found near the rib cage for both supine and prone positions, where the parenchymal tissues are the most constrained by structures.

compared to the three lobes in the right lung. Ventilation seems thus predominantly influenced by lung position in relation to gravity, constraints of the chest wall, and primary respiratory muscles.

SPEF and SEF25 depict similar patterns to TV (see the Appendix). ADI, however, appears rather insensitive to the gravity effects induced by the different lying positions. Higher anisotropy is found near the posterior region for both supine and prone positions, which might be directly induced by lung morphology and respiratory muscle activity. Elevated ADI values in basal regions are attributed to diaphragmatic action, which predominantly operates in the superior-inferior direction.

Table 4.4 and Table 4.5 summarize the contribution of each lung lobe to the overall ventilation. The global contribution represents the percentage of total ventilation attributed to each lobe, reflecting the actual ventilation distribution. Relative contributions adjust global contribution to the end-of-expiratory volume of each lobe, providing a normalized perspective on ventilation contribution. The

coefficient of variation is computed as the ratio of standard deviation to the mean over the lung volume.

Global and relative contributions are provided together with the coefficient of variation. This coefficient of variation can be interpreted as an inhomogeneity score to quantify the variability of measures within each lobe. Collectively, these metrics offer a comprehensive view of the lung's ventilation efficiency and distribution patterns, which are critical for understanding pulmonary function.

The contributions are inhomogeneous, with lower ventilation for the middle right lobe and higher ventilation for the inferior lung lobes. The prone position depicts more homogeneous contributions than the supine position. As larger contributions come from the anatomically larger lobes, once TV is normalized to the lobar functional residual volume, the normalized ventilation appears more homogeneous. Higher anisotropy is found in the inferior lobes closer to the rib cage.

During free breathing, spatial variations of ventilatory patterns are mainly driven by the diaphragm along the superior-inferior direction and induced by gravity along the anterior-superior direction while the subject is lying supine or prone. Positioning the subject could be strategically employed to better reveal ventilation abnormalities in segmental regions that are typically targeted.

Supine position	LS lobe	LI lobe	RS lobe	RM lobe	RI lobe
TV					
Global contribution (%)	22	22	15	6.7	33
Relative contribution (%)	20	20	17	16	23
Coefficient of variation (%)	36	48	39	27	33
SPEF					
Global contribution (%)	22	22	16	7.1	33
Relative contribution (%)	20	19	17	17	23
Coefficient of variation (%)	40	53	41	31	36
SEF25					
Global contribution (%)	23	22	16	6.9	32
Relative contribution (%)	21	19	17	17	23
Coefficient of variation (%)	41	54	42	33	37
ADI					
Global contribution (%)	18	23	13	10	35
Relative contribution (%)	16	21	14	25	25
Coefficient of variation (%)	38	43	38	37	32

Table 4.4: Quantitative analysis of ventilation in the supine position for each lung lobe: left superior (LS), left inferior (LI), right superior (RS), right middle (RM), right inferior (RI). This table summarizes the lobar integral measurements inferred from the 3D MR spirometry atlases. For each functional map (TV, SPEF, SEF25, ADI), the atlas was computed as the Euclidean barycenter over 25 healthy volunteers normalized maps. Global and relative contributions are provided together with the coefficient of variation. This coefficient of variation can be interpreted as an inhomogeneity score to quantify the variability of measures within each lobe. In supine, strong differences in ventilation are reported, with higher ventilation from the inferior right lobe. Higher anisotropy is found in the posterior region constrained by the rib cage.

Prone position	LS lobe	LI lobe	RS lobe	RM lobe	RI lobe
TV					
Global contribution (%)	20	22	13	7.1	34
Relative contribution (%)	19	20	17	20	20
Coefficient of variation (%)	43	37	42	35	36
SPEF					
Global contribution (%)	20	23	13	7.0	35
Relative contribution (%)	19	20	17	20	21
Coefficient of variation (%)	43	40	42	38	36
SEF25					
Global contribution (%)	20	23	13	7.0	34
Relative contribution (%)	19	20	17	20	21
Coefficient of variation (%)	45	39	44	38	36
ADI					
Global contribution (%)	17	26	11	7.8	35
Relative contribution (%)	16	22	13	22	21
Coefficient of variation (%)	44	37	39	38	35

Table 4.5: Quantitative analysis of ventilation in the prone position for each lung lobe: left superior (LS), left inferior (LI), right superior (RS), right middle (RM), right inferior (RI). This table summarizes the lobular measurements performed on 3D MR spirometry atlases. For each functional map (TV, SPEF, SEF25, ADI), the atlas was computed as the Euclidean barycenter over 25 healthy volunteers normalized maps. Global and relative contributions are provided together with the coefficient of variation. This coefficient of variation can be interpreted as an inhomogeneity score to quantify the variability of measures within each lobe. In the prone, ventilation patterns seem more homogeneous over the lung than in the supine position (4.4), with very similar relative contributions for each lobe.

4.3.3 Histogram distribution in healthy lungs

The distribution of the functional parameters is also assessed in terms of the distribution of value occurrences over the lung, that is, through histograms of the functional maps. Figure 4.16 displays the distributions for TV, SPEF, SEF25, and ADI for the supine and prone positions. The histograms (blue lines) are presented with fitted Gaussian curves (red dashed lines). Although an assumption of normality could be used as a first intention, we can see that this is not completely the case. Specifically, most biomarkers have a lower standard deviation than their associated Gaussian fit (except ADI), and some have an asymmetric curve (mainly ADI).

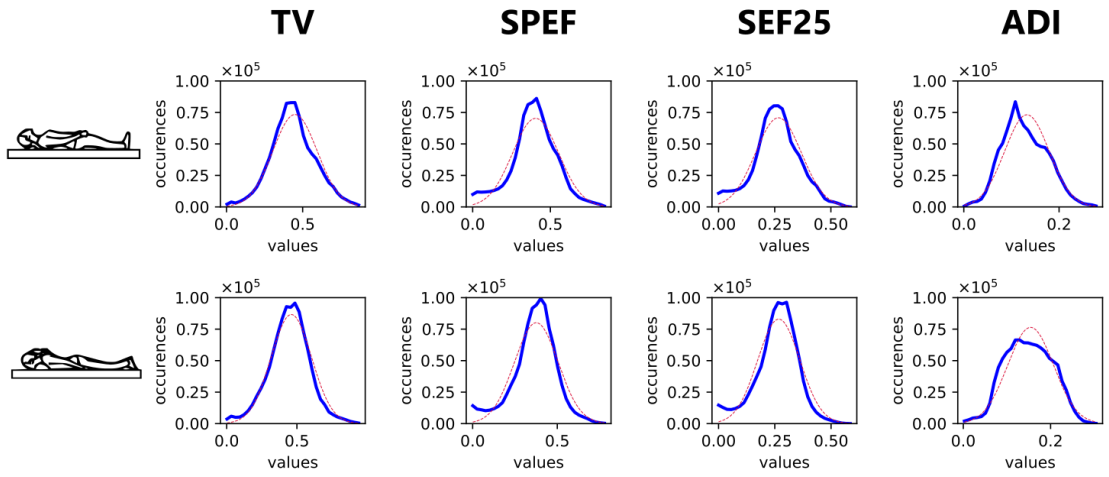

Figure 4.16: Histograms of 3D MR spirometry atlases for lying supine (top) and prone positions (bottom). Distributions of occurrences are plotted for functional maps (TV, SPEF, SEF25, ADI). The blue lines represent the observed distributions for each biomarker, while the dashed red lines indicate the corresponding Gaussian fits. The difference between experimental histograms and their Gaussian fits suggests further research for lung function modeling and using non-parametric tools for ventilation defect binning based on such histograms.

Other distribution models could be explored, such as log-normal distributions, which show a similar dissymmetry as the histograms shown in Figure 4.16 ,[220,227] or a mixture of normal distributions. The observed patterns justify the use of ventilation binning of the Box-Cox transformation before linearly binning the histograms,[228]

[220] Hooman Hamedani et al. *The Journal of physiology*, 2021.
[227] J. P. Whiteley et al. *Journal of Theoretical Biology*, 1998.
[228] Mu He et al. *Academic radiology*, 2020.

or employing non-parametric methods such as k-means clustering, as evocated in a previous Chapter 2.3. Alternative modeling can uncover hidden indicators in data beyond standard assumptions, leading to a richer representation of complex behaviors. Better modeling is key to understanding intricate biological processes and variability, helping for pathological discrimination.

Ongoing work aims to compare 3D MR spirometry to standard spirometer measurements with standard spirometry exams (forced breathing in a sitting position) and during the MR acquisition with an MR-compatible spirometer. The data is being acquired, but not yet available for analysis. Using the provided atlases and nominal measurements of the ventilatory function computed on the cohort of 25 healthy volunteers, it is interesting to investigate now the specificity of the features provided by 3D MR spirometry in patients to restrictive and obstructive syndromes.

5

Preliminary findings in obstructive and restrictive diseases

The methodology of 3D MR spirometry has been developed, and its reliability in exploring regional ventilation patterns has been established. In this chapter, we investigate the sensitivity of the method for obstructive and restrictive pathologies in a few case reports. Combining prior knowledge of standard spirometry biomarkers sensitive to obstructive or restrictive syndromes with the specific pathophysiology of each disease, 3D MR spirometry analysis protocols are proposed to characterize 1) neuromuscular diseases, 2) long-COVID-19 syndrome, and 3) asthmatic and COPD diseases.

5.1 Evaluation of 3D MR spirometry patterns in patients with neuromuscular dystrophia

The diaphragm is the primary respiratory muscle, and its dysfunction is a major prognostic factor, particularly in neuromuscular diseases. The Smart Imaging department of Ambroise Paré Hospital worked on a non-invasive exploration protocol to characterize the diaphragmatic function using MRI. Three-dimensional MR spirometry was included in the protocol. This research was carried out by Prof. Mostafa El Hajjam and was part of Dr Anass Chehboun's master's thesis.[229]

5.1.1 Design of the study

Current explorations of the diaphragmatic function commonly rely on standard spirometry but, as already pointed out in the first chapter 1, it lacks the desired sensitivity and specificity.[230,231] With the advent of new therapies, early diagnosis of muscle dysfunction is critical to managing symptoms and slowing disease

[229] Anass Chehboun and Mostafa El Hajjam. *IRM diaphragmatique : Séquences conventionnelles et spirométrie 3D à temps d'Echo Ultra-Court Evaluation chez les volontaires sains et les Dystrophies Neuro-Musculaires.* PhD thesis. APHP Ambroise Paré, 2023.

[230] Jeremy Hull et al. *Thorax*, 2012.

[231] Jonathan D. Finder et al. *American Journal of Respiratory and Critical Care Medicine*, 2004.

progression.[232,233] This study aims to assess a non-invasive diaphragm-specific exploration protocol using MRI.

A. Context of the protocol

Patients with neuromuscular diseases followed in the reference center Raymond Poincaré Hospital were included in Ambroise Paré Hospital for the protocol. The study aims to improve these patients' follow-ups through the exploration of new MRI protocols. Data were acquired with Laurence Delor, MRI electroradiology technician, Xavier Maître, and Anass Chebhoun, a junior radiologist under the supervision of Prof. Mostafa El Hajjam. Anass Chebhoun analyzed pulmonary functional tests (PFT) and additional clinical routine MR acquisitions.

B. Population

All subjects gave verbal consent, as respiratory MRI is non-invasive and routine in patient care. All healthy volunteers were staff members of the Smart Imaging Department of the Hospital Ambroise Paré. Ten participants were included in the study: 5 healthy volunteers and 5 patients with genetic muscle disorders without respiratory symptoms. The genetic muscle disorders covered in our study include one case of Duchenne muscular dystrophy, one case of Becker muscular dystrophy, and three cases of facioscapulohumeral muscular dystrophy (FSH). However, for the 3D MR spirometry exam, only one healthy volunteer, one patient from the Duchenne group, and one patient from the FSH group were included. Both patients exhibited normal PFT results but muscular damage to the girdles (pelvis and shoulders).

The practical implementation, management, and parametrization of the 3D UTE research sequence is complex. Four acquisitions performed on 3 included patients (one returning for a second examination) were unexploitable due to poor

[232] Dongsheng Duan et al. *Nature Reviews Disease Primers*, 2021.
[233] Kenji Rowel Q. Lim and Toshifumi Yokota. *Frontiers in Pharmacology*, 2021.

image quality. Finally, on the 3D MR spirometry analysis, one healthy volunteer, one patient with Duchenne dystrophy, and one patient with FSH dystrophy were included (Table 5.1).

Subject	Healthy	Duchenne	FSH
Sex	M	M	M
Age (year)	30	34	52
Height (cm)	178	176	182
Weight (kg)	85	81	81

Table 5.1: Main characteristics of the three subjects included in the protocol on neuromuscular dystrophia for whom the 3D MR spirometry data could be exploited.

C. MR protocol

The MR examination was performed on a 1.5 T MR scanner (Optima MR450W, GE Healthcare) with a thoracic coil (32 channels). The protocol comprised two clinical routine sequences and the 3D UTE research sequence for 3D MR spirometry. A Dixon sequence was utilized for morphological assessment, facilitating the measurement of diaphragmatic pillar thickness and quantification of intramuscular fat content. A FIESTA sequence enabled dynamic imaging of respiration, from which diaphragmatic displacement and deformation are evaluated. Finally, the 3D UTE sequence was implemented for the first time at 1.5 T to compute 3D MR spirometry functional maps. The same parameters and trajectory as the one described in Boucneau *et al.*[105] were used. The main parameters of the 3D UTE sequence were TE = 14 µs, TR = 2 ms, BW = ±100 kHz and α = 3°. The voxel size was 1.5 mm isotropic.

D. Biomarkers of the lung function

The parameters extracted by Dr Chehboun from clinical routine acquisitions assess lung elongation along the superior-inferior and anterior-posterior axes, as well

[105] Tanguy Boucneau et al. *Scientific Reports*, 2020.

as the deformation of the diaphragm between end-expiratory and end-inspiratory states (see Figure 5.1 and Figure 5.2):

- Craniocaudal diameters (DCC): they give the distance separating the pulmonary apex and the diaphragmatic apex
- Antero-posterior diameters (DAP): they give the distance that separates the vertical delimitations of the anterior and posterior pulmonary borders
- Diaphragmatic height (HD): it calculates the distance that separates the diaphragmatic apex from the line joining the costo-diaphragmatic angles
- Area under the curve (ASC): the surface area between the diaphragmatic apex and the line joining the costo-diaphragmatic angles
- Diaphragmatic angle (DA): it gives the angle between the diaphragmatic apex and each costo-diaphragmatic angle.

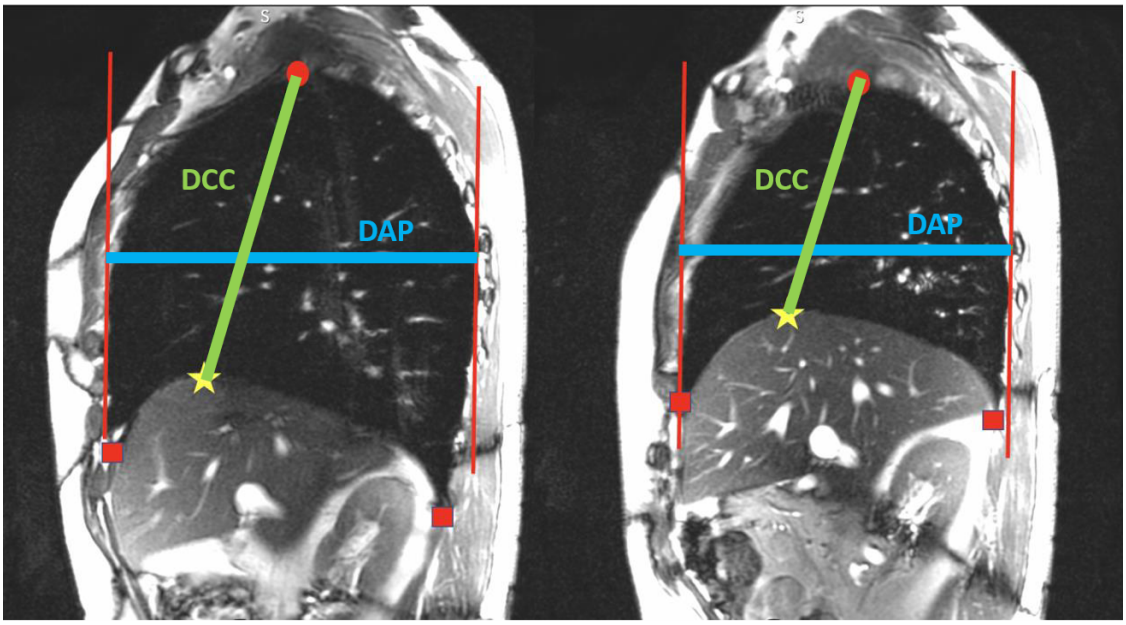

Figure 5.1: Pulmonary capacity parameters at the end of maximal inspiration (left) and deep expiration (right) are extracted in a sagittal view of a healthy volunteer in apnea at a certain breath-hold. Craniocaudal diameters are shown in green (DCC): they give the distance separating the pulmonary apex (red circles) and the diaphragmatic apex (yellow star). Antero-posterior diameters are shown in blue (DAP): they give the distance that separates the vertical delimitations of the anterior and posterior pulmonary borders (red lines).

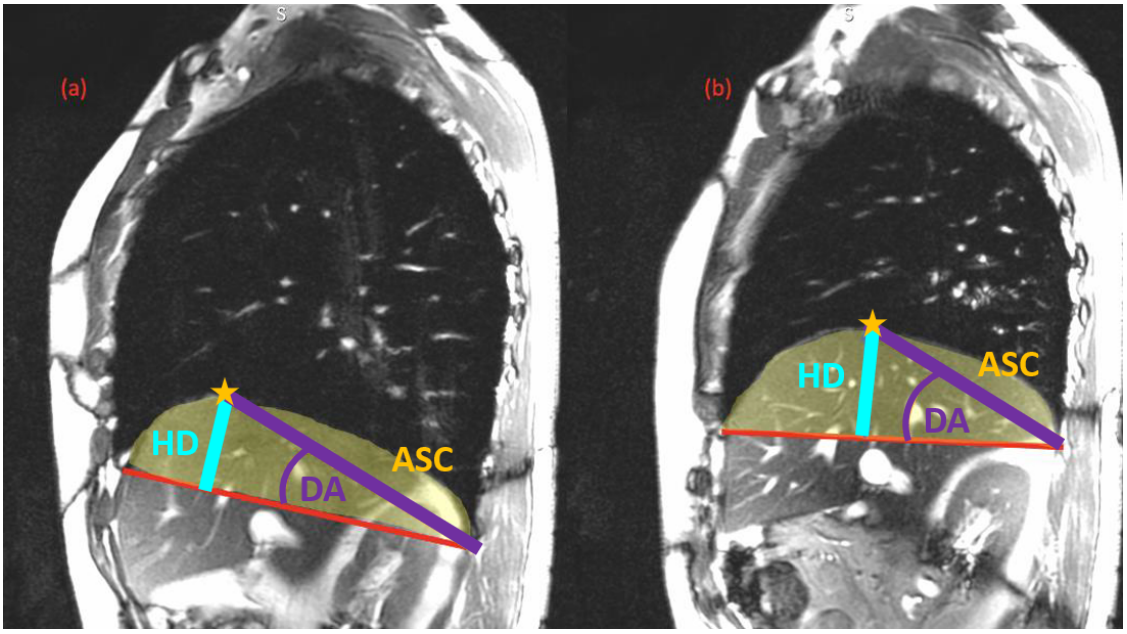

Figure 5.2: Diaphragmatic parameters at the end of maximal inspiration (left) and deep expiration (right) are extracted in a sagittal view of a healthy volunteer in apnea at a certain breath-hold. Diaphragmatic height is shown in cyan (HD): it calculates the distance that separates the diaphragmatic apex (yellow star) from the line joining the costo-diaphragmatic angles (red line). The area under the curve is shown in yellow (ASC): the surface area between the diaphragmatic apex and the line joining the costo-diaphragmatic angles (red line). The diaphragmatic angle is shown in purple (DA): it gives the angle between the diaphragmatic apex and each costo-diaphragmatic angle (joined by the red line).

For the 3D MR spirometry, TV, SPEF, SEF25 and ADI were computed for every voxel of the lung. Moreover, the 3D+t strain component of the Green-Lagrange tensor was calculated for every physiological axis (superior-inferior, anterior-posterior, left-right), and the anisotropic deformation index (ADI) was deduced. The maximum value of local ADI along the respiratory cycle was computed to retrieve three-dimensional maps.

5.1.2 Clinical MR routine findings

Dr Chehboun reported a direct relationship between the diaphragm's movement and the lung's movement, suggesting that when the diaphragm moves, the lungs move in synchrony. Additionally, there was a correlation between the area under the diaphragmatic curve and the surface area of the lungs involved in breathing. Furthermore, vital capacity, measured by standard spirometry, correlates positively with lung dimensions and surface area differences. Conversely, compared to the healthy group values, there was a negative correlation between the ratio of diaphragmatic height and vital capacity, suggesting that as diaphragmatic height decreases relative to healthy function, vital capacity tends to increase. These findings demonstrate the intricate relationship between lung and diaphragmatic motion and their impact on lung function. The details of these reported findings can be found in Dr Cheboun's thesis.[229]

5.1.3 Preliminary findings of 3D MR spirometry

Using 3D MR spirometry, the possible impairments of respiratory function will be assessed on global TV, SPEF, SEF25, ADI, and FRC. The ratio TV/FRC is computed for inter-subject comparison. TV maps will be compared to the healthy baseline defined in Chapter 4.2.1). Muscular weaknesses will be questioned by the normal strains along the anatomical axis. Finally, the inhomogeneity of regional ventilation will be evaluated with the coefficient of variations (CV) over the lung volume.

Dr Chehboun manually segmented the lungs and the apical and basal regions of the lungs for the three subjects. Inhomogeneity scores were computed for each 3D map as the ratio of the standard deviation to the mean of the parameter value over the lung volume. Ventilation patterns can also be evaluated by comparing the parametric maps to the healthy reference baseline presented in the previous chapter 4 for the 25 healthy volunteers in the supine position. Normalization is

applied for each parametric map to this reference dataset, with elastic registration for morphological normalization and rescaling on global values, see section 4.2.1. The healthy distribution maps_{ref} consists of concatenating three-dimensional functional maps along each volunteer. Distances are computed for every voxel from the median and interquartile range (IQR) along the participant dimension. The distance map between an individual functional map_i and the reference baseline maps_{ref} is calculated as:

$$d(\text{map}_i, \text{maps}_{\text{ref}}) = \frac{\text{map}_i - \text{median}(\text{maps}_{\text{ref}})}{\text{IQR}(\text{maps}_{\text{ref}})}$$

Once normalized, the median distance over the lung volume can indicate if the distribution patterns are near the nominal baseline. Quadratic mean normal strains (ϵ), along the three anatomical directions, were also computed to report the role of the muscles in respiratory function. They were calculated based on the sum of squared elongations along each direction over the lung volume.

A. Global spirometric measurements

Statistics on 3D MR spirometry values integrated over the lung volume (as if measured at the mouth) are provided in Table 5.2. The functional residual capacity (FRC) has been computed from the segmented lung volume at the end of expiration using a mean lung density correction of 0.26.[234]

Global lung function	Healthy	Duchenne	FSH
TV (mL)	496	726	357
SPEF (mL/s)	500	1365	472
SEF25 (mL/s)	74	161	88
ADI (x 10^4)	7.5	14.6	7.4
FRC (L)	1.9	2.9	2.8
TV/FRC	0.194	0.189	0.098

Table 5.2: Measurements of 3D MR spirometry and the ratio of TV/FRC integrated over the lung volume for the three participants of the study.

[234] Boran Zhou and Xiaoming Zhang. *Ultrasonics*, 2018.

FRC is reported to remain stable with neuromuscular diseases,[235] while TV is reduced.[236] The ratio of TV/FRC can thus be an indicator of neuromuscular dystrophy. I found a similar ratio between the healthy subject and Duchenne patient. However, the FSH patient presents a much lower ratio.

The optimal tidal volume is expected to range between 6 to 8 mL per kilogram of weight, whereas it was found to be only 357 mL, say 4.4 mL/kg for this FSH patient. The respiratory frequency is slightly higher for Duchenne and FSH patients, respectively, 18 and 19 breaths per minute, compared to a frequency of 16 breaths per minute for the healthy volunteer. These indices of fast and shallow breathing can suggest a weaker ventilation function in the FSH patient. However, since all patients were asymptomatic on standard PFT exams, these differences may be linked to interindividual variability only.

B. Regional ventilation

Regional analysis is then performed to outline ventilation patterns and compute the distance of ventilation patterns compared to a healthy baseline (25 healthy volunteers presented in Chapter 4.1.1). Maps of tidal volume (TV) are provided for the three subjects in Figure 5.3. Local tidal volumes are similar for the healthy and Duchenne volunteers, but they are clearly lower for the FSH patient. However, no clear pattern specificities are exhibited here.

The ratio of the mean of tidal volumes between basal and apical regions was higher than 1 for the three subjects (1.04 for the healthy volunteer and 1.2 and 1.11 for the Duchenne and FSH patients, respectively), demonstrating higher ventilation in the basal region. Hypothetically, in the case of diaphragmatic dysfunction, the lack of flattening and the reduction in excursion would lead to a decrease in the ventilation of adjacent pulmonary regions.

[235] Jackie Chiang et al. *Children*, 2018.
[236] Antonella Lo Mauro and Andrea Aliverti. *Breathe*, 2016.

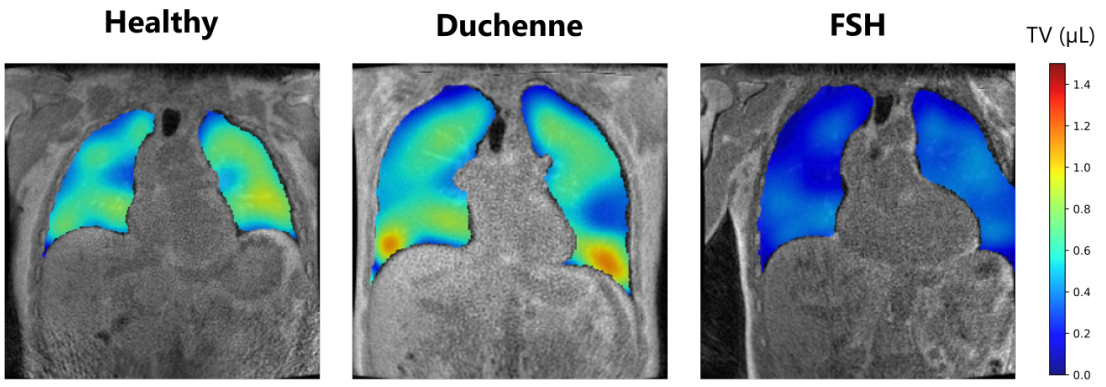

Figure 5.3: Coronal views of tidal volumes computed from 3D MR spirometry of the three participants (healthy volunteer, Duchenne, and FSH patients). The FSH patient presents much lower local tidal volumes.

The inhomogeneity scores of the tidal volumes (Figure 5.3) are found to be similar for the healthy volunteer ($CV = 0.49$) and the two patients ($CV = 0.46$ for Duchenne patient and $CV = 0.53$ for FSH).

Figure 5.4 presents the maps obtained on the cohort after morphological and feature scaling normalization (top) and the maps of their associated distance to the baseline established over the 25 healthy volunteers (bottom).

For the three subjects, the healthy volunteer, the Duchenne, and FSH patients, median distances of 0.11 (IQR 0.86), 0.02 (IQR 0.99), and 0.08 (IQR 0.81) are respectively found. Therefore, ventilation patterns seem nominal for all of them. The low ventilation of the FSH subject seems thus to be homogeneous over the lung volume, with ventilation patterns similar to those of the nominal baseline.

C. Muscle involvements

The quadratic means of the normal strains are reported in Table 5.3.

The magnitude of the normal strains is more shared along the different directions in the healthy subject than in the two patients. Unexpectedly, Duchenne and FSH patients seem to rely more on their diaphragm than on the thoracic muscles with larger elongations along the superior-inferior direction than along the

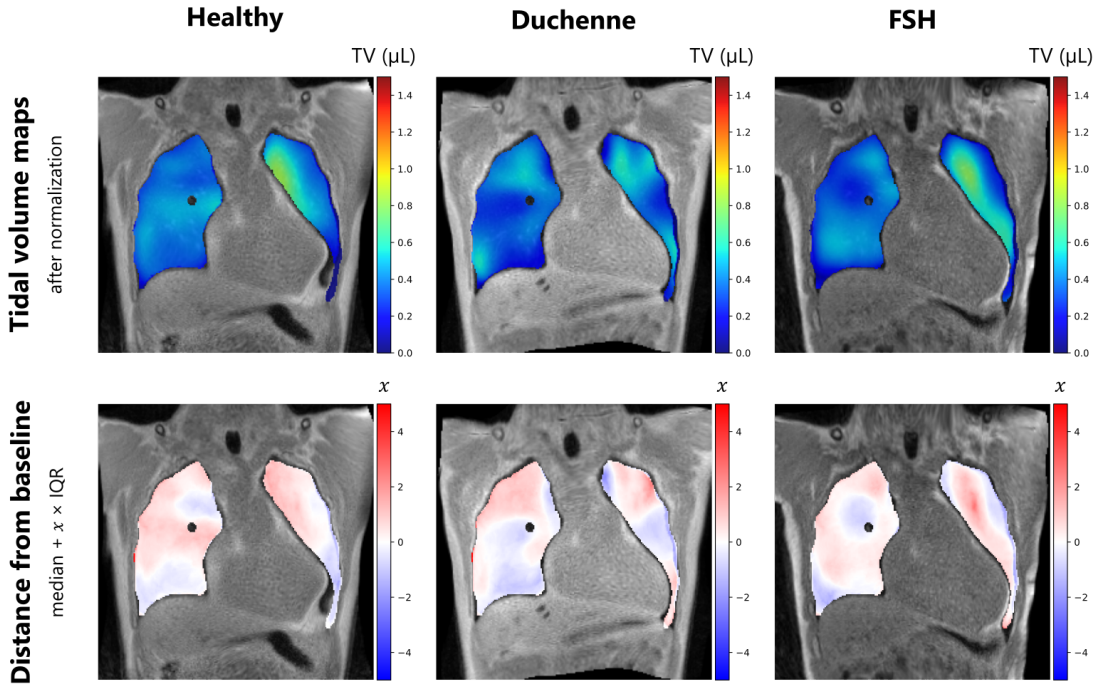

Figure 5.4: Maps of tidal volumes after morphological and feature scaling normalization (top), and maps of the distance of local tidal volumes to the 25 healthy volunteer baseline normalized (bottom). The median and interquartile range (IQR) are computed in every voxel among the healthy participants.

	$\epsilon_{\mathbf{SI}}$ (%)	$\epsilon_{\mathbf{AP}}$ (%)	$\epsilon_{\mathbf{LR}}$ (%)
Healthy subject	53	29	18
Duchenne patient	63	25	12
FSH patient	64	22	14

Table 5.3: Quadratic means of normal strains or elongations in percentage in a healthy volunteer and two patients with early neuromuscular diseases (Duchenne and FSH) along the three anatomical axes: superior-inferior (SI), anterior-posterior (AP), and left-right (LR).

two others. Different breathing patterns could explain this, as shallow breathing is observed (frequent breathing with lower inhaled volumes) and leads to primary involvement of the diaphragmatic muscles and fewer thoracic muscles. These breathing patterns could be linked to interindividual variability or to neuromuscular diseases.

Another hypothesis could be a condition primarily affecting the thoracic muscles early before the disease alters the diaphragm muscle. Times of peak elongation

along the three physiological axes are in phase for the healthy subject and the FSH patient. In contrast, the Duchenne patient seems to first use the diaphragm with the maximal elongation of the superior-inferior axis at 40 % of time of the respiratory cycle duration ($t = 0.4 \times T_{\mathrm{resp}}$), while anterior-posterior at 43 % and left-right at 46 %.

5.1.4 Discussion

We found that the FSH patient adopted shallower breathing than the healthy baseline, combined with a diaphragmatic muscle that seems to contribute more to the ventilation. FSH cases with intercostal damage have already been reported with respect to the diaphragmatic function. However, these preliminary explorations and insights into ventilation patterns in FSH and Duchenne patients must be cautiously taken as no clinical findings can support restrictive patterns or thoracic muscle impairments. Specifically, the first known indicator for impaired diaphragmatic function is a low vital capacity, which was not reported for the two patients who were neither using PFT nor MR imaging of maximal end-of-inspiration and maximal end-of-expiration. The shallow breathing patterns obtained for the two patients should be investigated on a larger cohort to assess whether this is a group effect or interindividual variability. Moreover, the literature on intercostal damage is scarce for neuromuscular diseases, with a focus on the diaphragm as being the main muscle involved in respiration and being easier to evaluate through imaging techniques. Since the mechanical work of breathing is shared jointly with thoracic and diaphragmatic function, the assessment of the thoracic function should be investigated. Finally, a study describes an alternation between diaphragmatic and thoracic respiration mode for a Duchenne patient.[236] Such respiration variations cannot be studied with 3D MR spirometry, as it integrates respiratory cycles over 10 min to deduce an average respiration.

[236] Antonella Lo Mauro and Andrea Aliverti. *Breathe*, 2016.

5.2 Long COVID-19 syndrome: a case report

At the time of this doctoral work, the context of the global COVID-19 epidemic introduced specific interrogations about lung function, specifically on some symptoms that were initially invisible to clinicians. After the pandemic, the long COVID-19 syndrome was reported. It is defined as persistent symptoms lasting beyond four weeks after the acute phase of COVID-19 infection.

Long COVID-19 syndrome is a very recent pathology of pulmonary function, yet little is known about it. Its incidence is high (10 % to 35 % for those who have been infected, and 80 % for those infected and hospitalized),[237] with severe symptoms that can affect the quality of life of the patients.[238] The main common symptoms include shortness of breath, chest pain, and fatigue. Schlemmer *et al.* reported that some patients exhibited restrictive lung defects, impaired diffusing capacity of the lung for carbon monoxide, and notable radiological sequelae.[239] Respiratory muscles dysfunction has also been reported.[240] In situations where standard pulmonary function tests fail to detect these symptoms, functional imaging may sometimes uncover unusual ventilatory patterns. Specifically, it has been documented that an increased ventilation inhomogeneity throughout the lung volume for long COVID-19 patients.[241] Moreover, a restriction is noticed with higher ventilation defect percentages compared to the healthy population.[242] In the two quoted studies, gas distribution is imaged from parenchymal tissue changes during respiration (as gas is inhaled).

A patient with long COVID-19 symptoms was examined in a routine follow-up at Bicêtre Hospital. The patient underwent a dynamic 3D UTE sequence, allowing 3D MR spirometry processing.

[237] Helena C. Maltezou et al. *Vaccines*, 2021.
[238] Sebastian Havervall et al. *JAMA*,. 2021.
[239] Frédéric Schlemmer et al. *European Respiratory Journal*, 2023.
[240] Jan K. Hennigs et al. *Infection*, 2022.
[241] Gaetano Scaramuzzo et al. *BMC Pulmonary Medicine*, 2022.
[242] Jens Vogel-Claussen. *Radiology*, 2023.

5.2.1 Pulmonary functional testing clinical findings

The main characteristics of the patient are reported in Table 5.4. The patient is suffering from respiratory syndromes arising from a COVID-19 infection. The pulmonary impairments are highlighted through the Nijmegen questionnaire.[243] The questionnaire was initially elaborated to detect hyperventilation syndrome, but its interest in other pulmonary dysfunctions was later demonstrated.[244] The long COVID-19 patient reported very often short breathing and chest tightening with pains. The score was higher than the threshold proposed for ventilation dysfunction (31/64 against the threshold of 23/64).

	Long COVID-19
Sex	F
Age (year)	52
Height (cm)	165
Weight (kg)	64

Table 5.4: Main characteristics of the long COVID-19 patient.

Despite the significant symptoms and discomfort described in daily life, standard spirometry results are normal. The obstructive pattern is not demonstrated: the expiratory volume at one second (FEV1) and forced vital capacity (FVC) are found respectively at 110 % and 107 % of reference values, with a Tiffeneau coefficient (FEV1/FVC) of 0.81. A restrictive pattern is also not found with a total pulmonary capacity at 96 % of reference values. The DLCO examination also rules out the presence of diffusional abnormalities (see section C.).

In this particularly complex case, imaging exams were conducted to assess possible local damage. High-resolution CT imaging failed to identify morphological defects but the patient underwent a 3D MR spirometry exam at BioMaps.

[243] J. van Dixhoorn and H. J. Duivenvoorden. *Journal of Psychosomatic Research*, 1985.
[244] Jan van Dixhoorn and Hans Folgering. *ERJ Open Research*, 2015.

5.2.2 3D MR spirometry patterns

A. 3D MR spirometry study design

Using 3D MR spirometry, the expected breathing restriction may be assessed by a reduction of expiratory flows and tidal volumes. Muscular weaknesses will be questioned by the normal strains along the anatomical axis as done in the former study on neuromuscular dystrophia. Finally, the inhomogeneity of regional ventilation will be evaluated with the coefficient of variations (CV) over the lung volume.

The MR acquisition was performed at 3 T (GE Signa PET/MR) at BioMaps. The same parameters and trajectory implemented in section 4.1.1 were used. Thus, the main parameters of the 3D UTE sequence were TE = 14 µs, TR = 2 ms, BW = ±100 kHz and α = 3. The voxel size was 1.5 mm isotropic. The patient was freely breathing in the supine position.

The 3D MR spirometry outcomes for the long-COVID patient were compared to those obtained on a paired healthy volunteer with similar physical characteristics (female, 45 years old, 160 cm, 58 kg).

B. Regional ventilation of a long COVID-19 patient

Functional maps are presented in Figure 5.5 for local tidal volumes (TV), peak expiratory flows (SPEF), and flows at 25% of remaining expiratory volumes (SEF25), and anisotropy deformation index (ADI).

As the volunteer describes dyspnea with shallow breathing, we could expect low tidal volumes and flows throughout the lung. However, the parametric maps depict similar values across the lung volume between the healthy volunteer and the patient.

Global TV is lower for the long COVID-19 patient than the healthy subject, with 239 mL and 361 mL ventilated respectively. Similarly, global expiratory flow is lower, with 233 mL/s for the long COVID-19 patient and 309 mL/s for the healthy subject. When the ratio of global tidal volume with functional residual

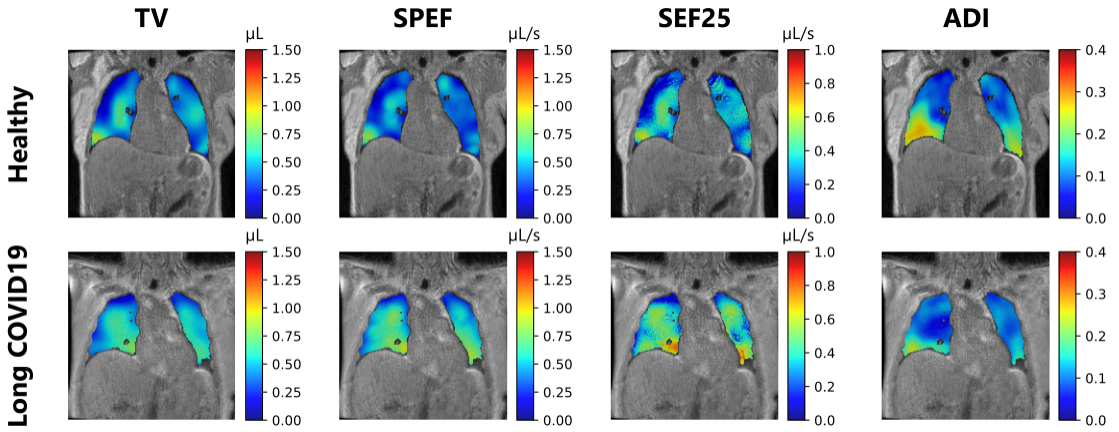

Figure 5.5: Central coronal view of 3D maps of TV, SPEF, SEF25 and ADI of a healthy volunteer (top) and the patient suffering from long COVID respiratory symptoms (bottom).

capacity (FRC) is computed, we found the same coefficients of 0.17, as FRC is also lower for the patient than for the healthy subject (1.05 L compared to 1.6 L). However, COVID-19 pneumonia might decrease lung volumes, and thus the FRC.[245] In this case, the TV/FRC ratio might not be of interest as a decrease in FRC compensates for a decrease in TV. Nevertheless, it can be noticed the patient had a lower global tidal volume than all the healthy volunteers included in the previous study (minimum reported of 251 mL in Table 4.2), in addition to being inferior to the morphometrically closest healthy volunteer. The restriction cannot, however, be established as the characteristics of the patients (sex, height, weight) suggest lower ventilation than most of the healthy baseline cohorts.

The inhomogeneity was assessed for every parametric map as the coefficient of variation over the lung volume ($CV = \frac{\text{std}}{\text{mean}}$). The values are reported in Table 5.5.

The long COVID-19 patient demonstrates better homogeneity compared to the healthy volunteers, despite the lower FRC, contrary to what has been reported for other long COVID-19 patients.[241]

The mean normal strains (ϵ) are provided for every anatomical direction in Table 5.6.

[245] Francesco Lombardi et al. *BMC Pulmonary Medicine*, 2021.
[241] Gaetano Scaramuzzo et al. *BMC Pulmonary Medicine*, 2022.

Coefficient of variation (CV)	Long COVID-19 patient	Healthy subject
TV	0.40	0.49
SPEF	0.35	0.47
SEF25	0.50	0.57
ADI	0.55	0.60

Table 5.5: Coefficients of variations (CV) were computed over the lung for the four 3D MR spirometry functional maps (Figure 5.5) for the patient with long COVID-19 and a paired healthy volunteer. Lower CVs are found for the patient, suggesting more homogeneous ventilation throughout the lung compared to the healthy subject.

	$\epsilon_{\mathbf{SI}}$ (%)	$\epsilon_{\mathbf{AP}}$ (%)	$\epsilon_{\mathbf{LR}}$ (%)
Long COVID-19	0.48	0.35	0.17
Healthy	0.55	0.29	0.16

Table 5.6: Quadratic means of normal strains or elongations in percentage along the three anatomical axes: superior-inferior (SI), anterior-posterior (AP), and left-right (LR). Each ratio was calculated based on the sum of squared of local maximal elongations along each axis over the lung volume.

The main superior-inferior elongation driven by the diaphragm is lower for the long COVID-19 patient than for the healthy subject, whereas the elongation is higher along the anterior-posterior and left-right direction, ruled by the thoracic muscles. These findings support the diaphragmatic dysfunction that has already been reported in long COVID-19 patients.[246] They also reveal the enhanced contribution of thoracic muscles, which might compensate for the reduced diaphragmatic effort, thus leading to more homogeneous ventilation as clearly depicted on the functional maps (TV, SPEF, and SEF25 on Figure 5.5) with more isotropic deformations (ADI on Figure 5.5).

To evaluate ventilation patterns, tidal volumes (TV) of both the healthy subject and the long COVID-19 patient were normalized (Figure 5.6 top row). The normalization includes an elastic registration for morphological normalization and rescaling on global values on a reference dataset, as described in the previous section 4.2.1. The 3D maps of the distance to the normalized baseline distribution constructed in chapter4 are shown in Figure 5.6 (bottom row).

[246]Katarzyna Anna Pietranis et al. *Journal of Clinical Medicine*, 2024.

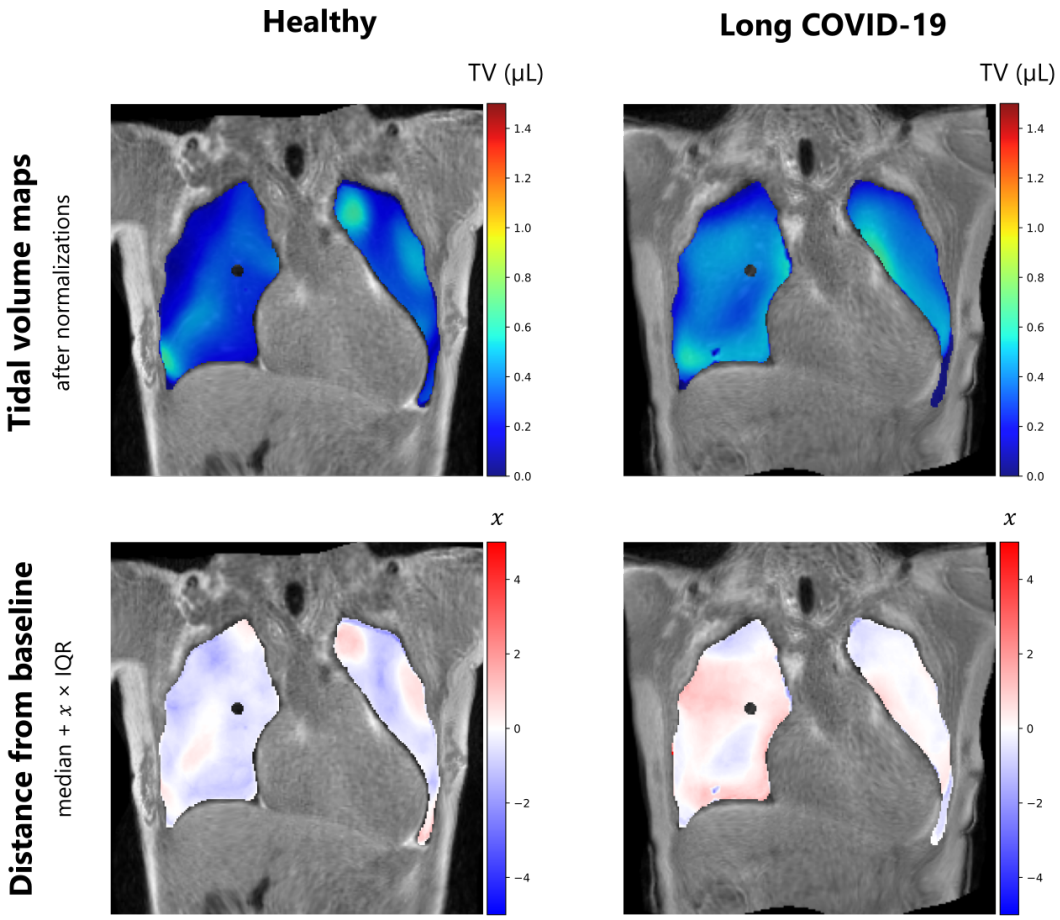

Figure 5.6: Maps of tidal volumes after morphological and feature scaling normalization for the paired healthy subject and the long COVID-19 patient on the 25 healthy volunteer reference (top), and maps of the distance of local tidal volumes to the 25 healthy volunteer baseline (bottom). The median and interquartile range (IQR) are computed in every voxel among the healthy participants.

The healthy subject has a median distance of -0.04 (IQR = 0.89) to the baseline, while the long COVID-19 patient has a median distance of 0.20 (IQR = -1.18). The spatial ventilation patterns of the patient are 5 times more distant from the normal distribution; however, they have a high variability of local distances.

5.2.3 Discussion

The long COVID-19 remains a syndrome poorly understood and defined by the scientific community due to its recent appearance only 4 years ago. The normal standard PFT fails to point out the affection, while the symptoms experienced on

a daily basis are significant and disabling.

Three-dimensional MR spirometry found low volumes and flows at the local and global scales, which sensitivity might be explained by a greater effort for ventilation in the supine position, where the diaphragm is under greater stress. Compared to a paired healthy subject with similar physical values, the diaphragmatic function of the long COVID-19 patient seems reduced, while the thoracic muscles contribute more to the ventilation. It explains the higher homogeneity of the ventilation, as parenchymal tissues might deform more homogeneously with thoracic respiration than diaphragmatic respiration. This feature is, however, contrary to some reported long COVID-19 cases.[241,242] However, it might be consistent with the physiopathology for post-pneumonia tissues, possibly wetter and less compliant, where the thoracic muscles are involved to relieve diaphragmatic function.[247,248]

This case report only compares one patient's outcomes to a paired healthy subject's outcomes, which might not reflect the long COVID-19 group. Besides, it has been reported a high variability between patients, suggesting the definition of subgroups to improve clinical diagnosis, follow-up, and care.[249]

[241] Gaetano Scaramuzzo et al. *BMC Pulmonary Medicine*, 2022.
[242] Jens Vogel-Claussen. *Radiology*, 2023.
[247] L. Zocchi et al. *The American Review of Respiratory Disease*, 1993.
[248] M. B. Hershenson et al. *Journal of Applied Physiology*, 1989.
[249] Jong Hyuk Lee et al. *Respiratory Research*, 2022.

5.3 Reversibility in asthma and COPD patients

As part of my doctoral project, a second clinical study with Bicêtre Hospital was launched to evaluate the diagnostic performance of 3D MR spirometry. A reversibility study is carried out on healthy subjects, asthmatic and COPD patients in order to evaluate the sensitivity of the technique to the effects of a bronchodilator. Longitudinal follow-ups are also planned for severe asthmatic patients to evaluate the effect of biotherapy. However, administrative procedures were significantly delayed, with the start of the inclusion in May 2023. Only preliminary results are presented here on a modest cohort. This study will be deepened in the ongoing doctoral work of Ithar Gharmaoui.

5.3.1 Design of the study

A. Population

The study was approved by the local ethics committee (CPP Ouest IV, 22.00822.000074). The principal investigator is Pr Vincent Lebon, and we acquired data with Ithar Gharmaoui, Adrien Duwat, Anna Reitmann, Angéline Nemeth, and Xavier Maître. Twenty-one participants were included between May 2023 and April 2024, the time of the following analysis: 14 healthy volunteers, 3 asthmatic patients, and 4 COPD patients. The main characteristics of the population are summarized in Table 5.7. One asthmatic patient with a planned biotherapy experienced a second visit 6 months after the start of the biotherapy. All participants received detailed information about the protocol, were included by the investigators, and gave informed consent. The generic inclusion criteria for the study were the age (between 18 and 45 years old for healthy volunteers), the absence of a known pulmonary disease, the ability to stay inside an MR scanner without moving during the acquisition, and informed consent. For asthmatic patients, inclusion extends to those aged 18-80 years with moderate to severe asthma, while COPD patients aged 40-80

years with moderate to severe COPD are included. Exclusion criteria encompass contraindications to MRI or spirometry exams, individuals with a BMI over 35, pregnant or breastfeeding women, and those with contraindications for MRI. Asthmatic and COPD patients are excluded if they experienced exacerbation within the past month, are oxygen-dependent, or present bronchodilator intolerance.

Description of the population	**Healthy (n=14)**	**Asthmatic (n=3)**	**COPD (n=4)**
Age (y)			
Median ± inter-quartile range	30 ± 16	61 ± 20	60 ± 1
Range	21 - 67	27 - 67	59 - 62
Sex			
Female	7	1	0
Male	7	2	4
Weight (kg)			
Median ± inter-quartile range	64 ± 18	53 ± 14	77 ± 14
Range	40 - 88	49 - 77	55 - 82
Height (cm)			
Median ± inter-quartile range	171 ± 12	168 ± 10	173 ± 7
Range	155 - 192	166 - 186	166 - 185

Table 5.7: Descriptive statistics of the population included for the study: 14 healthy volunteers, 3 asthmatic patients, and 4 COPD patients, included between May 2023 and April 2024.

The protocol is completed by an ancillary study on the objectification and acceptance of 3D spirometry by magnetic resonance. Interviews are to be conducted before and after the examinations on a sample of each population (in green blocks on the schematics). However, results are not provided as not yet available.

B. Data acquisition

Study participants are first included at Bicêtre Hospital, where standard spirometry is performed in a sitting position and a lying supine position. They are then transported to BioMaps, where 3D MR spirometry is performed three times while participants are spontaneously breathing in the supine and prone positions: two

initial repeated acquisitions before bronchodilator administration and one acquisition after. The administration of bronchodilator (Salbutamol) is done using a pressurized dose inhaler and an inhalation chamber at a dosage of 100 g with 4 inhalations (totaling 400 g).

Like in Chapter 4 and before for the long COVID-19 patient, the MR acquisition was performed at 3 T (GE Signa PET/MR). The main parameters of the 3D UTE sequence were $TE = 14$ µs, $TR = 2$ ms, $BW = \pm 100$ kHz and $\alpha = 3°$.

C. Challenge 3D MR spirometry to bronchodilator effect

Bronchodilators widen the airways in the lungs by relaxing the smooth muscles surrounding the bronchial tubes. By opening up the air passages, bronchodilators facilitate breathing and alleviate symptoms of respiratory obstructive syndromes such as asthma and, to a lesser extent, chronic obstructive pulmonary disease. It is expected that flows will increase for asthmatic and COPD patients after Salbutamol inhalation.

The bronchodilator reversibility test evaluates the responsiveness of a patient's airways to bronchodilator medication with improved ventilation. The diagnosis of obstructive syndrome with spirometry combined with bronchodilation response has been recommended as the main diagnostic indicator for asthma.[250] Typically, spirometry is performed before and after administering a bronchodilator, such as Salbutamol, to measure changes in lung function. An immediate increase in lung function post-bronchodilator suggests reversible airflow obstruction, like asthma, rather than irreversible conditions, like COPD. However, the specificity of the test is still a subject of research discussion as COPD patients can also demonstrate reversibility.[251,252]

[250] R. Pellegrino et al. *The European Respiratory Journal*, 2005.
[251] Christer Janson et al. *The European Respiratory Journal*, 2019.
[252] Igor Barjaktarevic et al. *International Journal of Chronic Obstructive Pulmonary Disease*, 2019.

Repeatability is evaluated in this clinical study, together with the bronchodilator response, in order to discriminate the effects of intrinsic respiratory variability and those of the bronchodilator.

5.3.2 Lung function assessment

A. Standard spirometry

Standard spirometry results are summarized in Table 5.8. COPD patients have severe obstruction with low FEV1/FVC (median value of 43.49 % of reference value calculated from the Global Lung Initiative (GLI) [11]). Asthmatic patients have moderate to no visible obstruction at rest using standard spirometry.

Population	Healthy (n=14)	Asthmatic (n=3)	COPD (n=4)
FVC (L)			
Median ± inter-quartile range	3.88 ± 1.45	3.84 ± 0.65	3.95 ± 0.80
Range	2.55 – 6.19	3.24 – 4.53	2.93 – 5.38
FEV1 (L)			
Median ± inter-quartile range	3.17 ± 1.07	2.43 ± 0.73	1.83 ± 0.67
Range	1.86 – 4.74	2.07 – 3.53	0.99 – 2.51
FEV1/FVC (%)			
Median ± inter-quartile range	82.30 ± 6.89	63.74 ± 7.38	43.49 ± 22.23
Range	72.96 – 90.09	63.28 – 78.05	30.48 – 61.76

Table 5.8: Descriptive statistics of the population included between May 2023 and April 2024 for the study: 14 healthy volunteers, 3 asthmatic patients, and 4 COPD patients.

B. Global 3D MR Spirometry Statistics

Main 3D MR spirometry biomarkers are computed for this study: local tidal volumes (TV), peak expiratory flows (SPEF), flows at the remaining 25% of expiratory volumes (SEF25), and anisotropic deformation index (ADI). The functional residual capacity (FRC) is estimated from the segmented volume at the end-expiratory

[11] Graham L. Hall et al. *The European Respiratory Journal*, 2021.

state, with a mean lung density correction of 0.26.[234] Table 5.9 gathers biomarker medians and interquartile ranges integrated over the lung volume for the healthy, asthma, and COPD populations. As the cohort of patients is small, the statistics in this part are descriptive.

	Healthy	**Asthma**	**COPD**
TV (mL)			
Median ± IQR	331 ± 161	363 ± 91	438 ± 200
Range	138 - 557	296 - 522	239 - 615
SPEF ($\mathbf{mL{\cdot}s^{-1}}$)			
Median ± IQR	479 ± 187	507 ± 358	572 ± 165
Range	166 - 1386	248 - 1238	342 - 821
SEF25 ($\mathbf{mL{\cdot}s^{-1}}$)			
Median ± IQR	293 ± 110	295 ± 95	402 ± 91
Range	114 - 404	235 - 378	273 - 538
ADI			
Median ± IQR	87 ± 54	95 ± 42	113 ± 26
Range	27 - 161	61 - 127	75 - 159
FRC (mL)			
Median ± IQR	761 ± 335	868 ± 127	1089 ± 342
Range	340 - 1071	610 - 993	725 - 1447

Table 5.9: Summary statistics for biomarkers in 14 healthy individuals, 3 asthmatic patients, and 4 COPD patients: median and inter-quartile intervals (IQR), and maximal and minimal global values of 3D MR spirometry are provided for each participant group.

COPD patients present higher volumes, higher flows, and a higher deformation anisotropy than asthmatic patients and healthy volunteers. These higher values could be easily associated to the subjects' forced vital capacity (FVC in Table 4.2). Yet, the higher functional residual capacity found in asthma and COPD patients could also be attributed to gas trapping, leading to a greater work of breathing for these patients.[253,254]

[234] Boran Zhou and Xiaoming Zhang. *Ultrasonics*, 2018.
[253] Ronald L. Sorkness et al. *Journal of Applied Physiology (Bethesda, Md.: 1985)*, 2008.
[254] Kun Li et al. *International Journal of Chronic Obstructive Pulmonary Disease*, 2019.

C. Reversibility with 3D MR spirometry

The reversibility is expected to remove obstructions and so primarily alter the respiratory flows. It is recorded by standard spirometry at forced breathing and even at spontaneous breathing for some severe obstruction.[255,256]

Median flow rates are stable for the COPD and healthy participants (respectively, 538 mL/s to 511 mL/s, and 192 mL/s to 196 mL/S), but global SPEF values, increase from 235 mL/s to 457 mL/s reached for the asthmatic patient (Table 5.9). Moreover, a reduced FRC is found for both asthmatic and COPD patients (from 2.62 L to 2.58 L and from 3.95 L to 3.90 L, respectively), while FRC is slightly increased for the healthy participant (from 1.66 L -to 1.70 L). These reductions in asthmatic and COPD patients might reflect the expected lessening of air trapping, but variations are too slight, and the statistics too small to conclude.

To gain some regional insights, Figure 5.7 maps flows at the remaining 25 % of expiratory volumes for 3 participants (one healthy, one asthmatic, one COPD) before and after bronchodilator inhalation. A strong reversibility in the asthmatic patient (severe asthma, which is included in biotherapy) is observed, particularly at the lung base.

On the SEF25 maps Figure 5.7, the healthy volunteer (left) does not present any reversibility effects after inhalation of the bronchodilator. The flow spatial distribution is modified for the COPD patient (middle) but without any global functional enhancement. The increased ventilation observed in the left lower lobe is compensated by reduced ventilation in the lower right lobe. The asthmatic patient presents strong overall reversibility, with higher flows, particularly near the lung base.

The reversibility is assessed on all the cohorts, for each group, using violin plots presented in Figure 5.8. Global measurements of ratios between flows at the remaining 25 % of expiratory volumes and functional residual capacities (SEF25/FRC)

[255] N.G. Koulouris and G. Hardavella. *European Respiratory Review*, 2011.
[256] M J Morris and D J Lane. *Thorax*, 1981.

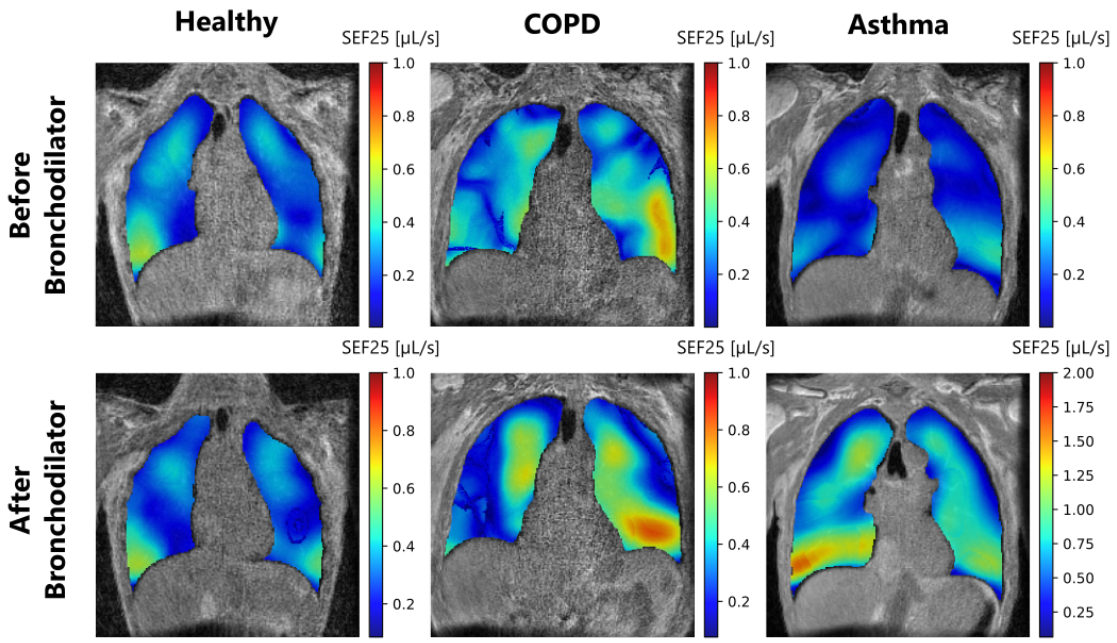

Figure 5.7: Coronal views of flows at remaining 25% of expiratory volumes (SEF25) for a healthy volunteer (left), a COPD patient (center), and an asthmatic patient (right) before (top row) and after bronchodilator inhalation (bottom row). Along the reversibility test, there is no noticeable modification in the flows for the healthy volunteer, whereas the flows are spatially redistributed between the lobes for the COPD patient but without any global change, and they are largely spatially redistributed and increased for the asthmatic patient.

are plotted before the bronchodilator inhalation for the two repeated measurements (ante-bronchodilator 1 and ante-bronchodilator 2) and after the inhalation (post-bronchodilator).

The administered salbutamol is expected to enhance the values of the ratios with increased flows (reduced obstruction) combined with a decrease in residual volume (reduced air trapping). Moreover, the ratio SEF25/FRC provides a flow measurement normalized to the global lung capacity. Despite the small cohort, the preliminary results obtained for each group are consistent with the findings in the literature. The healthy group depicts stable measurements after the bronchodilator inhalation. The COPD group demonstrates a variable response without a clear increase of the ratio after the inhalation but a regional redistribution and an increased dispersion of the values. A consistent increase is found after bronchodilator

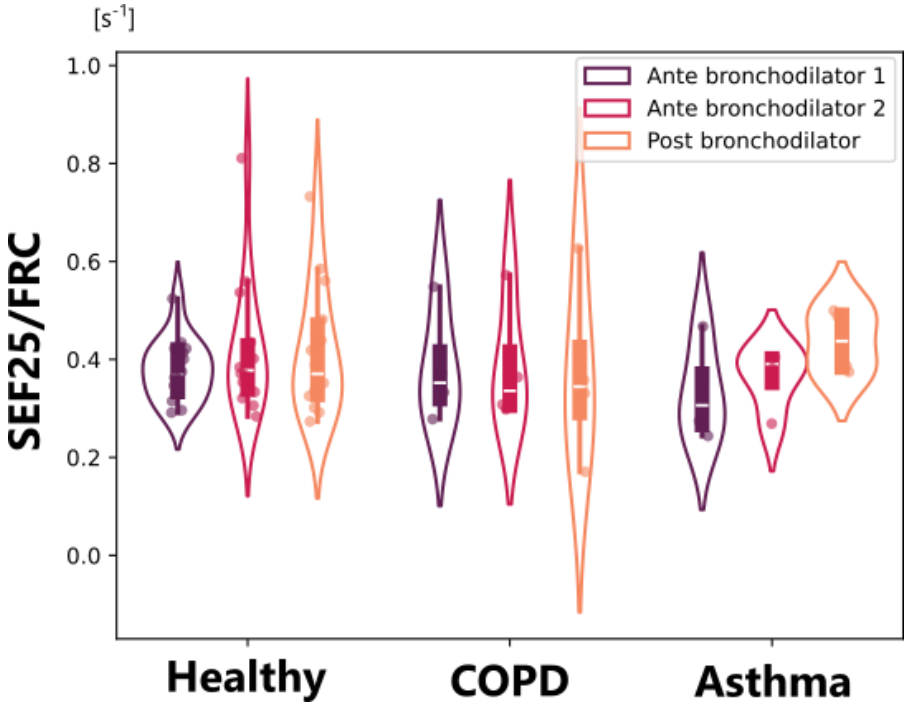

Figure 5.8: Violin plots of ratios between flows at the remaining 25 % of expiratory volumes (SEF25) and functional residual capacities (FRC): a kernel density plot of the distribution is superimposed on the raw data and on the quartiles box. Ratios are plotted before and after bronchodilator inhalations for each group: healthy (left), COPD (middle), and asthma (right). Before bronchodilator inhalations, two acquisitions are performed to assess the repeatability of the measurements (purple and red violin plots), allowing a direct comparison of intrinsic variations of ventilation against bronchodilator effects.

inhalation for asthmatic patients despite the intra-individual variability recorded between the two measurements repeated pre-bronchodilator.

The choice of biomarkers evaluated so far is based on a priori physiology knowledge and free-breathing standard spirometry literature. However, the study of local flow and strain parameters has never been studied locally in spontaneous breathing, inducing a blind spot in the optimal choice of biomarkers. Future analysis should include data-driven tools to reduce 3D MR spirometry dimensionality to its main components. Here, the dataset is too small to draw any conclusion from such an analysis. If groups can be robustly differentiated in a latent space, predictive models could be developed to classify groups and, eventually, discriminate subgroups for these pathologies.[252]

[252]Igor Barjaktarevic et al. *International Journal of Chronic Obstructive Pulmonary Disease*, 2019.

D. Therapeutic follow-up with 3D MR spirometry

The efficacity and safety of biotherapy for severe asthma has been demonstrated in clinical trials and real-world settings.[257,258] A severe asthmatic patient of the cohort had a planned biotherapy with Mepolizumab (a monoclonal antibody) after having been examined using standard spirometry, frequency oscillation technique (FOT), and 3D MR spirometry. Thus, six months later, the patient went through the same protocol.

When the patient returned to Bicêtre Hospital and BioMaps after six months of biotherapy, the patient reported an improved ventilatory function and greater comfort in everyday living. This can not really be measured using standard spirometry as the forced flow-volume loops are very similar (Figure 5.9, left).

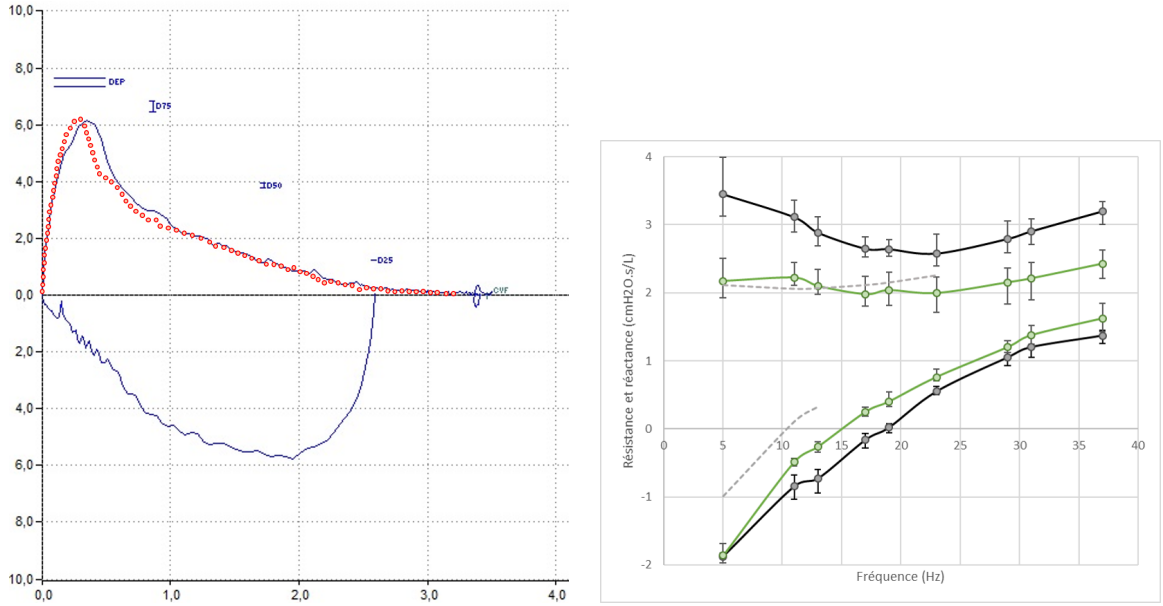

Figure 5.9: Standard forced spirometry flow-volume loops (left) and FOT (Frequency Oscillation Technique) resistance and reactance curves (right) before and six months after the introduction of biotherapy. For the spirometry measurements, the red curves were obtained before biotherapy, and no significant differences are found after biotherapy (black). For the FOT measurements, a reduced thoracic-pulmonary resistance is found between before (black lines) and after (green lines) biotherapy.

Only a small increase in FEV1 (80 mL, i.e. +3.9 %) and FVC (270 mL, i.e.

[257] Patrick Flood-Page et al. *American Journal of Respiratory and Critical Care Medicine*, 2007.
[258] Colin Powell et al. *Cochrane Database of Systematic Reviews*, 2015.

+8.3 %) can be noted: $FEV1_{post}$ = 2150 mL (79 %) for $FEV1_{pre}$ = 2070 mL (76 %), FVC_{post} = 3510 mL (101 %) for FVC_{pre} = 3240 mL (93 %). Additional measurements were performed using plethysmography and FOT. The most significant variation comes with the plethysmographic residual volume (RV), which is reduced by 700 mL, i.e. -22.2 % (from 3610 mL, 156 %, to 2460 mL, 120 %), whereas the functional residual capacity (FRC) is barely modified (from 3760 mL, 121 %, to 3730 mL, 120 %). In FOT, there is also a significant reduction, -37 %, in the total thoracic-pulmonary resistance: R5Hz goes from 3.45 $cmH_2O{\cdot}s{\cdot}L^{-1}$ down to 2.17 $cmH_2O{\cdot}s{\cdot}L^{-1}$ (Figure 5.9). Besides, the frequency-dependence of the resistance (R5-20) is reduced, which can be interpreted as a reduction of the ventilation inhomogeneity.

The lung capacity measured with 3D MR spirometry is decreased by 118 mL after the biotherapy, suggesting a significantly reduced air trapping. Before the biotherapy, the bronchodilation induces a decrease in the functional residual capacity of 48 mL (from 2624 mL to 2576 mL). After the biotherapy, the functional residual capacity decreased even more, at 2506 mL before bronchodilator inhalation and 2443 mL after inhalation. These values largely differ from the values recorded with plethysmography, which are roughly the same before and after biotherapy, respectively, 3760 mL and 3730 mL. The density correction applied in 3D MR spirometry to produce FRC could be questioned and refined, so could the plethysmography measurements as they are already known to be biased with the manufacturers (e.g., 670 mL difference was reported by Alter *et al.*[259]). Moreover, the reversibility effect might be sensitive to the position, as it is known the FRC is decreased from the sitting position to the lying supine position because of airway closure of some lung regions.[260] The flow maps of SEF25 are provided in Figure 5.10 before and six months after the introduction of the biotherapy and before and after the administration of the bronchodilator.

[259] Peter Alter et al. *International Journal of Chronic Obstructive Pulmonary Disease*, 2022.

[260] Erin Hopkins and Sandeep Sharma. "Physiology, Functional Residual Capacity". In: *StatPearls*. Treasure Island (FL): StatPearls Publishing, 2024.

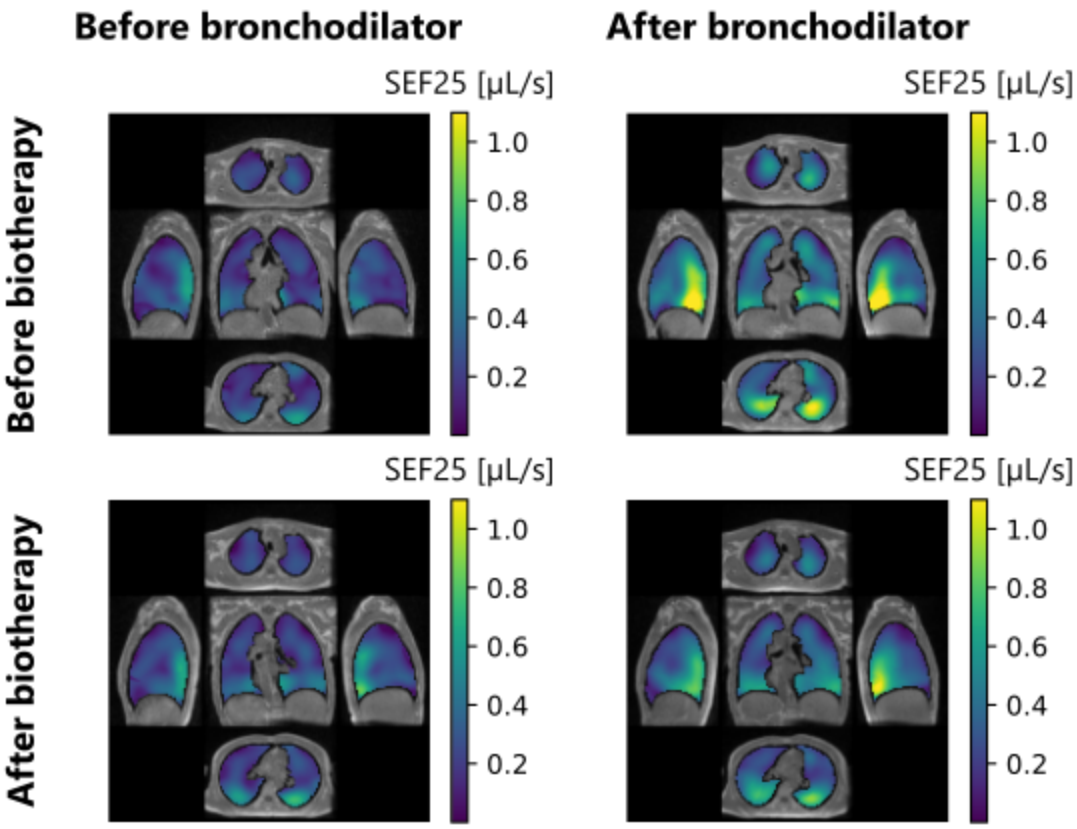

Figure 5.10: Polyptychs views of the expiratory flows at the remaining 25% of the tidal volume (SEF25) for a patient with severe asthma before and after bronchodilation (rows), before and after biotherapy (columns). The views are plotted for a central coronal slice, two axial slices in the apical and basal lung, and two sagittal slices in the right and left lungs. SEF25 slightly increases after biotherapy, and the reversibility to a bronchodilator is reduced after the biotherapy. These results suggest an improved lung function.

Moreover, the expiratory flows are increased, indicating a reduced obstruction in the airways. A lower homogeneity is found when the lung function is improved: it might be due to the decrease of the lung volume, which is known as a factor of increased inhomogeneity.[220]

Although the present data are from a single patient, 3D MR spirometry shows results consistent with physiology, which appears to be sensitive to improvements in lung function.

[220] Hooman Hamedani et al. *The Journal of physiology*, 2021.

5.3.3 Discussion

Finally, this preliminary study in 3 asthmatic patients, 4 COPD patients, and 14 healthy volunteers presented the first results on the sensitivity of 3D MR spirometry to reversibility and therapy. Despite the small group size, reversibility effects were reported mainly in asthmatic patients and, to a lesser extent, in COPD patients, which is corroborated by usual clinical findings. Increased tidal flows, indicating a reduction of obstruction, combined with reduced functional capacity, indicating reduced air trapping, are reported. These results need to be confirmed with the complete cohort for statistical significance. If the parameters are indeed sensitive, a dimensionality reduction combined with learning methods could make it possible to classify patients and perhaps to highlight subgroups (for example, reversible vs non-reversible COPD).

Moreover, 3D MR spirometry was able to measure the effects of biotherapy on one severe asthmatic patient, with higher flow measurements than before the biotherapy and a functional capacity that was reduced after six months therapy for both before and after Salbutamol inhalation. It can indicate a durable reduction in air trapping and functional residual capacity.

Apart from the cohort size, a limitation of the study is the absence of a spirometry exam after the bronchodilator inhalation to compare reversibility sensitivity between standard spirometry and 3D MR spirometry. Besides, despite the presence of local measurements, the study of local ventilation statistics and variations needs to be better exploited. Finally, structural measurements could be added from our images, such as diaphragm flattening (for emphysematous patients), to use all information made available by MRI.

Conclusions and perspectives

General conclusion

Three-dimensional MR spirometry unveils a captivating exploration of spontaneous respiration from within. Through quantitative mapping of the ventilation dynamics, this technique offers a view of ventilation grounded in the intricate motion and deformations of the lung tissues. By harnessing the innocuity and clinical routine of standard magnetic resonance imaging, three-dimensional respiratory ventilations are captured for subjects without any special cooperation while they are lying in the MRI, with the possibility of longitudinal follow-up. However, 3D MR spirometry was introduced only a year before the start of this work, and it needs to be further developed to ensure the robustness and reliability required for clinical applications.

Several developments have been carried and original clinical findings have emerged during this doctoral work, bringing 3D MR spirometry from basic exploration to clinical research. Methodologically, the signal-to-image processing was thoughtfully refined to improve the robustness and reliability of the technique. Specifically, a new soft-gating approach was introduced to capture the respiratory states efficiently in the phase portrait of the MR respiratory signal so the lung dynamic can be recovered over 32 ventilation phases. Lung lobe segmentation was augmented using deep learning, which now necessitates only a few seconds of computation instead of 10 minutes before. The extraction of the deformation fields was grouped and regularized along the temporal direction, optimizing a robust flow derivation. Inspired by standard spirometry, quantitative maps were defined from local flow-volume loops, reducing the dimension to three-dimensional views of ventilation-sensitive

features. These methodological advancements were validated through the comparison to global segmentation approaches, demonstrating the repeatability and precision of the technique.

In clinical exploration, ventilation patterns were investigated among healthy individuals and patients with restrictive and obstructive conditions. By normalizing functional maps and establishing an atlas from a healthy baseline, reproducible patterns of nominal ventilation were identified, including a significant sensitivity to the expected gravity lung dependence. The research was extended at the end of the doctoral work to explore 3D MR spirometry features on a few patients with neuromuscular diseases, long COVID-19 syndrome, asthma, and COPD. Notably, a biotherapy follow-up on a severe asthmatic patient uncovered functional improvements beyond standard spirometric measures. These discoveries deepen our comprehension of healthy to dysfunctional ventilation dynamics and patterns, paving the way for tailored treatment strategies that cater to each respiratory condition.

While further improvements are already envisioned, our work demonstrates the interest in 3D MR spirometry for further clinical investigations. The following paragraphs present some perspectives and ideas for pursuing this work.

Dynamic lung MRI

The image quality achieved by combining the UTE sequence with AZTEK is among the best available for lung imaging, with a high signal-to-noise ratio (SNR), visibility of the vascular tree, and temporal sampling of respiratory motion. However, there are potential limitations, including the lack of robustness among acquisitions and subjects and the lack of visibility of most distal vessels. ZTE stands out for its quiet operation and its broad availability in clinics on GE scanners. Meanwhile, bSSFP enhances vascularization signals remarkably, which is crucial for assessing respiratory-induced lung deformation in 3D MR spirometry. Recent investigations focus on new trajectories, including Sparkling scheme [261] and density-

[261] Carole Lazarus et al. *NMR in biomedicine*, 2020.

compensation with variable readout gradients [57], to reduce acquisition times while maintaining a high image quality. Additionally, functional lung MRI could benefit from new contrasts at low and ultra-low fields,[67] and explorations are ongoing for a 3D MR spirometry implementation at 0.55 T and 0.1 T.

Assessing ventilatory function

This doctoral work developed quantitative markers for 3D MR spirometry, thus offering a comprehensive view of the ventilation mechanics: volumes, dynamics, and directions of respiratory motion. In standard MRI, i.e. hydrogen-based and without contrast agent, intensity-based and Jacobian-based techniques are the two surrogates used to infer the local ventilation from the variations of the local expansion of parenchymal tissues. These two ventilation surrogates do not measure physical phenomena similar to tracer gas, and the different phenomena involved are actually not decomposed and modelized. Good correlations can be found, but the remaining variations can be important and unexplained. Between Fourier decomposition and Jacobian techniques, the observed phenomenon is the same, but the measurements are different, and the resulting ventilatory patterns are found to be very different. A work of consistency between these measurements, with the corrections that will be necessary to bring the methods closer together, should be opened, improving the understanding of ventilation physics. Finally, although it is known that free ventilation is inhomogeneous, nominal ventilation patterns are currently not considered when defining ventilation defects. Work on clinical data can be continued to define defects consistent with the nominal ventilation patterns highlighted during this doctoral work.

[57] Kevin M. Johnson et al. *Magnetic Resonance in Medicine*, 2013.
[67] Rabea Klaar et al. *Radiation Oncology*, 2023.

Reliability of 3D MR spirometry

Assessing the precision and accuracy of 3D MR spirometry measurements presents a formidable challenge when considering the inherent complexity of lungs, with its intrinsic ventilatory variability, which can be influenced by daytime, mood, respiratory control mechanism, etc .[262] The evaluation on a phantom is a recurrent subject of discussion, but no optimal phantom has been found yet. For this, repeatability, reproducibility, and overall accuracy are our only indicators of the technique's reliability. The repeatability of 3D MR spirometry has been established globally for healthy volunteers within the bounds of the known intrinsic variability of spontaneous respiration. Despite low precisions in low-ventilated regions, the local ventilation patterns are repeatable and reproducible. The global accuracy has been demonstrated against lung volume segmentation. It could be further developed to provide a lobular analysis. Measurements could also be validated using a magnetic-compatible spirometer (currently under development in the laboratory). The comparison of the technique with other modalities, such as hyperpolarized lung MRI or PREFUL, would be desirable in cohorts of patients and healthy volunteers. Apart from these evaluations, some processing steps could be optimized to improve the robustness of the technique. It includes a more robust self-navigator definition (which can be noisy and reverted), the segmentation of finer lung structures (the lung segments), the registration (validate the groupwise registration for a temporal regularization, a more robust handle of the sliding motion), or some biomarkers computation (time-based biomarkers specifically can be artifacted from local noisy flow-volume loops).

Clinical investigations

The technique was validated on healthy subjects, leading to initial explorations and outcomes of the sensitivity and specificity of 3D MR spirometry. Clinical

[262]Michael C. K Khoo. *Respiration Physiology*, 2000.

research is ongoing on various sites to challenge the interest of 3D MR spirometry in diagnosing various physiological effects and lung diseases for adults and children at different magnetic fields. The clinical protocols developed in the European consortium *V/LF-Spiro3D* are summarized in Figure 5.11. The consortium aims to consolidate the technique, explore ventilation features for various lung conditions, and translate lung MRI toward very low-field MRI. The technique will notably be compared in clinical protocols to the quantification of ventilation by Fourier decomposition, the clinical sensitivity of which has already been established for numerous pulmonary pathologies and treatments. The data produced by these studies will be heavy (around 2 To of raw data), thus posing two main challenges to address. The first one is the reconstruction of the 3D MR spirometry maps, which requires expensive processing, resulting in 2h30 of machine time on an Intel Xeon Gold 5218R (32 respiratory phase lung dynamic reconstruction and 3D MR spirometry computation). A way of reducing computation time could be using deep learning techniques, particularly for reconstructing dynamic images and extracting deformation fields from image registration. Furthermore, the dimensionality of the data should be further investigated to reduce the outcomes to the most important information needed for a diagnosis in each study.

Final words

Over the past two decades, ventilation MRI without tracer gas has become a powerful and practical modality widely deployed in clinical research. Recently developed 3D MR spirometry has the potential to provide reliable quantitative estimation of ventilatory dynamics and mechanics. Significant improvements to the original technique have been produced during this PhD work, which has led to promising sensitivity performances and reliability within an unconstrained MR protocol. The analysis framework holds great promise for refining 3D MR spirometry exams, facilitating precise spatial mapping, and respiratory function monitoring in clinical settings.

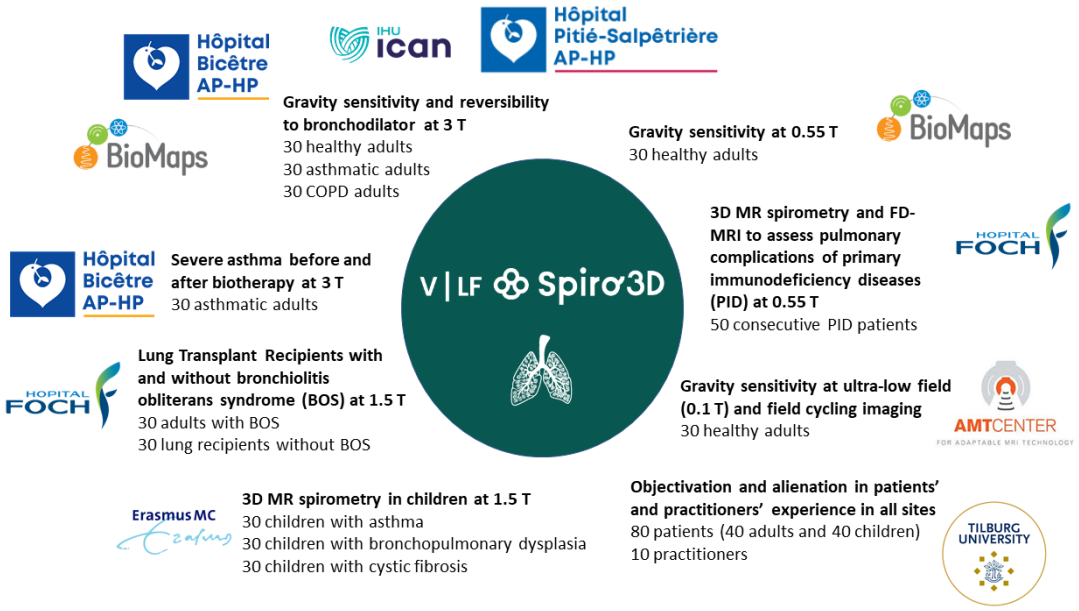
Hôpital Bicêtre AP-HP
IHU ican
Hôpital Pitié-Salpêtrière AP-HP
BioMaps
Gravity sensitivity and reversibility to bronchodilator at 3 T
30 healthy adults
30 asthmatic adults
30 COPD adults
Gravity sensitivity at 0.55 T
30 healthy adults
BioMaps
V|LF Spiro3D
Hôpital Bicêtre AP-HP
Severe asthma before and after biotherapy at 3 T
30 asthmatic adults
3D MR spirometry and FD-MRI to assess pulmonary complications of primary immunodeficiency diseases (PID) at 0.55 T
50 consecutive PID patients
HOPITAL FOCH
HOPITAL FOCH
Lung Transplant Recipients with and without bronchiolitis obliterans syndrome (BOS) at 1.5 T
30 adults with BOS
30 lung recipients without BOS
Gravity sensitivity at ultra-low field (0.1 T) and field cycling imaging
30 healthy adults
AMTCENTER
Erasmus MC
3D MR spirometry in children at 1.5 T
30 children with asthma
30 children with bronchopulmonary dysplasia
30 children with cystic fibrosis
Objectivation and alienation in patients' and practitioners' experience in all sites
80 patients (40 adults and 40 children)
10 practitioners
TILBURG UNIVERSITY

Figure 5.11

Résumé du travail doctoral

La recherche en imagerie pulmonaire a connu un essor considérable ces dernières années, avec un intérêt croissant pour l'imagerie par résonance magnétique (IRM) du noyau d'hydrogène qui a démontré sa capacité à quantifier la ventilation régionale à partir de protocoles simples et accessibles en pratique clinique. Le laboratoire BioMaps a développé une nouvelle méthode de quantification des dynamiques ventilatoires locales basées sur le tenseur de déformation de Green-Lagrange : la spirométrie 3D par IRM. Une séquence IRM dynamique à temps d'écho ultra-court associée à une trajectoire adaptative permet d'acquérir efficacement le signal du parenchyme pulmonaire au cours de la respiration libre en position allongée. A partir d'un cycle respiratoire moyen, le Jacobien des déformations et sa dérivée temporelle permettent d'inférer les courbes débit-volume pour chaque voxel du volume pulmonaire. La thèse vise à valider cette technique, à l'amener de la recherche fondamentale à la recherche clinique, et à approfondir la compréhension de la mécanique ventilatoire de poumons sains et obstrués.

Chapitre 1 - Physiopathologie du système respiratoire

Le système respiratoire humain est vital pour maintenir l'équilibre entre les besoins de l'organisme en dioxygène et son besoin d'éliminer les déchets de dioxyde de carbone en permettant les échanges entre l'intérieur du corps et l'environnement extérieur. Ce chapitre introduit la physiopathologie du système respiratoire. Spécifiquement l'anatomie arborescente du poumon, sa fonction, les principaux troubles respiratoires et les examens cliniques associés. Comprendre la physiopathologie du poumon humain est essentiel pour concevoir des stratégies diagnostiques et thérapeutiques efficaces, qui prennent en compte la variabilité de la respiration et sa nature tridimensionnelle.

Chapitre 2 - Imagerie du poumon en IRM

Les techniques d'imagerie permettent d'accéder à une sensibilité régionale et ainsi à une compréhension tensorielle de la physiopathologie pulmonaire. L'innocuité de l'IRM permet des études dynamiques et longitudinales de la fonction pulmonaire, et les progrès techniques augmentent et révèlent son potentiel pour caractériser pleinement la fonction pulmonaire locale. La théorie de l'IRM est présentée conjointement aux enjeux d'imagerie du poumon, avec des tissus hautement inhomogènes, ainsi que le mouvement de la respiration. Depuis les travaux de Bauman *et al.*, Kolb *et al.*, Boucneau *et al.*, l'IRM fonctionnelle pulmonaire est réalisable et prometteuse à partir d'acquisitions standards.

Un travail de revue de littérature des 5 dernières années a été réalisé pour identifier les principaux enjeux de la caractérisation locale de défauts de ventilation par IRM. Les différents biomarqueurs ont été recensés et classifiés selon les informations physiologiques portées, et sont présentés sur la figure 5.12. Les différences de nature physique des estimateurs de ventilation sont décrits. Dans la littérature, la variabilité de la distribution spatiale de la ventilation en fonction des volumes inhalés est relevée, malgré des définitions de défauts de ventilation aveugles aux variations spatiales nominales pour tous types de respirations.

Chapitre 3 - Développements méthodologiques pour la spirométrie 3D en IRM

L'objectif de cette thèse est de développer les travaux initiés par Boucneau *et al.*, en les amenant de la faisabilité à la recherche clinique. Du fait de son caractère multidimensionnel, la spirométrie 3D par IRM fournit des informations importantes sur la mécanique pulmonaire. Cependant, avant d'être éprouvée sur des cohorte de patients, la technique doit être questionnée et validée. Ce chapitre présente son cadre original et ses limites. Les développements méthodologiques entrepris au cours de ce travail doctoral sont ensuite présentés, avec en particulier

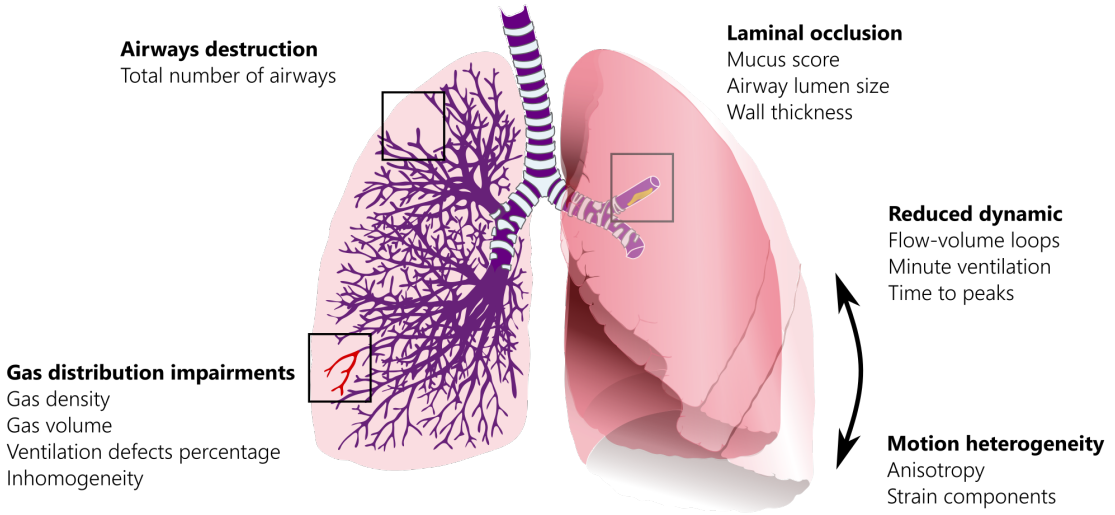

Figure 5.12: Revue des biomarqueurs de la fonction ventilatoire utilisés dans le diagnostic de pathologies obstructives pour l'IRM. Des informations physiologiques complémentaires peuvent ainsi être obtenues, sur la distribution des gaz, la dynamique, la structure ou les descripteurs de mouvement. Ces biomarqueurs permettent d'évaluer la destruction des voies respiratoires, l'occlusion laminaire, les altérations de la distribution locale des gaz et la réduction de l'hétérogénéité du mouvement dynamique. Les biomarqueurs structuraux locaux sont calculés uniquement à partir de l'IRM des gaz hyperpolarisés, tandis que les descripteurs dynamiques et de mouvement sont fournis par l'imagerie dynamique pulmonaire à l'hydrogène en IRM. Les biomarqueurs ventilatoires peuvent être combinés, lorsque disponibles, avec l'analyse des échanges gazeux et de la perfusion pour améliorer la sensibilité des dysfonctionnements pulmonaires.

une évaluation de la fiabilité des cartes paramétriques obtenues chez des volontaires sains respirant librement en position allongée. La chaîne d'acquisition et de traitement est représentée en figure 5.13.

En particulier, la reconstruction de la dynamique pulmonaire a été optimisée par un algorithme de rephasage des données optimisé dans un domaine analogue de la spirométrie. Une segmentation en quelques secondes du volume pulmonaire et de ses lobes a été réalisée avec un réseau de neurones convolutifs. La reconstruction des courbes débit-volumes a été améliorée pour être plus robuste aux variations temporelles, à la fois lors de l'estimation du champs de déformation, mais également lors de la dérivations des débits. Des biomarquers quantitatifs et absolus ont été extraits à partir de connaissances physiologiques issues de la spirométrie standard.

Le poumon humain étant un organe complexe à modéliser, de part ses tissus

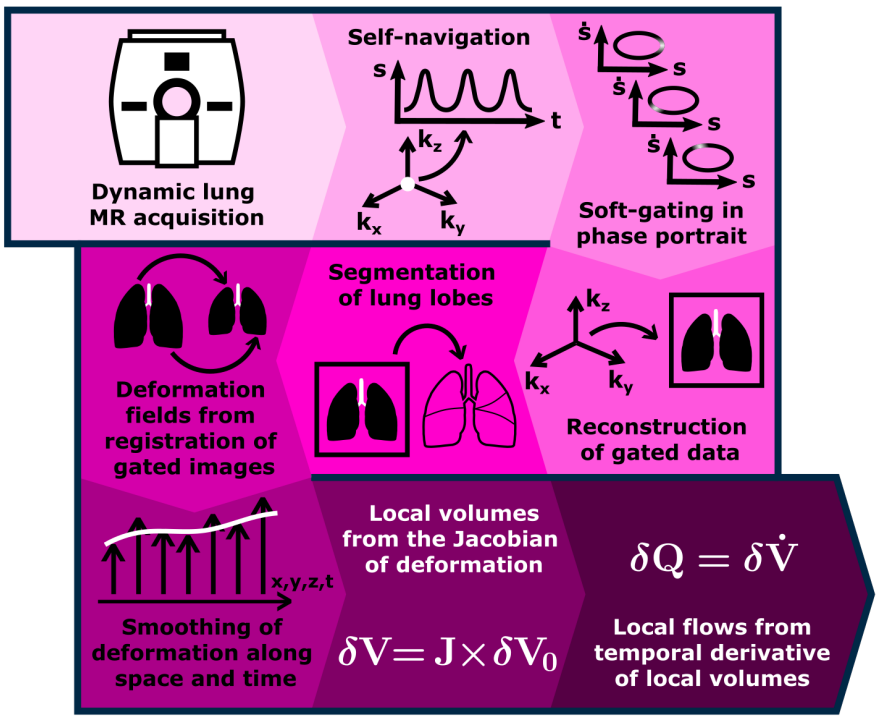

Figure 5.13: Pipeline de spirométrie 3D par IRM : acquisition dynamique en IRM pulmonaire 3D, rephasage rétrospectif des données sur un cycle respiratoire moyen, segmentation du volume pulmonaire et de ses lobes, calcul des champs de déformation, et quantification absolues des boucles débit-volume locales.

poro-élastiques et son mouvement cyclique irrégulier, la métrologie de la spirométrie 3D par IRM est complexe et difficile à décorréler de la physiologie. Dans ce travail doctoral, la fiabilité de la technique a été approchée selon deux critères : sa répétabilité et son exactitude. Une étude sur 25 volontaires sains respirant librement a été menée, avec des acquisitions répétées en décubitus ventral et dorsal. La répétabilité globale est excellente, avec des variations du même ordre que la variabiltié intrinsèque de la ventilation. Par ailleurs, les mesures globales correspondent aux mesures de la segmentation du volume pulmonaire. Localement, la variabilité est importante, mais la répétabilité reste satisfaisante au regard de la littérature. Les cartes obtenues sont néanmoins relativement différentes de celles obtenues par d'autres techniques, questionnant ainsi la consistance et la comparabilité des différentes méthodologies de l'IRM de la ventilation.

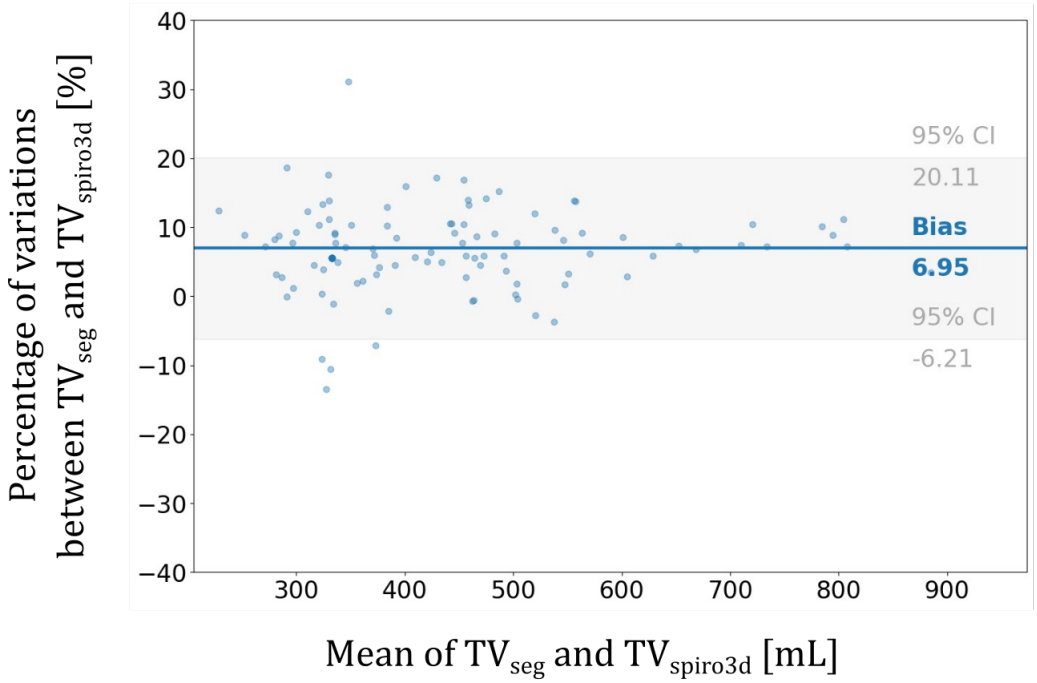

Figure 5.14: Graphique de Bland-Altman montrant l'accord entre les volumes courants globaux obtenus à partir de la segmentation des volumes pulmonaires (TV_{seg}) et l'intégration des volumes courants locaux mesurés par la spirométrie IRM 3D sur le poumon ($TV_{spiro3D}$). Un biais de 6.95% pour TV_{seg} indique une légère sous-estimation des volumes par la spirométrie 3D.

Chapitre 4 - Caractéristiques nominales de la fonction ventilatoire

La spirométrie IRM 3D a démontré sa capacité à produire des cartes paramétriques fiables, permettant d'accéder à la physiologie respiratoire régionale. Ce chapitre présente une étude prospective réalisée sur des volontaires sains afin de tester la sensibilité de cette méthode et d'explorer ses distributions nominales. Un changement de position des volontaires, de décubitus dorsal à ventral a été effectué afin d'évaluer la sensibilité de la technique à un phénomène physiologique connu : la dépendance de la ventilation à la gravité, induisant un gradient de ventilation vers la région la plus dépendante. Cette influence de la gravité sur la distribution de la ventilation du volume pulmonaire est un facteur majeur, mais pas le seul, démontrant l'existence d'inhomogénéités intrinsèques à la respiration libre.

Pour explorer la distribution spatiale de la ventilation, nous avons appliqué des stratégies de normalisation pour étudier les motifs nominaux de la ventilation pulmonaires régionalement. Ces normalisation permettent non seulement de faire correspondre les morphologies, mais également de pallier aux différences de capacité pulmonaires correspondantes et à la variabilité globale de la ventilation. Des atlas ont été établis, avec des motifs reproductibles de la ventilation sur la cohorte.

Chapitre 5 - Résultats préliminaires de spirométrie 3D par IRM sur des syndrômes restrictifs et obstructifs

Le développement de la spirométrie par IRM 3D a permis de mettre en évidence les motifs de ventilation régionale. Ce chapitre explore sa capacité à diagnostiquer les motifs propres aux pathologies obstructives et restrictives à travers plusieurs études de cas, en proposant des nouveaux protocoles d'analyse. Pour cela les connaissances des biomarqueurs courants de spirométrie standard sont combinés avec les connaissances pathophysiologiques propres à chaque pathologie étudiée : les maladies neuromusculaires, le syndrome de COVID-19 longue durée, ainsi que l'asthme et la BPCO.

Les études de cas ont permis de révéler des résultats concordant aux connaissances physiopathologiques et ouvrant de nouvelles pistes d'études sur des cohortes. Ces études soulignent l'intérêt à clarifier les modes respiratoires chez les patients de syndromes restrictifs, en particulier pour évaluer des dysfonctionnements au niveau des muscles respiratoires thoraciques et diaphragmatiques. Par exemple, nous avons observé chez un patient souffrant d'une dystrophie musculaire facio-scapulo-humérale qu'il présentait une ventilation globale faible avec une forte contribution du diaphragme. Dans le cas du COVID-19 long, nous avons observé une fonction diaphragmatique réduite avec une utilisation accrue des muscles thoraciques.

Ce chapitre présente également des résultats préliminaires sur une étude prospective de cohorte. La population incluse jusqu'ici et étudiée comportait 3 patients asthmatiques, 4 patients atteints de BPCO et 14 volontaires sains. L'analyse a

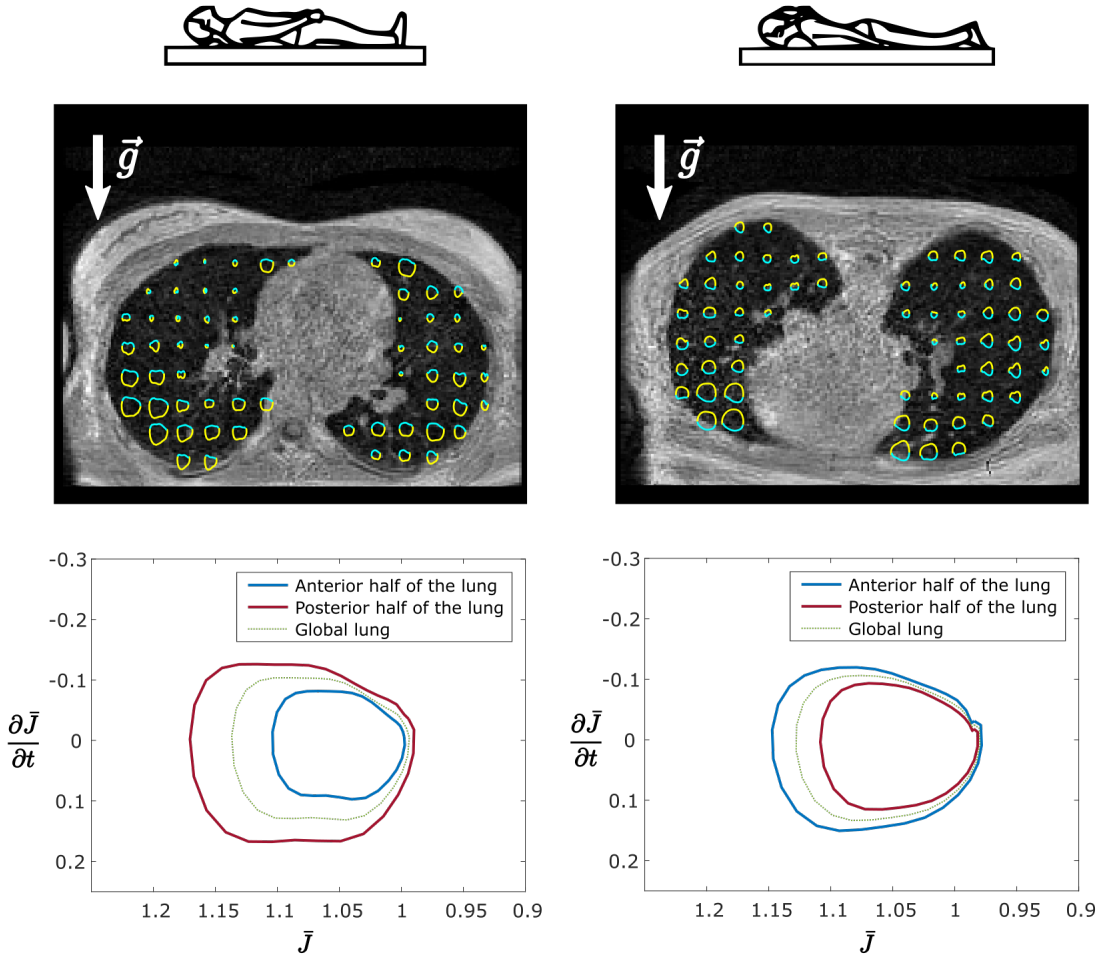

Figure 5.15: Résultats de spirométrie 3D par IRM chez un volontaire sain en décubitus dorsal (à gauche) et ventral (à droite). Ici les courbes spirométriques correspondent au Jacobien en fonction de la dérivée temporelle du Jacobien. Sur une coupe axiale des poumons, les courbes spirométriques locales sont représentées (en haut, avec un voxel sur 20 représenté pour une meilleure visibilité). L'aire des boucles augmente vers la région la plus dépendante. La ligne inférieure montre la moyenne des boucles spirométriques sur les régions antérieurs et postérieurs du poumon. Les boucles de volume d'écoulement globales sur le poumon sont similaires en décubitus dorsal ou ventral. Cependant, lorsqu'elles sont intégrées sur les moitiés antérieures et postérieures, les boucles diffèrent largement entre les régions dépendantes et non dépendantes, ce qui confirme la sensibilité à la gravité de la spirométrie IRM 3D.

testé la sensibilité de la spirométrie par IRM 3D aux effets des bronchodilatateurs et de la biothérapie. Les résultats ont montré une amélioration notable chez les patients asthmatiques, tandis que les patients BPCO n'ont pas montré de changements significatifs indiquant une réduction de l'obstruction des voies respiratoires et du piégeage de l'air. Ces découvertes initiales doivent être confirmées par une étude plus vaste pour affirmer leur signification et envisager l'utilisation de l'apprentissage automatique pour classifier les patients et identifier des sous-groupes pertinents. L'étude a aussi mis en évidence l'efficacité de la biothérapie dans la réduction du piégeage de l'air chez un patient asthmatique sévère.

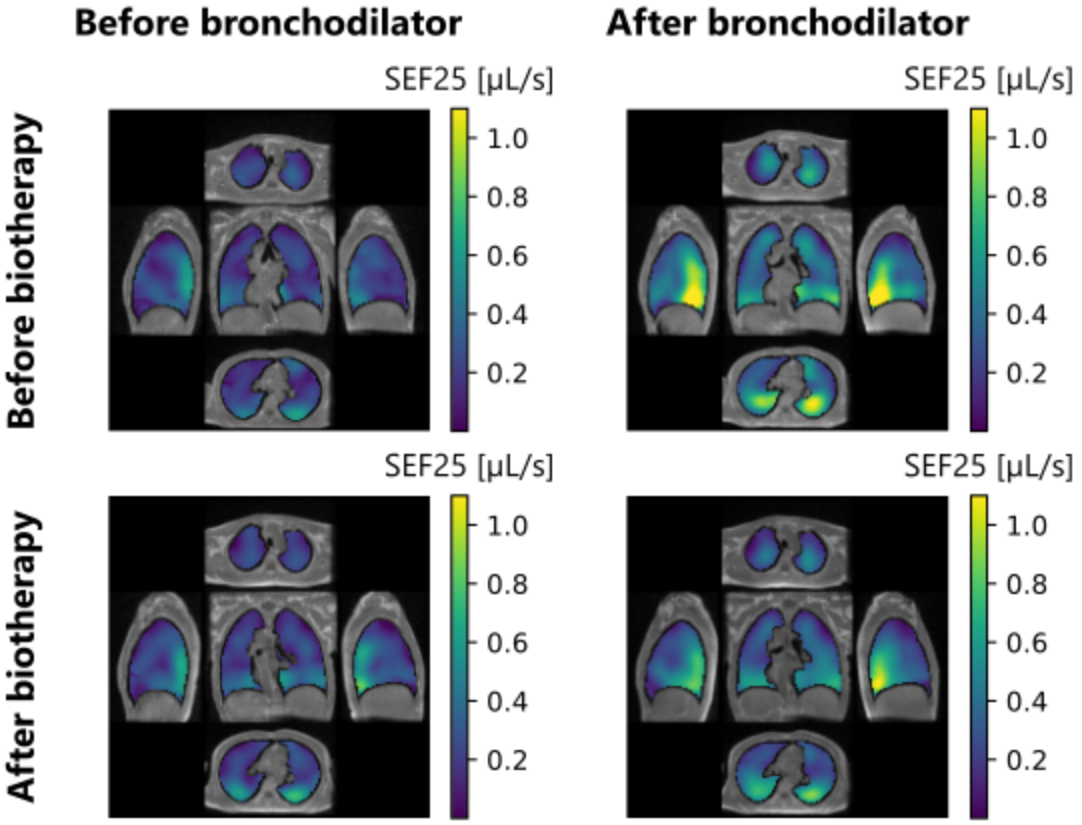

Figure 5.16: Vues axiales, sagittales et coronales des débits à 25% de volume expiratoire restant (SEF25) pour un patient souffrant d'asthme sévère avant et après bronchodilatation (lignes), avant et après biothérapie (colonnes). Les vues sont tracées pour une coupe coronale centrale, deux coupes axiales dans le poumon apical et basal, et deux coupes sagittales dans les poumons droit et gauche. Le SEF25 augmente légèrement après la biothérapie, et la réversibilité à un bronchodilatateur est réduite après la biothérapie. Ces résultats suggèrent une amélioration de la fonction ventilatoire après une biothérapie, qui devra être validée sur d'autres patients.

Conclusion

La spirométrie 3D par IRM est une technique récente qui a le potentiel de fournir une estimation quantitative fiable de la dynamique et de la mécanique ventilatoire. Des améliorations significatives au niveau de la méthodologie et de la robustesse de la spirométire 3D ont été proposées au cours de ce travail de thèse, ce qui a conduit à des performances de sensibilité prometteuses et à une fiabilité accrue dans le cadre d'un protocole IRM en respiration libre. Le cadre méthodologique proposé offre de grandes perspectives afin de permettre une cartographie spatiale précise et un suivi de la fonction respiratoire en milieu clinique.

Appendices

Euclidean atlases of the healthy ventilatory function

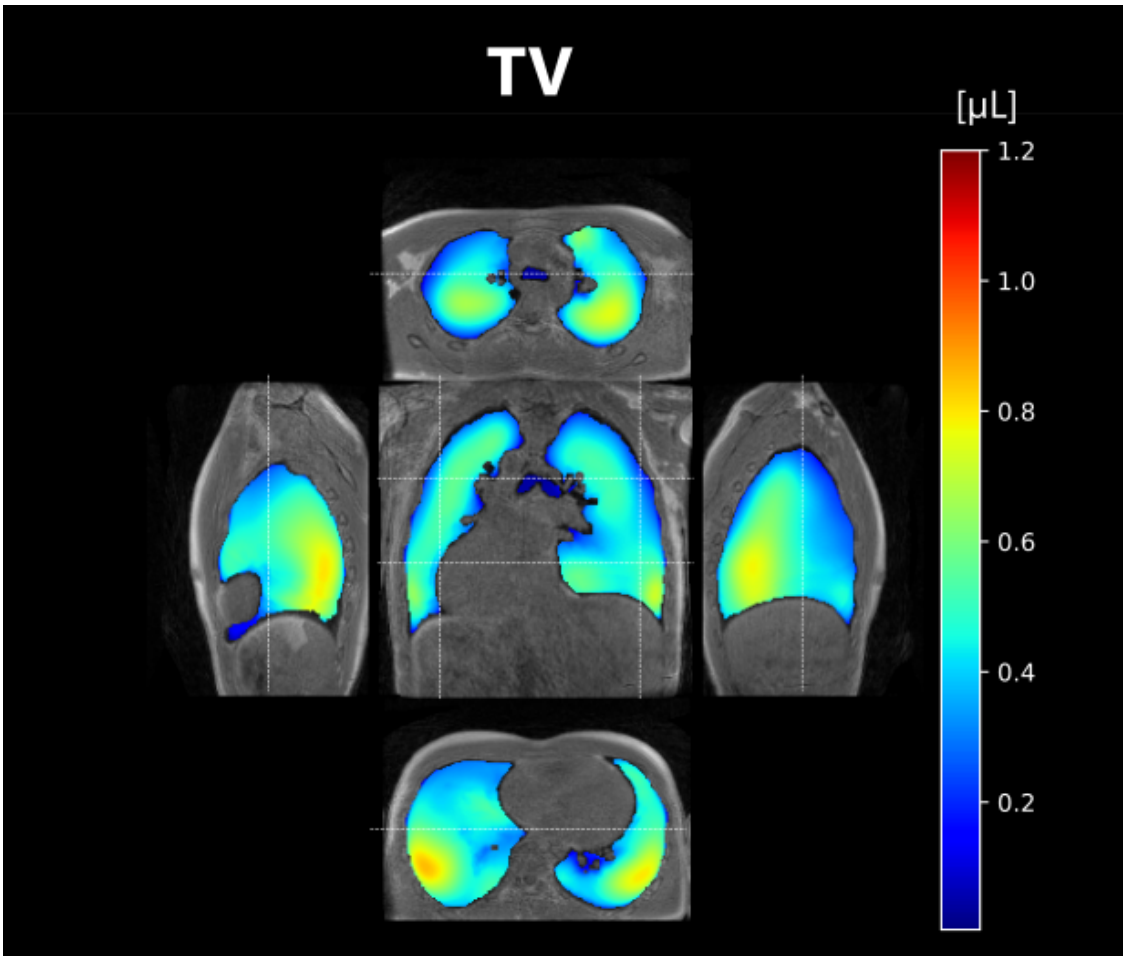

Figure 17: Exploded views of local tidal volumes (TV) atlas computed over 25 healthy volunteers freely breathing in the supine position. The atlas was built after elastic registration of individual parametric maps and global feature scaling on a reference dataset. White dash lines indicate the positions of the central coronal view, side right and left sagittal views, and apical and basal axial views.

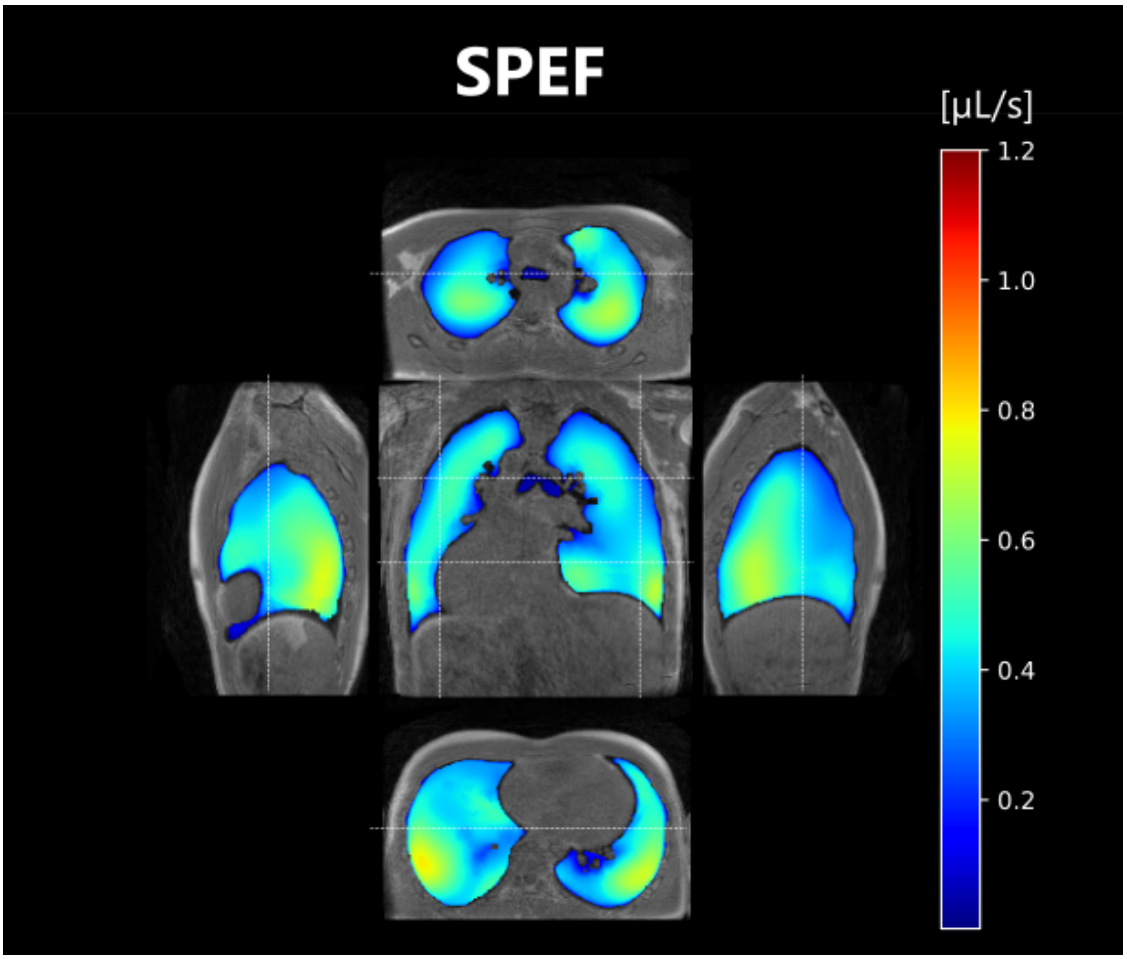

Figure 18: Exploded views of local peak expiratory flows (SPEF) atlas computed over 25 healthy volunteers freely breathing in the supine position. The atlas was built after elastic registration of individual parametric maps and global feature scaling on a reference dataset. White dash lines indicate the positions of the central coronal view, side right and left sagittal views, and apical and basal axial views.

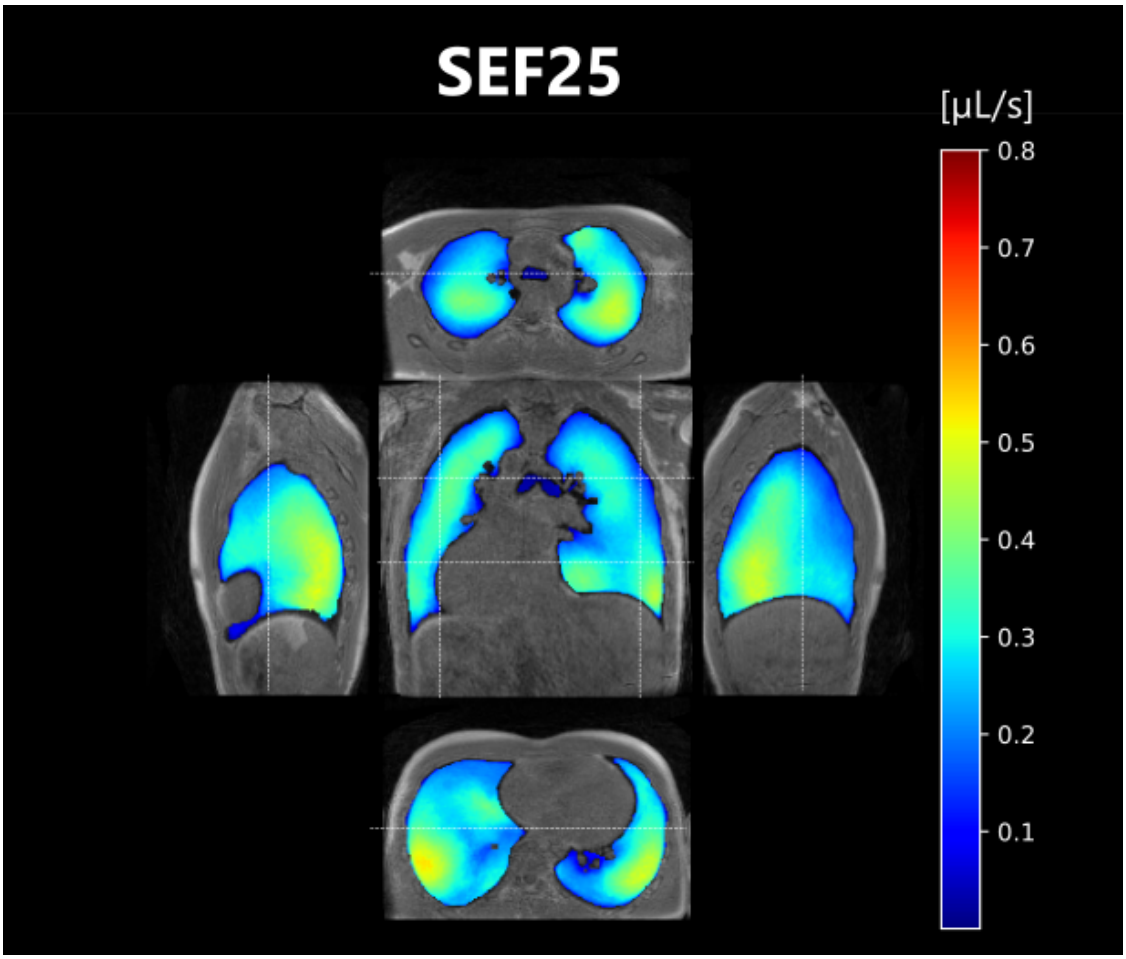

Figure 19: Exploded views of local flows at remaining 25% of expiration (SEF25) atlas computed over 25 healthy volunteers freely breathing in the supine position. The atlas was built after elastic registration of individual parametric maps and global feature scaling on a reference dataset. White dash lines indicate the positions of the central coronal view, side right and left sagittal views, and apical and basal axial views.

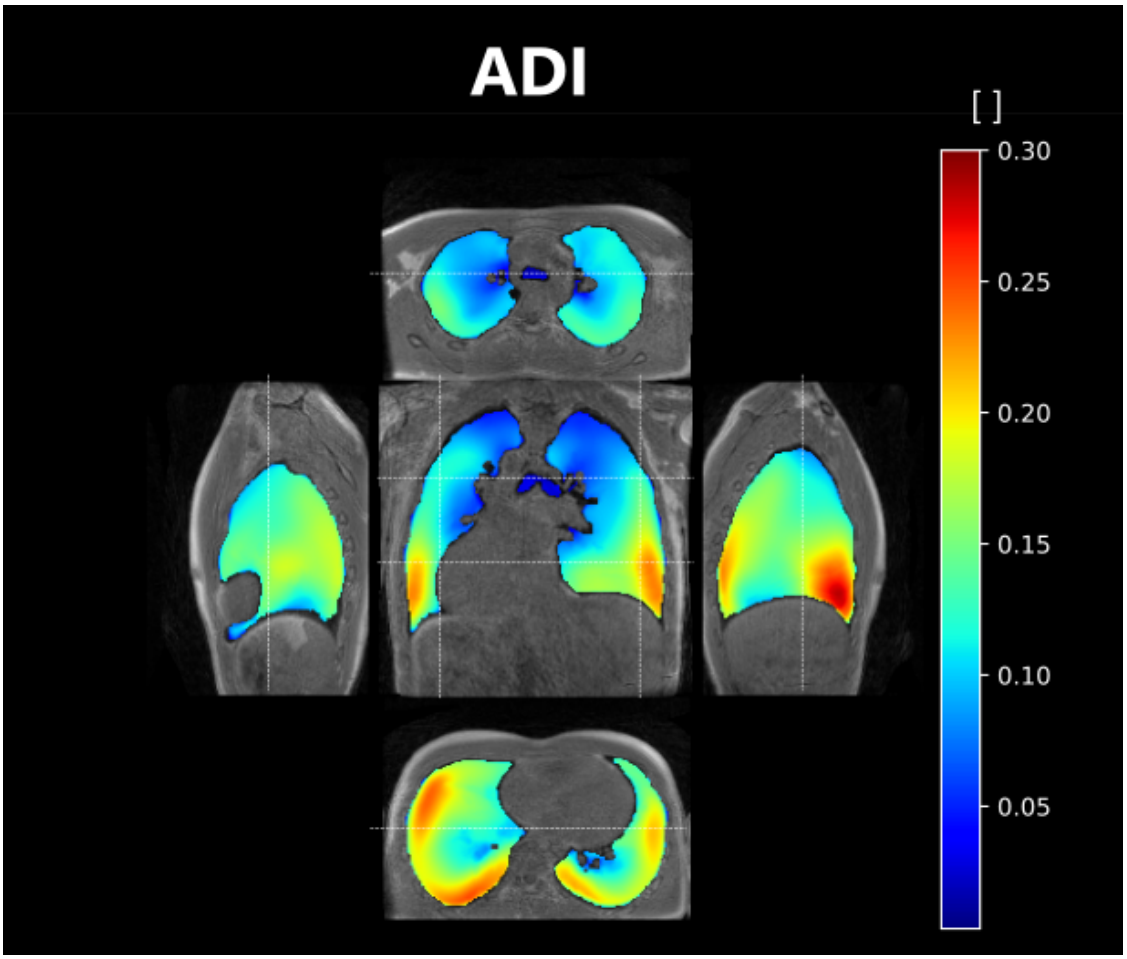

Figure 20: Exploded views of local anisotropic deformation index (ADI) atlas computed over 25 healthy volunteers freely breathing in the supine position. The atlas was built after elastic registration of individual parametric maps and global feature scaling on a reference dataset. White dash lines indicate the positions of the central coronal view, side right and left sagittal views, and apical and basal axial views.

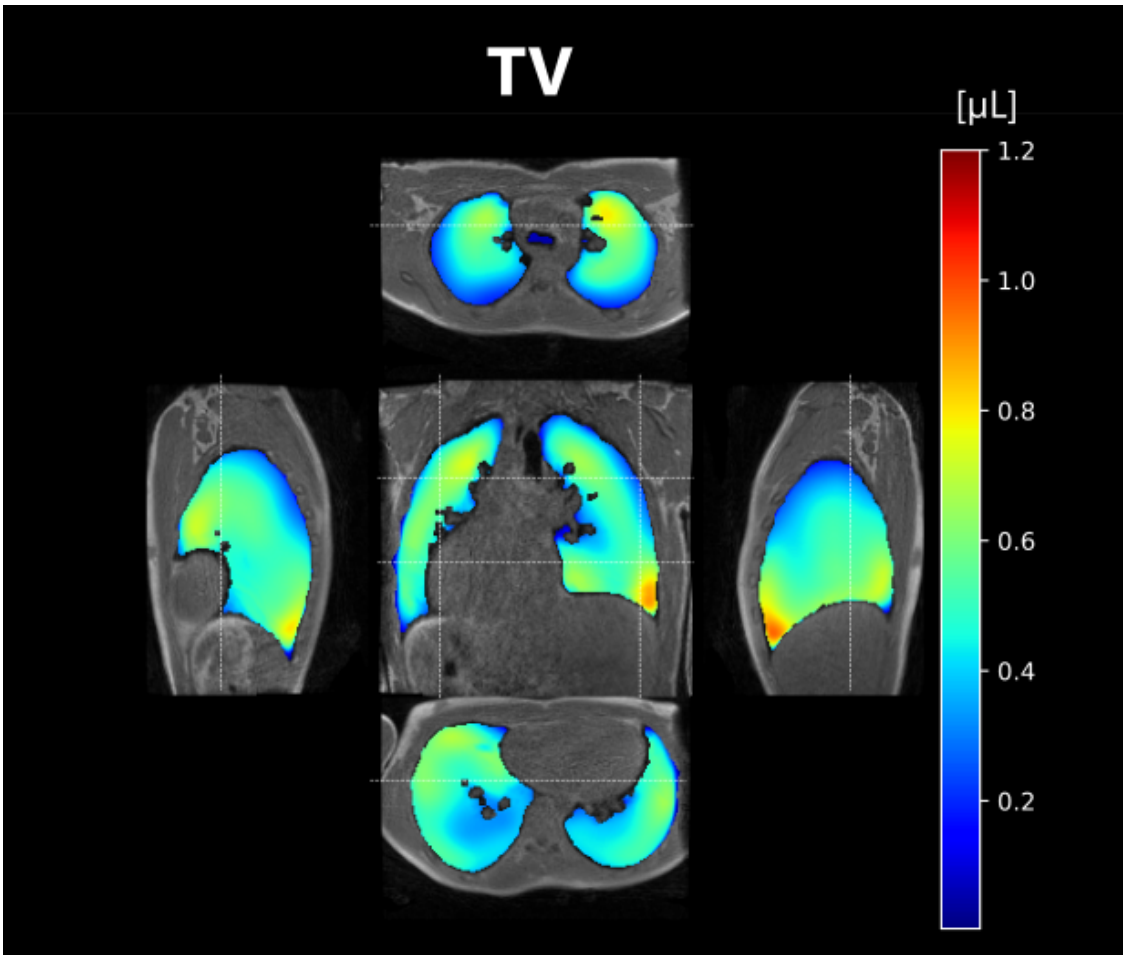

Figure 21: Exploded views of local tidal volumes (TV) atlas computed over 25 healthy volunteers freely breathing in the prone position. The atlas was built after elastic registration of individual parametric maps and global feature scaling on a reference dataset. White dash lines indicate the positions of the central coronal view, side right and left sagittal views, and apical and basal axial views.

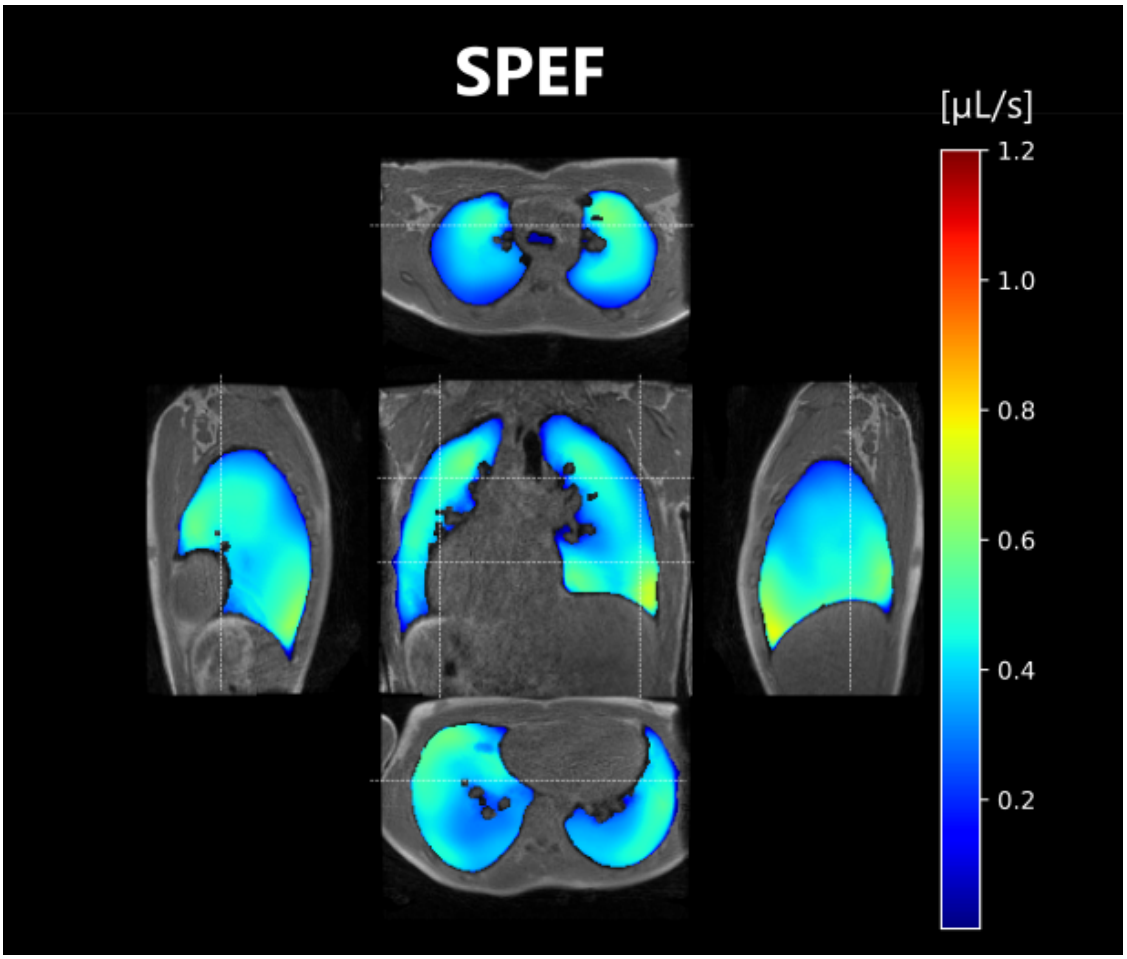

Figure 22: Exploded views of local peak expiratory flows (SPEF) atlas computed over 25 healthy volunteers freely breathing in the prone position. The atlas was built after elastic registration of individual parametric maps and global feature scaling on a reference dataset. White dash lines indicate the positions of the central coronal view, side right and left sagittal views, and apical and basal axial views.

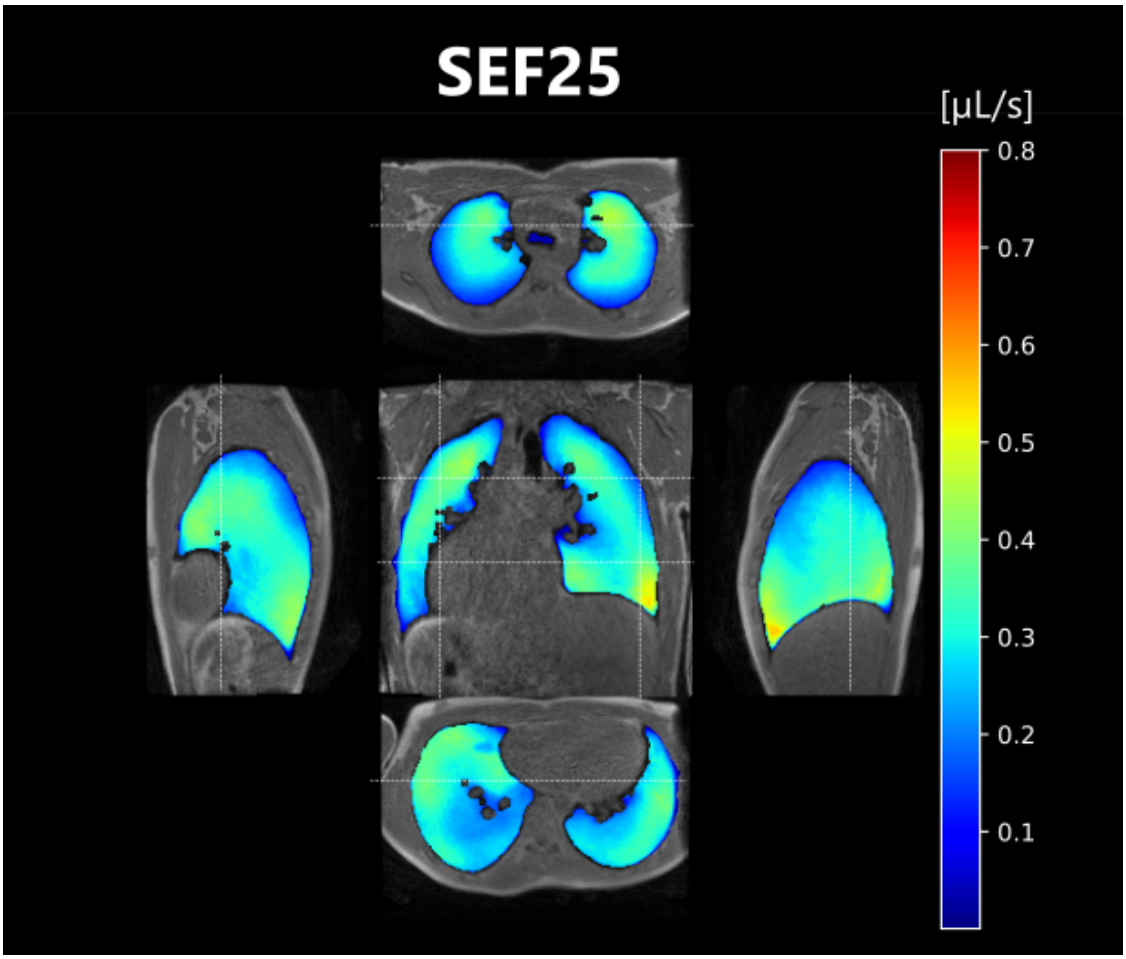

Figure 23: Exploded views of local flows at remaining 25% of expiration (SEF25) atlas computed over 25 healthy volunteers freely breathing in the prone position. The atlas was built after elastic registration of individual parametric maps and global feature scaling on a reference dataset. White dash lines indicate the positions of the central coronal view, side right and left sagittal views, and apical and basal axial views.

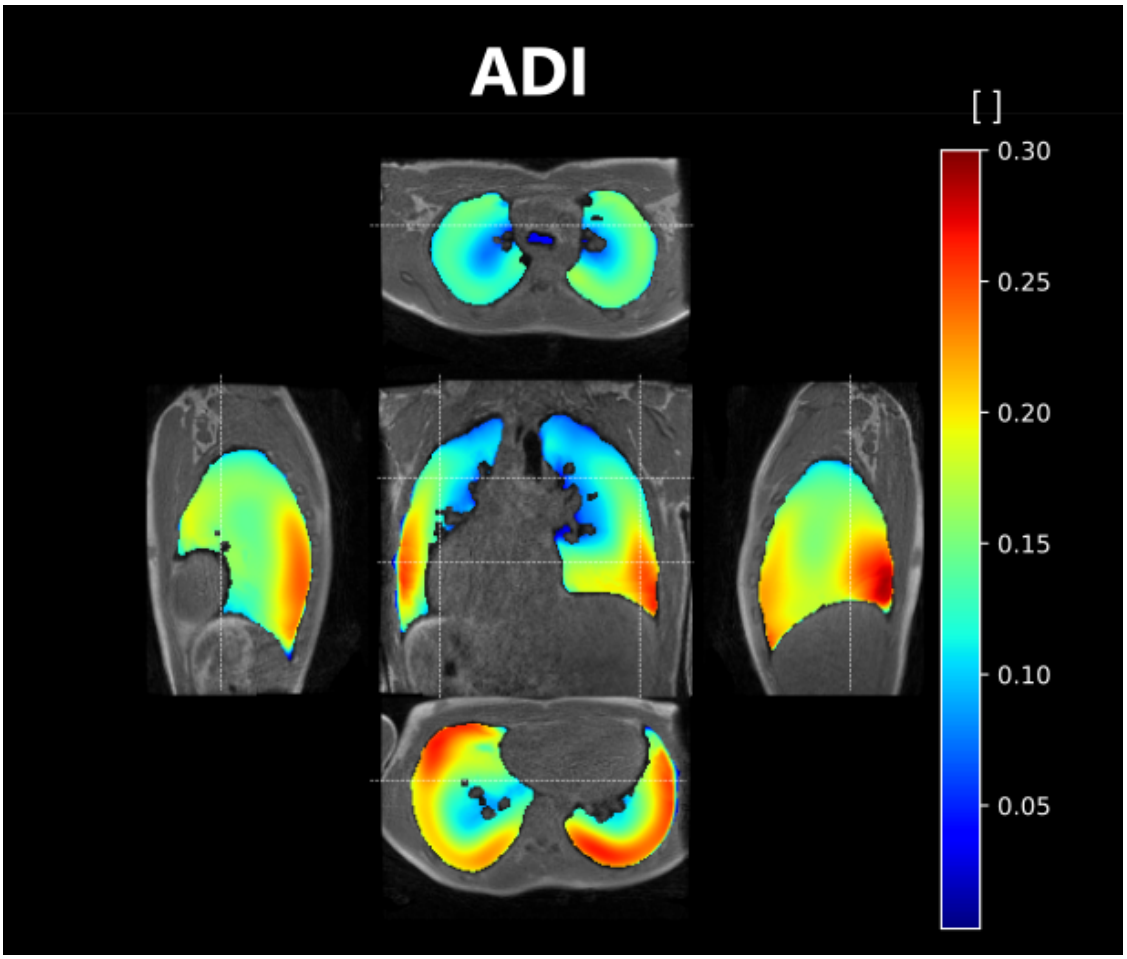

Figure 24: Exploded views of local anisotropic deformation index (ADI) atlas computed over 25 healthy volunteers freely breathing in the prone position. The atlas was built after elastic registration of individual parametric maps and global feature scaling on a reference dataset. White dash lines indicate the positions of the central coronal view, side right and left sagittal views, and apical and basal axial views.

Reference dataset

	Reference healthy volunteer
Sex	M
Age (year)	27
Height (cm)	185
Weight (kg)	70

Table 10: Main characteristics of the reference healthy volunteer.

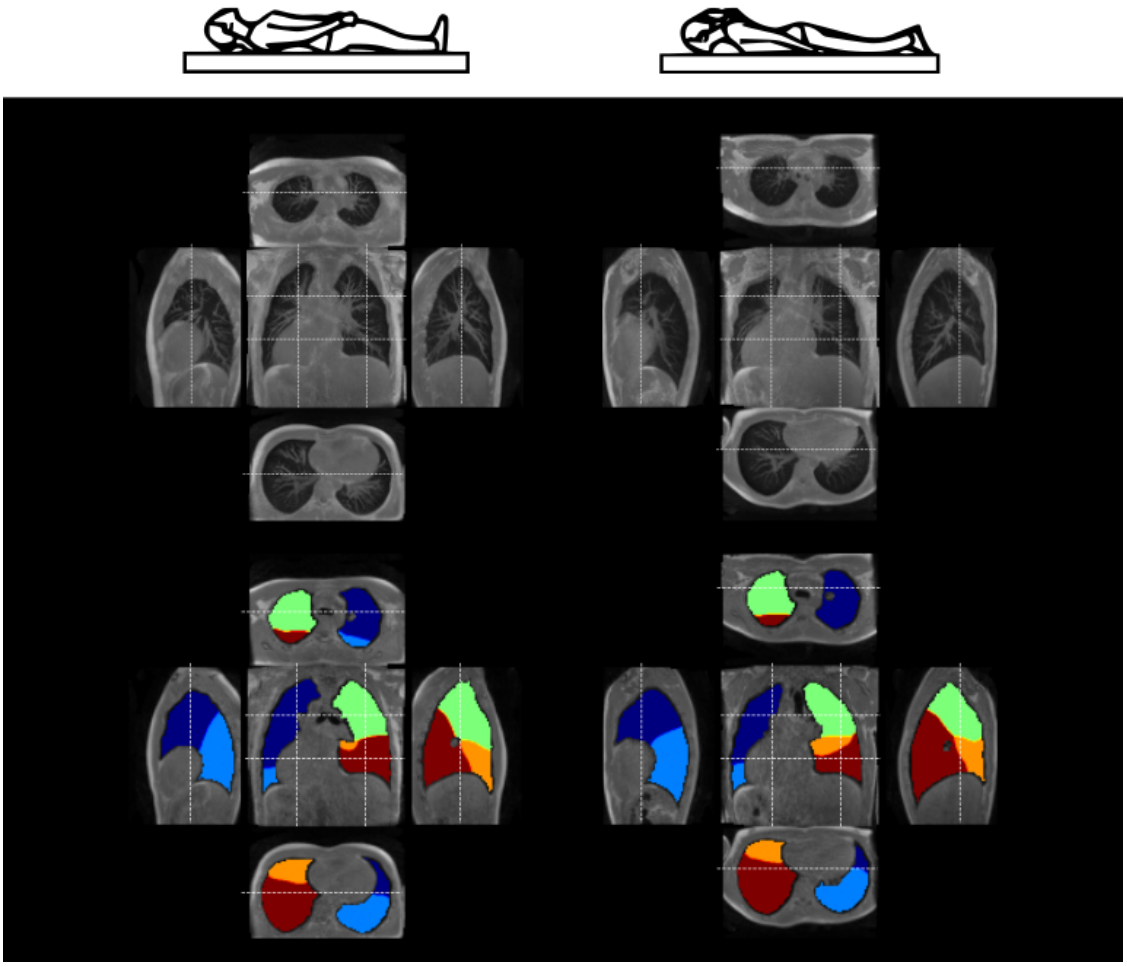

Figure 25: Maximal intensity projections (top) over 3 cm for coronal, sagittal, and axial views of the reference dataset used in Chapter 4 for normalization. The lung lobe segmentation performed by the ARTEMIS team (bottom) is displayed. The images correspond to the end-of-expiratory state for the lying supine (left) and lying prone (right) positions. The healthy volunteer is a 27-year-old male included in February 2021. White dash lines indicate the positions of the central coronal view, side right and left sagittal views, and apical and basal axial views.

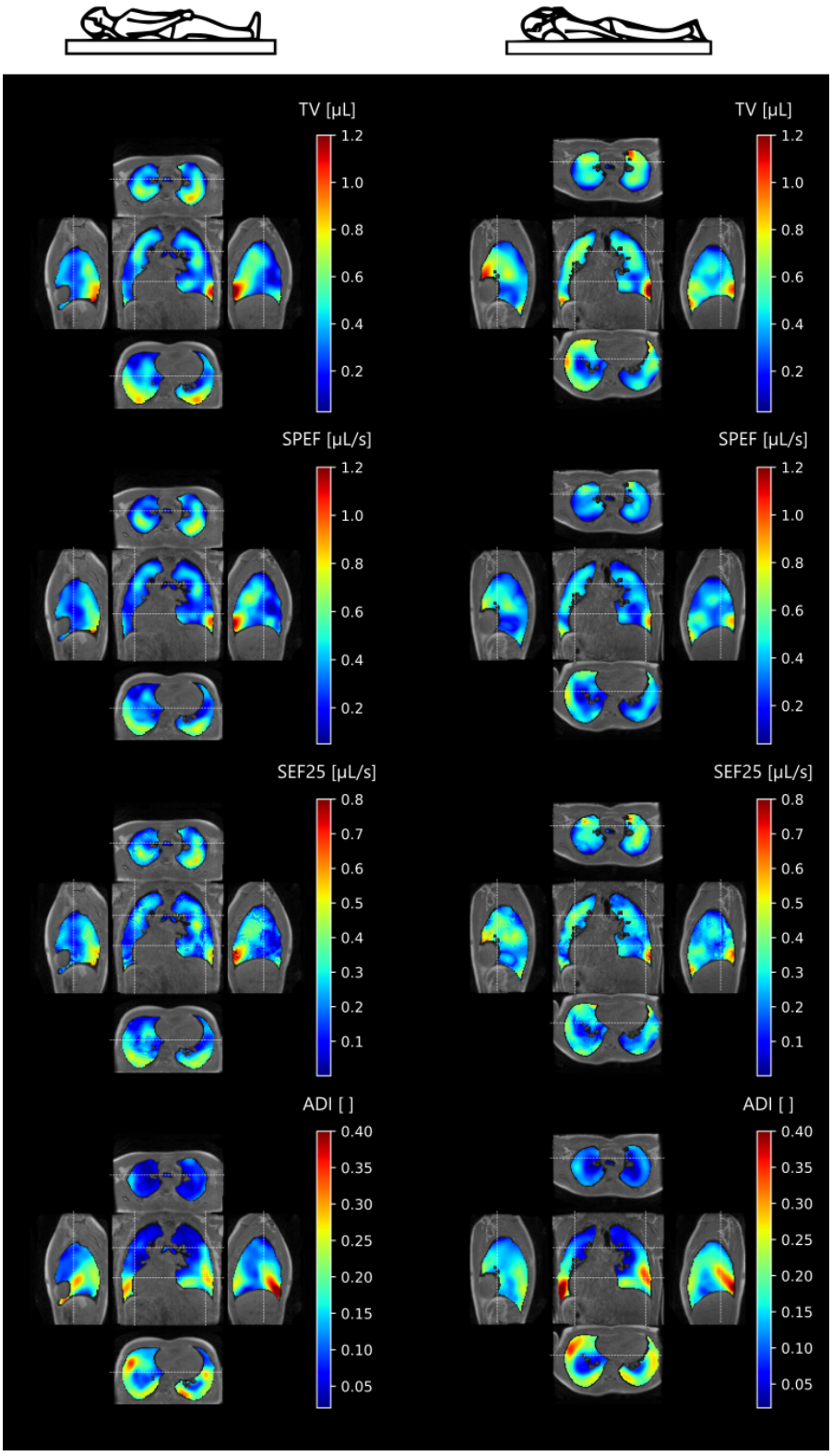

Figure 26: Exploded views of TV, SPEF, SEF25, ADI for the supine and prone position obtained on the reference dataset used in Chapter 4 for normalization. White dash lines indicate the positions of the central coronal view, side right and left sagittal views, and apical and basal axial views. The healthy volunteer is a 27-year-old male of 70 kg and 185 cm in height. He was included in February 2021 and underwent 3D MR spirometry exam for the protocol described in Chapter 4.

References

[1] Camillo Peracchia and Nasr Anaizi. “Lung function in health and disease. Basic concepts of respiratory physiology and pathophysiology”. Mar. 2014.

[2] Matthias Ochs et al. “The Number of Alveoli in the Human Lung”. *American Journal of Respiratory and Critical Care Medicine*, 2004. DOI: 10.1164/rccm.200308-1107OC.

[3] E. R. Weibel. “What makes a good lung?” *Swiss Medical Weekly*, 2009. DOI: 10.4414/smw.2009.12270.

[4] P. Gehr, M. Bachofen, and E. R. Weibel. “The normal human lung: ultrastructure and morphometric estimation of diffusion capacity”. *Respiration Physiology*, 1978. DOI: 10.1016/0034-5687(78)90104-4.

[5] Kohn Hans. “Zur Histologie der Indurirenden Fibrinosen Pneumonie”. *Muench Med Wochnschr*, 1893.

[6] Bertrand Maury, Delphine Salort, and Christine Vannier. “Trace theorems for trees and application to the human lungs”. *Networks and Heterogeneous Media*, 2009. DOI: 10.3934/nhm.2009.4.469.

[7] Deniz Inal-Ince and Aslihan Cakmak. “Chapter 19 - Kinesiology of respiration”. In: *Comparative Kinesiology of the Human Body*. Ed. by Salih Angin and Ibrahim Engin Şimşek. Academic Press, Jan. 2020. DOI: 10.1016/B978-0-12-812162-7.00019-9.

[8] John B. West. “Ventilation-Perfusion Relationships”. *American Review of Respiratory Disease*, 1977. DOI: 10.1164/arrd.1977.116.5.919.

[9] John Palmer, Ulrika Bitzén, Björn Jonson, and Marika Bajc. “Comprehensive Ventilation/Perfusion SPECT”. *Journal of Nuclear Medicine*, 2001.

[10] X. Baur et al. “Lung Function Testing: The Dilemma of Predicted Values in Relation to the Individual Variability”. *Respiration*, 2009. DOI: 10.1159/000196531.

[11] Graham L. Hall et al. “Official ERS technical standard: Global Lung Function Initiative reference values for static lung volumes in individuals of European ancestry”. *The European Respiratory Journal*, 2021. DOI: 10.1183/13993003.00289-2020.

[12] Robert B. Schoene. “Limits of human lung function at high altitude”. *Journal of Experimental Biology*, 2001. DOI: 10.1242/jeb.204.18.3121.

[13] Boris I. Medarov, Valentin A. Pavlov, and Leonard Rossoff. “Diurnal Variations in Human Pulmonary Function”. *International Journal of Clinical and Experimental Medicine*, 2008.

[14] S. A. Shea and A. Guz. “Personnalité ventilatoire — An overview”. *Respiration Physiology*, 1992. DOI: 10.1016/0034-5687(92)90012-L.

[15] G. Benchetrit, S. A. Shea, T. P. Dinh, S. Bodocco, P. Baconnier, and A. Guz. "Individuality of breathing patterns in adults assessed over time". *Respiration Physiology*, 1989. DOI: 10.1016/0034-5687(89)90064-9.

[16] J. Milic-Emili, J. A. Henderson, M. B. Dolovich, D. Trop, and K. Kaneko. "Regional distribution of inspired gas in the lung". *Journal of Applied Physiology*, 1966. DOI: 10.1152/jappl.1966.21.3.749.

[17] Michael A. Roman, Harry B. Rossiter, and Richard Casaburi. "Exercise, ageing and the lung". *European Respiratory Journal*, 2016. DOI: 10.1183/13993003.00347-2016.

[18] Joan B. Soriano et al. "Prevalence and attributable health burden of chronic respiratory diseases, 1990–2017: a systematic analysis for the Global Burden of Disease Study 2017". *The Lancet Respiratory Medicine*, 2020. DOI: 10.1016/S2213-2600(20)30105-3.

[19] A. V. Raveendran, Rajeev Jayadevan, and S. Sashidharan. "Long COVID: An overview". *Diabetes & Metabolic Syndrome: Clinical Research & Reviews*, 2021. DOI: 10.1016/j.dsx.2021.04.007.

[20] Pedro J. Martinez-Pitre, Bhanusivakumar R. Sabbula, and Marco Cascella. "Restrictive Lung Disease". In: *StatPearls*. Treasure Island (FL): StatPearls Publishing, 2023.

[21] Earl S. Ford, David M. Mannino, Anne G. Wheaton, Wayne H. Giles, Letitia Presley-Cantrell, and Janet B. Croft. "Trends in the Prevalence of Obstructive and Restrictive Lung Function Among Adults in the United States". *Chest*, 2013. DOI: 10.1378/chest.12-1135.

[22] Bhavika Kaul, Vincent Cottin, Harold R. Collard, and Claudia Valenzuela. "Variability in Global Prevalence of Interstitial Lung Disease". *Frontiers in Medicine*, 2021. DOI: 10.3389/fmed.2021.751181.

[23] Stephanie M. Levine and Darcy D. Marciniuk. "Global Impact of Respiratory Disease". *Chest*, 2022. DOI: 10.1016/j.chest.2022.01.014.

[24] Theo Vos et al. "Global, regional, and national incidence, prevalence, and years lived with disability for 310 diseases and injuries, 1990–2015: a systematic analysis for the Global Burden of Disease Study 2015". *The Lancet*, 2016. DOI: 10.1016/S0140-6736(16)31678-6.

[25] GBD 2019 Diseases and Injuries Collaborators. "Global burden of 369 diseases and injuries in 204 countries and territories, 1990-2019: a systematic analysis for the Global Burden of Disease Study 2019". *Lancet (London, England)*, 2020. DOI: 10.1016/S0140-6736(20)30925-9.

[26] Enrique Diaz-Guzman, Kevin McCarthy, Alan Siu, and James K. Stoller. "Frequency and causes of combined obstruction and restriction identified in pulmonary function tests in adults". *Respiratory Care*, 2010.

[27] Philip H. Quanjer et al. "Multi-ethnic reference values for spirometry for the 3-95-yr age range: the global lung function 2012 equations". *The European Respiratory Journal*, 2012. DOI: 10.1183/09031936.00080312.

[28] Cole Bowerman et al. “A Race-neutral Approach to the Interpretation of Lung Function Measurements”. *American Journal of Respiratory and Critical Care Medicine*, 2023. DOI: 10.1164/rccm.202205-0963OC.

[29] Claudio Tantucci, Damiano Bottone, Andrea Borghesi, Michele Guerini, Federico Quadri, and Laura Pini. “Methods for Measuring Lung Volumes: Is There a Better One?” *Respiration*, 2016. DOI: 10.1159/000444418.

[30] Kindred Grey. “Lung volumes detected by spirometry”. Jan. 2022.

[31] John-B. West. “La physiologie respiratoire”. 6e édition. Maloine, Nov. 2003.

[32] Paul D. Robinson, Michael D. Goldman, and Per M. Gustafsson. “Inert Gas Washout: Theoretical Background and Clinical Utility in Respiratory Disease”. *Respiration*, 2009. DOI: 10.1159/000225373.

[33] Xiaosong Wang, Yifan Peng, Le Lu, Zhiyong Lu, Mohammadhadi Bagheri, and Ronald M. Summers. “ChestX-ray8: Hospital-scale Chest X-ray Database and Benchmarks on Weakly-Supervised Classification and Localization of Common Thorax Diseases”. In: *2017 IEEE Conference on Computer Vision and Pattern Recognition (CVPR)*. July 2017. DOI: 10.1109/CVPR.2017.369.

[34] Thomas Flohr, Martin Petersilka, Andre Henning, Stefan Ulzheimer, Jiri Ferda, and Bernhard Schmidt. “Photon-counting CT review”. *Physica Medica*, 2020. DOI: 10.1016/j.ejmp.2020.10.030.

[35] Matthias Michael Woeltjen et al. “Low-Dose High-Resolution Photon-Counting CT of the Lung: Radiation Dose and Image Quality in the Clinical Routine”. *Diagnostics*, 2022. DOI: 10.3390/diagnostics12061441.

[36] E. Immonen et al. “The use of deep learning towards dose optimization in low-dose computed tomography: A scoping review”. *Radiography*, 2022. DOI: 10.1016/j.radi.2021.07.010.

[37] Paul J. Roach, Geoffrey P. Schembri, and Dale L. Bailey. “V/Q Scanning Using SPECT and SPECT/CT”. *Journal of Nuclear Medicine*, 2013. DOI: 10.2967/jnumed.113.124602.

[38] Michael Puderbach and Hans-Ulrich Kauczor. “Can lung MR replace lung CT?” *Pediatric Radiology*, 2008. DOI: 10.1007/s00247-008-0844-7.

[39] F. Bloch. “The Principle of Nuclear Induction”. *Science (New York, N.Y.)*, 1953. DOI: 10.1126/science.118.3068.425.

[40] Robert W. Brown, Y.-C. Norman Cheng, E. Mark Haacke, Michael R. Thompson, and Ramesh Venkatesan. “Magnetic Resonance Imaging: Physical Principles and Sequence Design”. 2e édition. Wiley-Blackwell, May 2014.

[41] Matt A. Bernstein, Kevin F. King, and Xiaohong Joe Zhou. “Handbook of MRI Pulse Sequences”. 1st edition. Amsterdam ; Boston: Academic Press, Sept. 2004.

[42] Hans-Ulrich Kauczor and Mark Oliver Wielpütz. “MRI of the Lung”. Softcover reprint of the original 2nd ed. 2018 édition. Springer Nature Switzerland AG, Dec. 2019.

[43] Lars G. Hanson. “Is quantum mechanics necessary for understanding magnetic resonance?” *Concepts in Magnetic Resonance Part A*, 2008. DOI: 10.1002/cmr.a.20123.

[44] M. N. Hood, V. B. Ho, J. G. Smirniotopoulos, and J. Szumowski. "Chemical shift: the artifact and clinical tool revisited". *Radiographics: A Review Publication of the Radiological Society of North America, Inc*, 1999. DOI: 10.1148/radiographics.19.2.g99mr07357.

[45] Devesh Raj, Derek P. Paley, Adam W. Anderson, Richard P. Kennan, and John C. Gore. "A model for susceptibility artefacts from respiration in functional echo-planar magnetic resonance imaging". *Physics in Medicine & Biology*, 2000. DOI: 10.1088/0031-9155/45/12/321.

[46] C J Bergin, G H Glover, and J M Pauly. "Lung parenchyma: magnetic susceptibility in MR imaging." *Radiology*, 1991. DOI: 10.1148/radiology.180.3.1871305.

[47] Hiroto Hatabu et al. "Expanding Applications of Pulmonary MRI in the Clinical Evaluation of Lung Disorders: Fleischner Society Position Paper". *Radiology*, 2020. DOI: 10.1148/radiol.2020201138.

[48] R. Pethig and D. B. Kell. "The passive electrical properties of biological systems: their significance in physiology, biophysics and biotechnology". *Physics in Medicine & Biology*, 1987. DOI: 10.1088/0031-9155/32/8/001.

[49] Jiangsheng Yu, Yiqun Xue, and Hee Kwon Song. "Comparison of Lung T2* During Free-Breathing at 1.5T and 3.0T with Ultrashort Echo Time (UTE) Imaging". *Magnetic Resonance in Medicine*, 2011. DOI: 10.1002/mrm.22829.

[50] Charlotte Zaeske, Gert-Peter Brueggemann, Steffen Willwacher, Daniela Maehlich, David Maintz, and Grischa Bratke. "The behaviour of T2* and T2 relaxation time in extrinsic foot muscles under continuous exercise: A prospective analysis during extended running". *PLOS ONE*, 2022. DOI: 10.1371/journal.pone.0264066.

[51] P. C. Lauterbur. "Magnetic resonance zeugmatography". *Pure and Applied Chemistry*, 1974. DOI: 10.1351/pac197440010149.

[52] P. Mansfield. "Proton spin imaging by nuclear magnetic resonance". *Contemporary Physics*, 1976. DOI: 10.1080/00107517608219056.

[53] J. Brady Scott and Ramandeep Kaur. "Monitoring Breathing Frequency, Pattern, and Effort". *Respiratory Care*, 2020. DOI: 10.4187/respcare.07439.

[54] Andreas Voskrebenzev and Jens Vogel-Claussen. "Proton MRI of the Lung: How to Tame Scarce Protons and Fast Signal Decay". *Journal of Magnetic Resonance Imaging*, 2021. DOI: 10.1002/jmri.27122.

[55] David M. L. Lilburn, Galina E. Pavlovskaya, and Thomas Meersmann. "Perspectives of hyperpolarized noble gas MRI beyond 3He". *Journal of Magnetic Resonance*, 2013. DOI: 10.1016/j.jmr.2012.11.014.

[56] "Pulmonary imaging". June 2022.

[57] Kevin M. Johnson, Sean B. Fain, Mark L. Schiebler, and Scott Nagle. "Optimized 3D ultrashort echo time pulmonary MRI". *Magnetic Resonance in Medicine*, 2013. DOI: 10.1002/mrm.24570.

[58] Markus Weiger, Klaas P. Pruessmann, and Franciszek Hennel. "MRI with zero echo time: hard versus sweep pulse excitation". *Magnetic Resonance in Medicine*, 2011. DOI: 10.1002/mrm.22799.

[59] Shuyi Yang et al. “Clinical Potential of UTE-MRI for Assessing COVID-19: Patient- and Lesion-Based Comparative Analysis”. *Journal of Magnetic Resonance Imaging*, 2020. DOI: 10.1002/jmri.27208.

[60] Govind B. Chavhan, Paul S. Babyn, Bhavin G. Jankharia, Hai-Ling M. Cheng, and Manohar M. Shroff. “Steady-State MR Imaging Sequences: Physics, Classification, and Clinical Applications”. *RadioGraphics*, 2008. DOI: 10.1148/rg.284075031.

[61] Grzegorz Bauman and Oliver Bieri. “Balanced steady-state free precession thoracic imaging with half-radial dual-echo readout on smoothly interleaved archimedean spirals”. *Magnetic Resonance in Medicine*, 2020. DOI: 10.1002/mrm.28119.

[62] Grzegorz Bauman, Nam G. Lee, Ye Tian, Oliver Bieri, and Krishna S. Nayak. “Submillimeter lung MRI at 0.55 T using balanced steady-state free precession with half-radial dual-echo readout (bSTAR)”. *Magnetic Resonance in Medicine*, 2023. DOI: 10.1002/mrm.29757.

[63] Mathieu Lederlin and Yannick Crémillieux. “Three-dimensional assessment of lung tissue density using a clinical ultrashort echo time at 3 tesla: a feasibility study in healthy subjects”. *Journal of magnetic resonance imaging: JMRI*, 2014. DOI: 10.1002/jmri.24429.

[64] Guillaume Chassagnon et al. “Use of Elastic Registration in Pulmonary MRI for the Assessment of Pulmonary Fibrosis in Patients with Systemic Sclerosis”. *Radiology*, 2019. DOI: 10.1148/radiol.2019182099.

[65] Adrienne E. Campbell-Washburn. “2019 American Thoracic Society BEAR Cage Winning Proposal: Lung Imaging Using High-Performance Low-Field Magnetic Resonance Imaging”. *American Journal of Respiratory and Critical Care Medicine*, 2020. DOI: 10.1164/rccm.201912-2505ED.

[66] Maren Zapke et al. “Magnetic resonance lung function–a breakthrough for lung imaging and functional assessment? A phantom study and clinical trial”. *Respiratory Research*, 2006. DOI: 10.1186/1465-9921-7-106.

[67] Rabea Klaar et al. “Ventilation and perfusion MRI at a 0.35 T MR-Linac: feasibility and reproducibility study”. *Radiation Oncology*, 2023. DOI: 10.1186/s13014-023-02244-1.

[68] Grzegorz Bauman, Orso Pusterla, and Oliver Bieri. “Ultra-fast Steady-State Free Precession Pulse Sequence for Fourier Decomposition Pulmonary MRI”. *Magnetic Resonance in Medicine*, 2016. DOI: 10.1002/mrm.25697.

[69] R. L. Ehman and J. P. Felmlee. “Adaptive technique for high-definition MR imaging of moving structures”. *Radiology*, 1989. DOI: 10.1148/radiology.173.1.2781017.

[70] Stefan Weick et al. “DC-gated high resolution three-dimensional lung imaging during free-breathing”. *Journal of Magnetic Resonance Imaging*, 2013. DOI: 10.1002/jmri.23798.

[71] Thomas A. Spraggins. “Wireless retrospective gating: Application to cine cardiac imaging”. *Magnetic Resonance Imaging*, 1990. DOI: 10.1016/0730-725X(90)90001-I.

[72] Y Wang, P J Rossman, R C Grimm, S J Riederer, and R L Ehman. "Navigator-echo-based real-time respiratory gating and triggering for reduction of respiration effects in three-dimensional coronary MR angiography." *Radiology*, 1996. DOI: 10.1148/radiology.198.1.8539406.

[73] Edward Brian Welch, Armando Manduca, Roger C. Grimm, Heidi A. Ward, and Clifford R. Jack Jr. "Spherical navigator echoes for full 3D rigid body motion measurement in MRI". *Magnetic Resonance in Medicine*, 2002. DOI: 10.1002/mrm.10012.

[74] James G. Pipe. "Periodically Rotated Overlapping ParallEL Lines with Enhanced Reconstruction (PROPELLER) MRI: Application to Motion Correction". 1999.

[75] Wenwen Jiang et al. "Motion robust high resolution 3D free-breathing pulmonary MRI using dynamic 3D image self-navigator". *Magnetic Resonance in Medicine*, 2018. DOI: 10.1002/mrm.26958.

[76] Christoph Kolbitsch, Radhouene Neji, Matthias Fenchel, Andrew Mallia, Paul Marsden, and Tobias Schaeffter. "Respiratory-resolved MR-based attenuation correction for motion-compensated cardiac PET-MR". *Physics in Medicine & Biology*, 2018. DOI: 10.1088/1361-6560/aaca15.

[77] Guang Li et al. "Direct comparison of respiration-correlated four-dimensional magnetic resonance imaging (4DMRI) reconstructed based on concurrent internal navigator and external bellows". *International journal of radiation oncology, biology, physics*, 2017. DOI: 10.1016/j.ijrobp.2016.11.004.

[78] Xucheng Zhu, Marilynn Chan, Michael Lustig, Kevin M. Johnson, and Peder E. Z. Larson. "Iterative motion-compensation reconstruction ultra-short TE (iMoCo UTE) for high-resolution free-breathing pulmonary MRI". *Magnetic Resonance in Medicine*, 2020. DOI: 10.1002/mrm.27998.

[79] Fei Tan et al. "Motion-compensated low-rank reconstruction for simultaneous structural and functional UTE lung MRI". *Magnetic Resonance in Medicine*, 2023. DOI: 10.1002/mrm.29703.

[80] Can Wu, Guruprasad Krishnamoorthy, Victoria Yu, Ergys Subashi, Andreas Rimner, and Ricardo Otazo. "4D lung MRI with high-isotropic-resolution using half-spoke (UTE) and full-spoke 3D radial acquisition and temporal compressed sensing reconstruction". *Physics in Medicine & Biology*, 2023. DOI: 10.1088/1361-6560/acace6.

[81] Yoshiharu Ohno, Hiroto Hatabu, and Hans-Ulrich Kauczor. "Pulmonary Functional Imaging: Basics and Clinical Applications". 1st ed. 2021 édition. Springer Nature Switzerland AG, Dec. 2020.

[82] R. R. Edelman, H. Hatabu, E. Tadamura, W. Li, and P. V. Prasad. "Noninvasive assessment of regional ventilation in the human lung using oxygen-enhanced magnetic resonance imaging". *Nature Medicine*, 1996. DOI: 10.1038/nm1196-1236.

[83] Edwin J.R. van Beek, Jim M. Wild, Hans-Ulrich Kauczor, Wolfgang Schreiber, John P. Mugler III, and Eduard E. de Lange. "Functional MRI of the lung using hyperpolarized 3-helium gas". *Journal of Magnetic Resonance Imaging*, 2004. DOI: 10.1002/jmri.20154.

[84] Bilal A. Tahir et al. "Spatial Comparison of CT-Based Surrogates of Lung Ventilation With Hyperpolarized Helium-3 and Xenon-129 Gas MRI in Patients Undergoing Radiation Therapy". *International Journal of Radiation Oncology*Biology*Physics*, 2018. DOI: 10.1016/j.ijrobp.2018.04.077.

[85] Marcus J. Couch et al. "Pulmonary ultrashort echo time 19F MR imaging with inhaled fluorinated gas mixtures in healthy volunteers: feasibility". *Radiology*, 2013. DOI: 10.1148/radiol.13130609.

[86] Ahmed F. Halaweish et al. "Perfluoropropane gas as a magnetic resonance lung imaging contrast agent in humans". *Chest*, 2013. DOI: 10.1378/chest.12-2597.

[87] Grzegorz Bauman et al. "Non-contrast-enhanced perfusion and ventilation assessment of the human lung by means of fourier decomposition in proton MRI". *Magnetic Resonance in Medicine*, 2009. DOI: 10.1002/mrm.22031.

[88] J. Biederer, C. P. Heussel, M. Puderbach, and M. O. Wielpuetz. "Functional magnetic resonance imaging of the lung". *Seminars in Respiratory and Critical Care Medicine*, 2014. DOI: 10.1055/s-0033-1363453.

[89] S. Sivaram Kaushik et al. "Single-Breath Clinical Imaging of Hyperpolarized 129Xe in the Airspaces, Barrier, and Red Blood Cells using an Interleaved 3D Radial 1-Point Dixon Acquisition". *Magnetic resonance in medicine*, 2016. DOI: 10.1002/mrm.25675.

[90] Susan R. Hopkins, Mark O. Wielpütz, and Hans-Ulrich Kauczor. "Imaging lung perfusion". *Journal of Applied Physiology (Bethesda, Md.: 1985)*, 2012. DOI: 10.1152/japplphysiol.00320.2012.

[91] Christopher S. Johns, Andrew J. Swift, Paul J. C. Hughes, Yoshiharu Ohno, Mark Schiebler, and Jim M. Wild. "Pulmonary MR angiography and perfusion imaging—A review of methods and applications". *European Journal of Radiology*, 2017. DOI: 10.1016/j.ejrad.2016.10.003.

[92] Yaron Gordon et al. "Dynamic contrast-enhanced magnetic resonance imaging: fundamentals and application to the evaluation of the peripheral perfusion". *Cardiovascular Diagnosis and Therapy*, 2014. DOI: 10.3978/j.issn.2223-3652.2014.03.01.

[93] Satoru Morita, Ai Masukawa, Kazufumi Suzuki, Masami Hirata, Shinya Kojima, and Eiko Ueno. "Unenhanced MR angiography: techniques and clinical applications in patients with chronic kidney disease". *Radiographics: A Review Publication of the Radiological Society of North America, Inc*, 2011. DOI: 10.1148/rg.312105075.

[94] Andrew J. Wheaton and Mitsue Miyazaki. "Non-contrast enhanced MR angiography: Physical principles". *Journal of Magnetic Resonance Imaging*, 2012. DOI: 10.1002/jmri.23641.

[95] Åsmund Kjørstad et al. "Quantitative lung perfusion evaluation using Fourier decomposition perfusion MRI". *Magnetic Resonance in Medicine*, 2013. DOI: 10.1002/mrm.24930.

[96] Åsmund Kjørstad, Dominique M. R. Corteville, Thomas Henzler, Gerald Schmid-Bindert, Frank G. Zöllner, and Lothar R. Schad. "Non-invasive quantitative pulmonary V/Q imaging using Fourier decomposition MRI at 1.5T". *Zeitschrift Fur Medizinische Physik*, 2015. DOI: 10.1016/j.zemedi.2015.02.002.

[97] Rui Carlos Sá et al. "Measurement of the distribution of ventilation-perfusion ratios in the human lung with proton MRI: comparison with the multiple inert-gas elimination technique". *Journal of Applied Physiology*, 2017. DOI: 10.1152/japplphysiol.00804.2016.

[98] Ryan Amelon, Kunlin Cao, Kai Ding, Gary E. Christensen, Joseph M. Reinhardt, and Madhavan L. Raghavan. "Three-dimensional characterization of regional lung deformation". *Journal of Biomechanics*, 2011. DOI: 10.1016/j.jbiomech.2011.06.009.

[99] Khurram Saleem Khan, James Meaney, Ignacio Martin-Loeches, and Daniel V. Collins. "MRI Assessment of Global and Regional Diaphragmatic Motion in Critically Ill Patients Following Prolonged Ventilator Weaning". *Medical Sciences (Basel, Switzerland)*, 2019. DOI: 10.3390/medsci7050066.

[100] Ayako Shimada et al. "Dynamic Quantitative Magnetic Resonance Imaging Assessment of Areas of the Lung During Free-Breathing of Patients with Chronic Obstructive Pulmonary Disease". *Academic Radiology*, 2022. DOI: 10.1016/j.acra.2021.03.034.

[101] Jing Cai et al. "Dynamic MRI of Grid-Tagged Hyperpolarized Helium-3 for the Assessment of Lung Motion during Breathing". *International journal of radiation oncology, biology, physics*, 2009. DOI: 10.1016/j.ijrobp.2009.03.051.

[102] Q. Chen, V. M. Mai, A. A. Bankier, V. J. Napadow, R. J. Gilbert, and R. R. Edelman. "Ultrafast MR grid-tagging sequence for assessment of local mechanical properties of the lungs". *Magnetic Resonance in Medicine*, 2001. DOI: 10.1002/1522-2594(200101)45:1<24::aid-mrm1004>3.0.co;2-6.

[103] Yogesh K. Mariappan, Kevin J. Glaser, Rolf D. Hubmayr, Armando Manduca, Richard L. Ehman, and Kiaran P. McGee. "MR elastography of human lung parenchyma: Technical development, theoretical modeling and in vivo validation". *Journal of Magnetic Resonance Imaging*, 2011. DOI: 10.1002/jmri.22550.

[104] Faisal Fakhouri, Huiming Dong, and Arunark Kolipaka. "Magnetic resonance elastography of the lungs: A repeatability and reproducibility study". *NMR in biomedicine*, 2019. DOI: 10.1002/nbm.4102.

[105] Tanguy Boucneau, Brice Fernandez, Peder Larson, Luc Darrasse, and Xavier Maître. "3D Magnetic Resonance Spirometry". *Scientific Reports*, 2020. DOI: 10.1038/s41598-020-66202-7.

[106] Chuan T. Foo, David Langton, Bruce R. Thompson, and Francis Thien. "Functional lung imaging using novel and emerging MRI techniques". *Frontiers in Medicine*, 2023. DOI: 10.3389/fmed.2023.1060940.

[107] Åsmund Kjørstad et al. "Quantitative lung ventilation using Fourier decomposition MRI; comparison and initial study". *Magnetic Resonance Materials in Physics, Biology and Medicine*, 2014. DOI: 10.1007/s10334-014-0432-9.

[108] André Fischer et al. "SElf-gated Non-Contrast-Enhanced FUnctional Lung imaging (SENCEFUL) using a quasi-random fast low-angle shot (FLASH) sequence and proton MRI". *NMR in Biomedicine*, 2014. DOI: 10.1002/nbm.3134.

[109] L. Mendes Pereira et al. "UTE-SENCEFUL: first results for 3D high-resolution lung ventilation imaging". *Magnetic Resonance in Medicine*, 2019. DOI: 10.1002/mrm.27576.

[110] Andreas Voskrebenzev et al. "Feasibility of quantitative regional ventilation and perfusion mapping with phase-resolved functional lung (PREFUL) MRI in healthy volunteers and COPD, CTEPH, and CF patients". *Magnetic Resonance in Medicine*, 2018. DOI: 10.1002/mrm.26893.

[111] Filip Klimeš et al. "3D phase-resolved functional lung ventilation MR imaging in healthy volunteers and patients with chronic pulmonary disease". *Magnetic Resonance in Medicine*, 2021. DOI: 10.1002/mrm.28482.

[112] Grzegorz Bauman and Oliver Bieri. "Matrix pencil decomposition of time-resolved proton MRI for robust and improved assessment of pulmonary ventilation and perfusion". *Magnetic Resonance in Medicine*, 2017. DOI: 10.1002/mrm.26096.

[113] David Bondesson et al. "Nonuniform Fourier-decomposition MRI for ventilation- and perfusion-weighted imaging of the lung". *Magnetic Resonance in Medicine*, 2019. DOI: 10.1002/mrm.27803.

[114] Christian Plathow, Max Schoebinger, Felix Herth, Siegfried Tuengerthal, Heinz-Peter Meinzer, and Hans-Ulrich Kauczor. "Estimation of pulmonary motion in healthy subjects and patients with intrathoracic tumors using 3D-dynamic MRI: initial results". *Korean Journal of Radiology*, 2009. DOI: 10.3348/kjr.2009.10.6.559.

[115] Christoph Kolb et al. "Regional Lung Ventilation Analysis Using Temporally Resolved Magnetic Resonance Imaging". *Journal of Computer Assisted Tomography*, 2016. DOI: 10.1097/RCT.0000000000000450.

[116] K. Toska and M. Eriksen. "Respiration-synchronous fluctuations in stroke volume, heart rate and arterial pressure in humans". *The Journal of Physiology*, 1993. DOI: 10.1113/jphysiol.1993.sp019958.

[117] Jie J. Cao et al. "Effects of respiratory cycle and body position on quantitative pulmonary perfusion by MRI". *Journal of magnetic resonance imaging: JMRI*, 2011. DOI: 10.1002/jmri.22527.

[118] Christian Fink et al. "Effect of inspiratory and expiratory breathhold on pulmonary perfusion: assessment by pulmonary perfusion magnetic resonance imaging". *Investigative Radiology*, 2005. DOI: 10.1097/01.rli.0000149252.42679.78.

[119] Gerhard A. Brecher and Charles A. Hubay. "Pulmonary Blood Flow and Venous Return During Spontaneous Respiration". *Circulation Research*, 1955. DOI: 10.1161/01.RES.3.2.210.

[120] Fei Tan. "Structural and Functional Ultra-short Echo Time (UTE) Proton Lung MRI: Techniques and Clinical Applications". PhD thesis. UCSF, 2023.

[121] Lukas Ebner, Jeff Kammerman, Bastiaan Driehuys, Mark L. Schiebler, Robert V. Cadman, and Sean B. Fain. "The role of hyperpolarized 129xenon in MR imaging of pulmonary function". *European Journal of Radiology*, 2017. DOI: 10.1016/j.ejrad.2016.09.015.

[122] M. S. Albert et al. "Biological magnetic resonance imaging using laser-polarized 129Xe". *Nature*, 1994. DOI: 10.1038/370199a0.

[123] Peter Bachert et al. "Nuclear magnetic resonance imaging of airways in humans with use of hyperpolarized 3He". *Magnetic Resonance in Medicine*, 1996. DOI: 10.1002/mrm.1910360204.

[124] Ummul Afia Shammi et al. "Comparison of Hyperpolarized 3He and 129Xe MR Imaging in Cystic Fibrosis Patients". *Academic Radiology*, 2022. DOI: 10.1016/j.acra.2021.01.007.

[125] Ziyi Wang et al. "Diverse cardiopulmonary diseases are associated with distinct xenon magnetic resonance imaging signatures". *The European respiratory journal*, 2019. DOI: 10.1183/13993003.00831-2019.

[126] Helen Marshall, Neil J. Stewart, Ho-Fung Chan, Madhwesha Rao, Graham Norquay, and Jim M. Wild. "In vivo methods and applications of xenon-129 magnetic resonance". *Progress in Nuclear Magnetic Resonance Spectroscopy*, 2021. DOI: 10.1016/j.pnmrs.2020.11.002.

[127] Ramanpreet Sembhi et al. "Feasibility of Dynamic Inhaled Gas MRI-Based Measurements Using Acceleration Combined with the Stretched Exponential Model". *Diagnostics (Basel, Switzerland)*, 2023. DOI: 10.3390/diagnostics13030506.

[128] Agilo Luitger Kern et al. "Regional investigation of lung function and microstructure parameters by localized 129Xe chemical shift saturation recovery and dissolved-phase imaging: A reproducibility study". *Magnetic Resonance in Medicine*, 2019. DOI: 10.1002/mrm.27407.

[129] Naz P. Taskiran et al. "Mapping Alveolar Oxygen Partial Pressure in COPD Using Hyperpolarized Helium-3: The Multi-Ethnic Study of Atherosclerosis (MESA) COPD Study". *Tomography (Ann Arbor, Mich.)*, 2022. DOI: 10.3390/tomography8050190.

[130] Ziyi Wang et al. "Using hyperpolarized 129Xe gas-exchange MRI to model the regional airspace, membrane, and capillary contributions to diffusing capacity". *Journal of Applied Physiology*, 2021. DOI: 10.1152/japplphysiol.00702.2020.

[131] Helen Marshall et al. "Peripheral and proximal lung ventilation in asthma: Short-term variation and response to bronchodilator inhalation". *Journal of Allergy and Clinical Immunology*, 2021. DOI: 10.1016/j.jaci.2020.11.035.

[132] Paul J. C. Hughes et al. "Assessment of the influence of lung inflation state on the quantitative parameters derived from hyperpolarized gas lung ventilation MRI in healthy volunteers". *Journal of Applied Physiology*, 2019. DOI: 10.1152/japplphysiol.00464.2018.

[133] Marcel Gutberlet et al. "Repeatability of Regional Lung Ventilation Quantification Using Fluorinated (19F) Gas Magnetic Resonance Imaging". *Academic Radiology*, 2019. DOI: 10.1016/j.acra.2018.10.021.

[134] Mary A. Neal et al. “Optimized and accelerated 19 F-MRI of inhaled perfluoropropane to assess regional pulmonary ventilation”. *Magnetic Resonance in Medicine*, 2019. DOI: 10.1002/mrm.27805.

[135] Ipshita Bhattacharya et al. “Oxygen-enhanced functional lung imaging using a contemporary 0.55T MRI system”. *NMR in biomedicine*, 2021. DOI: 10.1002/nbm.4562.

[136] Eric T. Geier, Rebecca J. Theilmann, Chantal Darquenne, G. Kim Prisk, and Rui Carlos Sá. “Quantitative Mapping of Specific Ventilation in the Human Lung using Proton Magnetic Resonance Imaging and Oxygen as a Contrast Agent”. *Journal of Visualized Experiments: JoVE*, 2019. DOI: 10.3791/59579.

[137] Lee R. Dice. “Measures of the Amount of Ecologic Association Between Species”. *Ecology*, 1945. DOI: 10.2307/1932409.

[138] Wei Zha, Scott K. Nagle, Robert V. Cadman, Mark L. Schiebler, and Sean B. Fain. “Three-dimensional Isotropic Functional Imaging of Cystic Fibrosis Using Oxygen-enhanced MRI: Comparison with Hyperpolarized 3He MRI”. *Radiology*, 2019. DOI: 10.1148/radiol.2018181148.

[139] Yubing Tong et al. “Quantitative Dynamic Thoracic MRI: Application to Thoracic Insufficiency Syndrome in Pediatric Patients”. *Radiology*, 2019. DOI: 10.1148/radiol.2019181731.

[140] Francesca Pennati et al. “Quantitative multivolume proton-magnetic resonance imaging in patients with cystic fibrosis lung disease: comparison with clinical indicators”. *European Respiratory Journal*, 2019. DOI: 10.1183/13993003.02020-2017.

[141] A. Voskrebenzev et al. “Detection of chronic lung allograft dysfunction using ventilation-weighted Fourier decomposition MRI”. *American Journal of Transplantation: Official Journal of the American Society of Transplantation and the American Society of Transplant Surgeons*, 2018. DOI: 10.1111/ajt.14759.

[142] Tawfik Moher Alsady et al. “MRI-derived regional flow-volume loop parameters detect early-stage chronic lung allograft dysfunction”. *Journal of magnetic resonance imaging: JMRI*, 2019. DOI: 10.1002/jmri.26799.

[143] Jens Vogel-Claussen et al. “Phase-resolved Functional Lung (PREFUL) MRI-derived Ventilation and Perfusion Parameters Predict Future Lung Transplant Loss”. *Radiology*, 2023. DOI: 10.1148/radiol.221958.

[144] Gesa H. Pöhler et al. “Repeatability of Phase-Resolved Functional Lung (PREFUL)-MRI Ventilation and Perfusion Parameters in Healthy Subjects and COPD Patients”. *Journal of magnetic resonance imaging: JMRI*, 2021. DOI: 10.1002/jmri.27385.

[145] Andreas Voskrebenzev et al. “PREFUL MRI Depicts Dual Bronchodilator Changes in COPD: A Retrospective Analysis of a Randomized Controlled Trial”. *Radiology. Cardiothoracic Imaging*, 2022. DOI: 10.1148/ryct.210147.

[146] Till F. Kaireit et al. “Flow Volume Loop and Regional Ventilation Assessment Using Phase-Resolved Functional Lung (PREFUL) MRI: Comparison With 129 Xenon Ventilation MRI and Lung Function Testing”. *Journal of magnetic resonance imaging: JMRI*, 2021. DOI: 10.1002/jmri.27452.

[147] Samal Munidasa et al. “Inter- and intravisit repeatability of free-breathing MRI in pediatric cystic fibrosis lung disease”. *Magnetic Resonance in Medicine*, 2023. DOI: 10.1002/mrm.29566.

[148] J. P. Dyke et al. “Assessment of lung ventilation of premature infants with bronchopulmonary dysplasia at 1.5 Tesla using phase-resolved functional lung magnetic resonance imaging”. *Pediatric Radiology*, 2023. DOI: 10.1007/s00247-023-05598-6.

[149] Efe Ilicak et al. “Phase-cycled balanced SSFP imaging for non-contrast-enhanced functional lung imaging”. *Magnetic Resonance in Medicine*, 2022. DOI: 10.1002/mrm.29302.

[150] Edward Castillo et al. “Robust CT ventilation from the integral formulation of the Jacobian”. *Medical Physics*, 2019. DOI: 10.1002/mp.13453.

[151] Fei Tan et al. “Pulmonary Ventilation Analysis Using 1H Ultra-Short Echo Time (UTE) Lung MRI: A Reproducibility Study”. *bioRxiv*, 2023. DOI: 10.1101/2023.10.22.563196.

[152] Bilal A. Tahir et al. “Comparison of CT ventilation imaging and hyperpolarised gas MRI: effects of breathing manoeuvre”. *Physics in Medicine and Biology*, 2019. DOI: 10.1088/1361-6560/ab0145.

[153] Julius Frederik Heidenreich et al. “Lung Function in Patients with Cystic Fibrosis before and during CFTR-Modulator Therapy Using 3D Ultrashort Echo Time MRI”. *Radiology*, 2023. DOI: 10.1148/radiol.230084.

[154] Kamran Poorbahrami, David G. Mummy, Sean B. Fain, and Jessica M. Oakes. “Patient-specific modeling of aerosol delivery in healthy and asthmatic adults”. *Journal of Applied Physiology*, 2019. DOI: 10.1152/japplphysiol.00221.2019.

[155] David G. Mummy et al. “Hyperpolarized 129Xe MRI and Spectroscopy of Gas-Exchange Abnormalities in Nonspecific Interstitial Pneumonia”. *Radiology*, 2021. DOI: 10.1148/radiol.2021204149.

[156] Mu He, Wei Zha, Fei Tan, Leith Rankine, Sean Fain, and Bastiaan Driehuys. “A Comparison of Two Hyperpolarized 129Xe MRI Ventilation Quantification Pipelines: The Effect of Signal to Noise Ratio”. *Academic Radiology*, 2019. DOI: 10.1016/j.acra.2018.08.015.

[157] Laurie J. Smith et al. “Patterns of regional lung physiology in cystic fibrosis using ventilation magnetic resonance imaging and multiple-breath washout”. *European Respiratory Journal*, 2018. DOI: 10.1183/13993003.00821-2018.

[158] S. Sivaram Kaushik et al. “Diffusion-weighted hyperpolarized 129Xe MRI in healthy volunteers and subjects with chronic obstructive pulmonary disease”. *Magnetic Resonance in Medicine*, 2011. DOI: 10.1002/mrm.22697.

[159] Y. Xiao et al. “Evaluation of MRI to Ultrasound Registration Methods for Brain Shift Correction: The CuRIOUS2018 Challenge”. *IEEE Transactions on Medical Imaging*, 2020. DOI: 10.1109/TMI.2019.2935060.

[160] Anne-Christianne Kentgens et al. “Simultaneous multiple breath washout and oxygen-enhanced magnetic resonance imaging in healthy adults”. *Respiratory Medicine and Research*, 2023. DOI: 10.1016/j.resmer.2023.100993.

[161] Joseph G. Mammarappallil et al. "Utilization of 19F MRI for Identification of Iraq-Afghanistan War Lung Injury". *Military Medicine*, 2020. DOI: 10.1093/milmed/usz284.

[162] Mitchell Chen et al. "Delayed ventilation assessment using fast dynamic hyperpolarised Xenon-129 magnetic resonance imaging". *European Radiology*, 2020. DOI: 10.1007/s00330-019-06415-1.

[163] F. Klimeš et al. "Free-breathing quantification of regional ventilation derived by phase-resolved functional lung (PREFUL) MRI". *NMR in Biomedicine*, 2019. DOI: 10.1002/nbm.4088.

[164] Filip Klimeš et al. "Repeatability of dynamic 3D phase-resolved functional lung (PREFUL) ventilation MR Imaging in patients with chronic obstructive pulmonary disease and healthy volunteers". *Journal of magnetic resonance imaging: JMRI*, 2021. DOI: 10.1002/jmri.27543.

[165] Yubing Tong et al. "Thoracic Quantitative Dynamic MRI to Understand Developmental Changes in Normal Ventilatory Dynamics". *Chest*, 2021. DOI: 10.1016/j.chest.2020.07.066.

[166] Hana Kim et al. "Scoliosis Imaging: What Radiologists Should Know". *RadioGraphics*, 2010. DOI: 10.1148/rg.307105061.

[167] Laura L. Walkup et al. "Cyst Ventilation Heterogeneity and Alveolar Airspace Dilation as Early Disease Markers in Lymphangioleiomyomatosis". *Annals of the American Thoracic Society*, 2019. DOI: 10.1513/AnnalsATS.201812-880OC.

[168] Haidong Li et al. "Damaged lung gas exchange function of discharged COVID-19 patients detected by hyperpolarized 129Xe MRI". *Science Advances*, 2021. DOI: 10.1126/sciadv.abc8180.

[169] K. H. Carlsen and K. C. Lødrup Carlsen. "Tidal breathing analysis and response to salbutamol in awake young children with and without asthma". *The European respiratory journal*, 1994. DOI: 10.1183/09031936.94.07122154.

[170] Tawfik Moher Alsady, Jakob Ruschepaul, Andreas Voskrebenzev, Filip Klimes, Gesa Helen Poehler, and Jens Vogel-Claussen. "Estimating ventilation correlation coefficients in the lungs using PREFUL-MRI in chronic obstructive pulmonary disease patients and healthy adults". *Magnetic Resonance in Medicine*, 2024. DOI: 10.1002/mrm.29982.

[171] Laura L. Walkup et al. "Xenon-129 MRI detects ventilation deficits in paediatric stem cell transplant patients unable to perform spirometry". *The European respiratory journal*, 2019. DOI: 10.1183/13993003.01779-2018.

[172] Brian B. Avants, Nicholas J. Tustison, Jue Wu, Philip A. Cook, and James C. Gee. "An Open Source Multivariate Framework for n-Tissue Segmentation with Evaluation on Public Data". *Neuroinformatics*, 2011. DOI: 10.1007/s12021-011-9109-y.

[173] Peter J. Niedbalski and Zackary I. Cleveland. "Improved preclinical hyperpolarized 129 Xe ventilation imaging with constant flip angle 3D radial golden means acquisition and keyhole reconstruction". *NMR in biomedicine*, 2021. DOI: 10.1002/nbm.4464.

[174] Cheng Wang et al. "Abnormal dynamic ventilation function of COVID-19 survivors detected by pulmonary free-breathing proton MRI". *European Radiology*, 2022. DOI: 10.1007/s00330-022-08605-w.

[175] Nancy Y. Lin et al. "129Xe MRI as a measure of clinical disease severity for pediatric asthma". *Journal of Allergy and Clinical Immunology*, 2021. DOI: 10.1016/j.jaci.2020.11.010.

[176] David G. Mummy et al. "Mucus Plugs in Asthma at CT Associated with Regional Ventilation Defects at 3He MRI". *Radiology*, 2022. DOI: 10.1148/radiol.2021204616.

[177] Sarah Svenningsen et al. "Reproducibility of Hyperpolarized 129Xe MRI Ventilation Defect Percent in Severe Asthma to Evaluate Clinical Trial Feasibility". *Academic Radiology*, 2021. DOI: 10.1016/j.acra.2020.04.025.

[178] Jessica M. Oakes, David G. Mummy, Kamran Poorbahrami, Wei Zha, and Sean B. Fain. "Patient-Specific Computational Simulations of Hyperpolarized ^3He MRI Ventilation Defects in Healthy and Asthmatic Subjects". *IEEE Transactions on Biomedical Engineering*, 2019. DOI: 10.1109/TBME.2018.2872845.

[179] Kun Qing et al. "Probing changes in lung physiology in COPD using CT, perfusion MRI and hyperpolarized xenon-129 MRI". *Academic radiology*, 2019. DOI: 10.1016/j.acra.2018.05.025.

[180] Yoshinori Fuseya et al. "Complementary regional heterogeneity information from COPD patients obtained using oxygen-enhanced MRI and chest CT". *PLoS ONE*, 2018. DOI: 10.1371/journal.pone.0203273.

[181] Dave Singh et al. "Effect of indacaterol/glycopyrronium on ventilation and perfusion in COPD: a randomized trial". *Respiratory Research*, 2022. DOI: 10.1186/s12931-022-01949-3.

[182] Tanguy Boucneau. "Magnetic resonance imaging of respiratory mechanics". PhD thesis. Université Paris Saclay (COmUE), July 2019.

[183] Tanguy Boucneau et al. "AZTEK: Adaptive zero TE k-space trajectories". *Magnetic Resonance in Medicine*, 2021. DOI: 10.1002/mrm.28483.

[184] Jeffrey Tsao and Sebastian Kozerke. "MRI temporal acceleration techniques". *Journal of Magnetic Resonance Imaging*, 2012. DOI: 10.1002/jmri.23640.

[185] Martin Uecker. "Berkeley Advanced Reconstruction Toolbox". In. Toronto, 2015.

[186] S. Klein, M. Staring, K. Murphy, M. A. Viergever, and J. P. W. Pluim. "elastix: A Toolbox for Intensity-Based Medical Image Registration". *IEEE Transactions on Medical Imaging*, 2010. DOI: 10.1109/TMI.2009.2035616.

[187] Damien Garcia. "Robust smoothing of gridded data in one and higher dimensions with missing values". *Computational Statistics & Data Analysis*, 2010. DOI: 10.1016/j.csda.2009.09.020.

[188] Ethan K. Brodsky, Alexey A. Samsonov, and Walter F. Block. "Characterizing and correcting gradient errors in non-cartesian imaging: Are gradient errors linear time-invariant (LTI)?" *Magnetic Resonance in Medicine*, 2009. DOI: 10.1002/mrm.22100.

[189] John Jackson, Albert Macovski, and Dwight Nishimura. “Low-frequency restoration”. *Magnetic Resonance in Medicine*, 1989. DOI: 10.1002/mrm.1910110213.

[190] Hákon Gudbjartsson and Samuel Patz. “The Rician Distribution of Noisy MRI Data”. *Magnetic resonance in medicine*, 1995.

[191] Sebastian Rosenzweig, H. Christian M. Holme, and Martin Uecker. “Simple auto-calibrated gradient delay estimation from few spokes using Radial Intersections (RING)”. *Magnetic Resonance in Medicine*, 2019. DOI: 10.1002/mrm.27506.

[192] Nicholas J. Tustison et al. “N4ITK: improved N3 bias correction”. *IEEE transactions on medical imaging*, 2010. DOI: 10.1109/TMI.2010.2046908.

[193] J. G. Sled, A. P. Zijdenbos, and A. C. Evans. “A nonparametric method for automatic correction of intensity nonuniformity in MRI data”. *IEEE transactions on medical imaging*, 1998. DOI: 10.1109/42.668698.

[194] Jon Louis Bentley. “Multidimensional binary search trees used for associative searching”. *Communications of the ACM*, 1975. DOI: 10.1145/361002.361007.

[195] Christoph Forman, Davide Piccini, Robert Grimm, Jana Hutter, Joachim Hornegger, and Michael O. Zenge. “Reduction of respiratory motion artifacts for free-breathing whole-heart coronary MRA by weighted iterative reconstruction”. *Magnetic Resonance in Medicine*, 2015. DOI: 10.1002/mrm.25321.

[196] T.F. Chan and L.A. Vese. “Active contours without edges”. *IEEE Transactions on Image Processing*, 2001. DOI: 10.1109/83.902291.

[197] Alejandro F. Frangi, Wiro J. Niessen, Koen L. Vincken, and Max A. Viergever. “Multiscale vessel enhancement filtering”. In: *Medical Image Computing and Computer-Assisted Intervention — MICCAI’98*. Ed. by William M. Wells, Alan Colchester, and Scott Delp. Lecture Notes in Computer Science. Berlin, Heidelberg: Springer, 1998. DOI: 10.1007/BFb0056195.

[198] Nobuyuki Otsu. “A Threshold Selection Method from Gray-Level Histograms”. *IEEE Transactions on Systems, Man, and Cybernetics*, 1979. DOI: 10.1109/TSMC.1979.4310076.

[199] Catalin I. Fetita, Françoise Prêteux, Catherine Beigelman-Aubry, and Philippe Grenier. “Pulmonary airways: 3-D reconstruction from multislice CT and clinical investigation”. *IEEE transactions on medical imaging*, 2004. DOI: 10.1109/TMI.2004.826945.

[200] Khiati Rezkellah Noureddine. “Vessel-based lung lobe partitioning in ultra-short time echo proton MRI for regional ventilation assessment | SPIE Medical Imaging”. In. San Diego, 2024.

[201] Fabian Isensee, Paul F. Jaeger, Simon A. A. Kohl, Jens Petersen, and Klaus H. Maier-Hein. “nnU-Net: a self-configuring method for deep learning-based biomedical image segmentation”. *Nature Methods*, 2021. DOI: 10.1038/s41592-020-01008-z.

[202] Nathalie Barrau et al. “Segmentation des lobes pulmonaires par nnUNet pour la spirométrie par IRM”. In. Grenoble, 2024.

[203] Damien Garcia. "smoothn (https://www.mathworks.com/matlabcentral/fileexchange/25634-smoothn), MATLAB Central File Exchange. Retrieved December 6, 2023." Dec. 2023.

[204] C. T. Metz, S. Klein, M. Schaap, T. van Walsum, and W. J. Niessen. "Nonrigid registration of dynamic medical imaging data using nD+t B-splines and a groupwise optimization approach". *Medical Image Analysis*, 2011. DOI: 10.1016/j.media.2010.10.003.

[205] Cécile Patte. "Personalized pulmonary mechanics : modeling, estimation and application to pulmonary fibrosis". PhD thesis. Institut Polytechnique de Paris, Dec. 2020.

[206] Frank Wilcoxon. "Individual Comparisons by Ranking Methods". *Biometrics Bulletin*, 1945. DOI: 10.2307/3001968.

[207] Andreas Voskrebenzev, Marcel Gutberlet, Lena Becker, Frank Wacker, and Jens Vogel-Claussen. "Reproducibility of fractional ventilation derived by Fourier decomposition after adjusting for tidal volume with and without an MRI compatible spirometer". *Magnetic Resonance in Medicine*, 2016. DOI: 10.1002/mrm.26047.

[208] James F. Morris, Arthur Koski, and Lavon C. Johnson. "Spirometric Standards for Healthy Nonsmoking Adults". *American Review of Respiratory Disease*, 1971. DOI: 10.1164/arrd.1971.103.1.57.

[209] Raphael Vallat. "Pingouin: statistics in Python". *Journal of Open Source Software*, 2018. DOI: 10.21105/joss.01026.

[210] K. Kaneko, J. Milic-Emili, M. B. Dolovich, A. Dawson, and D. V. Bates. "Regional distribution of ventilation and perfusion as a function of body position". *Journal of Applied Physiology*, 1966. DOI: 10.1152/jappl.1966.21.3.767.

[211] Abhilash S. Kizhakke Puliyakote et al. "Prone positioning redistributes gravitational stress in the lung in normal conditions and in simulations of oedema". *Experimental Physiology*, 2022. DOI: 10.1113/EP089037.

[212] Susan R. Hopkins et al. "Vertical gradients in regional lung density and perfusion in the supine human lung: the Slinky effect". *Journal of Applied Physiology (Bethesda, Md.: 1985)*, 2007. DOI: 10.1152/japplphysiol.01289.2006.

[213] Merryn H. Tawhai, Martyn P. Nash, Ching-Long Lin, and Eric A. Hoffman. "Supine and prone differences in regional lung density and pleural pressure gradients in the human lung with constant shape". *Journal of Applied Physiology (Bethesda, Md.: 1985)*, 2009. DOI: 10.1152/japplphysiol.00324.2009.

[214] K. C. Lødrup Carlsen, P. Magnus, and K. H. Carlsen. "Lung function by tidal breathing in awake healthy newborn infants". *The European Respiratory Journal*, 1994. DOI: 10.1183/09031936.94.07091660.

[215] Francisco Moreno and Harold A. Lyons. "Effect of body posture on lung volumes". *Journal of Applied Physiology*, 1961. DOI: 10.1152/jappl.1961.16.1.27.

[216] Johan Petersson et al. “Regional lung blood flow and ventilation in upright humans studied with quantitative SPECT”. *Respiratory Physiology & Neurobiology*, 2009. DOI: 10.1016/j.resp.2009.01.008.

[217] A. Cortney Henderson, Rui Carlos Sá, Rebecca J. Theilmann, Richard B. Buxton, G. Kim Prisk, and Susan R. Hopkins. “The gravitational distribution of ventilation-perfusion ratio is more uniform in prone than supine posture in the normal human lung”. *Journal of Applied Physiology (Bethesda, Md.: 1985)*, 2013. DOI: 10.1152/japplphysiol.01531.2012.

[218] Guido Musch et al. “Topographical distribution of pulmonary perfusion and ventilation, assessed by PET in supine and prone humans”. *Journal of Applied Physiology (Bethesda, Md.: 1985)*, 2002. DOI: 10.1152/japplphysiol.00223.2002.

[219] Annalisa J. Swan, Alys R. Clark, and Merryn H. Tawhai. “A computational model of the topographic distribution of ventilation in healthy human lungs”. *Journal of Theoretical Biology*, 2012. DOI: 10.1016/j.jtbi.2012.01.042.

[220] Hooman Hamedani, Stephen Kadlecek, Kai Ruppert, Yi Xin, Ian Duncan, and Rahim R. Rizi. “Ventilation Heterogeneity Imaged by Multibreath Wash-ins of Hyperpolarized 3He and 129Xe in Healthy Rabbits”. *The Journal of physiology*, 2021. DOI: 10.1113/JP281584.

[221] Gary H. Glover. “Overview of Functional Magnetic Resonance Imaging”. *Neurosurgery Clinics*, 2011. DOI: 10.1016/j.nec.2010.11.001.

[222] K. J. Friston and W. Penny. “Posterior probability maps and SPMs”. *NeuroImage*, 2003. DOI: 10.1016/s1053-8119(03)00144-7.

[223] Karl. J. Friston, J. Ashburner, C. D. Frith, J.-B. Poline, J. D. Heather, and R. S. J. Frackowiak. “Spatial registration and normalization of images”. *Human Brain Mapping*, 1995. DOI: 10.1002/hbm.460030303.

[224] K. J. Friston. “SPM - Statistical Parametric Mapping”.

[225] L. V. Kantorovich. “Mathematical Methods of Organizing and Planning Production”. *Management Science*, 1960. DOI: 10.1287/mnsc.6.4.366.

[226] Ying Huang et al. “Construction of Spatiotemporal Infant Cortical Surface Functional Templates”. *Medical image computing and computer-assisted intervention : MICCAI ... International Conference on Medical Image Computing and Computer-Assisted Intervention*, 2020. DOI: 10.1007/978-3-030-59728-3_24.

[227] J. P. Whiteley, D. J. Gavaghan, and C. E. W. Hahn. “A Mathematical Evaluation of the Multiple Breath Nitrogen Washout (MBNW) Technique and the Multiple Inert Gas Elimination Technique (MIGET)”. *Journal of Theoretical Biology*, 1998. DOI: 10.1006/jtbi.1998.0772.

[228] Mu He et al. “Generalized Linear Binning to Compare Hyperpolarized 129Xe Ventilation Maps Derived from 3D Radial Gas Exchange versus Dedicated Multi-Slice Gradient Echo MRI”. *Academic radiology*, 2020. DOI: 10.1016/j.acra.2019.10.016.

[229] Anass Chehboun and Mostafa El Hajjam. "IRM diaphragmatique : Séquences conventionnelles et spirométrie 3D à temps d'Echo Ultra-Court Evaluation chez les volontaires sains et les Dystrophies Neuro-Musculaires". PhD thesis. APHP Ambroise Paré, 2023.

[230] Jeremy Hull et al. "British Thoracic Society guideline for respiratory management of children with neuromuscular weakness". *Thorax*, 2012. DOI: 10.1136/thoraxjnl-2012-201964.

[231] Jonathan D. Finder et al. "Respiratory care of the patient with Duchenne muscular dystrophy: ATS consensus statement". *American Journal of Respiratory and Critical Care Medicine*, 2004. DOI: 10.1164/rccm.200307-885ST.

[232] Dongsheng Duan, Nathalie Goemans, Shin'ichi Takeda, Eugenio Mercuri, and Annemieke Aartsma-Rus. "Duchenne muscular dystrophy". *Nature Reviews Disease Primers*, 2021. DOI: 10.1038/s41572-021-00248-3.

[233] Kenji Rowel Q. Lim and Toshifumi Yokota. "Genetic Approaches for the Treatment of Facioscapulohumeral Muscular Dystrophy". *Frontiers in Pharmacology*, 2021. DOI: 10.3389/fphar.2021.642858.

[234] Boran Zhou and Xiaoming Zhang. "Lung Mass Density Analysis using Deep Neural Network and Lung Ultrasound Surface Wave Elastography". *Ultrasonics*, 2018. DOI: 10.1016/j.ultras.2018.05.011.

[235] Jackie Chiang, Kevan Mehta, and Reshma Amin. "Respiratory Diagnostic Tools in Neuromuscular Disease". *Children*, 2018. DOI: 10.3390/children5060078.

[236] Antonella Lo Mauro and Andrea Aliverti. "Physiology of respiratory disturbances in muscular dystrophies". *Breathe*, 2016. DOI: 10.1183/20734735.012716.

[237] Helena C. Maltezou, Androula Pavli, and Athanasios Tsakris. "Post-COVID Syndrome: An Insight on Its Pathogenesis". *Vaccines*, 2021. DOI: 10.3390/vaccines9050497.

[238] Sebastian Havervall et al. "Symptoms and Functional Impairment Assessed 8 Months After Mild COVID-19 Among Health Care Workers". *JAMA*, 2021. DOI: 10.1001/jama.2021.5612.

[239] Frédéric Schlemmer et al. "Respiratory recovery trajectories after severe-to-critical COVID-19: a 1-year prospective multicentre study". *European Respiratory Journal*, 2023. DOI: 10.1183/13993003.01532-2022.

[240] Jan K. Hennigs et al. "Respiratory muscle dysfunction in long-COVID patients". *Infection*, 2022. DOI: 10.1007/s15010-022-01840-9.

[241] Gaetano Scaramuzzo et al. "Long-term dyspnea, regional ventilation distribution and peripheral lung function in COVID-19 survivors: a 1 year follow-up study". *BMC Pulmonary Medicine*, 2022. DOI: 10.1186/s12890-022-02214-5.

[242] Jens Vogel-Claussen. "Ventilation Defects at 129Xe MRI in Postacute COVID-19 Syndrome: Back to Normal after 1 Year?" *Radiology*, 2023. DOI: 10.1148/radiol.230113.

[243] J. van Dixhoorn and H. J. Duivenvoorden. "Efficacy of Nijmegen Questionnaire in recognition of the hyperventilation syndrome". *Journal of Psychosomatic Research*, 1985. DOI: 10.1016/0022-3999(85)90042-x.

[244] Jan van Dixhoorn and Hans Folgering. "The Nijmegen Questionnaire and dysfunctional breathing". *ERJ Open Research*, 2015. DOI: 10.1183/23120541.00001-2015.

[245] Francesco Lombardi et al. "Residual respiratory impairment after COVID-19 pneumonia". *BMC Pulmonary Medicine*, 2021. DOI: 10.1186/s12890-021-01594-4.

[246] Katarzyna Anna Pietranis et al. "Effects of Pulmonary Rehabilitation on Respiratory Function and Thickness of the Diaphragm in Patients with Post-COVID-19 Syndrome: A Randomized Clinical Trial". *Journal of Clinical Medicine*, 2024. DOI: 10.3390/jcm13020425.

[247] L. Zocchi, J. W. Fitting, U. Majani, C. Fracchia, C. Rampulla, and A. Grassino. "Effect of pressure and timing of contraction on human rib cage muscle fatigue". *The American Review of Respiratory Disease*, 1993. DOI: 10.1164/ajrccm/147.4.857.

[248] M. B. Hershenson, Y. Kikuchi, G. E. Tzelepis, and F. D. McCool. "Preferential fatigue of the rib cage muscles during inspiratory resistive loaded ventilation". *Journal of Applied Physiology*, 1989. DOI: 10.1152/jappl.1989.66.2.750.

[249] Jong Hyuk Lee, Jae-Joon Yim, and Jimyung Park. "Pulmonary function and chest computed tomography abnormalities 6–12 months after recovery from COVID-19: a systematic review and meta-analysis". *Respiratory Research*, 2022. DOI: 10.1186/s12931-022-02163-x.

[250] R. Pellegrino et al. "Interpretative strategies for lung function tests". *The European Respiratory Journal*, 2005. DOI: 10.1183/09031936.05.00035205.

[251] Christer Janson et al. "Bronchodilator reversibility in asthma and COPD: findings from three large population studies". *The European Respiratory Journal*, 2019. DOI: 10.1183/13993003.00561-2019.

[252] Igor Barjaktarevic et al. "Clinical Significance of Bronchodilator Responsiveness Evaluated by Forced Vital Capacity in COPD: SPIROMICS Cohort Analysis". *International Journal of Chronic Obstructive Pulmonary Disease*, 2019. DOI: 10.2147/COPD.S220164.

[253] Ronald L. Sorkness et al. "Lung function in adults with stable but severe asthma: air trapping and incomplete reversal of obstruction with bronchodilation". *Journal of Applied Physiology (Bethesda, Md.: 1985)*, 2008. DOI: 10.1152/japplphysiol.00329.2007.

[254] Kun Li et al. "Influence of Emphysema and Air Trapping Heterogeneity on Pulmonary Function in Patients with COPD". *International Journal of Chronic Obstructive Pulmonary Disease*, 2019. DOI: 10.2147/COPD.S221684.

[255] N.G. Koulouris and G. Hardavella. "Physiological techniques for detecting expiratory flow limitation during tidal breathing". *European Respiratory Review*, 2011. DOI: 10.1183/09059180.00001911.

[256] M J Morris and D J Lane. "Tidal expiratory flow patterns in airflow obstruction." *Thorax*, 1981.

[257] Patrick Flood-Page et al. "A Study to Evaluate Safety and Efficacy of Mepolizumab in Patients with Moderate Persistent Asthma". *American Journal of Respiratory and Critical Care Medicine*, 2007. DOI: 10.1164/rccm.200701-085OC.

[258] Colin Powell, Stephen J. Milan, Kerry Dwan, Lynne Bax, and Nicola Walters. "Mepolizumab versus placebo for asthma". *Cochrane Database of Systematic Reviews*, 2015. DOI: 10.1002/14651858.CD010834.pub2.

[259] Peter Alter, Jan Orszag, Emiel F. M. Wouters, Claus F. Vogelmeier, and Rudolf A. Jörres. "Differences in the Measurement of Functional Residual Capacity Between Body Plethysmographs of Two Manufacturers". *International Journal of Chronic Obstructive Pulmonary Disease*, 2022. DOI: 10.2147/COPD.S363493.

[260] Erin Hopkins and Sandeep Sharma. "Physiology, Functional Residual Capacity". In: *StatPearls*. Treasure Island (FL): StatPearls Publishing, 2024.

[261] Carole Lazarus et al. "3D variable-density SPARKLING trajectories for high-resolution T2*-weighted magnetic resonance imaging". *NMR in biomedicine*, 2020. DOI: 10.1002/nbm.4349.

[262] Michael C. K Khoo. "Determinants of ventilatory instability and variability". *Respiration Physiology*, 2000. DOI: 10.1016/S0034-5687(00)00157-2.